



TECHNISCHE  
UNIVERSITÄT  
DARMSTADT

**Exploring first-order hiatal surfaces: mineralogical, geo-  
chemical and petrological characteristics of the post-Var-  
iscan nonconformity in Central Europe**

**at the Materials- and Geosciences**

**of the Technischen Universität Darmstadt**

submitted in fulfilment of the requirements for the  
degree of Doctor rerum naturalium  
(Dr. rer. nat.)

**Doctoral thesis  
by Fei Liang**

First assessor: Prof. Dr. Matthias Hinderer

Second assessor: Prof. Dr. Christoph Schüth

Darmstadt 2023

---

Fei, Liang – Exploring first-order hiatal surfaces: mineralogical, geo-chemical and petrological characteristics of the post-Variscan nonconformity in Central Europe

Darmstadt, Technische Universität Darmstadt,

Year thesis published in TUprints 2023

Date of the viva voce 31.05.2023

Published under CC BY-SA 4.0 International

<https://creativecommons.org/licenses/>

---

---

***11.12.2016, sunny***



---

## Declaration

Ich erkläre hiermit, die vorliegende Dissertation ohne Hilfe Dritter und nur mit den angegebenen Quellen und Hilfsmitteln angefertigt zu haben. Alle Stellen, die aus Quellen übernommen wurden, sind als solche kenntlich gemacht worden. Diese Arbeit hat in dieser oder ähnlicher Form noch keiner Prüfungsbehörde vorgelegen. Die schriftliche Fassung stimmt mit der elektronischen Fassung überein.

I hereby certify that the complete work to this Ph.D. thesis was done by myself and only with the use of the referenced literature and the described methods.

Darmstadt, den

Liang Fei



---

---

## Acknowledgment

---

During the three and a half years, with the great support from people here, I finally can complete the work for my Ph.D. project, I would like to express my sincerest appreciation to:

**Prof. Dr. Matthias Hinderer** for the supervision during my whole Ph.D. period and the possibility for me to be a Ph.D. student at the Institute of Applied Geosciences, T.U. Darmstadt. It was really a rough period during the first several months when I first arrived in Germany, without his support, my life in Germany would not get back on track that fast. I really learned a lot from him during the discussions, not only academic knowledge but also how to conduct scientific research. He is not just an excellent professor, but also a man with great quality.

**Dr. Jens Hornung** for his valuable suggestion for me to improve my English and reviews, and constructive advice for my manuscript.

**Dr. Adrian Linsel** for his sincerest help for nearly all the aspects in T.U. Darmstadt, including but not limited to revising the email content, showing me the university's facilities, driving, and helping me communicate with the scientific station for sample collection. He is really a nobleman.

**Dr. Dirk Scheuvs** for providing valuable professional advice on the petrographic characteristics and the time for reviewing my manuscript.

**Mr. Reimund Rosmann** for spending so much time helping me with these drill cores. There were a lot of trivial things, but he is always patient and helped me fix all the stuff.

**Ms. Gabriela Schubert** for her great support with all the sample preparation.

All other members of the Institute of Applied Geosciences, together with you, I really have a very enjoyable time.

**Scientific Center Grube Messel team, Dr. Sonja Wedmann, and Mr. Behr Bruno** provide precious samples to support most of my Ph.D. work.

The reviewers of my manuscripts for their constructive comments significantly improved the manuscripts.

**The China Scholarship Council** for providing very sufficient living expenses.

I would like to thank **Dr. Niu Jun** in particular, she did a lot of help and offered me great support during my Ph.D. period, she is one of the most important people in my life.

Finally, I would like to thank my parents **Liang Jihong** and **Wu Pingfang** for everything, for your special love and absolute trust.





---

---

## Preface

---

This Ph.D. project focuses on the alteration of the post-Variscan nonconformity in Central Europe, the cumulative thesis is structured into five parts and includes three papers with two published and one accepted.

**Chapter 1** introduced the thesis's overall topic, including a brief introduction of the geological background, the motivation of the Ph.D. project, and the analytical methods we applied for the research.

**Chapter 2** (first paper): Liang Fei, Niu Jun, Adrian Linsel, Matthias Hinderer, Dirk Scheuvs, Rainer Petschick, 2021, Rock alteration at the post-Variscan nonconformity: implications for Carboniferous–Permian surface weathering versus burial diagenesis and paleoclimate evaluation, *Solid Earth*, 12, 1165–1184. <https://doi.org/10.5194/se-12-1165-2021>

This article contributes the fundamental base for the subsequent research by distinguishing the supergene and the following overprint of hypogene alteration. A workflow to eliminate the influence of the burial diagenesis for the weathering degree evolution for a paleo-weathering profile is developed. Both the surface weathering and burial diagenesis are carefully illustrated and the evolution of the weathering profile with climate variation and the diagenetic activity are also depicted.

**Chapter 3** (second paper): Liang Fei, Matthias Hinderer, Jens Hornung, 2022, Quantification of physical and chemical palaeo-weathering at the microscale: a new concept, *International Journal of Earth Sciences*, <https://doi.org/10.1007/s00531-022-02281-3>

This article develops a method for quantitatively evaluating the physical weathering degree. The physical weathering degree is represented by the index of physical weathering (IPW). After evaluating the chemical weathering degree with an optimized workflow for chemical weathering evaluation, the relationship between rock strength and chemical weathering degree (CIA) is developed based on the data from previous studies. With the relationship, the IPW is normalized as  $IPW_N$  to reflect the physical weathering intensity and enable the comparison of physical weathering among different types of rock.

In addition, based on the weathering rate of different minerals in the natural environment, a method for the normalization of chemical weathering is also developed. The result is represented as  $CIA_N$  (normalized chemical index of alteration) to reflect the chemical weathering intensity. Similar to the  $IPW_N$ , the  $CIA_N$  also enables the comparison of chemical weathering among different lithologies.

According to the results of both  $IPW_{(N)}$  and  $CIA_{(N)}$ , which may shed a light on paleoclimate research.

**Chapter 4** (third paper): Liang Fei, Matthias Hinderer, Jens Hornung, Palaeo-weathering of different basement rocks along a first order nonconformity - case study at the post-Variscan nonconformity (Germany) (accepted by CATENA):

<https://authors.elsevier.com/tracking/article/details.do?aid=107070&jid=CATENA&surname=Liang>).

This article summarizes the weathering characteristics of different types of rock along the Variscan nonconformity in SW Germany. Based on the methods developed in the previous two manuscripts, the weathering characteristics of macro/mesoscale, microscale, and the mineralogical, and geochemical characteristics for a spectrum of granitoid with similar texture

---

together with gabbroic diorite and basaltic andesite, which have similar composition but different texture are carefully described. This research set up a model for the weathering characteristics among the three different scales.

**Chapter 5** is the integrated result and conclusion of the three papers. In this part, all the methods and data are summed, and the applicability of the research aims is listed. The helpfulness of the methods and model proposed in all three papers for the weathering studies is presented, and the perspective of the applications for research such as paleoclimate and nonconformity reservoirs are discussed.

---

## Abstract

---

The post-Variscan nonconformity was formed during Permo-Carboniferous and widely distributed in Central Europe. While the tectonic evolution of the Variscan Orogeny has been well studied, research about the subsequent weathering and burial diagenesis is fairly scarce. The basement of the post-Variscan nonconformity in southwestern Germany contains different types of plutonic rock, which is partly covered by volcanic rock. The weathering profiles of both are well preserved. Compare to the modern weathering profiles, the paleo-weathering profile was overprinted by hypogene diagenesis. If it would be possible to compare quantitatively the weathering conditions with respect to the exposure time of different rocks, it would be possible to construct regional palaeoclimate and alteration models. Based on these quantitative models, predictions of rock alteration and its resulting properties are possible, which may help to assess reservoir and fluid flow characteristics. To achieve these goals the following scientific questions arise: (i) how to distinguish the supergene and hypogene alteration and minimize the errors of the weathering degree evaluation. In addition, for the weathering research about both the modern and paleo-weathering profiles, the physical weathering characteristics were less mentioned compared to the chemical weathering. Among these research, the physical weathering characteristics were only qualitatively described, which surely leads to inconvenience for the weathering research. Therefore, (ii) it is necessary to develop a method to quantify the physical weathering degrees. However, as the susceptibilities of different types of rock to both physical and chemical weathering are varied, (iii) the weathering indices need to be normalized by the susceptibility to reflect the weathering intensity, which also enables the comparison of weathering characteristics among different types of rock. (iv) Finally, previous studies focus mainly on one aspect of the weathering characteristics, a systemically model among macro/mesoscale, microscale, and mineralogical and geochemical data never accrues, therefore, a systemically model for weathering evaluation is urgently needed.

To figure out the questions above, in total four drill cores with different basement lithologies and overlaid volcanic rock (gabbroic diorite and basaltic andesite, granodiorite, tonalite, and granite) from southern Germany (Sprendlinger Horst and Langenthal) were selected. In total 69 samples were collected and prepared into powder and thin section groups. The collected samples were measured by Inductively Coupled Plasma Mass Spectrometry (ICP-MS), X-ray fluorescence (XRF), and X-Ray Diffraction (XRD) for trace elements, major elements, and mineral compositions, the thin sections were also made, which are for the analysis by scanning electron microscope (SEM), backscattering electron microscope (BSE) and polarizing microscope.

The proportion of primary minerals overall increases from the top to the bottom while the secondary minerals have an opposite trend. The XRD results indicate the clay minerals are dominated by illite and a mix-layer of illite and smectite (I/S) accompanied by a minority of kaolinite, vermiculite, and chlorite. Other secondary minerals are mainly composite of calcite and dolomite with a minority of metallic oxide. The depletion or enrichment degree of the elements is quantified by the  $\tau$  value model, which is based on the relationship between the mobile elements and the immobile elements, such as Ti and Zr. The chemical weathering degree is quantified by the chemical index of alteration (CIA).

To distinguish the supergene weathering and hypogene diagenesis for a paleo-nonconformity, a new workflow is established. The secondary clay mineral aspect is distinguished with the anhedral and euhedral forms observed under the SEM, the clay minerals with anhedral forms are attributed to supergene alteration while the euhedral forms are attributed to hypogene diagenesis. For the aspect of mineral compositions, the composition of the parent rock is considered,

---

To compare both physical and chemical weathering intensity among different rock types, the physical weathering degree should be first quantified. To quantify the physical weathering, a method based on the ratio between the fracture area and the total area of the thin section under the polarizing microscope was developed. This method establishes a new index of physical weathering (IPW). To apply it regionally, normalization of the relevant rock strength along the weathering profile is crucial and enables the comparison of the physical intensity among different lithologies. For the normalization of chemical weathering indices, two new conceptions, the total weathering mass (TWM) and chemical weathering ability (CWA) were proposed based on the weathering rate among different mineral types. Similar to the normalization of IPW, the chemical index of alteration (CIA) is normalized by CWA to reflect chemical weathering intensity. With the results of both physical and chemical weathering intensity, the climate condition can be evaluated.

With the optimized workflow for the evaluation of both physical and chemical weathering degrees along the paleo-weathering profile, the weathering characteristics among macro/mesoscale, microscale, mineralogical and geochemical characteristics along the basement of post-Variscan nonconformity are described. Based on this, a comprehensive workflow for the evaluation of weathering degree can be developed. This workflow integrated the weathering characteristics under different scales and set up relationships among different scales of these characteristics. The physical weathering was qualitatively classified at the macro/mesoscale and quantitatively at the microscale. The chemical weathering was quantified by the mineralogical and geochemical characteristics. Compare to previous studies, the physical and chemical weathering intensity are also compared among different lithologies which can be applied to evaluate the paleoclimate directly.

The model and methods developed in the thesis are applied to the nonconformity in Sprendlinger Horst and Langenthal in southwestern Germany. The results show that the weathering products were overprinted by hypogene diagenesis. The hypogene diagenesis led enrichment of K, Cs Rb, and Ca. The input of K caused the transformation of smectite to illite and/or I/S. Both the inputs of K and Ca affect the evaluation of the chemical weathering degree. After correction of these two elements' concentration, the CIA values along the surface of the nonconformity yield between 66 and 97. After being normalized by CWA, the chemical weathering intensity is between 70 and 83. The maximum physical weathering degree is between 1.5 and 18 while the physical weathering intensity is between 0.02 and 4. The higher the weathering degree the more depletion of the mobile elements will be. In addition, the transformation among clay minerals and the precipitation of minerals such as dolomite point to a temperature interval of 100 to 300 °C for the circulating fluids during burial.

By the combination of the data from both fieldwork and laboratory analysis, an integrated model for the weathering evaluation is set up. In this model, the quantified chemical versus physical weathering intensity may shed a light on the research of palaeoclimate under which the nonconformity formed.

---

---

## Contents

---

Acknowledgment	V
Preface	VII
Abstract	IX
Contents	XI
Abbreviations	XV
List of Figures	XVII
List of Tables	XXII
1. .... Introduction	1
1.1. State of the art in research about paleo-weathering along nonconformities.....	1
1.1.1. Chemical weathering.....	1
1.1.2. Physical weathering.....	3
1.1.3. Weathering profiles overprinted by hypogene diagenesis.....	3
1.1.4. Applications to the research about paleoclimate and reservoir geology.....	5
1.2. Geological background.....	6
1.2.1. Geological evolution in Central Europe.....	6
1.2.2. Geological background in the Research area.....	7
1.2.3. Climate evaluation during Permian in Central Europe.....	9
1.3. Aims and the overall research steps.....	9
1.4. Sampling strategy and analytical methods.....	10
1.4.1. Sampling strategy.....	10
1.4.2. Analytical Methods.....	11
1.5. Research steps.....	12
2. .... Rock alteration at the post-Variscan nonconformity: implications for Carboniferous-Permian surface weathering versus burial diagenesis and paleoclimate evaluation	13
2.1. Author contributions.....	13
2.2. Introduction.....	14
2.3. Geological Setting.....	15
2.4. Materials and Methods.....	18
2.5. Results.....	20
2.5.1. Petrographic characteristics.....	20
2.5.2. Mineral Composition.....	22
2.5.3. Geochemical characteristics.....	23
2.6. Discussion.....	26
2.6.1. Chemical alteration.....	26
2.6.2. Quantification of elements transfer.....	29
2.6.3. Burial diagenesis.....	34
2.6.4. Implications for paleoclimate.....	35
2.7. Scenario for alteration at the post-Variscan nonconformity.....	37

2.8.	Conclusions.....	40
2.9.	Code availability.....	41
2.10.	Data availability.....	41
2.11.	Sample availability.....	41
2.12.	Supplement.....	41
2.13.	Competing interests.....	41
2.14.	Acknowledgements.....	41
2.15.	Financial support.....	41
2.16.	Review statement.....	42
3.....	Quantification of Physical and Chemical Paleoweathering at the Microscale - A New Concept	43
3.1.	Author contributions.....	43
3.2.	Statements and Declarations.....	44
3.3.	Introduction.....	44
3.4.	Integrated concept for the quantification of paleo-weathering.....	46
3.5.	Physical weathering degree quantification.....	46
3.5.1.	Fracture recognition and classification.....	47
3.5.2.	Quantification of the fracturing.....	49
3.5.3.	Quantification of the influence of chemical alteration on the rock strength.....	51
3.5.4.	Calculation of the index.....	53
3.5.5.	Accounting for spatial heterogeneity.....	55
3.6.	Chemical weathering index normalization.....	56
3.6.1.	Chemical weathering ability (CWA).....	56
3.6.2.	Normalization of chemical weathering indices using CWA.....	57
3.7.	Integrative evaluation of weathering conditions.....	60
3.8.	Case study.....	61
3.8.1.	Geological Setting.....	61
3.8.2.	Analytical Methods.....	64
3.8.3.	Results.....	66
3.9.	Discussion.....	78
3.9.1.	Integrative weathering evaluation in the research area.....	78
3.9.2.	Implications for paleoclimate research and for heterogeneity assessment of nonconformity reservoirs.....	81
3.10.	Perspectives.....	84
3.11.	Summary and conclusions.....	85
3.12.	Acknowledgement.....	86
4.....	Palaeo-weathering of different basement rocks along a first order nonconformity - case study at the post-Variscan nonconformity (Germany)	87
4.1.	Author contributions.....	87
4.2.	Introduction.....	88
4.3.	Geological setting.....	92

4.4.	Materials and Methods.....	94
4.4.1.	Physical and chemical weathering degree evaluation.....	95
4.4.2.	Sampling and analytical methods.....	99
4.5.	Results.....	102
4.5.1.	Macro- to mesoscale visual weathering characteristics.....	102
4.5.2.	Microscale visual weathering characteristics.....	106
4.5.3.	Mineralogical characteristics.....	109
4.5.4.	Geochemical weathering characteristics.....	110
4.5.5.	Weathering characteristics at the post-Variscan nonconformity.....	114
4.6.	Discussion.....	122
4.6.1.	Implications for the integrative weathering degree.....	122
4.6.2.	Disentangling weathering from hypogene diagenesis and tectonic preconditioning...	124
4.6.3.	Multiscale weathering characteristics.....	126
4.6.4.	Implications of the reconstructed weathering degree for the Permian land surface...	129
4.7.	Conclusion.....	131
4.8.	Acknowledgement.....	132
5.....	Conclusion	133
5.1.	Contribution to the research about weathering.....	133
5.2.	Accounting for paleo-weathering profile.....	134
6.....	Perspectives	136
	Reference	138
	Appendix	165
	Appendix II-I	165
	Appendix III-I	175
	Appendix IV-I	190
	Appendix IV-II	216





---

---

## Abbreviations

---

ICP-MS	Inductively Coupled Plasma Mass Spectrometry
XRF	X-ray fluorescence
XRD	X-Ray Diffraction
SEM	Scanning electron microscope
SEM-EDX	Scanning electron microscopy–energy dispersive X-Ray analysis
BSE	Backscattering electron microscope
I/S	Mix-layer of illite and smectite
CIA	Chemical index of alteration
IPW	Index of physical weathering
TWM	Total weathering mess
CWA	Chemical weathering ability
PIA	Plagioclase index of alteration
V	Vogt’s Residual Index
WIP	Weathering index of Parker
LILE	Large ion lithophile element
HFSE	High field strength elements
REE	Rare earth element
MGCZ	Mid-German Crystalline Zone
LOI	Loss on ignition
PM	Polarizing microscope
CIW	Chemical index of weathering
UCS	Uniaxial compressive strength
F <sub>cl</sub>	Fracture filled by clay
F <sub>x</sub>	Fracture filled by oxide
F <sub>c</sub>	Fracture filled by calcite
F <sub>p</sub>	Fracture in the parent rock
F <sub>w</sub>	Fracture formed before and/or during weathering process
F <sub>v</sub>	Void fracture
F <sub>b</sub>	Fractures overprinted by burial diagenesis

---

$A_{(Fe)}$	Total inspected area
$A_{(Fv)}$	Area of void fracture
$A_{(Fc)}$	Area of fractures filled by calcite
$A_{(Fcl)}$	Area of fractures filled by clay minerals
$A_{(Fw)}$	Area of filled fracture in the weathering zone
$A_{(Fp)}$	Area of the fractures within the parent rock
UTS	Uniaxial tensile strength
$UCS_p$	UCS of the parent rock
$UCS_w$	UCS of the weathering zone
$UCS_A$	Average UCS between the parent rock and the weathered zone
$IPW_N$	Normalized Index of physical weathering
$CIA_N$	Normalized chemical index of alteration
MAP	Mean annual precipitation
MAT	Mean annual temperature
PPM	Paleosol-paleoclimate model

---

---

## List of Figures

---

Figure 1-1. Weathering and burial diagenesis evaluation in the A-CN-K diagram (Based on (Nesbitt and Young (1984) and Panahi et al. (2000)).	4
Figure 1-2. Evolution of Mid-German Crystalline Rise (modified after Henk (1995)).	7
Figure 1-3. Geological units of Odenwald and the Permian stratigraphic framework of Sprendlinger Horst and Kraichgau Sunken (based on Stein (2001) and Becker et al. (2012), Lippolt and Hess (1983)).	8
Figure 1-4. Climate evolution From Permo-Carboniferous to the end of the Permian in Central Europe (Roscher and Schneider, 2006).	9
Figure 1-5. Working steps of the overall workflow.	12
Fig.2-1. Location and geology of the research area with the lithological section of the drilling GA1; note gap between 30 and 54 m drilling depth. Blue stars indicate sampling spots.	19
Fig. 2-2. Petrographic characteristic of the basement and the overlying volcanic rock in the GA1 drill core. (a) fresh gabbroic diorite (PM, z = 55:5 m); (b) gabbroic diorite (PM, z = 20:6 m) and fractured quartz grain; (c) gabbroic diorite (PM, z = 23:5 m) and recrystallized quartz coupled with a calcite filled in fracture; (d) gabbroic diorite (BSE, z = 21:5 m) and dolomite accompanied by quartz; (e) gabbroic diorite (BSE, z = 20:6 m) and partly weathered plagioclase. (f) basaltic andesite (PM, z = 17:8 m) and fresh plagioclase grains with the amygdaloid consisting of calcite and zeolite and chalcedony; (g) basaltic andesite (BSE, z = 13:9 m) secondary clay minerals with intact primary grain shapes; (h) basaltic andesite (BSE, z = 13:9 m) and I-S surrounded by kaolinite within one residual plagioclase grain shape; (i) basaltic andesite (SEM, z = 13:9 m) with kaolinite and adularia filled in the void. The abbreviations used in the figure and caption are as follows: PM– polarizing microscopy, z – depth below ground surface, Amp – amphibole, Kln – kaolinite, Adl – adularia, Bt – biotite, Cal – calcite, Pl – plagioclase, Zeo – zeolite, Chc – chalcedony, Dol – dolomite and Qz – quartz.	21
Fig.2-3. Mineral compositions of both Permian volcanic lava and Paleozoic basement rock in the GA1 drill core (measured by powder XRD).	23
Fig.2-4. Classification of rocks of the GA1 well with the TAS diagram and Revised Winchester-Floyd diagram. (A) samples from fresh and nearly fresh parts of basement; (B) samples from overlain lava profile	24
Fig.2-5. Major elements content (in wt%) of the basaltic andesite (A) and the gabbroic diorite (B) along the drill core profile.	25
Fig. 2-6. Representative trace elements content (in ppm) of basaltic andesite (A) and gabbroic diorite (B) along the drill core profile.	25
Fig.2-7. REE pattern of basaltic andesite (A) and gabbroic diorite (B) in different depths	26
Fig.2-8. Weathering indices with A-CN-K diagram of both basaltic andesite and gabbroic diorite before and after K correction; based on (Fedó et al., 1995; Nesbitt and Markovics, 1997)	28

Fig. 2-9. Elements characteristic, (A) CaO-Sr cross-plot of the samples from the GA1 drill core; (B) Relationship between the $\tau$ value and the porosity in the gabbroic diorite; (C) Relationship among Rb, Cs and K <sub>2</sub> O among sedimentary rocks, basaltic andesite and gabbroic diorite.....	31
Fig. 2-10. $\tau$ value features of basaltic andesite (A) and gabbroic diorite (B) in GA1 well.....	32
Fig. 2-11. Theoretical weathering tendency and tendency during burial diagenesis (Fedo et al., 1995), a-observed weathering trend for both basaltic andesite and gabbroic diorite; b-theoretical weathering trend for basaltic andesite; c-K-metasomatism trend of topmost basaltic andesite; d-K-metasomatism trend of the rest part of basaltic andesite; e-theoretical weathering trend for gabbroic diorite; f- K-metasomatism trend for gabbroic diorite.....	34
Fig.2-12. Reconstructed alteration model of GA1 well in Sprendlinger Horst before volcanic eruption around ca. 300 Ma; Abbreviations: Anat- anatase; Bt-biotite; Chl-chlorite; Hbl-hornblende; Hem-hematite; Ill-illite; Pl-plagioclase; Sm-smectite; Vrm-vermiculite.....	38
Fig. 2-13. Reconstructed alteration model of GA1 well in Sprendlinger Horst after volcanic eruption around 290 Ma; Abbreviations: Px-pyroxene.....	39
Fig. 2-14. Reconstructed alteration model of GA1 well in Sprendlinger Horst during burial in the Jurassic and Cretaceous; Abbreviations: Adl- adularia.....	39
Fig. 3-1 Workflow for physical weathering degree quantification.....	46
Fig.3-2. Different types of fractures were recognized under the microscope. (A) Fractures filled by carbonate; (B) Void fracture and fractures filled by clay minerals; (C) Fracture patterns within the thin section.....	49
Fig. 3-3. Quantification of the fracturing with ImageJ software. For details of the procedure see the text.....	51
Fig. 3-4 Empirical relationship between UCS and CIA (data from Ceryan et al, 2008a, 2008b; Erişiş et al., 2019; Khanlari et al., 2012; Thomson et al., 2014; Tuğrul, 1997).....	53
Fig. 3-5 The variation in the IPW with increasing view number and view distribution on thin sections from three different rock types in this case. A: view distribution strategy B: basaltic andesite; C: granodiorite; D: granite.....	56
Fig. 3-6. Relationship and definition of total weathering mass (TWM) chemical weathering ability (CWA) and chemical index of alteration (CIA). The contribution to the weathering index CIA of each type of mineral is represented by the area of the gray part of the triangle (example based on granite and basaltic andesite in this case).....	58
Fig. 3-7 Workflow for integrative weathering evaluation.....	61
Fig. 3-8 Location and geology of the research area in S-Hessia (SW-Germany, central Europe). Solid black lines within the map of Germany (upper left corner) are federal political boundaries. (A) Tectonic units in the research area and research locations. The upper rectangle corresponds to Fig. 3-8B, and the lower rectangle corresponds to Fig. 3-8C; (B) Lithologic composition of the research area on the Sprendlinger Horst. (C) Lithologic composition of the research area in Langenthal.....	62

Fig. 3-9 Lithological section of the GA1, GA2 and BK2/05 drill cores with emphasis on the weathered interval. Blue stars indicate the sampling locations. Note, the weathering degree : “extremely weathered, intermediate weathered, incipient weathered and fresh” is based on Fedo et al. (1995).....	63
Fig. 3-10 Petrographic characteristics of the basement and the overlying volcanic rock in the GA1 and GA2 drill cores: (A): 1) fresh gabbroic diorite (30 m); 2) gabbroic diorite (3 m), fractured feldspar grain filled by clay and carbonate minerals and void fracture; 3) gabbroic diorite (0 m), fractured quartz grains filled by calcite and void fractures; (B): 1) fresh basaltic andesite (5.4 m); 2) basaltic andesite (0.4 m), fractures are rare; 3) basaltic andesite (0 m), completely weathered feldspar grains with intact shape; (C): 1) fresh granodiorite (17.6 m); 2) monzogabbro (2.6 m), slightly weathered plagioclase; 3) granodiorite (0 m), fractures filled by clay minerals and void fractures in the middle of earlier fractures; (D): 1) fresh granite (10.9 m); 2) granite (0.8 m), highly weathered, fracture filled by carbonate and clay minerals; 3) granite (0 m), fractures filled by calcite and clay minerals. Abbreviations used in the figure and caption are as follows: Kln – kaolinite, Bt – biotite, Pl –plagioclase, Zeo – zeolite, Chc – chalcedony, kfs – K-feldspar and Qz – quartz. ....	67
Fig. 3-11 Mineral characteristics along the drill core profiles; the lithology legend refers to Fig. 3-9 .....	68
Figure 3-12. Rose diagram of fracture angle, (A) basaltic andesite part of GA1; (B) gabbroic diorite basement of GA1; (C) granodiorite basement of GA2; (D) granite basement of BK2/05 .....	70
Fig. 3-13 Fracture distribution and IPW values along the profiles; the lithology legend refers to Fig. 3-9. ....	71
Fig. 3-14 Calculated $\delta^{18}O$ values versus estimated temperatures of formation waters for GA1 and GA2 based on Equation (14) (Friedman and O’Neil, 1977).....	72
Fig. 3-15 $IPW_N$ along the granodiorite in GA2, basaltic lava in GA1 and granite in BK2/05 drill core profiles.....	74
Fig. 3-16 Major elements and CIA values along the GA1, GA2 and BK2/05 profiles; the lithology legend refers to Fig. 3-9.....	75
Fig. 3-17 A–CN–K diagram of the samples from GA1, GA2 and BK2/05 before (A) and after (B) K correction based on Nesbitt and Markovics (1997).....	77
Fig. 3-18 Characteristics of the original CIA values and normalized CIA values of granodiorite, basaltic andesite and gabbroic diorite based on granite along drill core profiles GA2, GA1 and BK2/05. ....	78
Fig. 3-19 Comprehensive weathering characteristics for GA2, GA1 and BK2/05; note that A to D are based on chronological order. Numbers are ratios of indices. The legend refers to Fig. 3-9 and 3-17. ....	80
Fig. 3-20 Relationship between the IPW and CIA and $CIA_N$ . Legend refers to Fig.3-17.....	81

Fig. 4-1. Location maps and schematic cross section from the Kraichgau Basin through the Odenwald Crystalline Complex to the Sprendlinger Horst. Locations and geologic context of the drill cores used in this study are shown.....	94
Fig. 4-2. Integrated work flow to evaluate the weathering degree. Procedure for evaluation of burial diagenesis is in the red frame and described in Liang et al. (2021). CIA = Chemical index of alteration, IPW = Index of physical weathering. ....	96
Fig. 4-3 the A-CN-K diagram with the ideal weathering trend (b) and K- metasomatism weathering trend (a).....	98
Fig. 4-4. Macro to meso-scale visual characteristics of the drill cores. Weathering degree according to Aggisttalis et al. (1996) and Borrelli et al. (2014). Further explanation see text. ....	101
Fig. 4-5a. Macro- to mesoscale visual characteristics of GA1 and GA2 drill cores. Legend for lithological logs see Fig. 4-4.....	103
Fig. 4-5b. Macro- to mesoscale visual characteristics of TB8 and BK2/05 drill cores. Legend for lithological logs see Fig. 4-4.....	105
Fig. 4-6a. Microscale visual characteristics of GA1 and GA2 drill cores. Legend for lithological logs see Fig. 4-4.....	107
Fig. 4-6b. Microscale visual characteristics of TB8 and BK2/05 drill cores. Legend for lithological logs see Fig. 4-4.....	108
Fig. 4-7. Primary and secondary mineral characteristics of the drill cores according to XRD powder measurements. Legend for lithological logs see Fig. 4-4.....	110
Fig. 4-8. Chondrite-normalized REE patterns.....	111
Fig. 4-9. $\tau$ values according to Nesbitt (1979) of the weathering profiles GA1 (A), GA2 (B), TB8(C) and BK2/05(D).....	112
Fig. 4-10. Assessment of the index of physical weathering IPW from microfractures in thin sections for the drill cores according to the method of Liang et al., (2022). The fracture area ratio corresponds to the IPW before normalization. ....	115
Fig. 4-11. Normalized index of physical weathering with respect to rock type and tectonic fractures. ....	116
Fig. 4-12. The weathering profiles in the A-CN-K diagram before (A) and after (B) correction of Ca and K.....	117
Fig. 4-13. $\tau_K$ value and clay mineral characteristics from XRD measurements.....	118
Fig. 4-14. Cross plot of Sr-CaO according to Brandstätter et al., (2018). Deviation from regression lines is interpreted as diagenetic overprint. ....	119
Fig.4-15. Original $CIA_{original}$ , corrected $CIA_{corr}$ for Ca and K, normalized $CIA_R$ based on granite in BK2/05 and time-normalized $CIA_N$ along the drill core profiles. ....	121

---

Fig. 4-16. (A) Angular rim of the fracture filled by clay minerals (TB8, z=14.5 m, SEM). (B) dissolved rim of the fracture filled by clay minerals (TB8, z=6.4 m, SEM), the abbreviations used in the figure and caption are as follows: z - depth, Pl - plagioclase.....125

Fig. 4-17. Comprehensive weathering characteristics along the drill core profiles. ....128

---

---

## List of Tables

---

Table 1-1 Chemical weathering indices .....	2
Table 1-2. Parameters values of different minerals for equation (1-1).....	3
Table 3-1 Parameter values of different minerals for Eq. 3-7 (White and Brantley, 2003).....	56
Table 3-2. Results from the methods proposed by Sheldon (2006), Lukens et al. (2016) and this study, note the unit for MAP is mm and MAT is °C. ....	83
Table 4-1. Difference of chemical weathering parameters for the selected lithologies according to Liang et al, (2022).....	120







---

## 1. Introduction

---

Nonconformity refers to a discontinuity in the geological record ranging over large temporal scales with a magmatic or metamorphic rock basement (Catuneanu, 1996). The remainder of the information in the basement plays a key role to understand the supergene and the subsequent hypogene alteration (Riebe et al., 2001, 2003). While the supergene alteration such as weathering, erosion is the key factor to understanding the interactions among lithosphere, atmosphere, and hydrosphere (Perri, 2020), the hypogene alteration provide a chance to understand the subsequent evolution of the weathering profile, such as the activities of the diagenetic fluids (Dill, 2010; Dill et al., 2016).

This thesis focus on the weathering characteristics of post-Variscan nonconformity in Central Europe. To address the supergene and hypogene diagenesis evolution, a new workflow to distinguish the supergene alteration and hypogene diagenesis has been established. It comprises a new method for physical weathering quantification, a new method for the normalization of physical and chemical weathering indices, and a new method to characterize the relationship between visual scale and analytical data. The combination of these methods provides methods to systemically depict the weathering characteristics, and the concept shade light for research to predict and quantify paleoclimate and reservoir geology from information hidden in non-conformities.

### 1.1. State of the art in research about paleo-weathering along nonconformities

#### 1.1.1. Chemical weathering

Chemical weathering in both modern and paleo-nonconformity has been well-studied (Nesbitt and Markovics, 1997; Santos et al., 2017; Tripathi and Rajamani, 1999). Among these studies, various indices to quantify the chemical weathering degree were proposed (Table 1-1). The base mechanism for the chemical weathering degree quantification can be divided into two groups:

(1) During the chemical weathering process, accompanied by the primary minerals such as feldspar and hornblende gradually transform into secondary minerals, the “mobile elements” such as Na, Ca, Mg, and K within the primary minerals will be gradually depleted, while “immobile element” Al trends stay in suit (e.g. Das et al., 2005; Nesbitt and Young, 1982). Therefore, the chemical weathering degree can be quantified based on the ratio between the content of the sum of the remainder of mobile elements and the Al. The quantification of the chemical weathering degree was first performed by Vogt (1927), which is called Vogt’s Residual Index (V), and applied to evaluate the maturity of the residual sediments such as glacial tills and marine clays. In 1982, Nesbitt and Young proposed the chemical index of alteration (CIA) with the ratio between  $\text{Al}_2\text{O}_3$  and the sum of  $\text{Al}_2\text{O}_3$ , CaO,  $\text{Na}_2\text{O}$ , and  $\text{K}_2\text{O}$  in molecular percent, the index was first applied to evaluate the degree of chemical alteration of the fine-grain sediments, and the results are used to assess the paleoclimate condition, as the higher values point to a relatively humid climate condition. However, the K (represented by  $\text{K}_2\text{O}$  in CIA) is a special element that is particularly more abundant than that in the protolith due to the overprint of burial diagenesis for the paleo-weathering profile (Fedo, et al., 1996; Jian et al., 2019), this effect is recognized as K-metamorphism. To eliminate the effects, Fedo (1995) proposed the plagioclase index of alteration (PIA) as the modified version of CIA, the value is the ratio between  $(\text{Al}_2\text{O}_3 - \text{K}_2\text{O})$  and  $(\text{Al}_2\text{O}_3 - \text{K}_2\text{O} + \text{CaO} + \text{Na}_2\text{O})$ . The PIA focuses on the alteration degree of plagioclase, with the content of  $\text{Al}_2\text{O}_3$  minus  $\text{K}_2\text{O}$  to eliminate the influence of K-feldspar.

(2) The second group of the method for chemical weathering quantification is based on the susceptibility of different elements to weathering. This is expressed by the strength of the element-to-oxygen bonds (Parker, 1970). Elements being depleted from the primary minerals should first be broken from the element-to-oxygen bond and be ionic form. Based on this mechanism, the weathering index of Parker (WIP) is expressed by the sum of the ratio between element concentration and the bond strength of the element with oxygen. This index is appropriate for the evaluation of chemical weathering for the rocks under relatively humid conditions where hydrolysis is the main weathering process.

With the weathering indices, the weathering degree along a weathering profile can be quantitatively illustrated.

Table 1-1 Chemical weathering indices

Index	Equation	Reference
Vogt's Residual Index (V)	$V = \frac{Al_2O_3 + K_2O}{MgO + CaO + Na_2O}$	Vogt (1927)
Chemical Index of Alteration (CIA)	$CIA = \frac{100 * Al_2O_3}{Al_2O_3 + CaO + Na_2O + K_2O}$	Nesbitt and Young (1982)
Plagioclase Index of Alteration (PIA)	$PIA = \frac{100 * Al_2O_3 - K_2O}{Al_2O_3 + CaO + Na_2O - K_2O}$	Fedo et al. (1995)
Weathering Index of Parker (WIP)	$WIP = 100 * \left( \frac{2Na_2O}{0.35} + \frac{MgO}{0.9} + \frac{K_2O}{0.25} + \frac{CaO}{0.7} \right)$	Parker (1970)

However, due to the difference in mineral compositions among different types of rock, the value range of the weathering index is varied. Such as the CIA, the maximum value for different types of rock is 100 (Nesbitt and Young, 1982), however, for fresh basaltic rock, the CIA values range between 30 and 45, while for the granites and granodiorite, the values are from 45 to 55 (McLennan, 1993).

Another issue is that for different minerals the susceptibility to chemical, weathering is also different (White et al., 2001a). This means under the same chemical weathering intensity, different types of lithologies show different chemical weathering degrees (Borrelli et al., 2014; Nesbitt and Young, 1984). On the other hand, if the chemical weathering indices such as CIA are normalized by the corresponding weathering susceptibility, the chemical weathering intensity among different lithologies can be compared among different lithologies. Previous studies did a lot of efforts to simulate the chemical weathering rate for minerals such as plagioclase, K-feldspar, biotite, and hornblende (e.g. Beig and Lüttge, 2006; Chou. and Wollast, 1985; Chou and Wollast, 1984; Oelkers and Schott, 1995; Schott et al., 1981). Most of the experiments were conducted in the laboratory and performed with fresh minerals, however, the weathering rate of these minerals between the laboratory and natural environment is different (White and Brantley, 2003). Finally, based on an experiment last more than six-year, White and Brantley (2003) developed the relationships between the weathering rate of plagioclase, K-feldspar, biotite, and hornblende with time in the natural environment :

$$R = 10^A * t^b \quad \text{(Eq. 1-1)}$$

Table 1-2. Parameters values of different minerals for equation (1-1).

Minerals	A	b	r (coefficient)
K-feldspar	-12.49±0.32	-0.647 ± 0.076	0.83
Hornblende	-12.67±0.22	-0.623 ± 0.067	0.92
Biotite	-12.32±0.25	-0.603 ± 0.073	0.83
Plagioclase	-12.46±0.16	-0.564 ± 0.046	0.89

Which provides a chance to normalize the chemical weathering indices and reflect the chemical weathering intensity.

### 1.1.2. Physical weathering

The definition of physical weathering refers to the process that breaks rocks apart without changing their chemical composition (Earle, 2015). The rock may be fractured and broken into fragments due to such as frequent temperature variation and frost wedging. Until present, most of the research about physical weathering is qualitative. The research about physical weathering mainly focuses on the factors that influence the physical weathering process. Camuffo (1995) reviewed the physical agents for physical weathering, which detailed discussed the influence of wind and water. Matsuoka et al. (1996) describe the influence of the salts content in the rock, that with more saline in the rock, the rock will easier to be weathered. McFadden et al. (2005) dated the characteristics of macro/mesoscale fractures under the direction of solar heating in a desert zone, and the relationship between thermal stress variation and the sunlight direction was depicted. In addition, the relationship between physical weathering and landscape evolution is also well illustrated (Phillips, 2005).

For the evaluation of the physical weathering degree, Aggistalis et al. (1996) developed a Rock Weathering Classification based on the physical property such as hardness. The diagram was gradually optimized and enriched by subsequent research and divide the weathering degree into five degrees: fresh, slightly weathered, moderately weathered, highly weathered, and completely weathered (Ceryan et al., 2008c; Chiu and Ng, 2014; Moon and Jayawardane, 2004a). However, the physical weathering degree is only a part of the diagram. Until 2006, a method for physical weathering quantification was proposed by Qin et al. (2006), in this research, a total dissolved solids (TDS) flux of the sediments per year in a river was applied to evaluate the regional physical weathering intensity. Another method for the physical weathering intensity evaluation was proposed by Shoenfelt et al. (2019), in the research, the content of primary Fe(II) silicates in the dust source was applied for the evaluation of physical weathering intensity, because of that, with more Fe(III) indicates a relative intense chemical weathering, in another way round, the physical weathering is weaker. Similar to the TDS, this research also describes the regional physical weathering intensity and can only be applied to modern physical weathering. The methods for physical weathering degree within a relatively small scale, such as a weathering profile are not appropriate, and both methods are not appropriate for the paleo-weathering profile.

### 1.1.3. Weathering profiles overprinted by hypogene diagenesis

For the research about the weathering of the paleo-weathering profile, the overprint of the hypogene diagenesis should always be considered. Because the hypogene diagenesis may promote the water-rock interaction process and change the chemical and mineral composition of the weathering profile, this will give distorted information and mislead the evaluation of the results of the weathering characteristics (Fedo, et al., 1996; Panahi et al., 2000; Zhou et al., 2022).

To eliminate the influence, based on the relations of the elements depletion rate of Na, Ca, and K during the weathering process and the weathering products, Nesbitt and Young (1984) developed the A-CN-K diagram to predict the weathering trend for the rock from the upper continental crust (Fig 1-1). Where A refers to the  $Al_2O_3$ , CN means the sum of CaO and  $Na_2O$ , and K refers to  $K_2O$ , all the content is in molecular weight, and the theoretical weathering trend should parallel to the A-CN axis for the rock in the upper continental crust (Fig.1-1a) (Nesbitt and Young, 1989a). With the lithologies including different contents of K, the weathering products are also different, for the lithologies containing a little amount of K, the weathering products tend to form smectite directly to kaolinite, and the illite is less expected regardless of the climate condition (Nesbitt and Young, 1984). While the weathering profile was buried and overprinted by hypogene alteration, the K will be preferentially enriched, and this situation reflected in the A-CN-K diagram will be the weathering trend excursing to the K apex (Fig.1-1c). Trend b reflects the transformation trend of weathering products. Based on the characteristics of the ideal weathering trend in the A-CN-K diagram, Panahi et al. (2000) proposed a method to correct the K content:

$$K_2O_{corr} = \frac{(m \cdot A + m \cdot CN)}{(1 - m)} \quad (\text{Eq. 1-2})$$

where

$$m = \frac{K}{(A + CN + K)} \quad (\text{Eq. 1-3})$$

In these two equations, the K, A and CN values for **m** calculation are from the protolith sample.

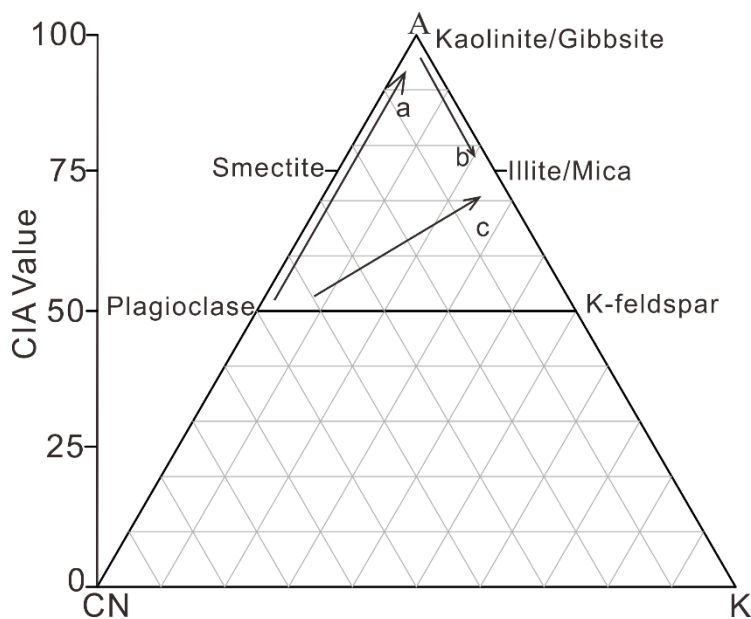


Figure 1-1. Weathering and burial diagenesis evaluation in the A-CN-K diagram (Based on (Nesbitt and Young (1984) and Panahi et al. (2000)).

Another element that needs to pay attention to is Ca. During hypogene alteration, the Ca from the diagenetic fluids may precipitate in the porosity as carbonate, if the diagenetic environment is alkaline. This will lead to a much enrichment of Ca compared to the original weathering profile and reduce the CIA value (Di Figlia et al., 2007; McLennan, 1993). To avoid this, the content of CaO should be from silicate minerals only. However, as it is difficult to separate the secondary Ca-

---

minerals and some accessory minerals such as apatite, McLennan (1993) proposed to use Na content as a reference to correct the Ca, and the detailed method is :  $\text{CaO}_{\text{rest}} = \text{CaO} - \text{P}_2\text{O}_5 \cdot 10/3$ , whereas the  $\text{P}_2\text{O}_5$  is related to apatite,  $\text{CaO}^* = \text{CaO}_{\text{rest}}$  when  $\text{CaO}_{\text{rest}} < \text{Na}_2\text{O}$ , otherwise,  $\text{CaO}^* = \text{Na}_2\text{O}$ . With both K and Ca correction, the CIA value for the evaluation of the original weathering degree can be acquired and accompanied by the A-CN-K diagram, the mineral transformation process can also be clarified.

#### **1.1.4. Applications to the research about paleoclimate and reservoir geology**

The results of the weathering characteristics have been widely applied for research such as paleoclimate and reservoir geology. Especially for the results of chemical weathering characteristics that are applied for the evaluation of paleoclimate (Nesbitt and Young, 1982). This is due to the consumption of  $\text{CO}_2$  in the atmosphere by the weathering of silicate minerals. With the decrease in the  $\text{CO}_2$ , the global temperature will also be decreased, together with the increase of the pH value of the ocean, thus, the biotype may also be adjusted (Kiehl and Shields, 2005; Schau and Henderson, 1983). Furthermore, with the decreasing temperature, a glacial epoch may appear and the chemical weathering intensity will be reduced. This would lead to a gradual increase of the  $\text{CO}_2$  concentration to increase the temperature and adjust the pH in the ocean (Berner, 1992; Berner and Berner, 1997; Huh, 2003). Therefore, a higher weathering degree may represent a more humid climate condition (Berner, 1992; Rasmussen et al., 2011). At present, these studies are generally performed with fine-grained sediments, and the climate condition is determined by the weathering degree and the weathering products (Reinhardt and Ricken, 2000; Sinisi et al., 2014). However, due to the effects such as multiple provenances and the overprint of burial diagenesis, the sediment materials may not able to reflect the weathering condition in the provenance area, this will mislead the evaluation of the paleo-climate (Jian et al., 2019; Liang et al., 2021). Another issue is that the weathering degree and the weathering products are varied for different types of rock under the same weathering condition. Therefore, it would be more meaningful to normalize the weathering degree (the value of weathering indices) to acquire the weathering intensity. Through this, a more accurate climate condition can be acquired.

As the physical weathering will fracture and break the basement rock, and the chemical weathering process will dissolve the rock and form porous minerals such as illite, and smectite, thus, with the weathering process going on, the petrophysical characteristics in the basement will also be modified (Taylor and Howard, 1998, 2000). Based on the petrophysical and mineralogical evolution of a weathering profile, Walter et al. (2018) illustrated the permeability, porosity, and porosity diameter variations. Since a nonconformity basement may consist of a variety range of lithologies, the key issue is still that, the responses of different rock types to the same weathering condition are different. This may also result from the heterogeneity of the nonconformity reservoir.

In summary, at present, research conducted on the paleo-weathering profile is more emphasis on chemical weathering. The chemical weathering characteristics, such as chemical weathering degree, mineral variations, and elements depletion and/ or enrichment can all be described quantitatively for both modern and paleo-weathering profiles. However, a systemic workflow to evaluate the weathering degree of the paleo-weathering profile and separate the surface weathering and burial diagenesis still hesitate. Moreover, other noticeable problems include that, the physical weathering degree is still not well quantified on a small scale, such as within a weathering profile or along the drill cores, especially for the paleo-weathering profile. Both chemical and physical weathering intensity is still not well comparable among different lithologies. In addition, while the research about chemical weathering focuses on the analytical data, the

---

microscale visual characteristics are somehow weekly mentioned, and the physical weathering focus on the macro/ meso-visual, a systemically model for the weathering characteristics among analytical scale, microscale, and macro/mesoscale visual characteristics is still not well developed.

## **1.2. Geological background**

### **1.2.1. Geological evolution in Central Europe**

The Variscan Orogeny was formed due to the convergence of the Gondwana and Laurussia continents accompanied by several microplates such as Avalonia and Armorica (Powell and Conaghan, 1973; Ziegler and Dèzes, 2005). With the southward subduction of Avalonia beneath the Armorica, in Central Europe, the Rheic Ocean gradually vanished and the Rheohercynian and Saxothuringian terranes collided and formed a magmatic arc which named Mid-German Crystalline Rise (MGCR) (Dörr and Stein, 2019a; Stein, 2001; Willner et al., 1991). Later, due to the exhumation of the oceanic lithosphere which began during the early Carboniferous, and ceased at the end of Carboniferous, the MGCR was uplifted and formed a highland (Willner et al., 1991), this highland was continuously weathered and eroded (Fig 1-2). The maximum exhumation rate was documented as 1.3mm/a from 363 to 334 Ma and yielded an average rate of 0.01mm/a, until Permo-Carboniferous, thermal subsidence dominated Central Europe (Henk, 1995). Meanwhile, the area was accumulated by the typical Permian red bed sediments which were called Rotliegend sediments. The age of the sediments was documented as around  $290 \pm 6$  Ma probable (Lippolt and Hess, 1983). Subsequently, the post-Variscan nonconformity was formed as the first-order nonconformity.

During early Permian, with the end of the Variscan orogeny, the magmatic activity was intensively throughout Central Europe and interfingering with the accumulated coarse-grained, arkosic alluvial fan to fluvial deposits (Becker et al., 2012a; Breitzkreuz et al., 2021). A time gap of around 30 Myrs is evaluated between the basement and the Permian Rotliegend basement (McCann et al., 2006; Opluštil and Cleal, 2007). The geological records are roughly consistently hiatus during the mid-Permian in Central Europe, during later Permian, with the transgression process, the region was flooded by a saline, epicontinental sea, and subsequently formed the Zechstein formation which yield an age around 257 Ma (Hagdorn and Mutter, 2011; Stolz et al., 2013).

During the whole Mesozoic, the geological background is relatively stable (Timar-Geng et al., 2006). From the early Triassic, several hundred meters of sediments consist of fluvial, lacustrine to eolian red-beds sediments which formed the so-called Buntsandstein formation (Scholze et al., 2017). From the mid-Triassic to the Jurassic, the sediments mainly consisted of clastic rock, carbonate, and evaporites, which formed the formations such as Muschelkalk and Keuper (Ziegler, 1982; Ziegler and Dèzes, 2005). The maximum thickness of the sediments is evaluated during the Jurassic (Schäfer, 2011). During this period, hydrothermal activities were ubiquitous throughout Central Europe. Especially in central and SW Germany, a temperature between 180 °C to around 270 °C is documented (Burisch et al., 2017)

From the late Cretaceous to Eocene, due to the Alpine Orogeny, subsequently formed the Upper Rhine Graben, the graben shoulder rose during the upper Pliocene at around 5 Ma accompanied by the sink of the graben axis which accumulated various fluvial, lacustrine, and marine sediments (Behrmann et al., 2005; Schumacher, 2002; Schwarz and Henk, 2005).



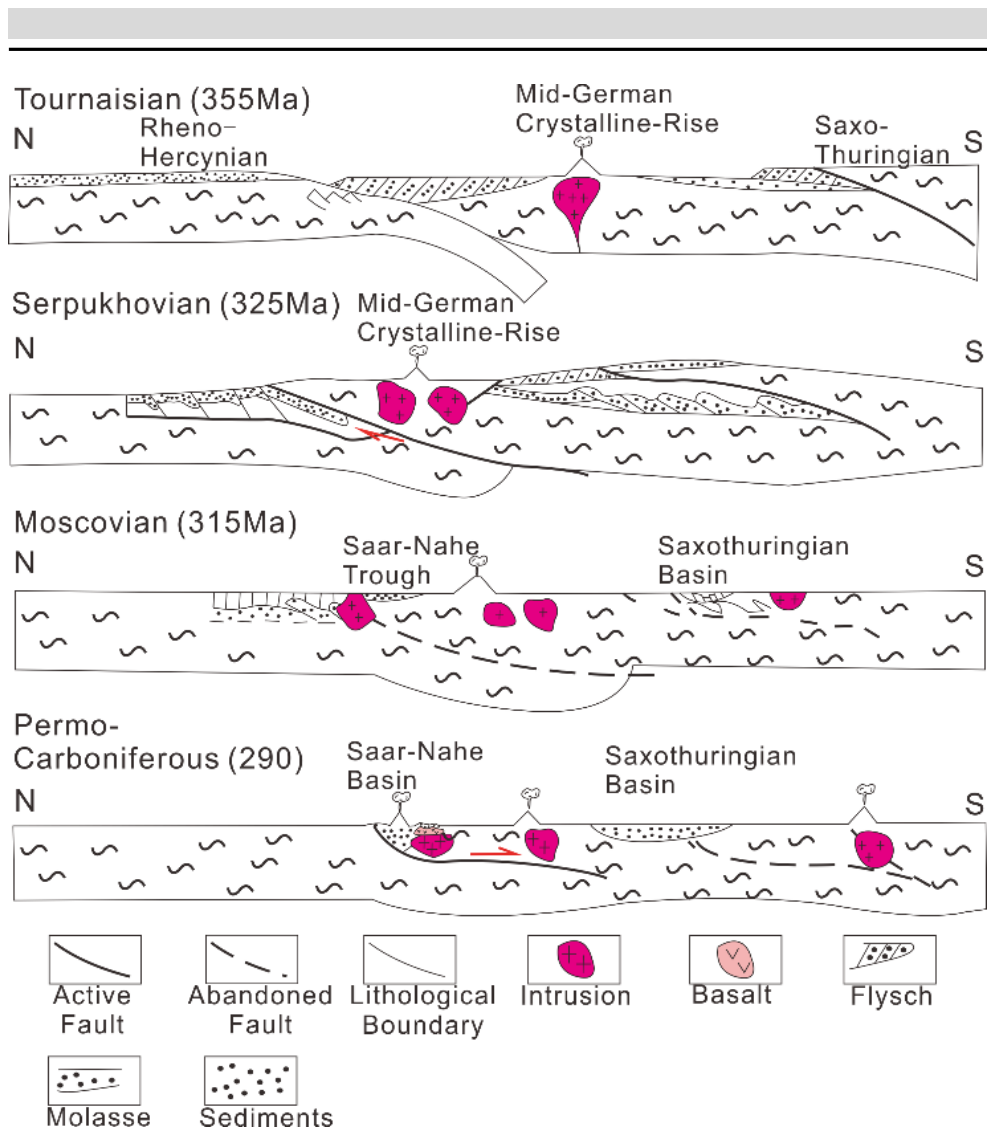


Figure 1-2. Evolution of Mid-German Crystalline Rise (modified after Henk (1995)).

### 1.2.2. Geological background in the Research area

The Odenwald is the biggest basement window of the post-Variscan basement in Central Europe (Zeh and Gerdes, 2010), it consists of two main parts which are separated by the Otzberg Fault, with the Böllstein Odenwald in the east and the Bergsträsser Odenwald in the west (Stein, 2001) (Fig 1-3). The main part of the Odenwald is the Bergsträsser Odenwald, which can be further divided into Unit I, Unit II, and Unit III from north to south. Unit I is the Frankensteiner complex which consists of amphibolite, diorite, and gabbros. Unit II is the so-called Flasergranitoid Zone, this unit consists mainly of granitoid such as gabbro, diorite, tonalite, granodiorite, and granite. Besides, there is also a minority of metamorphic rock, which is dominated by orthogneiss and paragneiss. Unit III can be subdivided into two parts, with the Weschnitz Pluton in the north and consists of paragneiss and magmatic gneiss and the Heidelberg granite and Tromm Granite in the south (Dörr and Stein, 2019a; Zeh and Will, 2008).

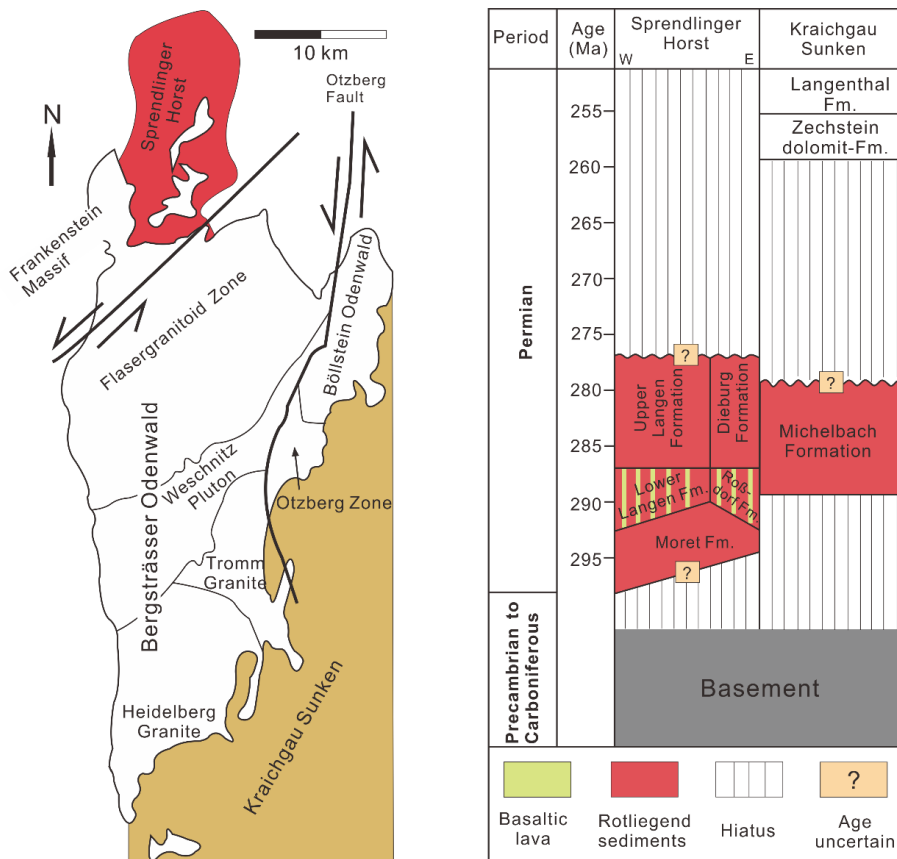


Figure 1-3. Geological units of Odenwald and the Permian stratigraphic framework of Spredlinger Horst and Kraichgau Sunken (based on Stein (2001) and Becker et al. (2012), Lippolt and Hess (1983)).

The Spredlinger Horst is in the north of the Odenwald, and the basement of the Spredlinger Horst is the extension of Unit I of the Odenwald, which consists of gabbroic rock and granitic rock. Overlying the basement (McCann, 1999), only Permian sediments remain with a maximum depth of c.a. 250 m (Marell, 1989; Mezger et al., 2013). The sediments consist of three groups: Moret Formation, Lower Langen Formation, and Upper Langen Formation (Becker et al., 2012a). The Moret Formation consists of coarse-grained fluvial sediments, which include breccias, coarse-grained sandstone, and siltstone; The Lower Langen Formation consists of coarse-grained alluvial sediments, which includes matrix-rich breccias, wackes, and siltstones, the sediments are interfingering with volcanic lava; The Upper Langen formation also consists of alluvial sediments but the volcanic lava is not found. Other younger sediments were eroded during exhumation (Matte, 1991; McCann, 1999), according to the characteristics of the nearby outcrop strata, a Zechstein formation with a thickness of 60 m is evaluated and followed by Buntsandstein formation with a thickness of up to 400 m. In the south of Unit III of Odenwald is Kraichgau Sunken, the basement of the extension of the Heidelberg Granite. The oldest sediment overlying the basement is Michelbach Formation, this formation consists of red-brown, light-brown, and grey color breccias with intercalated sandstone beds (Hug and Vero, 2008), which yield an age between 290 and 280 Ma (Edgar and Hubert, 2009). The Michelbach formation is followed by Zechstein and Buntsandstein formation, after a geological time gap of around 235 Ma is assumed, the sediments at the top belong to the Quaternary period (Hug and Vero, 2008).

### 1.2.3. Climate evaluation during Permian in Central Europe

During Permo-Carboniferous, with the formation of the supercontinent Pangaea, Central Europe was under a continental climate condition, and the climate was gradually changed from humid to super-arid during the whole Permian (Parrish, 1993). However, the overall aridization trend was interrupted by six relatively wet phases from the later Carboniferous to the end of the Permian. Based on the chronological order, the wet phases are documented as the Westphalian C/D, the Stephanian A, the Stephanian C, the lower Rotliegend, the upper Rotliegend I, and the wet phase during the later Permian (Fig. 1-4). These “wet phases” can be observed throughout the European region and are attributed the reason to the deglaciation events of the Gondwana ice cap (Roscher and Schneider, 2006).

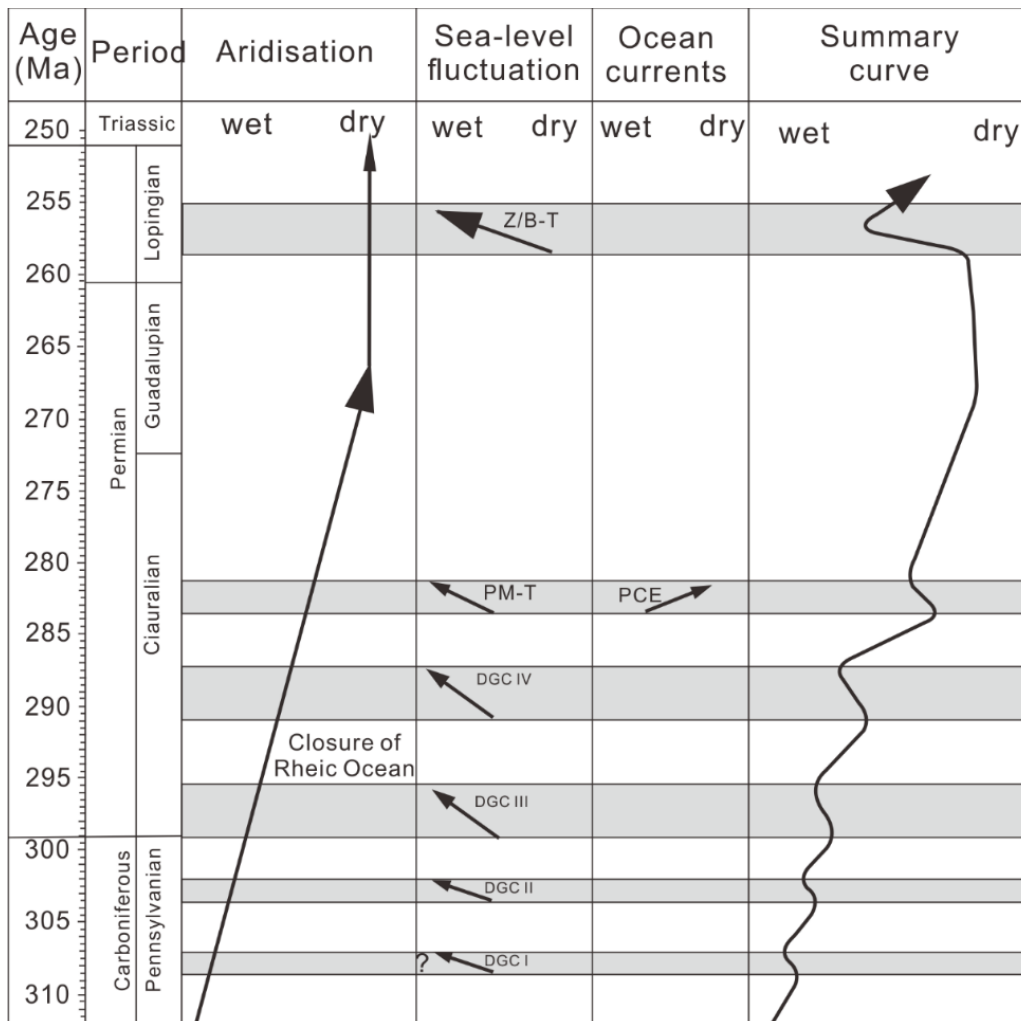


Figure 1-4. Climate evolution From Permo-Carboniferous to the end of the Permian in Central Europe (Roscher and Schneider, 2006).

### 1.3. Aims and the overall research steps

Based on the international research status of weathering and the geological background of SW Germany, with the samples from southwest Germany and the dates presented in this thesis, the study intends to address the following key issues:

- i. Illustrating both the chemical and physical weathering characteristics in post-Variscan nonconformity.

- 
- ii. Analyzing the burial diagenesis and the relevant overprint to the weathering profile.
  - iii. Distinguishing weathering and burial alteration processes (supergene vs. hypogene).
  - iv. Extracting the paleo-climate and paleo-environmental information contained in the weathering profile.
  - v. Developing a method for physical weathering quantification.
  - vi. Developing methods to compare both the chemical and physical weathering intensity among different types of rock.
  - vii. Deduce the influence of the weathering on the petrophysical characteristics and the application to reservoir geology.
  - viii. Set up a model to describe the relationship among analytical data, microscale, and macro/meso-scale visual characteristics.

## **1.4. Sampling strategy and analytical methods**

### **1.4.1. Sampling strategy**

Four representative drill cores penetrant the nonconformity from weathering to fresh part are selected for this thesis, the overlying sediments are at least 13 m to promise the basement part of the drill cores were not affected by the modern geological process. Among these, three of them are from the Spendlinger Horst (GA1, GA2, and TB8), and one is from the Kraichgau Sunken near Heidelberg (BK2/05). The drill core GA1 consists of Permian Rotliegend sediments, basaltic andesite, and the gabbroic diorite basement. Both the sediments and the basaltic andesite belong to Lower Langen Formation. The thickness of the former two parts is 13.9 m and 6.7 m, respectively, and the weathering part of the basement is around 3.9 m. Both GA2 and TB8 drill cores consist of Permian Rotliegend sediments and basement parts, and the overlying sediments in both drill cores belong to Moret Formation. While the lithology of the basement part in GA2 is granodiorite, the lithology in TB8 is tonalite. The thickness of the overlying sediments in GA2 and TB8 is around 55.7 m and 31 m respectively and the weathering depth in the basement is around 8.2 m and 14.5 m respectively. The thickness of the sediments in BK2/05 is 61.9 m, which consists of Permian Rotliegend, Zechstein sediments, Triassic Buntsandstein sediments, and the Quaternary sediments, and Permian Rotliegend sediments belong to Michelbach Formation with a thickness around 9.5 m, and the weathering depth in the granite basement is around 1.3 m.

In total 69 samples are collected for the analysis in this thesis. To figure out the influence of the overlying sediments, 7 samples from the sediment part of GA1 are collected from 6 m to 11 m with a sampling interval of 1 m. For the sampling along the basaltic andesite, the sampling interval is reduced to 0.4 m in the topmost part due to the rapid change of the weathering degree, and for the other part of this drill core and GA2 basement, the sampling interval is back to 1 m. Among these, 6 samples from the basaltic andesite, 11 samples from the basement of the GA1 drill core, and 13 samples from GA2 drill cores were collected. For the sampling work along the TB8 drill core, also due to the weathering variations from 0 to 1.5 m, the sampling interval is reduced to 0.5 m, and for the lower part from 1.5 to 14.5 m the interval is back to 1 m, and in total 17 samples were collected. Along the drill core BK2/05, to analyze the weathering variations within the centimeter scale, the sampling interval is mainly 0.2 m, and in total 22 samples were collected. All samples are stored at the Institute of Applied Geosciences, Technical University of Darmstadt, and can be required through the email: liang@geo.tu-darmstadt.de.

---

## 1.4.2. Analytical Methods

### *Petrographic characteristics analysis*

For the petrographic characteristics of the sample analysis, thin sections were made and analyzed by a polarizing microscope, scanning electron microscope (SEM), and backscattering electron microscope (BSE). The thin sections from the basement and the volcanic lava part were analyzed under the polarizing microscope for the analysis of the weathering characteristics. Based on the observation, the weathering characteristics along the drill core profile can be qualitatively described. For the physical weathering analysis, at least 15 visions were selected and the vision pictures were taken for further analysis step, the detailed process is described by Liang et al., (2022). As the weathering profile experienced both supergene and hypogene alteration (weathering and burial diagenesis), both processes may form the clay minerals such as illite and Kaolinite, however, for the minerals formed under different environments, the texture of the crystal is different, the minerals formed during burial diagenesis are trend to more euhedral (Clift et al., 2014; Raucsik and Varga, 2008). Besides, some minerals such as illite, and quartz can also act as a geothermometer. Therefore, to further describe the weathering characteristics and figure out the overprint of the burial diagenesis to the surface weathering, the SEM/BSE was applied.

### *Mineralogic characteristics analysis*

The mineral compositions and the proportions along the drill cores are measured by X-Ray Diffraction. Analysis was conducted on the bulk powder of both volcanic and basement rock. The technical details are described by (Liang et al., 2021) and Liang et al., (2022). With the results of the XRD, the mineralogic characteristics such as proportions and types can be quantitatively described and the weathering characteristics can be further described. Besides, the result also complements the petrographic characteristics. In case, due to the limitation of the chemical composition, the weathering process such as lithologies like tonalite, will be transformed directly from smectite to kaolinite, and the illite is less excepted. However, due to the weathering profile being overprinted by the burial diagenesis, the weathering products such as smectite and kaolinite may be transformed into illite with the K-rich diagenetic fluids during hypogene alteration. The primary weathering products can be predicted by the A-CN-K diagram, accompanied by the weathering trend in the A-CN-K diagram, and the mineral results can be further analyzed. Therefore, while applying the results, it is necessary to consider the types of protolith.

### *Bulk Geochemistry Analysis*

The major and trace elements were measured by X-ray fluorescence spectroscopy (XRF) and inductively coupled plasma mass spectrometry (ICP-MS), respectively. All the technical details are also documented by Liang et al., (2021) and Liang et al., (2022). During the weathering process, the mobile elements such as Na, Ca, K, Rb, and Cs tend to exist as ions in the fluids and are depleted from the protolith, while the relatively immobile elements such as Al, Ti, Zr, Nb are trend stay in the suit. The major elements, especially for Na, Ca, K, and Al, are applied for the calculation of weathering indices such as CIA and PIA to quantitatively describe the chemical weathering degree (Fedo, et al., 1996; Nesbitt and Young, 1982). The elements such as Ti and Zr are considered as immobile elements. Therefore, these two elements can be regarded as the reference elements to quantitatively evaluate the enrichment or depletion degree of other elements during both the surface weathering and /or burial diagenesis. The relative model is developed as the  $\tau$  value model, and a detailed explanation of the model is documented in by Liang et al., (2021). Based on the  $\tau$  value, the A-CN-K diagram, and the XRD results, the K-metasomatism can be analyzed and with

the method developed by Panahi et al. (2000), the K can be corrected to correct the CIA values and better evaluate the chemical weathering degree. Furthermore, with the  $\tau$  values, the depletion order of the elements from large ion lithophile element (LILE) to high field strength elements (HFSE) during weathering process and the elements enrichment during burial diagenesis and the transformation among clay minerals can be illustrated.

### 1.5. Research steps

Based on the sample types and data, the overall steps of the entire workflow are as follows:

- i. The workflow to separate the supergene and hypogene diagenesis and evaluate the chemical weathering degree is developed.
- ii. The methods for physical weathering degree quantification and the comparison among different types of lithologies for both physical and chemical weathering intensity are developed.
- iii. The model is set up to describe the weathering characteristics among analytical scale, microscale, and macro/mesoscale visual characteristics.

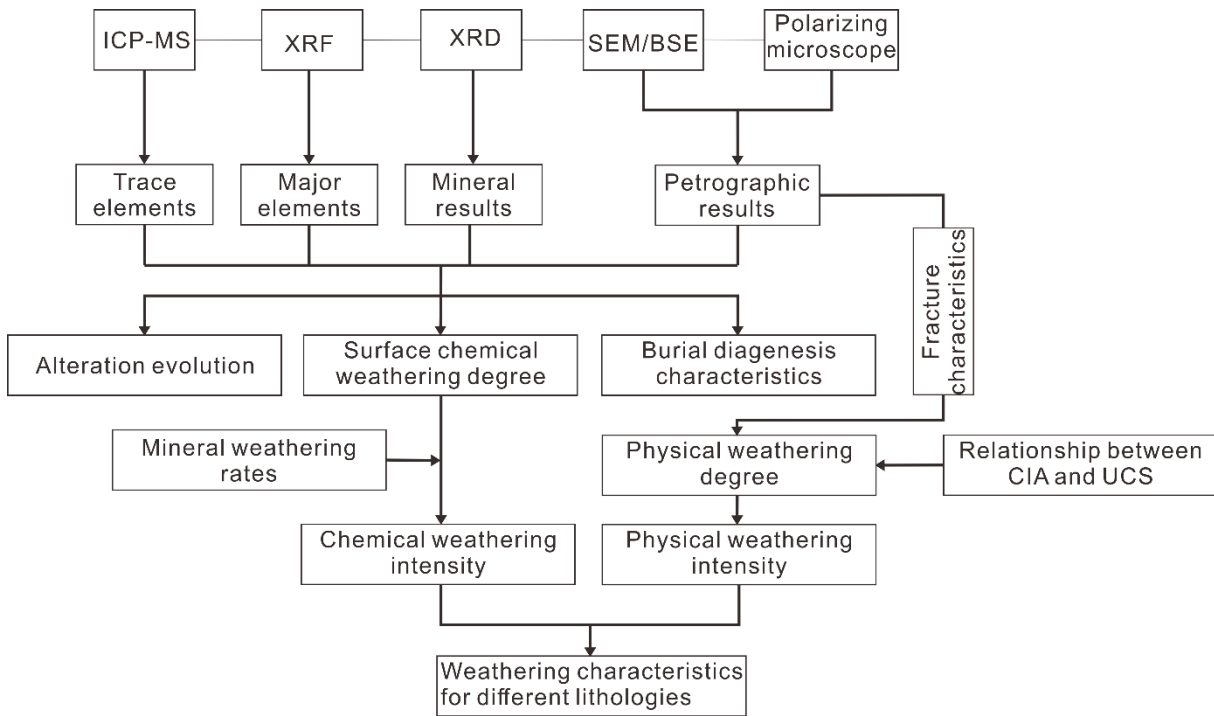


Figure 1-5. Working steps of the overall workflow.

---

## 2. Rock alteration at the post-Variscan nonconformity: implications for Carboniferous-Permian surface weathering versus burial diagenesis and paleoclimate evaluation

---

Fei Liang<sup>1</sup>, Jun Niu<sup>1,2\*</sup>, Adrian Linsel<sup>1</sup>, Matthias Hinderer<sup>1</sup>, Dirk Scheuvens<sup>1</sup> and Rainer Petschick<sup>3</sup>

<sup>1</sup>Material and Geosciences, Institute of Applied Geosciences, Technical University of Darmstadt, Darmstadt, 64287, Germany

<sup>2</sup>Faculty of Petroleum, China University of Petroleum-Beijing, Karamay Campus, Karamay, 834000, China;

<sup>3</sup>Faculty of Geosciences/ Geography, Goethe-University, Frankfurt, 60438, Germany

Correspondence to: Jun Niu (niu junmm@outlook.com)

Received: 29 December 2020 – Discussion started: 25 January 2021

Revised: 17 March 2021 – Accepted: 19 April 2021 – Published: 25 May 2021

*Published in: Solid Earth, 12:1165-1184 (<https://doi.org/10.5194/se-12-1165-2021>).*

### 2.1. Author contributions

(i) Fei Liang as the first author collected and prepared all the samples, conceptualized and prepared the paper.

(ii) Jun Niu provided the foundation and helped measure the trace and major elements.

(iii) Dirk Scheuvens and Rainer Petschick conducted the SEM and XRD measurements.

(iv) Matthias Hinderer and Adrian Linsel supervised this research.

**Abstract** A nonconformity refers to a hiatal surface located between metamorphic or igneous rocks and overlying sedimentary or volcanic rocks. These surfaces are key features with respect to understanding the relations among climate, lithosphere and tectonic movements during ancient times. In this study, the petrological, mineralogical and geochemical characteristics of Variscan basement rock as well as its overlying Permian volcano-sedimentary succession from a drill core in the Sprendlinger Horst, Germany, are analyzed by means of polarization microscopy, and environmental scanning electron microscope, X-Ray diffraction, X-ray fluorescence and inductively coupled plasma mass spectrometry analyses. In the gabbroic diorite of the basement, the intensity of micro- and macro-fractures increases towards the top, indicating an intense physical weathering. The overlying Permian volcanic rock is a basaltic andesite that shows less intense physical weathering compared with the gabbroic diorite. In both segments, secondary minerals are dominated by illite and a mixed-layer phase of illite and smectite (I-S). The corrected chemical index of alteration (CIA) and the plagioclase index of alteration (PIA) indicate an intermediate to unweathered degree in the gabbroic diorite and an extreme to unweathered degree in the basaltic andesite. The  $\tau$  values for both basaltic andesite and gabbroic diorite

---

indicate an abnormal enrichment of K, Rb and Cs that cannot be observed in the overlying Permian sedimentary rocks. Accompanying minerals such as adularia suggest subsequent overprint by (K-rich) fluids during burial diagenesis which promoted the conversion from smectite to illite. The overall order of element depletion in both basaltic andesite and gabbroic diorite during the weathering process is as follows: large-ion lithophile elements (LILEs) > rare earth elements (REEs) > high-field-strength elements (HFSEs). Concerning the REEs, heavy rare earth elements (HREEs) are less depleted than light rare earth elements (LREEs). Our study shows that features of supergene physical and chemical paleo-weathering are well conserved at the post-Variscan nonconformity despite hypogene alteration. Both can be distinguished by characteristic minerals and geochemical indices. Based on these results, a new workflow to eliminate distractions for paleoclimate evaluation and evolution is developed.

## **2.2. Introduction**

Nonconformities refer to contact surfaces between different lithologies in the geological record that were produced over long-lasting periods of non-deposition and/or erosion, which are of paramount importance for the subdivision and correlation of stratigraphic successions (Catuneanu, 1996). They also largely control the geometry of reservoirs for oil, gas, and water (Gardner, 1940). Moreover, nonconformities play a key role in understanding changes of past interactions of atmosphere, hydrosphere, and lithosphere as well as in elucidating driving mechanism for adaption and evolution of life on earth (Fedó et al., 1995; Nesbitt and Young, 1989a; Panahi et al., 2000) According to Catuneanu (1996), stratigraphic sequences and bounding surfaces are assigned to different orders based on their relative importance, being also known as a sequence hierarchy.

Especially for continental nonconformities the buried paleo-weathered surfaces provide an ideal opportunity to analyze the weathering and climate conditions during exposure (Jian et al., 2019; Zhou et al., 2017). This includes alteration and deformation of minerals, e.g. changes of crystal morphology of primary and secondary minerals during the weathering process, which is also called supergene alteration (Borrelli et al., 2014). After the paleo-weathered surface has been covered by sediments or volcanic rocks, burial commences leading to an increase in temperature and pressure as well as passage of diagenetic fluids. This second overprint during deep burial diagenesis is called hypergene alteration and has to be carefully distinguished from the primary supergene alteration (Dill, 2010).

The widespread post-Variscan nonconformity represents an important first-order bounding surface within the central and western European strata. The nonconformity is a result of the denudation of the Variscan orogen which mainly took place from the late Carboniferous to the early Permian (Henk, 1995; McCann, 1999; McCann et al., 2006; Zeh and Brätz, 2004). Locally,



---

however, the contact surface was overlain during the Triassic period. To date, the tectonic evolution in central Europe during post-Variscan times has been well studied (Matte, 1991; Ziegler et al., 2004). However, studies on weathering during the Permo-Carboniferous are fairly scarce. On the other hand, climate and palaeoenvironmental conditions are well known from coal-bearing paralic and lacustrine sediments in the sub-Variscan foredeep and post-Variscan intramontane basins which indicate an overall aridification trend from humid conditions in the Westphalian to hyperarid conditions in the Guadalupian (Upper Rotliegend). From Lopingian, the climate turned back to semiarid conditions (Roscher and Schneider, 2006).

For the reconstruction of the weathering conditions and the paleoclimate, fine-grained sediments such as siltstone or mudstone are usually investigated (Nesbitt and Young, 1982; Singer, 1988). However, caution is needed as these sediments may be multi-sourced, recycled and/or overprinted during transport and sedimentation (Fedó et al., 1995; Jian et al., 2019). To avoid this, it is feasible to analyze the weathering profile of igneous or metamorphic rocks in the source area itself. With this approach, more accurate in-situ information of the weathering conditions during a certain period can be acquired. This approach also applies to the diagenetic history of the rocks which are situated in direct proximity to the post-Variscan nonconformity (Dill, 2010). The Spredlinger Horst (Hesse, Germany) is a key area in southwestern Germany for investigating the rock alteration processes at the post-Variscan nonconformity, as plutonic Variscan basement rocks in this area are widely covered by only a thin layer of Cisuralian volcano-sedimentary rocks and the contact surface has been penetrated by numerous drillings (Kirsch et al., 1988).

For this study, we selected a representative drill core reaching from unweathered basement rock into the volcanic-sedimentary cover that was analyzed at high resolution, in particular near the nonconformity. This drill core allowed not only for the study of alteration in Variscan basement rocks, but also for the study of the subsequent alteration of overlying early Permian basalt. We carried out a detailed petrographical, mineralogical, and geochemical study and applied a new workflow to distinguish the supergene and hypogene alteration processes within a first-order nonconformity. The workflow is based on normalizing mineral types and geochemical weathering indices to un-overprinted conditions and quantifying the observed deviations. With corrected geochemical and mineral information of the weathered profile, the weathering and palaeoclimatic condition and the alteration scenario were addressed.

### **2.3. Geological Setting**

The Variscan orogen in Central Europe was formed due to the collision of the mega-continent Gondwana, Laurussia mega-continent and intervening microplates, namely Avalonia and Armorica. The final assemblage of these continents led to the formation of Pangea between ca. 360 and 320 Ma during Carboniferous time (Clive F., 1972; Schulmann et al., 2014). Due to a

---

southward-directed subduction of the oceanic lithosphere below the microplate Armorica, the so-called Mid-German Crystalline Zone (MGCZ) was formed as a magmatic arc at the northern margin of Armorica during Early Carboniferous; as a highland, this region continuously weathered and eroded until thermal subsidence began to dominate in central Europe (von Seckendorff et al., 2004a; Willner et al., 1991; Zeh and Brätz, 2004; Zeh and Gerdes, 2010). As a consequence, the post-Variscan nonconformity was formed, which represents a diachronous time gap of multiple tens to hundred millions years in central Europe (Henk, 1995; Kroner et al., 2007a; von Seckendorff et al., 2004b; Zeh and Brätz, 2004). The weathering surface was covered and, hence, preserved by Permian sedimentary or volcanic rocks summarized as Rotliegend Group (Becker et al., 2012b; Korsch and Schäfer, 1991; Stollhofen, 1998).

The Odenwald basement is the largest basement window of the MGCZ and consists of two major parts that are separated by the Oetzberg shear zone: The Bergsträsser Odenwald in the west and the Böllstein Odenwald in the east (Zeh and Gerdes, 2010). The Bergsträsser Odenwald is subdivided into three tectonic units which are composed of magmatic and metamorphic rocks. These are, ordered from north to south, Unit I, which includes the gabbro-dioritic Frankenstein Complex, Unit II with the so-called Neunkirchen Magmatic Suite and Unit III which is dominated by large intrusive bodies of the Weschnitz, Heidelberg and Tromm plutons (Kowalczyk, 2001; Zeh and Will, 2008). The basement rocks of the so-called Cenozoic Sprendlinger Horst belong to Unit I and represent a northern extension of the Odenwald basement, consisting of amphibolite, granite, diorite, gabbroic diorite and gabbro. Geochronological investigations of crystalline rocks of Unit I yield an emplacement age of 362 +/- 9 Ma for the Frankenstein gabbro (Kirsch et al., 1988). K/Ar and <sup>40</sup>Ar/<sup>39</sup>Ar amphibole cooling ages fall into a range between 363 and 334 Ma (Kirsch et al., 1988; Schubert et al., 2001). Cooling below 350 to 300 °C (approximate closure temperature for the K-Ar system in biotite) occurred at about 330 Ma (Kirsch et al., 1988). Thermal modeling for the southern Bergsträsser Odenwald implies that the exhumation rate reached a maximum of 1.3 mm/a with average rates of 0.2 mm/a from 338 Ma to 333 Ma (Henk, 1995). Recently, the basement rocks of Unit I on the Sprendlinger Horst were assigned to a Cadomian basement (Dörr and Stein, 2019b). The Dieburg metagranite in this region was dated to 540 +/- 8 Ma. According to these new findings, the investigated basement rocks are Cadomian relicts in the Variscan orogen.

The Cenozoic Sprendlinger Horst constituted a structural barrier between the nearby Saar-Nahe Basin in the west and the Hessian basin in the east already since the early Cisuralian (McCann, 1999). In the Saar-Nahe Basin, a subsidence rate of approximately 0.26 mm/a has been revealed by backstripping analyses for the time between Namurian und Saxonian (Schäfer, 2011). The oldest sedimentary rocks of the Sprendlinger Horst are represented by the Moret Formation

---

(Becker et al., 2012b). The Permian Moret Formation deposited in an alluvial environment mostly in wadi-like systems that contain poorly sorted conglomerates, pelites, coarse-grained sandstones/wackes and breccias. The fluvial sedimentary rocks of the overlying Lower Langen Formation are interbedded with basalts and basaltic andesites. These volcanic rocks are the product of a Permo-Carboniferous volcanism which took place throughout central Europe. Ar<sup>40</sup>/Ar<sup>39</sup> dating of the volcanic products in the eastern Saar-Nahe Basin imply ages of around 290 ± 6 Ma (Lippolt and Hess, 1983). This age approximately corresponds to the age of the Donnersberg Formation (Schäfer, 2011). The volcanic products in the Sprendlinger Horst are correlated to this formation accordingly (Marell, 1989). Mudstone compaction rates indicate that over 3000 m of sediments were eroded due to the inversion of the basin structure during the mid- and later Permian (Henk, 1993).

During Permo-Carboniferous time, due to continental climate conditions within the supercontinent Pangea, the paleoclimate in central Europe graduated from humid to hyperarid conditions (Parrish, 1993). In the Permian and Triassic, only the margins of the supercontinent attracted monsoonal rainfall and showed semiarid to subhumid condition (Parrish, 1993, 1995). The overall aridization is superimposed by several wet phases, namely the Westphalian C/D, the Stephanian A (303.6 Ma to 301.7 Ma), Stephanian C to early Lower Rotliegend (299.1 Ma to 295.5 Ma) and the Early Upper Rotliegend I wet phase (291 Ma to 287 Ma), respectively. These “wet phases” can be observed in the whole European region and are thought to be linked to deglaciation events of the Gondwana ice cap (Roscher and Schneider, 2006).

During the Mesozoic, the tectonic activity in Central Europe was relatively low and accompanied by continuous subsidence and marine transgression. In this phase, around 1500 m of sediments accumulated, which overlaid the Variscan basement and/or Permo-Carboniferous sediments and volcanic rocks (Timar-Geng et al., 2006). The maximum thickness of overburden is expected for the Jurassic (Schäfer, 2011). This is also the period of maximum heating and hydrothermal activity, which overprinted both the Variscan crystalline basement and the overlain sediments and volcanics locally. For this period, the formation of hydrothermal ores in central and southwest Germany is also well documented (Bons et al., 2014; Staude et al., 2011; Timar-Geng et al., 2004). Based on apatite fission track analysis in crystalline rocks of the Odenwald basement, Wagner et al. (1990) estimated temperatures of more than 130 °C for the Jurassic. Burisch et al. (2017) calculated homogenization temperatures from fluid inclusions in hydrothermal veins of 272–286 °C and 180 °C during the middle Jurassic and the Cretaceous, respectively. These temperatures can only be explained by higher heat flow and/or ascending hydrothermal fluids.

During the late Cretaceous and the Eocene, coupled with compressional intraplate stress of the Alpine Orogeny, the Upper Rhine Graben system was formed (Behrmann et al., 2005). In

---

conjunction with the formation of the Upper Rhine Graben, the Sprendlinger Horst was formed. The latter is bounded by the Rhine Graben fault system in the west and by the Gersprenz graben in the east. Most of the sediments that overlaid the post-Variscan crystalline basement in the research area have been eroded since the Cretaceous (Mezger et al., 2013; Schwarz and Henk, 2005b). In the nearby southeastern Odenwald region they are partly conserved and reach a thickness of 500 m for the Lower Triassic Buntsandstein (Marell, 1989). On the Sprendlinger Horst only Permian volcano-sedimentary rocks remained which decrease in thickness from north to south of Darmstadt from 250 to 0 m (Marell, 1989; Mezger et al., 2013)

#### **2.4. Materials and Methods**

Numerous drill cores in the Sprendlinger Horst were acquired by a scientific drilling project between 1996 and 2001. Many of the drill cores expose the post-Variscan nonconformity in shallow depths of up to 80 m below ground surface and, thus, provide a unique chance to investigate this palaeosurface at local scales. Along these drill cores, core GA1 was selected because it exposes three different lithological units namely the plutonic basement at the bottom, the Permian volcanic lava in the middle and overlying Permian Rotliegend sedimentary rocks at the top. The sedimentary rocks show a gradual transition from alluvial facies at the base to fluvial facies at the top (Fig. 2-1) and mainly consist of matrix-rich breccias, wackes and siltstones. Both the top of the basement rock and the top of the volcanic lava constitute paleo-surfaces that faced intense alteration throughout their exposure, which is supposed to be significantly shorter for the volcanic rocks. The macroscopic alteration underneath these surfaces is intense, this is expressed by a higher degree of fracturing, bleaching and grain disaggregation. The degree of macroscopic alteration decreases with increasing depth in these parts. The core offers the unique opportunity to study subsequent weathering intervals and to compare typical endmembers of rock types with weak (granodiorite) and strong (andesitic basalt) vulnerability to chemical weathering.

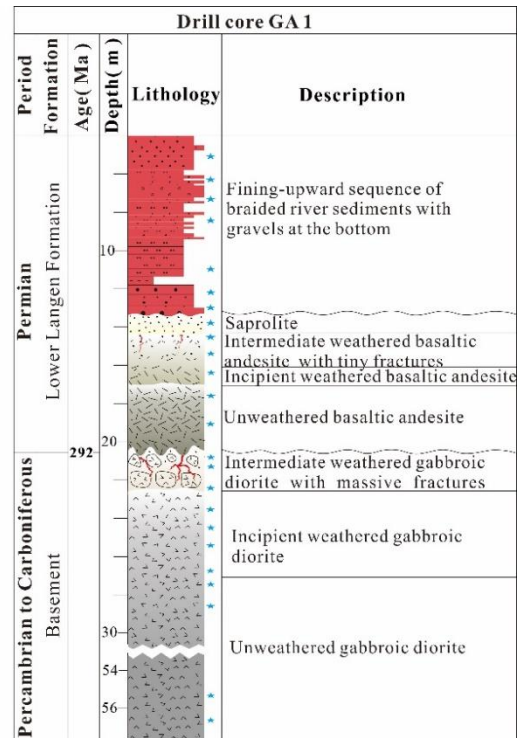
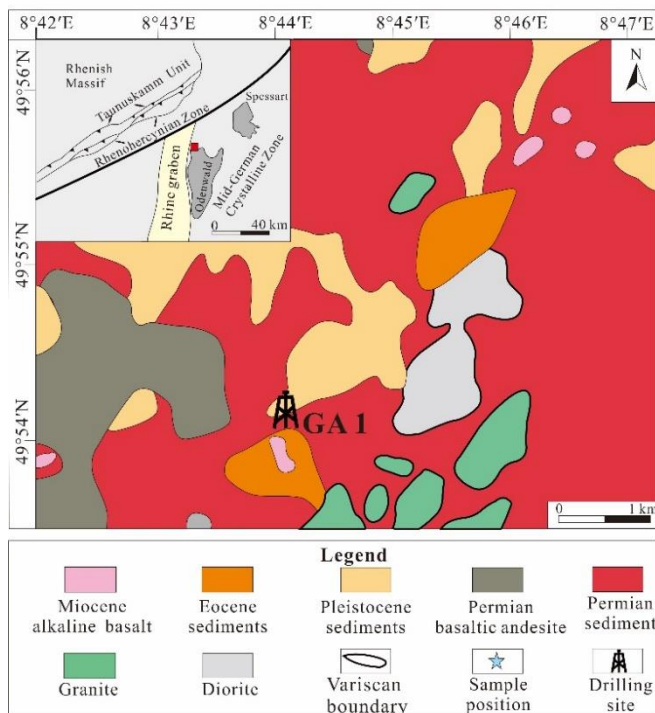


Fig.2-1. Location and geology of the research area with the lithological section of the drilling GA1; note gap between 30 and 54 m drilling depth. Blue stars indicate sampling spots.

In total 24 samples were extracted from the GA1 drill core: 11 belonged to the basement, 6 belonged to the overlying volcanic rock (Fig.2-1) and 7 belonged to the sedimentary rocks of the Lower Langen Formation. In order to capture the small-scale petrographic and geochemical variations in the weathering zones appropriately, we reduced the sampling interval in the topmost part of the volcanic rock and in the basement to 40 cm, for the rest of the core, the interval was around 1 m in order to avoid the fractures.

The samples were used to prepare thin sections that were analyzed by polarization microscopy and SEM-EDX (scanning electron microscopy–energy dispersive X-Ray analysis) for their petrographic characteristics. For mineral composition, trace element and major element analyses all samples were crushed and milled into a powder with a diameter of less than 63  $\mu\text{m}$ . One part of the powder was examined by X-ray diffraction (XRD) at Goethe University Frankfurt for whole rock mineral composition. Careful back-loading of the powder preparation was utilized for XRD in order to reduced preferred orientation. Using a PANalytical X'Pert diffractometer equipped with a Bragg-Brentano-Goniometer (Copper beam), each sample was scanned under 40 kV and 30 mA for 2 h. The start angle was 2.5°, the end angle was 70.0° and a step size of 0.008° was applied. The time for each step was 50 s. The mineral phase proportions were estimated by weighted XRD peak intensities after conversion with their typical Reference Intensity Ratios (RIR) as found in the powder diffraction file (PDF-2 and PDF-4 of the International Centre of Diffraction

---

Data: <https://www.icdd.com/>, last access: 12 June 2019; see Table 1) with MacDiff software (Petschick et al., 1996).

The powder samples were sent to State Key Laboratory of Isotope Geochemistry, Guangzhou Institute of Geochemistry, Chinese Academy of Science for examination of major elements by X-ray fluorescence (XRF) and examination of trace elements by Inductively Coupled Plasma Mass Spectrometry (ICP-MS). Before XRF analysis, samples were roasted under 900 °C for 3 hours and weighed before and after heating to measure the loss on ignition (LOI). Subsequently, 0.51-0.53 g of each sample was mixed with the ratio of 1:8 with Li<sub>2</sub>B<sub>4</sub>O<sub>7</sub> and fused at 1150 °C in a Pt crucible to make a glass disk for XRF analysis.

For trace and rare earth elements analysis, 40 mg sample powder was weighed and placed into high-pressure-resistant Savillex Teflon beakers to which 0.8 ml 1:1 HNO<sub>3</sub>, 0.8 mL HF and 0.5 ml 3N HClO<sub>4</sub> was added. The mixture was heated for 48 hours at 100 °C and then evaporated. A total of 0.8 mL 1:1 HNO<sub>3</sub> was then added and heated at 100 °C for 12 hours. Next, 0.8mL HF and 0.5mL 3N HClO<sub>4</sub> was added and the beaker was sealed and moved into an oven with a temperature of 190 °C for 48 hours to make sure the sample was completely dissolved. The beakers were then opened, the solution was evaporated and 4 mL 4N HNO<sub>3</sub> were added. Following this, the beakers were sealed and moved into the oven which was set at a temperature of 170 °C for 4 hours. Finally, the solution was diluted with 3% HNO<sub>3</sub> until the weight of the solution was 250 times the weight of the sample. A total of 0.25 g of the solution was taken and diluted with 3% HNO<sub>3</sub> to 2.00 g, mixed with 2.00 g Rh-Re internal standard solution and examined by ICP-MS. To monitor the analytical quality, international standards of GSR-1(granite), GSR-2(andesite), GSR-3(basaltic andesite) were applied.

## **2.5. Results**

### **2.5.1. Petrographic characteristics**

#### *Plutonic rock*

The Variscan basement in drill core GA1 consists of a coarse-grained plutonic rock with a conspicuous salt-and-pepper appearance and a phaneritic texture. Fractures are pervasive from 20.6 to 21.4 and from 21.7 to 22.3 m. The width of the fractures is around 1 cm. From 22.3 to 23.4 m, both fracture density and width gradually reduce downwards. Nearly all fractures are filled by secondary minerals (Fig. II-I). Under the microscope, the fresh parts of the plutonic basement rock mainly consist of plagioclase (oligoclase and labradorite), quartz, biotite and amphibole (Fig. 2-2a). With decreasing depth, primary minerals such as plagioclase and biotite were gradually altered and transformed into secondary minerals; fractures are also ubiquitous in

the thin sections in the topmost part. Primary grain shapes are distorted and most of them are filled with calcite (Fig. 2-2b). Moreover, recrystallized quartz coupled with calcite is found filled in the fractures (Fig. 2-2c). Some of the fractures are filled by dolomite accompanied with quartz (Fig. 2-2d). Even in the topmost part (20.6 m), the plagioclase grains are only partly altered (Fig. 2-2e).

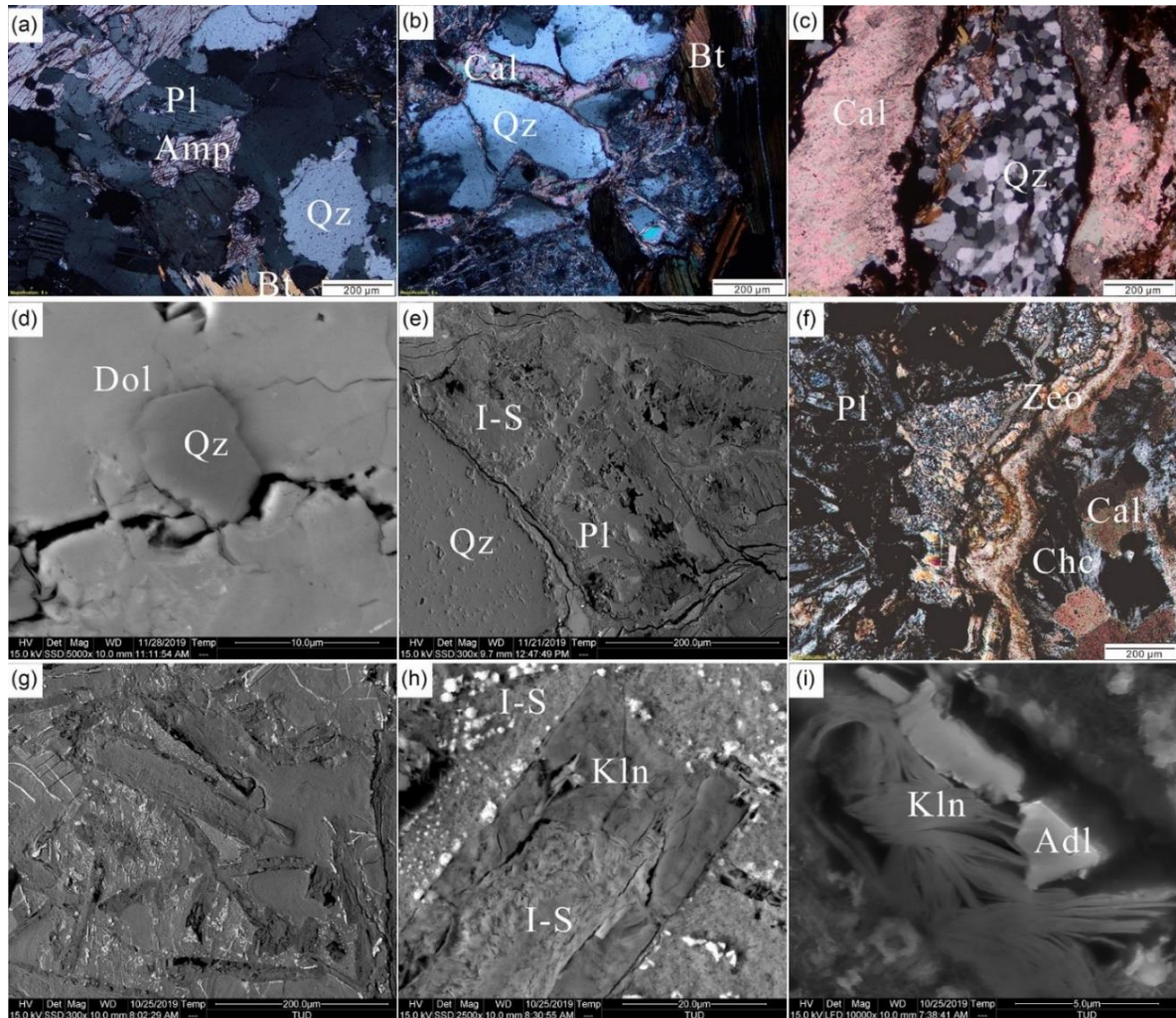


Fig. 2-2. Petrographic characteristic of the basement and the overlying volcanic rock in the GA1 drill core. (a) fresh gabbroic diorite (PM,  $z = 55:5$  m); (b) gabbroic diorite (PM,  $z = 20:6$  m) and fractured quartz grain; (c) gabbroic diorite (PM,  $z = 23:5$  m) and recrystallized quartz coupled with a calcite filled in fracture; (d) gabbroic diorite (BSE,  $z = 21:5$  m) and dolomite accompanied by quartz; (e) gabbroic diorite (BSE,  $z = 20:6$  m) and partly weathered plagioclase. (f) basaltic andesite (PM,  $z = 17:8$  m) and fresh plagioclase grains with the amygdaloid consisting of calcite and zeolite and chalcedony; (g) basaltic andesite (BSE,  $z = 13:9$  m) secondary clay minerals with intact primary grain shapes; (h) basaltic andesite (BSE,  $z = 13:9$  m) and I-S surrounded by kaolinite within one residual plagioclase grain shape; (i) basaltic andesite (SEM,  $z = 13:9$  m) with kaolinite and adularia filled in the void. The abbreviations used in the figure and caption are as follows: PM– polarizing microscopy,  $z$  – depth below ground surface, Amp – amphibole, Kln – kaolinite, Adl – adularia, Bt – biotite, Cal – calcite, Pl – plagioclase, Zeo – zeolite, Chc – chalcedony, Dol – dolomite and Qz – quartz.

---

## *Lava*

The lava has a phaneritic, amygdaloidal texture. Fractures in this part are very limited and occur between 13.8 and 14.7 m with a high angle to the horizon. The width is less than 1 mm, and the fractures are also filled with secondary minerals (Fig. II-1). The fresh part of the volcanic rock mainly consists of plagioclase (albite) crystals and amygdaloid bodies that are made up of calcite and zeolite locally accompanied with chalcedony (Fig. 2-2f). With a decrease in depth, the content of plagioclase gradually decreases under the microscope. However, the thin section in the topmost part of the lava (13.9 m) shows a sudden change compared with the samples from lower parts. Here, nearly all primary minerals were altered to secondary clay minerals, but the primary grain shapes are still relatively intact (Fig. 2-2g). Some residual grains consist of a kaolinite rim and a core of illite or illite-smectite (I-S) mixed layers (Fig. 2-2h). In the void, adularia with kaolinite can be observed (Fig. 2- 2i).

### **2.5.2. Mineral Composition**

#### *Plutonic rock*

The XRD results are listed in the Appendix II-I (Table A1) and are plotted in Fig. 2-3. The plutonic basement part is composed of plagioclase (oligoclase and labradorite), K-feldspar (only in one sample), quartz, amphibole (mainly Mg-hornblende) and mica phases, with secondary minerals of illite (not separable from micas), vermiculite, I-S mixed layers, minor kaolinite, anatase, hematite, calcite and dolomite. Amphibole abundance decreases in the middle section and disappears in the uppermost part. In the topmost portion (20.6–23.5 m), amphibole is not found. Furthermore, plagioclase decreases in abundance from around 40 % at the bottom to about 8 % at the top. Considering the mineralogical composition of the fresher parts of the plutonic rock, based on the quartz, alkali feldspar, plagioclase, feldspathoid (QAPF) diagram for plutonic rocks, the protolith of the basement rock can be classified as a quartz diorite/tonalite (Fig. II-II), which corresponds well with Mezger (2013).

#### *Lava*

The fresh samples of the volcanic rock are composed of augitic pyroxene and plagioclase (albite). In the weathered part, most of the phases appear as secondary minerals, such as quartz, hematite and anatase; clay minerals, such as illite, mixed layer illite-smectite (I-S), vermiculite and kaolinite; and carbonate minerals, like calcite and minor dolomite. The uppermost part of the lava is dominated by I-S mixed-layer minerals, the plagioclase content is less than 5 % and pyroxene is absent. The abundance of plagioclase (and pyroxene) gradually decreases from bottom to top, and illite and vermiculite exhibit an increasing tendency (Fig. 2-3). Based on the QAPF diagram for



volcanic rocks, the protolith of the weathered volcanic rock can be classified as a basalt or andesite (Fig. II-II).

### 2.5.3. Geochemical characteristics

#### *Geochemical rock classification*

In order to further verify the lithological type of the plutonic and volcanic rock for the basement part of the GA1 drill core, the geochemical data from comparatively fresh samples (23.5–56.5 m) are plotted in the total alkali silica (TAS) diagram (Middlemost, 1994) (Fig. 2-4). Here, the results mainly plot in the gabbroic diorite field (Fig. 2-4a), which is grossly consistent with the results from the petrographic classification (Fig. II-II). For the volcanic rock classification, a revised Winchester–Floyd diagram is applied, which is based on immobile trace elements (Pearce, 1996). Most lava samples fall into the andesite/basaltic andesite field (Fig. 2-4b), which is also in accordance with the petrographic classification result. In the following, we use the result of chemical classification and term the two protolith rocks as gabbroic diorite and basaltic andesite.

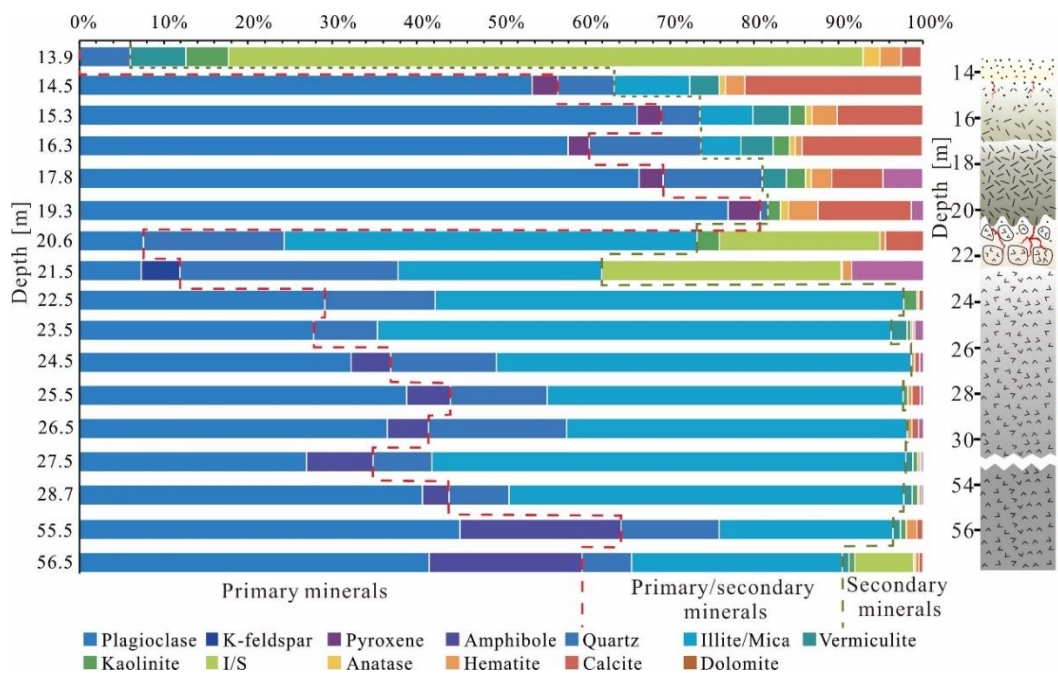


Fig.2-3. Mineral compositions of both Permian volcanic lava and Paleozoic basement rock in the GA1 drill core (measured by powder XRD).

#### *Major elements*

The concentrations of major elements are listed in the Appendix II-I (Table A2) and are visualized in 1-D profiles for both basaltic andesite (Fig. 2-5a) and gabbroic diorite (Fig. 2-5b). Within the lower relatively fresh part of the gabbroic diorite, major elements such as  $K_2O$ ,  $Na_2O$ ,  $P_2O_5$ ,  $CaO$  and  $MnO$  are almost constant.  $Al_2O_3$  and  $TiO_2$  fluctuate in the topmost part (20.6–21.5 m) and show an

overall slightly increasing tendency from top to bottom. For  $Fe_2O_3$ , the fluctuation is high in the topmost part and low in the lower part. There is a sharp shift in most concentrations when approaching the intensely altered part at the top of the profile. Despite the high fluctuation in most concentrations in the uppermost part, a significant increase in  $K_2O$  and decrease in  $Na_2O$  are observed from bottom to top (Fig. 2-5b).

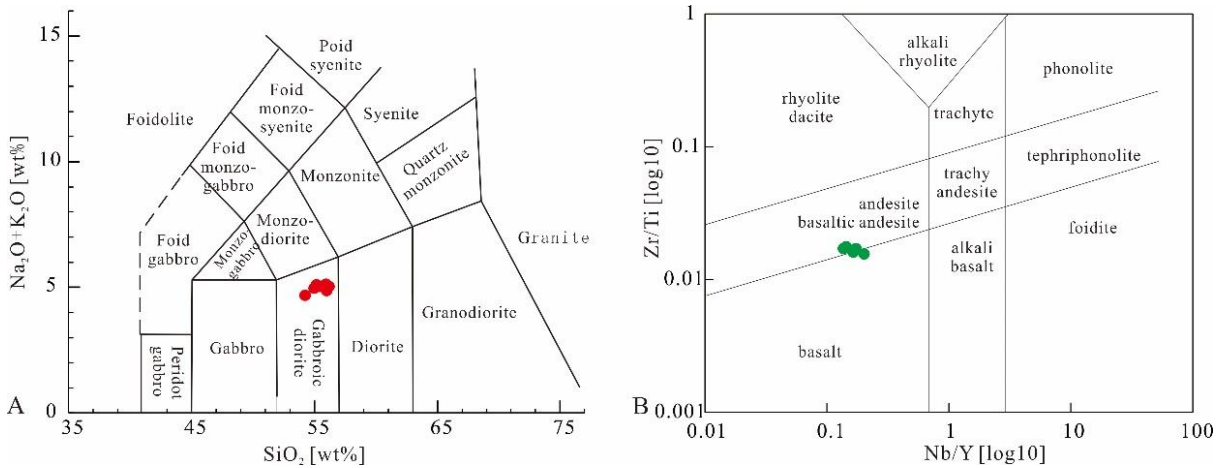


Fig.2-4. Classification of rocks of the GA1 well with the TAS diagram and Revised Winchester-Floyd diagram. (A) samples from fresh and nearly fresh parts of basement; (B) samples from overlain lava profile

Concerning the basaltic andesite, there are some clear trends with increasing  $Al_2O_3$ ,  $K_2O$ ,  $P_2O_5$  and  $TiO_2$  concentrations and with decreasing  $CaO$  and  $Na_2O$  concentrations towards the top. In contrast to the gabbroic diorite, a sharp shift in concentrations is observed in the uppermost sample for all elements except for  $Fe_2O_3$  which fluctuates along the profile (Fig. 2-5a).

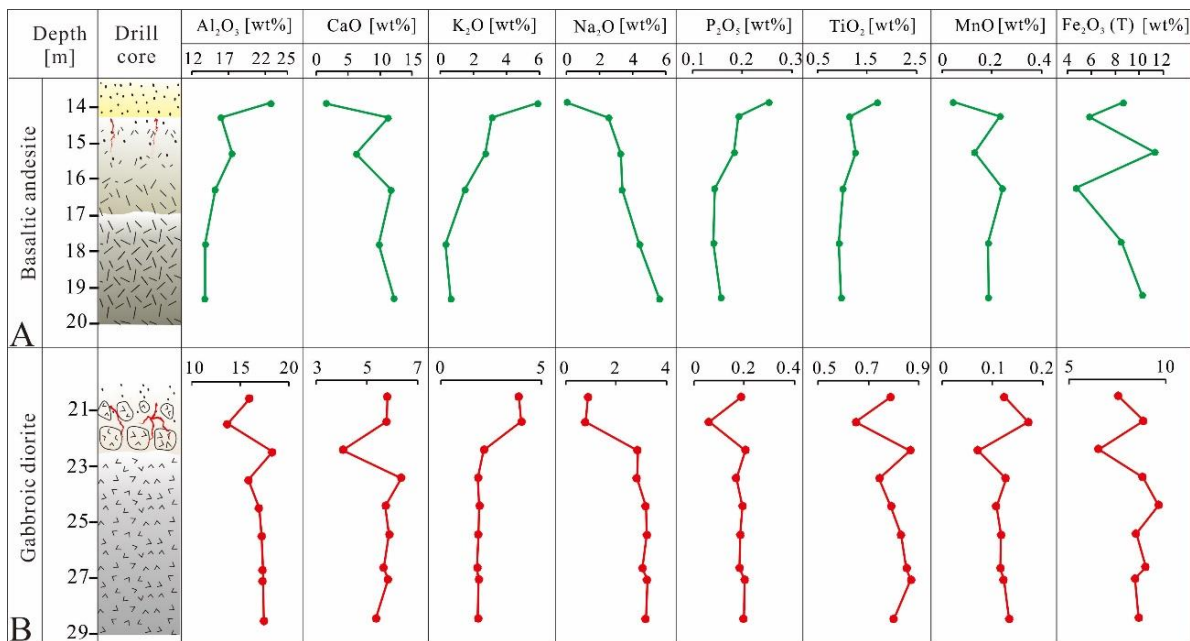


Fig.2-5. Major elements content (in wt%) of the basaltic andesite (A) and the gabbroic diorite (B) along the drill core profile.

*Trace elements*

Trace element data are also given in the Appendix II-I (Table A3). Variations in representative trace elements from both gabbroic diorite and basaltic andesite are shown in Fig. 2-6. In the gabbroic diorite, except for the topmost part, fluctuations in high-field-strength elements (HFSEs) such as Zr, Hf, Nb, Ta and Th (in parts per million, ppm) are limited or even constant. For large-ion lithophile elements (LILEs), Rb and Cs decrease from top to the bottom, whereas Sr increases from 61 to 348 ppm. Ba fluctuates in the upper part of the gabbroic diorite section but is almost constant in the lower part.

Concerning the basaltic andesite part, HFSEs such as Zr, Hf, Nb, Ta and Th (in ppm) all exhibit an increasing tendency from the bottom to the top, with a sharp increase in the topmost sample. LILEs such as Rb and Cs also show an increasing tendency, whereas Sr reveals an inverse trend, with a decrease from 123 ppm at the bottom to 47 ppm in the topmost part. The tendency for Ba is irregular compared with the other elements, but the overall trend is decreasing.

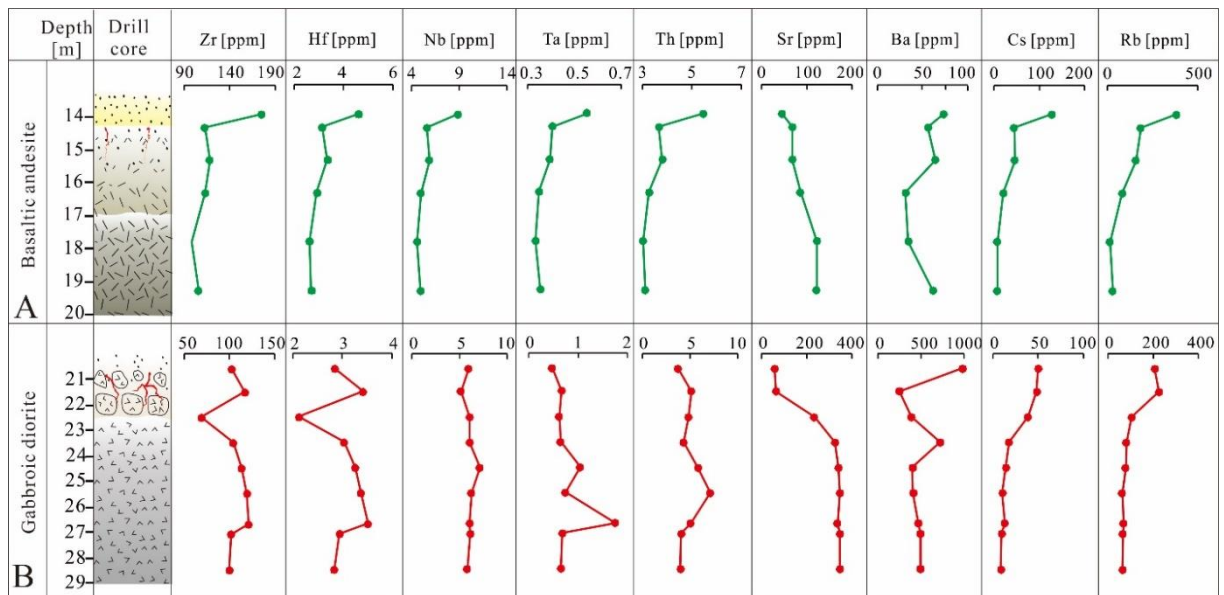


Fig. 2-6. Representative trace elements content (in ppm) of basaltic andesite (A) and gabbroic diorite (B) along the drill core profile.

*Rare Earth Elements (REEs)*

REE concentrations are listed in Appendix II-I (Table A4) and are shown as chondrite-normalized patterns (McDonough and Sun, 1995) in Fig. 2-7. The calculation for the anomalies of cerium (Ce) and europium (Eu) are defined as follows:

$$\frac{Ce}{Ce^*} = \frac{2 \times Ce_N}{La_N + Pr_N}, \quad (\text{Eq. 2-1})$$

and

$$\frac{Eu}{Eu^*} = \frac{2 \times Eu_N}{(Sm_N + Gd_N)}, \quad (\text{Eq. 2-2})$$

Here  $Ce^*$  and  $Eu^*$  are the hypothetical concentrations of trivalent Ce and Eu, and  $X_N$  represents the normalized value of the element X. The distribution patterns of both gabbroic diorite and basaltic andesite are nearly parallel at different depths and exhibit decreasing values from the bottom to the top (Fig. 2-7). All samples are moderately enriched in light rare earth elements (LREEs) and have gently right-dipping REE patterns. They exhibit no Ce anomalies and slightly negative Eu anomalies.

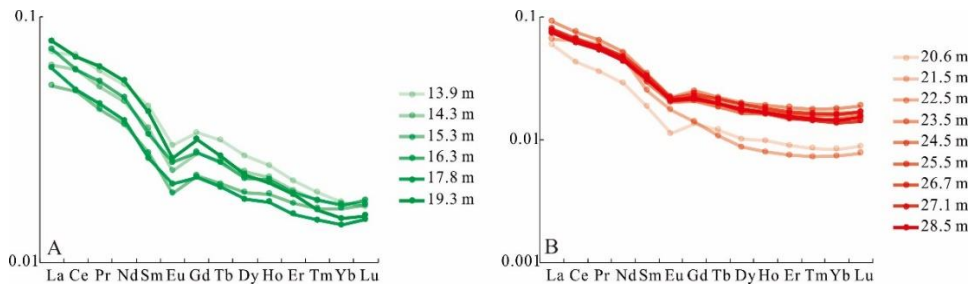


Fig.2-7. REE pattern of basaltic andesite (A) and gabbroic diorite (B) in different depths

## 2.6. Discussion

### 2.6.1. Chemical alteration

During chemical weathering, alkalis and alkaline earth elements contained in silicates such as feldspar, mica minerals, pyroxene and amphibole will be gradually depleted, whereas aluminum tends to remain in situ, generating clay minerals (Clift et al., 2014; Nesbitt and Young, 1982; Vázquez et al., 2016). Based on this mechanism, different types of weathering indices were developed to evaluate the weathering intensity. Among these, the chemical index of alteration (CIA) and the plagioclase index of alteration (PIA) were proposed by Nesbitt and Young (1982) and Fedo et al (1995), respectively. They are defined as:

$$CIA = \frac{Al_2O_3}{Al_2O_3 + CaO^* + Na_2O + K_2O} \times 100, \quad (\text{Eq. 2-3})$$

and

$$PIA = \frac{Al_2O_3 - K_2O}{Al_2O_3 + CaO^* + Na_2O - K_2O} \times 100, \quad (\text{Eq. 2-4})$$

respectively. Here, all portions are given in molecular weight, and (in both equations)  $CaO^*$  is the Ca content within silicate minerals only. Bulk rock analysis of altered rocks, however, is affected by Ca mobilization and secondary calcite precipitation. First, Ca may be transferred downward

---

during weathering in the top part and may precipitate there along fractures that were formed before by physical weathering and/or rock relaxation. Second, Ca may be transferred by fluids from underlying or overlying formations during the burial process, depending on the hydraulic conditions. Both cases will increase the Ca content. Hence, bulk geochemistry cannot be applied directly. For the correction of calcitic  $\text{CaO}^*$ , McLennan (1993) proposed an approximate approach is as following:  $\text{CaO}_{\text{rest}} = \text{CaO} - \text{P}_2\text{O}_5 \cdot 10/3$ , whereas the  $\text{P}_2\text{O}_5$  is related to apatite,  $\text{CaO}^* = \text{CaO}_{\text{rest}}$  when  $\text{CaO}_{\text{rest}} < \text{Na}_2\text{O}$ ,  $\text{CaO}^* = \text{Na}_2\text{O}$  otherwise. With this calculation, the CIA value for fresh feldspar is about 50, unaltered basaltic andesite is between 30 and 45, granitoids range between 45 and 55, illite is from 75 to 85, muscovite yields a value of 75, and kaolinite and chlorite have the highest value of nearly 100 (Fedo et al., 1995). As a modification of the CIA, the PIA value for fresh rock is around 50, whereas for clay minerals such as kaolinite, illite and gibbsite, it is close to 100 (Fedo et al., 1995; Patino et al., 2003).

In our case, the CIA and PIA decrease from top to bottom for both gabbroic diorite and basaltic andesite. The PIA values are clearly higher than the CIA values (Fig. 2-8a). In the topmost basaltic andesite part, the CIA is up to 77, which indicates an intermediate degree of weathering. The results from XRD and backscattered electron microscopy (BSE), however, indicate that the plagioclase is weathered and 74 % of the constituent is I-S. This is well expressed by the PIA, which yields a value of 98; hence, the PIA is more consistent with the mineralogical and petrographic character than the CIA.

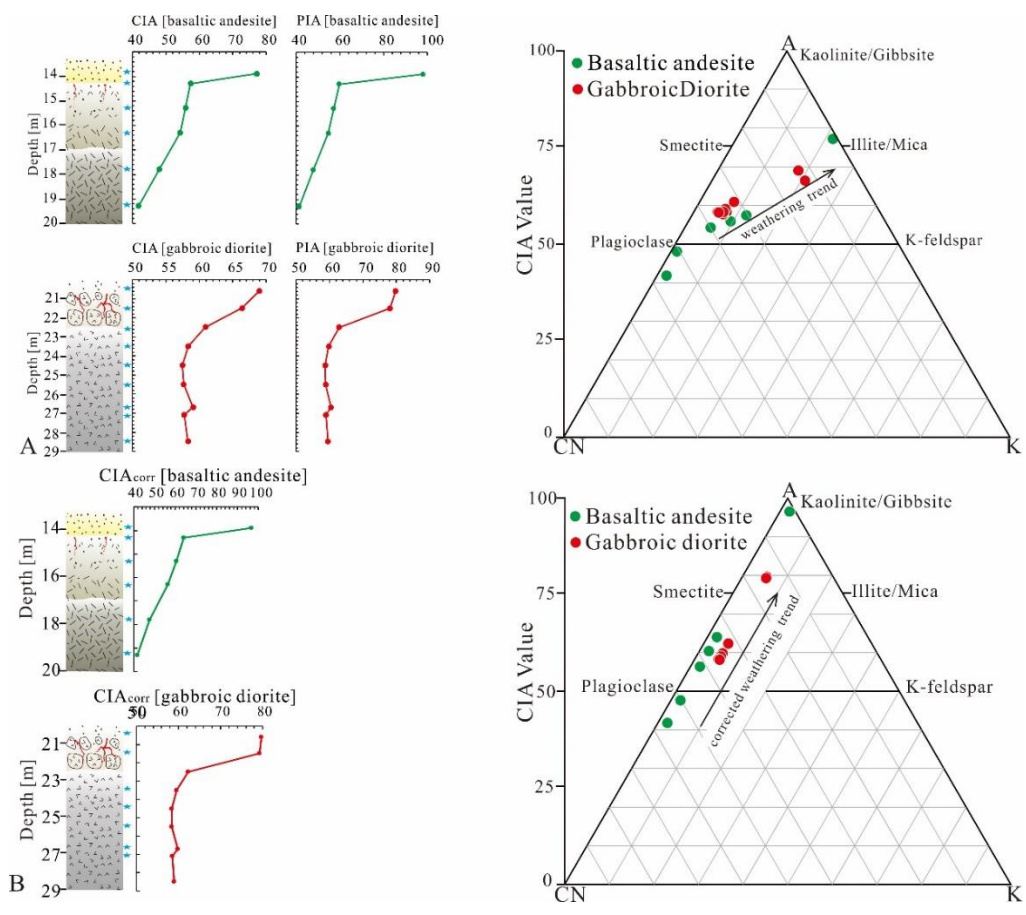


Fig.2-8. Weathering indices with A-CN-K diagram of both basaltic andesite and gabbroic diorite before and after K correction; based on (Fedo et al., 1995; Nesbitt and Markovics, 1997).

To better evaluate the weathering intensity, an A-CN-K ternary diagram is applied (Fedo et al., 1995; Nesbitt and Young, 1984). The letter A stands for  $Al_2O_3$ , CN for  $(CaO^*+Na_2O)$  and K is the content of  $K_2O$  all in molecular proportions. The ideal weathering trend for different types of parent rocks in the upper continental crust should be parallel to the A-CN axis, but the original data tend to deviate from the theoretical weathering trend due to diagenetic alteration (Babechuk et al., 2015; Fedo et al., 1995; Zhou et al., 2017). The trends for both basaltic andesite and gabbroic diorite samples uniformly deviate from the ideal weathering tendency and excuse to the K apex (Fig. 2-8a), which clearly indicates a relative K enrichment. In the literature, the enrichment of K is interpreted as K metasomatism due to conversion among clay minerals, such as the transformation from kaolinite to illite or from plagioclase to K-feldspar (Fedo et al., 1995; Nesbitt and Young, 1984; Zhou et al., 2017). K metasomatism results in a lower CIA value relative to the actual weathering intensity and can also explain the deviation from the PIA. To address this problem, Fedo et al. (1995) suggested that the proportion of “pre-metasomatic” compositions of the weathering products could be determined by correcting each point on the A-CN-K diagram back to its predicted position. The method proposed by Panahi et al. (2000) for the K correction is applied as follows:

$$K_2O_{\text{corr}} = \frac{m \cdot A_w + m \cdot CN_w}{1 - m} \quad (\text{Eq. 2-5})$$

The  $A_w$  and  $CN_w$  refer to the  $Al_2O_3$  and  $(CaO^* + Na_2O)$  content in the weathering zone, respectively, where

$$m = \frac{K}{A + CN + K} \quad (\text{Eq. 2-6})$$

and the  $K$ ,  $A$  and  $CN$  values for the calculation of  $m$  are from the protolith sample.

With corrected  $K_2O$  values, the trend of all sample points in the A–CN–K diagram is parallel to the A–CN axis (Fig. 2-8b). Moreover, the  $CIA_{\text{corr}}$  values are now consistent with the PIA value. The  $CIA_{\text{corr}}$  values of the gabbroic diorite indicate an intermediate to incipient chemical weathering degree, with  $CIA_{\text{corr}}$  values of 80 in the top part and values of 58 at the bottom (Fig. 2-8b). PIA values decrease from 83 to 59 (Fig. 2-8b). For both the  $CIA_{\text{corr}}$  and PIA values, inconsistent trends between the topmost part (20.6–21.5 m) and the remaining section (22.5–28.5 m) result from a sudden decrease in the weathering degree which forms a “discontinuity”. The  $CIA_{\text{corr}}$  and PIA values in the topmost part range from 79 to 80 and from 78 to 80, respectively; in the remaining section, the  $CIA_{\text{corr}}$  and PIA values decrease from 62 to 58 and from 63 to 59, respectively. Petrographic and mineralogical features correspond well to the corrected weathering indexes. Secondary alteration products are mainly illite, with a small quantity of kaolinite and vermiculite.

The corrected CIA values in the basaltic andesite suggest an extreme to incipient weathering degree, with the  $CIA_{\text{corr}}$  and PIA decreasing from respective values of 97 and 98 at the top to respective values of 42 and 41 at the bottom. Similar to the gabbroic diorite, a discontinuity exists between the topmost part (13.9 m) and the lower part (14.3–19.3 m) for both  $CIA_{\text{corr}}$  and PIA values. The high  $CIA_{\text{corr}}$  and PIA values in the topmost part of the basaltic andesite indicate extreme chemical weathering. In the lower part of the basaltic andesite, the  $CIA_{\text{corr}}$  and PIA values decrease from 64 at the top to 42 at the bottom and from 65 at the top to 41 at the bottom, respectively (Fig. 2-8b). These values are much lower than values from the topmost part and suggest an incipient weathering degree. Based on the XRD results, the plagioclase content at the bottom is 77 % and declines gradually up the section to 54 % at 14.5 m before it suddenly drops to 0 % at 13.9 m. At a depth of 14.5 m, the plagioclase grains are still mostly fresh, which is clearly different from the uppermost 0.5 m in which they are completely altered.

## 2.6.2. Quantification of elements transfer

For quantification of element transfer due to weathering and diagenesis the  $\tau$  model is applied (Anderson et al., 2002; Nesbitt, 1979a; Nesbitt and Markovics, 1997). The model uses the relation of the mobile element concentration in the sample ( $M_{\text{sample}}$ ) vs. the protolith ( $M_{\text{protolith}}$ ) and between the immobile element concentration in the sample ( $I_{\text{sample}}$ ) vs. the protolith ( $I_{\text{protolith}}$ ).

---

Among the immobile elements, Ti is widely used as a key element (Middelburg et al., 1988). Thus, the model is defined as:

$$\tau_M = \frac{M_{\text{sample}} \times Ti_{\text{protolith}}}{M_{\text{protolith}} \times Ti_{\text{sample}}} - 1, \quad (\text{Eq. 2-7})$$

When  $\tau_M > 0$ , element M is enriched during alteration, when  $\tau_M = 0$ , element M is immobile during alteration, when  $0 > \tau_M > -1$ , element M is depleted, when  $\tau_M = -1$ , element M is completely lost from the material. For the basaltic andesite and gabbroic diorite, the samples from the bottom (19.3 m for basaltic andesite and 55.5 and 56.5 m for gabbroic diorite) were selected as protoliths to provide the lowest degree of alteration based on the CIA values, petrographic features and XRD results.

The results for major and trace elements are listed in the Appendix II-I (Table A5) and are plotted in Fig. 2-9. In the basaltic andesite part, both Ca and Na are strongly depleted in the topmost section (13.9 m), with  $\tau_{\text{Ca}}$  and  $\tau_{\text{Na}}$  of  $-0.93$  and  $-0.99$ , respectively.  $\tau_{\text{Ca}}$  gradually increases from  $-0.60$  to  $-0.07$  and  $\tau_{\text{Na}}$  increases from  $-0.60$  to  $-0.18$  with increasing depth from 14.3 m down to 17.8 m. The discontinuity between the topmost part and the remaining section corresponds well to the CIA and PIA values. However, the  $\tau_{\text{Na}}$  values from the top gradually increase from  $-0.70$  (20.6 m) to  $-0.67$  (21.5 m) in the gabbroic diorite part, followed by a sharp increase in the lower section, with values between  $-0.12$  and  $0.06$ . This is consistent with the trends of both the CIA and PIA.  $\tau_{\text{Ca}}$  values show a high variability compared with  $\tau_{\text{Na}}$ . The sample from 20.6 m yields a  $\tau$  value of  $-0.03$ , which indicates a slight depletion in Ca, whereas the sample from 21.5 m shows a  $\tau$  value of  $0.17$ , which suggests a slight enrichment in Ca (Fig. 2-9b). A similar enrichment also occurs at 23.5 m, which yields a value of  $0.13$  (Table A5).

The Sr/Ca ratio can be applied as a parameter to distinguish different phases of diagenetic fluids (Berndt et al., 1988; Brandstätter et al., 2018). To figure out the source of Ca, the Sr-CaO diagram is applied (Fig. 2-9a). To figure out the source of Ca, the Sr-CaO diagram is applied (Fig. 2-9a). The ratios of at the top of the gabbroic diorite at depths of 20.6 and 21.5 m show a close relation to the ratios of the basaltic andesite, and they clearly deviate from the general trend of the gabbroic diorite and the overlying sedimentary rocks. This hints at a chemical overprint of the gabbroic diorite by the overlying basaltic andesite, whereas the Ca in the lower part appears to be primary. The spike in  $\tau_{\text{Ca}}$  at a depth of 23.5 m can also be explained by porosity data (Weinert et al., 2021), which can be considered as a measure of fracture density and grain disaggregation in igneous rocks. The porosity decreases sharply from 24 % at a depth of 21.5 m to 3 % at 23.6 m (Fig. 2-9b). This can be explained by the fact that the fractures provided pathways for meteoric water before the Permian basaltic to andesitic lava flow flooded the basement. Ca was leached by meteoric



water, transferred downward through these fractures and accumulated around the interface, where the porosity sharply decreases.

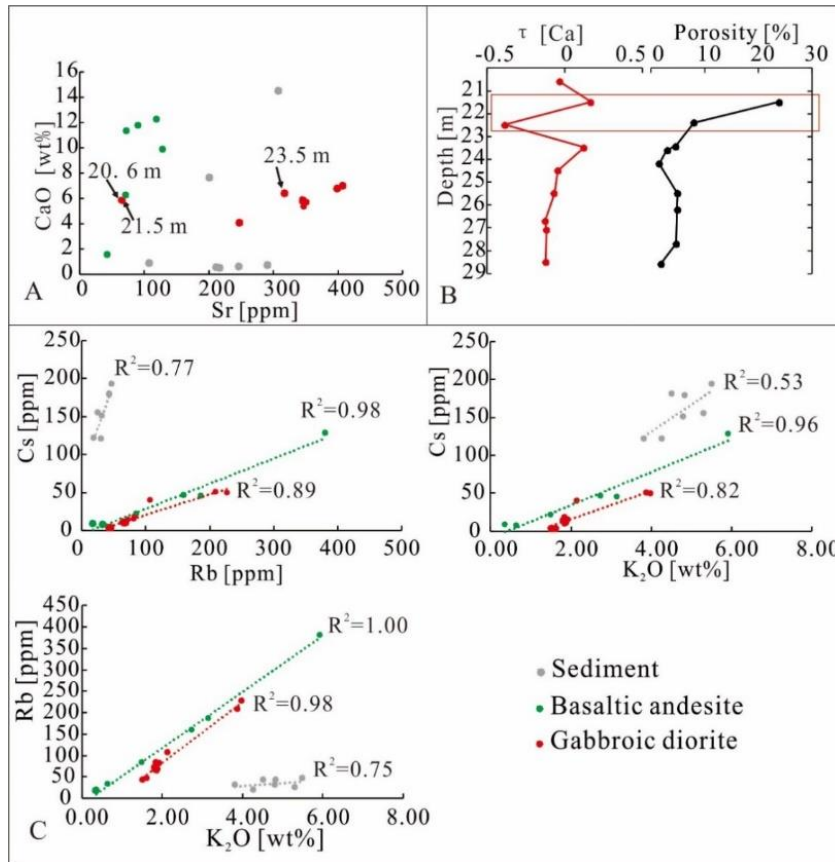


Fig. 2-9. Elements characteristic, (A) CaO-Sr cross-plot of the samples from the GA1 drill core; (B) Relationship between the  $\tau$  value and the porosity in the gabbroic diorite; (C) Relationship among Rb, Cs and K<sub>2</sub>O among sedimentary rocks, basaltic andesite and gabbroic diorite.

Based on the  $K_{corr}$ , K was depleted during the weathering process in both basaltic andesite and gabbroic diorite. The depletion trend of K from top to the bottom is similar to the trend of Na. In the topmost part of the basaltic andesite, is  $-0.59$  and gradually increases to  $-0.35$  and  $0.08$  at depths of  $14.3$  m and  $17.8$  m, respectively. In the top part of the gabbroic diorite, increases from  $-0.26$  ( $20.6$  m) to  $-0.23$  ( $21.5$  m) followed by a sharp increase to around  $0$  in the lowest part (Table A5). The  $\tau$  value trend of  $K_{corr}$  is in agreement with macroscopic and microscopic weathering trends, thereby supporting the applicability of the K correction.

In contrast to Ca and Na, elements closely related to clay formation such as K, Rb and Cs show significant enrichment (Fig. 2-6). In the gabbroic diorite part, the  $\tau$  values of K, Rb and Cs decrease from  $2.5$  to  $0.2$ , from  $5.4$  to  $0.5$  and from  $19.8$  to  $2.3$  from top to bottom, respectively. Similarly, they decrease in the basaltic andesite from  $4.2$  to  $-0.4$ , from  $5.5$  to  $-0.4$  and from  $8.4$  to  $0.2$  from top to bottom, respectively.

To search for the origin of this enrichment, correlation diagrams for gabbroic diorite, basaltic andesite and sediments are plotted (Fig. 2-9c). The linear and close relationships between Cs, Rb and K in the gabbroic diorite and basaltic andesite point to a joint alteration of both, whereas the overlying sediments can be excluded as a source. This is consistent with the conclusion of Molenaar et al.(2015), who claimed that the overlain Permian Rotliegend sediment on Sprendlinger Horst formed a “closed system” and diagenetic fluids did not transfer matter in and out of the system. Palmer and Edmond (1989) claimed that mobile elements such as K, Rb and Cs are very easily extracted by thermal fluids and transferred during hydrothermal activity. In addition to clay transformation, typical minerals formed from hot fluids are observed in thin sections and XRD, such as dolomite accompanied by secondary quartz and adularia (Fig. 2-3). This observation supports the model of a second alteration that was pervasive through the nonconformity and must have happened during burial diagenesis.

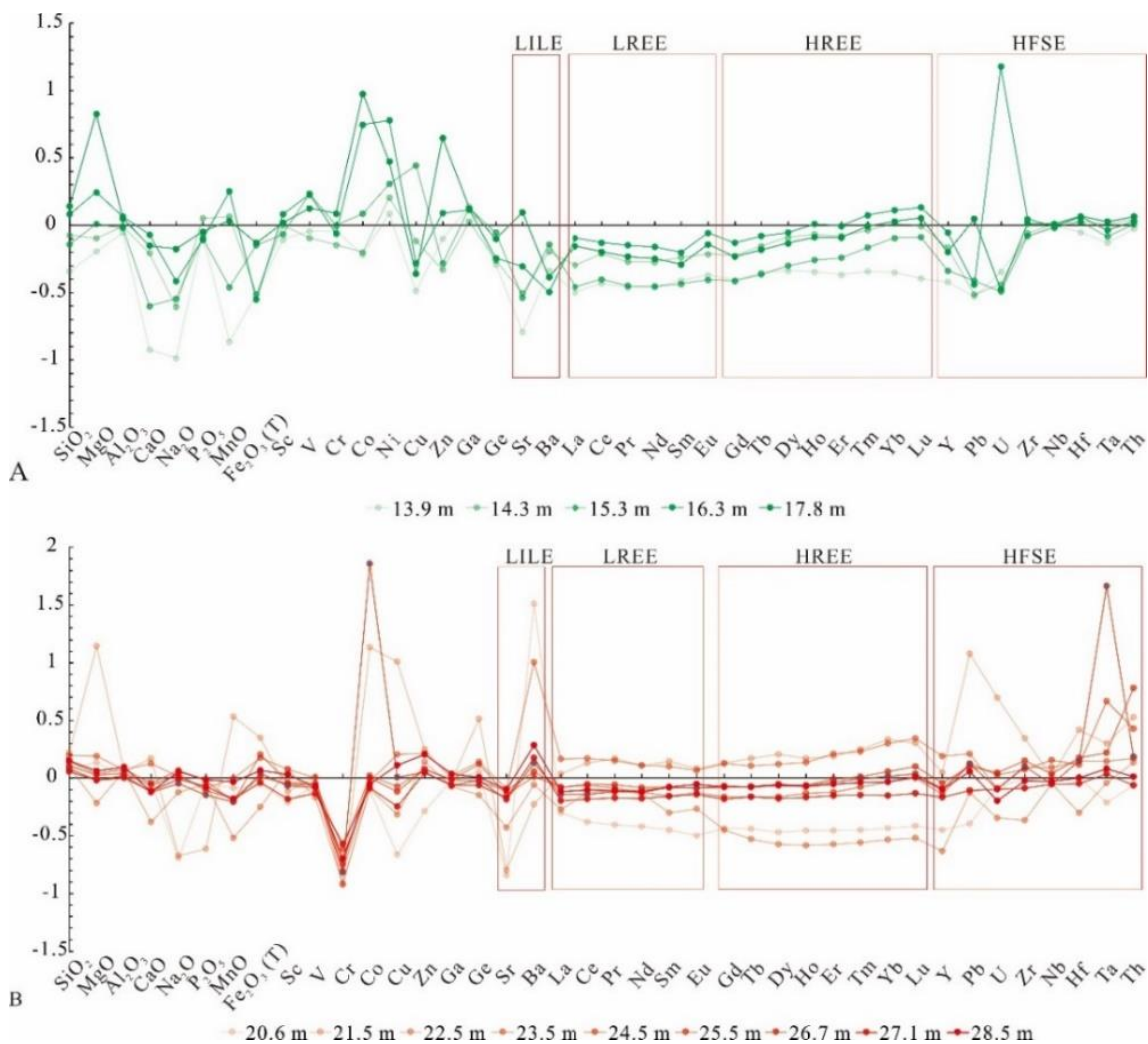


Fig. 2-10.  $\tau$  value features of basaltic andesite (A) and gabbroic diorite (B) in GA1 well

---

Figure 2-10 displays the  $\tau_M$  values for all elements. The large-ion lithophile elements (LILEs), K, Rb and Cs, are removed from the figure due to their strong enrichment which would affect the scaling of all other elements. The remaining LILEs, Sr and Ba, are enriched in the gabbroic diorite but depleted in the basaltic andesite. The enrichment in the gabbroic diorite is most probably associated with diffusive carbonate precipitation, which is missing in the basaltic andesite.

In both gabbroic diorite and basaltic andesite, the  $\tau$  values gradually increase from LREEs to HREEs (Fig. 2-10). This indicates that the depletion degree from LREEs to HREEs decreases during the alteration process if the same conditions exist. In a study of the weathering of a granodiorite, Nesbitt (1979) showed that REEs are removed by acidic leaching of meteoric water which becomes buffered with depth and loses its etching effect due to rising pH. Moreover, Nesbitt (1979) proposed that the fractionation of LREEs and HREEs may be controlled by the mineral type. Kaolinite and illite are favorable for LREEs, whereas vermiculite, Fe-Ti oxyhydroxides, relict hornblende and biotite are more favorable for HREEs. In our study, the decreasing depletion degree from LREEs to HREEs in both weathering profiles also indicates that LREEs are more mobile than HREEs in the same acid weathering environment. Moreover, REE fractionation of the gabbroic diorite is less systematic from the top down compared with the basaltic andesite (Fig. 2-10b). By comparison with rock textures, we assume that this is due to physical fracturing and more heterogeneous chemical alteration in the basement. The strongly depleted samples at depths of 20.6 and 22.5 m are close to fracture zones and possibly more affected by leaching. In contrast, the enriched samples from depths of 21.5 and 23.5 m do not have macro-fractures. This can be explained by acidic meteoric water that used the pathways provided by the macro-fractures in the topmost part of the gabbroic diorite. REEs in the fracture zone were leached, transported downward, and accumulated around the interface of macro-fracture- and macro-fracture-free zone. This is comparable to the behavior of Ca.

The high-field-strength elements (HFSEs), Zr, Nb, Hf, Ta and Th, are expected to be immobile. In the gabbroic diorite, the  $\tau$  values scatter significantly for specific elements within single samples. The samples from depths of 21.5 and 23.5 m show mostly enriched values as well as Pb and U, which is in line with REEs. Other element shifts appear to be controlled by heterogeneous conservation and alteration of specific minerals due to the fractured and granular texture of the rock. The depletion of Pb and U can be well explained by oxidation during weathering into the mobile species  $Pb^{6+}$  and  $U^{4+}$ , respectively, and subsequent leaching by meteoric water. In addition, from LILEs to HFSEs, the overall depletion degree decreased in both the basaltic andesite and gabbroic diorite part during the alteration process.

### 2.6.3. Burial diagenesis

In addition to correcting the alteration trend, the A–CN–K diagram can also be used to kinetically predict the primary weathering products of plutonic and volcanic rocks (Nesbitt and Young, 1984; Panahi et al., 2000). In this case, this concept is applied to differentiate surface weathering from burial diagenesis by comparing the remaining secondary minerals in the profile with the theoretical weathering products.

Due to the chemical composition restriction, rock types that contain only minor amounts of K tend to be weathered directly by forming smectite and kaolinite instead of illite regardless of the climate (Nesbitt and Young, 1989a). In our case, both gabbroic diorite and basaltic andesite contain minor K. However, secondary minerals mainly consist of illite which makes metasomatic addition of this element during burial diagenesis highly probable (Fedo et al., 1995). As discussed in Sect. 2.5.2, K metasomatism is possibly promoted by hydrothermal fluids. According to the A–CN–K diagram (Fig. 2-11), the initial weathering products of the gabbroic diorite should have mainly consisted of smectite, and a small quantity of kaolinite is expected in the top part (20.6–21.5 m). For the basaltic andesite (13.9 m), kaolinite with a small portion of smectite is expected, whereas smectite should be dominant in the lower part. ESEM (environment scanning electron microscopy) indicated kaolinite in two morphologies: vermiform (Fig. 2-2h) and booklet form (Fig. 2-2i). According to Chen et al. (2001) and Erkoyun and Kadir (2011), vermiform kaolinite is favored during the in situ formation of kaolinite, whereas the euhedral booklet form is favored during autogenic diagenesis (e.g. Bauluz et al. 2008). Kaolinite formed by chemical weathering is always more anhedral (Bauluz et al., 2008; Varajao et al., 2001), therefore, the influence of subrecent surface-related weathering can be excluded in our case. Based on the XRD results of the gabbroic diorite (Fig. 2-3), the remaining mineral in the topmost part (13.9 m) of the basaltic andesite is I–S, which can be explained by the conversion of kaolinite and smectite into I–S.

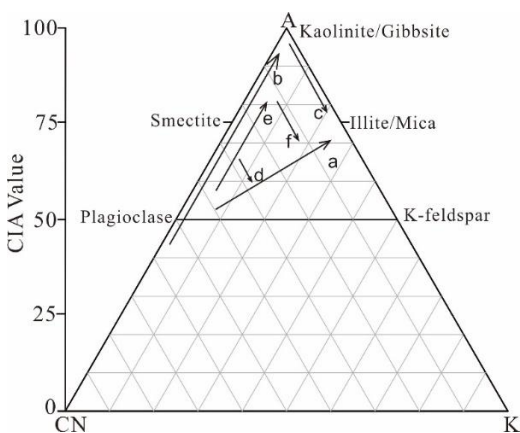


Fig. 2-11. Theoretical weathering tendency and tendency during burial diagenesis (Fedo et al., 1995), a-observed weathering trend for both basaltic andesite and gabbroic diorite; b-theoretical weathering trend for basaltic andesite; c-K-metasomatism trend of topmost basaltic andesite;

---

d-K-metasomatism trend of the rest part of basaltic andesite; e-theoretical weathering trend for gabbroic diorite; f- K-metasomatism trend for gabbroic diorite

Na and Ca, as needed for the I-S formation, may originate from the original smectite or from diagenesis fluids. The  $\tau$  values of Na and Ca in the topmost part are  $-0.99$  and  $-0.93$ , respectively; therefore, the influence on the CIA and PIA values for evaluating the weathering intensity is negligible. The remaining secondary mineral in the lower part (14.3–19.3 m) is illite, which can be explained by the conversion of smectite into illite. During the conversion from smectite into illite, Ca and Na will be further depleted. The depletion of these elements will surely increase the CIA and PIA values. Due to the higher content of weathering products (smectite), more Ca and Na will be lost. The influence on the CIA and PIA values will also be more evident. Therefore, in this case, due to the low content of original weathering products, the depletion of Ca and Na content should be limited, thereby resulting negligible effects on the CIA and PIA values. Similar to the basaltic andesite, in the gabbroic diorite, the first secondary minerals formed by weathering were predominantly smectite according to the A-CN-K diagram. During the overprint of diagenesis, the smectite was transformed into I-S in the topmost part (20.6–21.5 m); in the lower part (22.5–28.5 m), the smectite was all transformed into illite. Hence, the Ca and Na should be depleted and the CIA and PIA should increase. In the topmost part, this influence should be highest and should decrease with the decreasing content of the secondary minerals towards the lower part. In both basaltic andesite and gabbroic diorite, the illitization makes K addition from outside the system necessary, most probably by fluid migration through fractures. The smectite resulting from weathering in the gabbroic diorite would have been altered to pure illite in the presence of sufficient K. As we observe a high amount of I-S, the K supply was not sufficient to alter the smectite completely to illite in the topmost part of the gabbroic diorite (20.6–21.5 m). A similar mineral content pattern also exists in the basaltic andesite. The illite in the lower part (14.3–16.3 m) was most probably transformed from smectite. However, the K supply was not high enough in the topmost part where I-S and residual kaolinite are dominant (13.9 m) (Fig.2-3).

#### **2.6.4. Implications for paleoclimate**

The occurrence of weathering products, such as illite, smectite and kaolinite, can be applied as a useful tool to assess the paleoclimate (Clift et al., 2014; Raucsik and Varga, 2008; Singer, 1988). However, caution should be used when working with these parameters as clay minerals may be overprinted by transformation or neof ormation during burial diagenesis, and there is also the restriction due to the geochemical composition of rock type, as discussed in Sect. 2.5.3. It follows that, when the clay minerals in the sedimentary rocks are investigated to assess paleoclimatic conditions, the lithology of the source rocks should be considered. In particular, for the weathering profile of the igneous rock, all of the involved processes mentioned above will lead to

---

misjudgments regarding the paleoclimate conditions if working with raw data. Taking this study as an example and interpreting the original data from XRD and SEM analyses, I-S clay minerals would indicate a subhumid climate with prominent dry seasons (Raucsik and Varga, 2008; Singer, 1988). For the deeper parts of both basaltic andesite and gabbroic diorite, the clay minerals are dominated by illite, pointing to a cold or dry climate. According to this information, the profile would suggest that the climate alternated twice from a cold and dry climate to a seasonal and alternating wet and dry climate. However, due to the limited K availability, the dominant illite in gabbroic diorite and basaltic andesite must be a product of a diagenetic overprint. When correcting the A-CN-K diagram, the primary weathering product in the topmost part of the gabbroic diorite must have been smectite with negligible illite and possibly a small quantity of kaolinite (20.6–21.5 m). Furthermore, smectite can also not be applied to evaluate the paleoclimatic conditions in this case due to the K limitation of the lithology.

Although the CIA and PIA values may be misleading sometimes, they display the alteration intensity of the gabbroic diorite well, with much higher values in the topmost part (20.6–21.5 m). However, a related tendency of HFSEs is nonexistent (Fig. 2-6b). Due to leaching, these immobile elements are expected to become indirectly enriched, which is not observed. HFSE values and  $\tau$  values of representative LILEs, such as Na and Sr, show a positive correlation with porosity data, which suggests that the intensity of the leaching process was more dominated by the porosity formed by intense physical weathering than by other factors, such as the climate shifting to more humid conditions.

Correction of the A-CN-K diagram for the basaltic andesite section suggests that primary products of the altered basaltic andesite were dominated by kaolinite in the topmost part (13.9 m) and mainly by smectite in the lower part. Again, smectite cannot be applied as a climate parameter due to the restriction of the K content in basaltic andesite. Similar to the gabbroic diorite section, the CIA and PIA values, the mineral abundances and the petrographic features significantly change between the topmost part (13.9 m) and the lower part (14.3–19.3 m). In contrast to the gabbroic diorite, however, the relative content of high-field-strength elements (HFSEs), such as Nb, Ta, Zr, Hf and Ti, are all drastically shifted between the topmost part (13.9 m) and the lower part (Fig. 2-6a). The abnormal relative concentrations of these elements in the topmost part indicate more depletion of other relatively more mobile elements, which is confirmed by the  $\tau$  value of Na and Ca. All parameters together, i.e., the CIA, PIA, relative content of clay mineral types (additional kaolinite in the topmost part), and petrologic features indicate that the climate changed to humid conditions during basalt weathering. Moreover, the thin saprolite layer demonstrates that surficial weathering only lasted for a short period and that the basalt was rapidly covered by alluvial sediments.

---

As mentioned in Sect. 2.5.2, the weathering environment for the basaltic andesite was more acidic than for the gabbroic diorite. The acid present in the weathered profile can be attributed to CO<sub>2</sub> input from the atmosphere or organic acids produced by vegetation. Based on the drill core profile, vegetation was undeveloped at the paleo-surfaces on both the gabbroic diorite and basaltic andesite parts. Hence, the increased acid was probably due to an increase in CO<sub>2</sub> in the atmosphere (Berner, 1992; Neaman et al., 2005), which may also be the reason for the deglaciation event during the Permo-Carboniferous.

### **2.7. Scenario for alteration at the post-Variscan nonconformity**

As the weathering process and the paleoclimate is elucidated, the overall alteration process at the post-Variscan nonconformity can be separated into three subsequent steps (Figs. 2-12, 2-13, 2-14). Approximately at the Carboniferous–Permian boundary, the gabbroic diorite was firstly weathered under relatively arid conditions. This included fracturing by physical weathering and moderate chemical weathering. Plagioclase was transformed to smectite with negligible illite (Fig. 2-12, Eqs. 1–2). Other minerals such as amphibole and biotite were weathered to smectite and chlorite accompanied by the generation of hematite and vermiculite (Fig. 2-12, Eqs. 3–5). With the beginning of volcanism in the early Permian, the nonconformity was concealed by the basaltic andesite lava flow, which underwent a short but intense period of chemical weathering. Firstly, pyroxene and plagioclase were weathered to vermiculite and smectite (Fig. 2-13, Eqs. 6–7). Thereafter, more humid conditions initiated increased leaching and smectite was transformed to kaolinite (Fig. 2-13, Eq. 8). During these two stages, elements such as Na, Ca and K were depleted from the system, either by export or descendent enrichment in the profile. After a relatively short time interval, the basalt was concealed by sediments and the weathering process terminated. During burial diagenesis, fluids transformed smectite and kaolinite into illite in both gabbroic diorite and basaltic andesite (Fig. 2-13, Eqs. 9–10). The transformation of smectite to illite led to depletion of Ca and Na as well. This leaching process is accompanied by the formation of accessory minerals such as quartz, dolomite, calcite and adularia (Fig. 2-14, Eqs. 11–12), which indicate a temperature of around 200 °C (Stimac et al., 2015). Emplacement of calcitic veins is partly coupled with low-temperature migration recrystallization quartz (Fig. 2-2c), which indicates a temperature of around 300 °C (Stipp et al., 2002). This roughly coincides with temperatures from thermochronological apatite fission track studies in the surrounding basement of the Odenwald that indicate heating of up to more than 130 °C before 80–105 Ma and homogenization temperatures from fluid inclusions in hydrothermal veins of up to ca. 290 °C (Burisch et al., 2017; Wagner et al., 1990). Subsidence ceased in the uppermost Jurassic, as evident from surrounding sedimentary sequences in southern Germany. Relative stability can be expected until the early Cenozoic, when the European Cenozoic Rift System was initiated and also formed the

Sprendlinger Horst (Ziegler et al., 2004). Since the Eocene, the Mesozoic sedimentary cover of the Sprendlinger Horst has been subsequently removed. Most probably, exhumation of the basement did not take place before the upper Miocene (Sissingh, 2003). A further pulse of exhumation is proven for the Middle to Late Pleistocene (Lang, 2007).

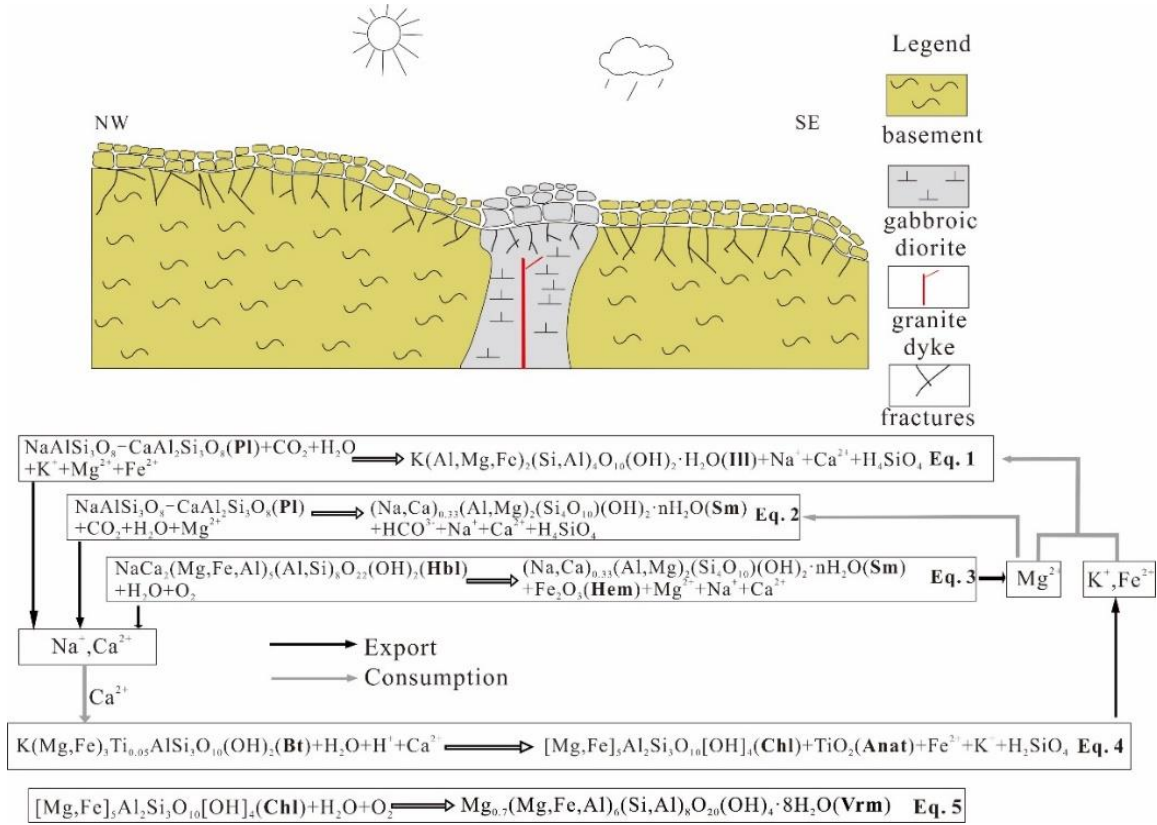


Fig.2-12. Reconstructed alteration model of GA1 well in Sprendlinger Horst before volcanic eruption around ca. 300 Ma; Abbreviations: Anat- anatase; Bt-biotite; Chl-chlorite; Hbl-hornblende; Hem-hematite; Ill-illite; Pl-plagioclase; Sm-smectite; Vrm-vermiculite.



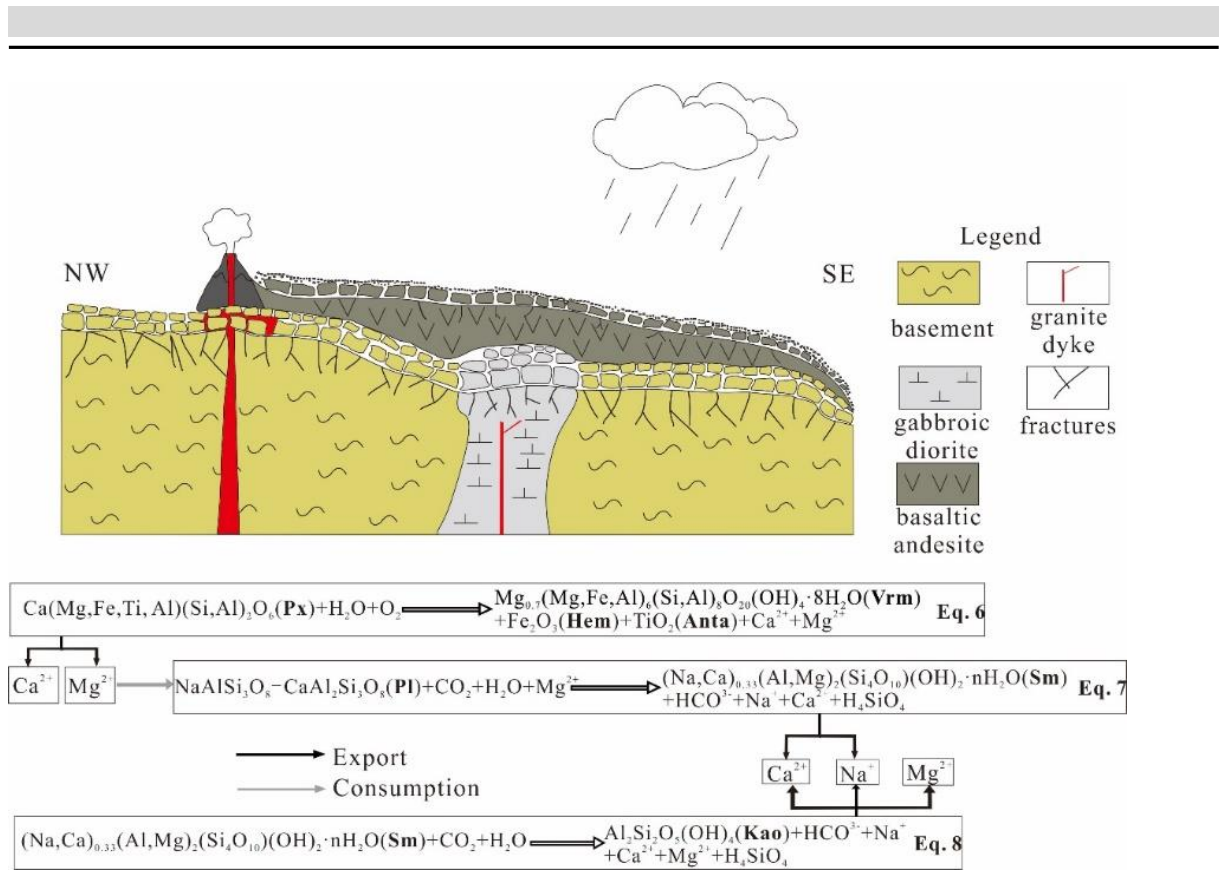


Fig. 2-13. Reconstructed alteration model of GA1 well in Sprendlinger Horst after volcanic eruption around 290 Ma; Abbreviations: Px-pyroxene.

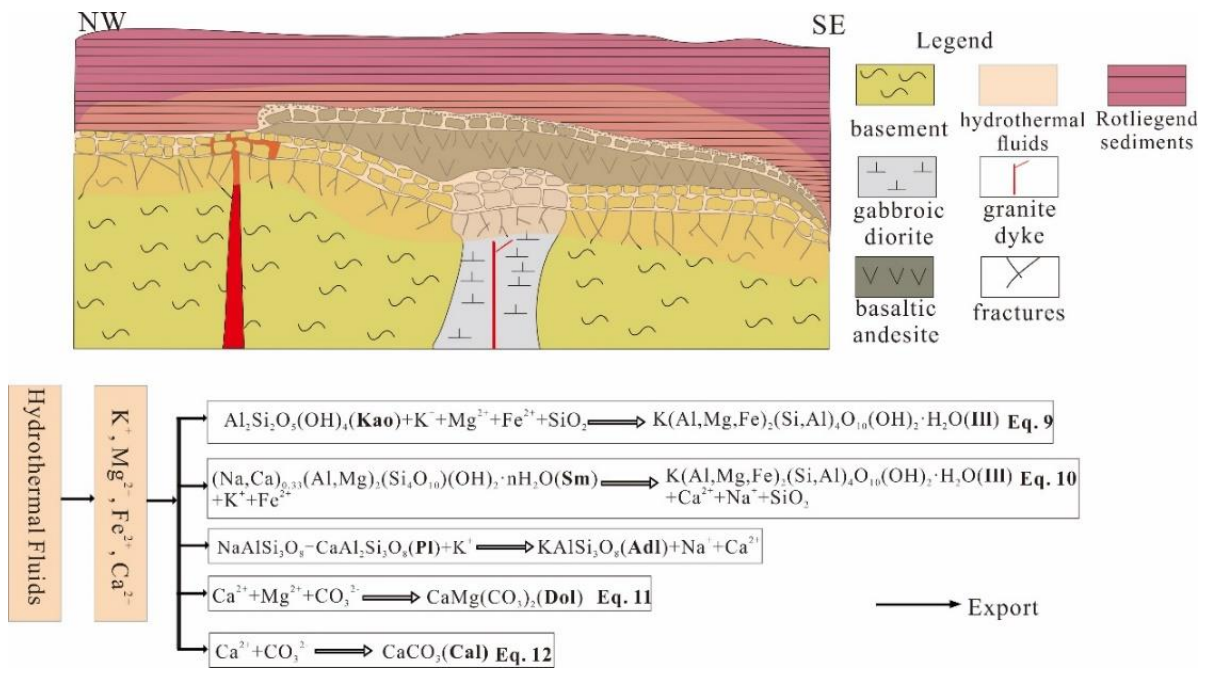


Fig. 2-14. Reconstructed alteration model of GA1 well in Sprendlinger Horst during burial in the Jurassic and Cretaceous; Abbreviations: Adl- adularia.

---

## 2.8. Conclusions

A combined study of mineralogy, petrography and geochemistry was performed on a drill core that penetrates the post-Variscan nonconformity on the Sprendlinger Horst (southwestern Germany). The aim of this study was to elucidate rock alteration at and across the nonconformity and to disentangle surficial weathering and its overprint by burial diagenesis. The unconformity is covered by a Permian lava flow followed by alluvial sediments of the Rotliegend. This allows for the study of two different lithologies and two subsequent periods of surficial weathering as well as the burial diagenesis affecting both in a later stage. The crystalline basement is composed of a gabbroic diorite, whereas the lava flow is a basaltic andesite.

In the gabbroic diorite, mineralogical and geochemical parameters show a gradual alteration trend with a maximum depth of around 10 m, whereas the andesitic basalt shows a shallower and more intense alteration with complete chemical alteration in the topmost part. Chemical alteration goes along with physical alteration which is evident from the fracture density. The different alteration steps were separated using thin section analysis, clay mineralogy and geochemistry. In addition, the trends of the A-CN-K diagram and element transfer ratios were used to determine pristine rock compositions.

Surficial weathering of both gabbroic diorite and basaltic andesite are all indicated by petrographic characteristics, increasing abundance of secondary minerals, increasing CIA and PIA values, and enrichment of immobile HFSEs due to the leaching process. In the gabbroic diorite, ubiquitous now filled fractures with a width of around 1 cm in the upmost part (20.6–21.4 m) suggest intense physical weathering combined with chemical weathering, preferentially along these fractures. The corrected clay mineral composition yields smectite with negligible illite and possibly a small quantity of kaolinite, pointing to an arid climate. Physical weathering in the basaltic andesite is much weaker compared with the gabbroic diorite. An overprint by burial diagenesis is indicated by K metasomatism, clay mineral transformation and neof ormation of minerals, as well as an enrichment of K, Rb and Cs in the alteration zone. In both the gabbroic diorite and andesitic basalt, the primary weathering products such as smectite and kaolinite were transformed into illite, and this will also have some influences on the evolution of weathering intensity.

At both nonconformities, distinct gradients from the top downward demonstrate that surficial weathering is the major alteration process. During burial diagenesis, fluids preferentially percolated along the post-Variscan nonconformity and at the basalt–sediment boundary, due to a higher permeability. This led to clay mineral transformation and some neof ormation of minerals, but it did not change the alteration pattern. Deeper parts of both parent rocks are pristine and are not affected by surficial weathering nor by fluids during burial diagenesis.

---

Our case study shows that surface weathering in the past is a primary control on the petrography and geochemistry and also guides fluids through the system during burial diagenesis. Moreover, we could demonstrate that the formation of the saprolite zone depends on rock composition, climatic conditions and the duration of the process. Our results have implications for paleoclimatic and burial diagenetic studies. In order to separate hypogene and supergene alteration, we provide a workflow for nonconformities and shed light on the use of paleo-weathering surfaces for paleoclimate research.

### **2.9. Code availability**

The PDF-2 and PDF-4 powder diffraction files applied in this paper are available from the International Centre of Diffraction Data at <https://www.icdd.com/pdf-2/> (last access: 10 May 2021) and <https://www.icdd.com/pdf-4-minerals/> (last access: 10 May 2021) (Gates-Rector and Blanton, 2019), respectively.

### **2.10. Data availability**

All of the original data presented in this study are documented in the Appendix related to this paper.

### **2.11. Sample availability**

All samples are available at the Institute of Applied Geoscience, TU Darmstadt, and can be requested from [liang@geo.tu-darmstadt.de](mailto:liang@geo.tu-darmstadt.de).

### **2.12. Supplement**

The supplement related to this article is available online at: <https://doi.org/10.5194/se-12-1165-2021-supplement>.

### **2.13. Competing interests**

The authors declare that they have no conflict of interest.

### **2.14. Acknowledgements**

The authors would like to thank the Senckenberg Research Station of Grube Messel, Sonja Wedmann and Bruno Behr, who provided drill cores for this work, and Reimund Rosmann, who provided a lot of help. We highly appreciate the constructive reviews from Reinhard Gaupp and Henrik Friis.

### **2.15. Financial support**

This research has been supported by the University Scientific Research Program of Xinjiang Uygur Autonomous Region Education Department (grant no. XJEDU2019Y070), Innovative Talents

---

Project of Karamay Science and Technology Bureau (grant no. 2019RC002A), and the China Scholarship Council (grant no. 201806400006).

### **2.16. Review statement**

This paper was edited by Johan Lissenberg and reviewed by Reinhard Gaupp and Henrik Friis.

---

### 3. Quantification of Physical and Chemical Paleoweathering at the Microscale - A New Concept

---

Fei Liang<sup>1\*</sup>, Matthias Hinderer<sup>1</sup>, Jens Hornung<sup>1</sup>

<sup>1</sup>Material and Geosciences, Institute of Applied Geosciences, Technical University of Darmstadt, Darmstadt 64287, Germany.

\* Correspondence. Liang Fei. Email: liang@geo.tu-darmstadt.de;

Received: 11 March 2022 / Accepted: 9 December 2022

Published in *International Journal of Earth Sciences* (<https://doi.org/10.1007/s00531-022-02281-3>)

#### 3.1. Author contributions

(i) Fei Liang as the first author developed the methodological concept, prepared all the figures, tables and verified the method with a case study.

(ii) Matthias Hinderer and Jens Hornung supervised this research and helped revise the manuscript.

**Abstract** Weathering is a basic geological process that refers to the breaking down or dissolving of rocks and minerals on the surface of the earth. However, weathering characteristics may vary among different lithologies even under similar conditions. To evaluate and quantitatively compare the physical and chemical index of alteration among different types of rock, new concepts of paleo-weathering such as the absolute weathering degree and the relative weathering degree are proposed for microscale studies. For the quantification of physical weathering, the index of physical weathering (IPW) is introduced. The index is defined as the ratio between the area of the fractures formed during different weathering stages and the total area of the thin section under the polarizing microscope and it is corrected by the corresponding rock strength. To quantitatively compare the chemical weathering intensity among different types of rock and minerals two new concepts are introduced: total weathering mass (TWM) and chemical weathering ability (CWA). While the TWM is an integral function of weathering rate and weathering time for minerals, the CWA is the sum of the TWM of each mineral in rock within a certain time period. As a case study, this concept is applied to the weathered crystalline basement below the post-Variscan nonconformity in southwestern Germany. The petrography and geochemistry of three drillings penetrating the nonconformity were investigated by polarizing microscopy, X-ray diffractometry (XRD), scanning electron microscope (SEM), X-ray fluorescence (XRF) and inductively coupled plasma-mass spectrometry (ICP-MS). The investigations illustrate how to better extract quantitative information for both, physical and chemical weathering.

**Keywords:** paleoweathering; physical weathering quantification; chemical weathering index normalization; weathering intensity; post-Variscan nonconformity; SW Germany

---

## 3.2. Statements and Declarations

The authors declare that they have no known competing financial interests or personal relationships that could have appeared to influence the work reported in this paper.

## 3.3. Introduction

Weathering as a consequence of physical and chemical factors is one of the most fundamental processes of the Earth's surface system (Babechuk et al., 2014; Riebe et al., 2003). For decades, traditional indices for the evaluation of weathering degrees, such as the CIA (chemical index of alteration) (Nesbitt and Young, 1982), PIA (plagioclase index of alteration) (Fedo et al., 1995), CIW (chemical index of weathering) (Harnois, 1988) and  $\Sigma$  bases/Al ratio (Retallack, 1999), have been used to interpret the influence of chemical regime (Nesbitt and Young, 1989a), time of exposure (Gallagher and Sheldon, 2013; Jian et al., 2019), climatic conditions (Sinisi et al., 2014), environment and influence of vegetation (Drever, 1994; Pokrovsky et al., 2005) on the formation of hiatal surfaces. However, among different types of rock mineral compositions, textures and susceptibility to physical and chemical weathering differ significantly (Nesbitt and Young, 1984; White et al., 2001b). This leads to the fact that even under the same weathering intensity, the weathering degree for different types of rock is different. When investigating hiatal surfaces at the regional scale, the results from different types of rock may be contradictory and not comparable, which makes comprehensive conclusions impossible. If it would be possible to normalize weathering patterns quantitatively for different rock types, regional-scale reconstructions of the conditions forming a hiatal surface would be possible. Such consistent results would allow for quantifying the duration and kind of sediment production processes, which can improve the mass balancing of sediment routing systems and sediment distribution models in basin analyses. Additionally, a quantitative and comparable measure of alteration in terms of mineralogical composition, permeability and porosity will enhance the accuracy of related reservoir models.

To find a method for the normalization of the chemical weathering index to mirror the chemical weathering intensity among different lithologies, the relationship of the weathering rate among different minerals must be considered. Experimental setups in the laboratory or field delivered a

---

wealth of mineral-specific dissolution rates (e.g. Chou. and Wollast 1985; White and Brantley 2003). These results can be used to determine the susceptibility to chemical weathering among different rock types. With the susceptibility, the chemical weathering indices can be normalized. An integrated concept of paleo-weathering also needs to consider physical weathering. In the natural environment, physical and chemical weathering are mutually reinforcing (Matsuoka, 1995; Moon and Jayawardane, 2004b). In contrast to the widely used indices for chemical weathering, quantitative evaluation of physical weathering is fairly scarce. One method for the quantification of physical weathering in a modern environment is to compare the relative content of primary Fe(II) silicates in the dust source (Shoenfelt et al., 2019); other methods quantified the physical weathering with the characteristics of suspended particulate material in the river (Qin et al., 2006). However, these methods are only suitable for investigations on a regional scale, and investigations of the physical weathering degree and the physical weathering intensity for specific paleo/weathering profiles at the local scale are still hesitant. Most previous studies on the physical weathering degree of paleosols are based on the Rock Weathering Classification diagram summarized by Aggisttalis et al. (1996). The diagram qualitatively describes seven different weathering degrees: fresh, faintly weathered, slightly weathered, moderately weathered, highly weathered, completely weathered and residual soil according to the exposed modern weathered profile, which is somehow a result of both features of physical and chemical weathering. Subsequent researchers optimized the table to five degrees by removing faintly weathered and residual soil (e.g. Ceryan et al. 2008). With the development of engineering, the form was enriched by parameters such as uniaxial compressive strength (UCS) (e.g. Chiu and Ng 2014). Some of the researchers introduced the major elements and/or chemical weathering indices into their studies (Ceryan, 2008; Tugrul and Gurpinar, 1997). The geochemical data are applied to estimate the mechanical properties of the rock under the five summarized weathering degrees. However, a physical index specifically for modern and paleoweathering profiles has yet to be created. Nevertheless, the relationship between the geochemical data and mechanical properties provides an ideal dataset to evaluate the susceptibility to physical weathering degree among different rock types.

---

This study uses an integrated quantification of chemical and physical weathering from the covered paleo-surface of the Variscan basement in southwestern Germany. The quantification of the physical weathering degree is mainly based on the detailed fracture characteristics at the microscale, and the results are expressed as the index of physical weathering (IPW). The normalization of IPW and chemical weathering indices is based on the susceptibility of different lithologies to weathering, and the results are supposed to reflect weathering intensity.

### 3.4. Integrated concept for the quantification of paleo-weathering

### 3.5. Physical weathering degree quantification

Physical weathering is a ubiquitous process in the upper crust and is crucial for providing materials for sedimentary rock and landscape modification (Camuffo, 1995; Matsuoka et al., 1996). However, an index for physical weathering is still not available. The physical weathering degree is reflected by the fracture density and width, as well as fragmentation of the rock matrix (Camuffo, 1995). The higher the physical weathering degree is, the denser the spacing and wider the fractures. Therefore, the physical weathering degree can be expressed, in principle, by the ratio between the fracture and the total area within a specific zone. This study concentrates on the microscale and uses petrographic analysis of thin sections. The quantification of the physical weathering degree and intensity is performed in five steps, as shown in Fig. 3-1, and detailed in the following sections.

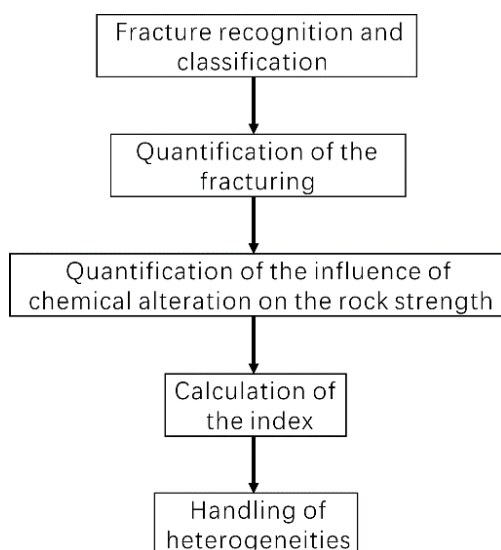


Fig. 3-1 Workflow for physical weathering degree quantification.



---

### 3.5.1. Fracture recognition and classification

Fractures may be formed due to weathering and/or other factors, such as tectonic stress in the natural environment. Regardless of whether the fractures are formed due to physical weathering or tectonic stress, they may be filled by secondary minerals, which may be products of chemical weathering and/or the minerals are formed due to burial diagenesis. The minerals formed during chemical weathering have different mineralogical and geochemical characteristics compared to those formed by burial diagenesis (Bauluz et al., 2008; Dill, 2010), which can be used to distinguish them. However, the fillings of fractures cannot be used to conclude whether the fractures are formed due to physical weathering or tectonic stress. To fix this problem, the method for tectonic fracture recognition with fracture angle or orientation proposed by Gol'braykh et al. (1966) is applied. In this case, the fractures are divided into four groups based on the mineralogical and geochemical characteristics of the fillings in the fractures and the angles of the fractures: i) fractures formed due to tectonic stress; ii) fractures formed before and/or during chemical weathering; iii) fractures formed at the end of chemical weathering; iv) Fractures overprinted by burial diagenesis (Fig. 3-2).

#### i) Fractures formed due to tectonic stress

The tectonic fractures may be formed before, during and/or after the chemical weathering process together with the fractures formed due to physical weathering. The fractures tend to have a preferential orientation and angle due to the influence of tectonic stress, while the fractures formed due to weathering, and orientation and/or the angle tend to show a random pattern (Caspari et al., 2020; Scarpato, 2013). Therefore, to recognize the preferential directions of the fractures, the rose diagram can be applied to illustrate the angle of the fracture along the drill cores. When the rose diagram shows a preferential angle, it indicates that the weathering profile contains both tectonic and weathering fractures. In this case, the fracture area of the tectonic fractures along the weathering profile within the thin sections corresponds to those fractures located in the parent rock ( $F_p$ ).

#### ii) Fractures formed before and/or during chemical weathering

---

The weathering products may be composed of stable minerals including clay and oxide (e.g.,  $\text{Fe}_2\text{O}_3$ ,  $\text{TiO}_2$ ), and unstable minerals such as calcite (Goldich, 1938). The fractures formed before and/or during chemical weathering include both tectonic and physical weathering fractures and therefore are filled by products of weathering, such as clay minerals, oxides and calcite. These fractures are classified as  $F_{cl}$  (fracture, clay),  $F_x$  (fracture oxide) and  $F_c$  (fracture calcite). Whereas stable minerals persist, unstable minerals will gradually be depleted (Harriss and Adams, 1966). Meanwhile, the unstable minerals formed during hydrolysis may transfer and precipitate, accompanied by stable minerals filling fractures in the lower part of the weathering profile (Nesbitt et al., 1980). These fractures formed before and/or during the weathering process are defined as  $F_w$ .

iii) Fractures formed at the end of chemical weathering

While the chemical weathering process comes to the latest stage with a significantly lower rate, the physical weathering process and/or tectonic process may continue, and new void fractures may form ( $F_v$ ).

iv) Fractures overprinted by burial diagenesis ( $F_b$ )

For a weathering profile that is overprinted by burial diagenesis, the void fractures may be filled by secondary minerals. If secondary mineral types are the same as unstable weathering products, such as calcite, which may be formed during both weathering and burial stages, the method proposed by Michel and Tabor (2016) can be applied. This method uses stable C and O isotopes of carbonates to distinguish the process of formation.

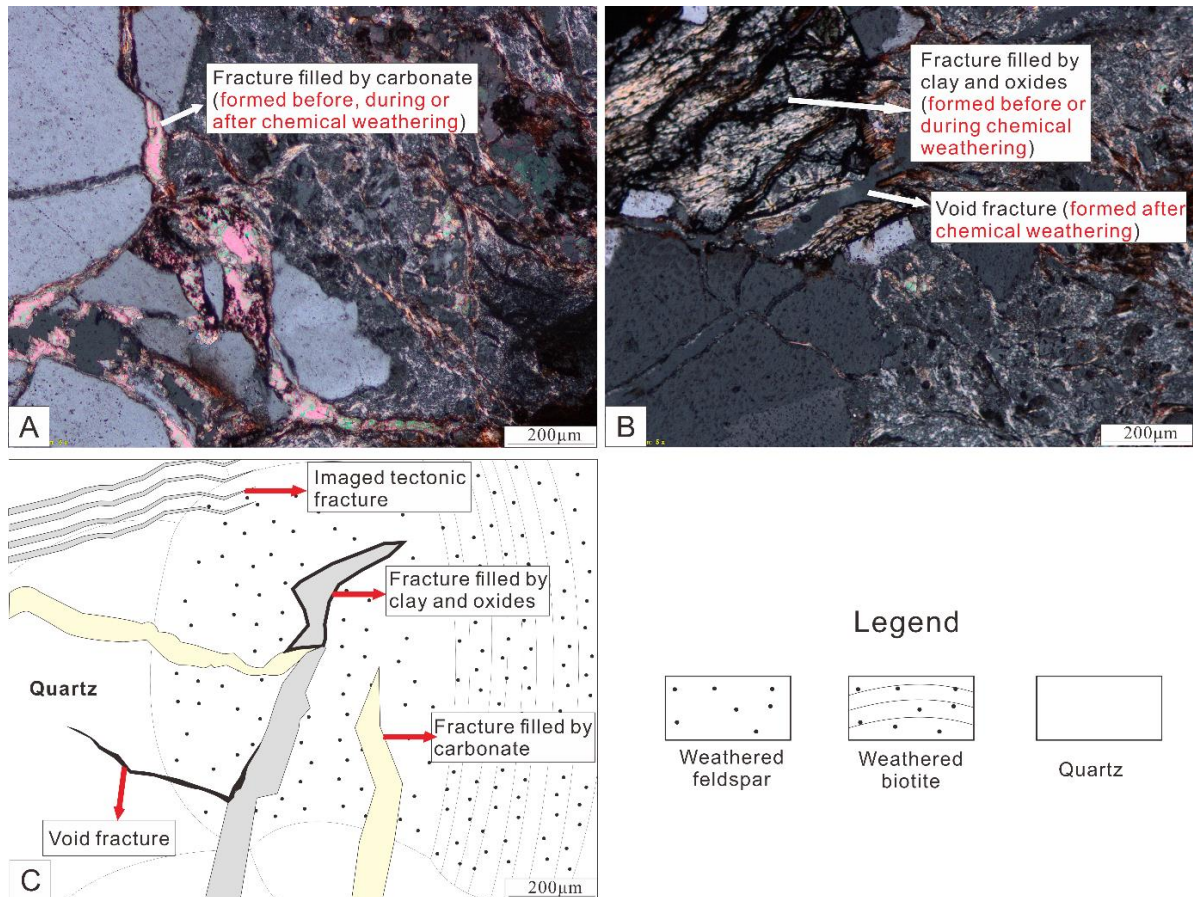


Fig.3-2. Different types of fractures were recognized under the microscope. (A) Fractures filled by carbonate; (B) Void fracture and fractures filled by clay minerals; (C) Fracture patterns within the thin section.

### 3.5.2. Quantification of the fracturing

The fracture area is analyzed under a microscale by a polarizing microscope. In our case, the best results were obtained under 10 eye pieces with 10 objective lenses. The pictures were taken by a single lens reflex camera connected to the microscope and controlled by Olympus Stream Basic software with a plotting scale. The resolution of the photograph was 2560\*1920. To measure the fracture and the inspected area, the thin-section photo taken under the polarizing microscope with a plotting scale was opened by the software ImageJ. To acquire the ratio between the fractures and the whole picture, three steps are shown in Fig. 3-3 and illustrated in the following paragraphs.

Step one: after opening the picture with ImageJ, the pixel unit can be seen in the upper left corner. With the "straight" button of the menu bar, A straight-line coincidence with the plotting scale line

---

should be first drawn. To ensure that the line that draws has the same length as the plotting scale line, the magnifying glass in the menu bar can be selected, and then, the plotting scale part can be clicked to amplify to an appropriate scale; then, the line can be drawn more accurately.

Step two: after drawing the line, the length of the line according to the plotting scale should be defined. To define the length, the “Analyze” button should be selected, and click the “set scale” in the submenu, fill the “Known distance” with the number of the plotting scale, in the example the number is 100, and “Unit of length” in this case is “ $\mu\text{m}$ ”. By clicking “OK” in the plane, the length of the line can be defined. Now, the pixel unit in the top-left corner changes to length unit ( $\mu\text{m}$ ), and with the length and width of the photograph, the area of the total inspected area ( $A_{(Ft)}$ ) can be calculated.

Step three: Select the “Polygon selections” and outline the fractures manually on the digital photograph. Similar to drawing the straight line, the fracture can also be magnified to ensure the accuracy of the outline, if necessary. After selecting the “Analyze” button and clicking “Measure” in the submenu, the area of the outlined area will appear to the right of the photograph. For the void fracture, the area is defined as  $A_{(Fv)}$ , the fractures filled by calcite are defined as  $A_{(Fc)}$ , the fractures filled by clay minerals are defined as  $A_{(Fcl)}$ , the sum of the area of filled fracture in the weathering zone is defined as  $A_{(Fw)}$ , and the area of the fractures within the parent rock is defined as  $A_{(Fp)}$ . The statistical error is less than  $250 \mu\text{m}^2$  with a mean value of approximately  $55 \mu\text{m}^2$ . With the area of both fractures and the photograph, the IPW (area ratio) can be acquired.

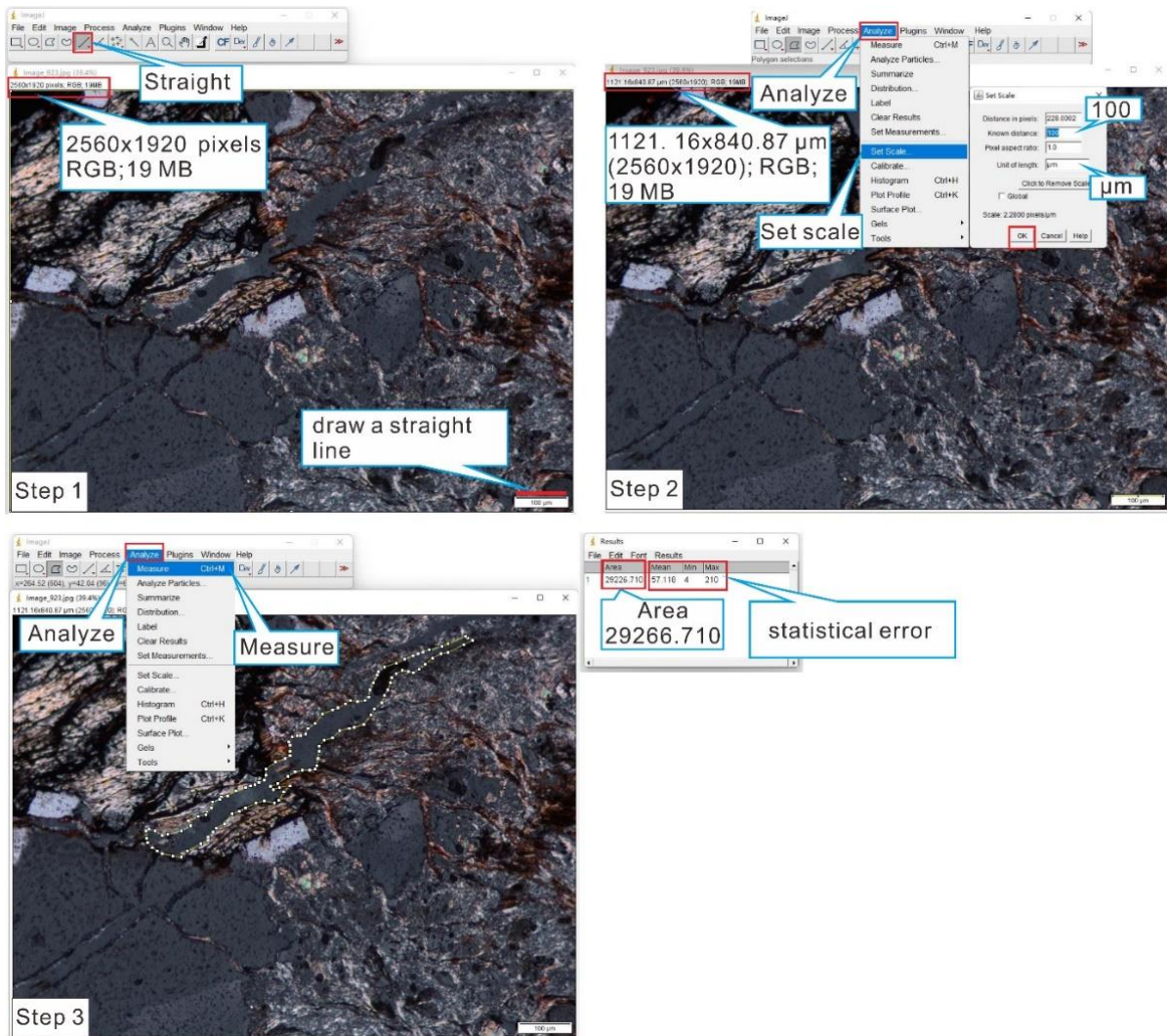


Fig. 3-3. Quantification of the fracturing with ImageJ software. For details of the procedure see the text.

### 3.5.3. Quantification of the influence of chemical alteration on the rock strength

The susceptibilities to physical weathering among different lithologies are intrinsically different. Previous studies indicate that the higher the strength of a rock is, the more resistant it is to physical weathering (Jayawardena and Izawa, 1994; Thomson et al., 2014). Therefore, the susceptibility of different lithologies to physical weathering can be represented and normalized by rock strength to enable the comparison of physical weathering intensity among different lithologies. Rock strength is an engineering geological term that is concerned with mineral composition, structure, texture and jointing (Golodkovskaia et al., 1975). It can be specified in terms of uniaxial tensile strength (UTS), uniaxial compressive strength (UCS), shear strength, and impact strength.

---

The formation of fractures during weathering is more related to the UTS than UCS (Aadnøy and Looyeh, 2019). While the UTS of rock refers to the required pulling force to rupture a rock sample divided by the area of the cross section of the sample, the UCS is the capacity of a rock to withstand loads tending to reduce size (Aadnøy and Looyeh, 2019; Aggisttalis et al., 1996). These two parameters are always in a linear relationship with the UTS at approximately 0.1 times the UCS (Aadnøy and Looyeh, 2019; Cuccuru et al., 2012; Gupta and Rao, 2001). This enables both UCS and UTS to be applied for the normalization of IPW. Within the previous studies, the UCS data are much better available than UTS. Hence, to acquire more data for a more accurate result, the UCS is applied for normalization in this study.

In a natural environment, physical and chemical weathering processes always interfere. The cracks formed due to physical weathering may provide pathways for fluids and accelerate the chemical weathering process (Bland and Rolls, 1998). Meanwhile, meteoric water and pore fluids can also penetrate the basement rock through the rock fabric and further increase the chemical index of alteration (Di Figlia et al., 2007). With the ongoing chemical weathering process the rock strength will gradually decrease (Chiu and Charles W.W., 2014; Khanlari et al., 2012). The decreased rock strength will clearly enhance the formation of the physical cracks which is rock-type specific. Therefore, the chemical index of alteration needs to be considered when the physical weathering degree is normalized. Since the 20th century, quantitative correlations between rock strength and chemical index of alteration have been developed (Korkanç et al., 2015; Tuğrul, 1997; Ündül and Tuğrul, 2012). Different researchers correlated physical parameters, such as UCS and P-wave velocity with chemical parameters, such as loss on ignition (LOI), weathering potential index (WPI) and other indices (Gupta and Rao, 2001; Mert, 2014; Ündül and Tuğrul, 2016). Moreover, previous studies developed empirical formulae of the relationship between the physical strength and the chemical weathering degree for basaltic and granitic rocks, among these chemical weathering indices, the Chemical Index of Alteration (CIA) has a strong relationship with the rock strength (e.g. Arel and Tugrul 2001; Tuğrul 2004). Therefore, based on these formulae and data for basaltic and granitic rock (Ceryan et al., 2008a, 2008b; Erişiş et al., 2019; Khanlari et al.,

2012; Thomson et al., 2014; Tuğrul, 1997), this study compiled data and created a regression out of two rock-specific empirical relationships between UCS and the chemical index of alteration (CIA) (Fig. 3-4):

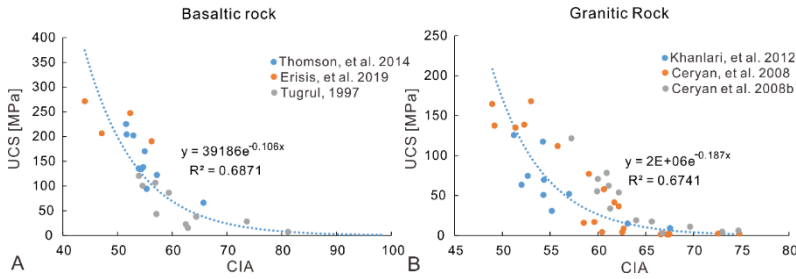


Fig. 3-4 Empirical relationship between UCS and CIA (data from Ceryan et al, 2008a, 2008b; Erişiş et al., 2019; Khanlari et al., 2012; Thomson et al., 2014; Tuğrul, 1997)

$$UCS_{\text{basalticrock}} = 39186e^{-0.106CIA} \quad (r = 0.83) \quad (\text{Eq. 3-1})$$

$$UCS_{\text{graniticrock}} = 2E + 6 * e^{-0.187CIA} \quad (r = 0.82) \quad (\text{Eq. 3-2})$$

With these two empirical formulae, the UCS of basaltic and granitic rock under different chemical indices of alteration can be assessed.

### 3.5.4. Calculation of the index

The index for the quantification of physical weathering is defined as the index of physical weathering (IPW). As the fractures along the weathering profile may contain both tectonic fractures and weathering-fractures, the tectonic fractures increase the area of the fractures within the weathering zone, which need to be eliminated. The area of the tectonic fractures can be represented with those in the parent rock. The fractures created by physical weathering in the weathering zone can be corrected as  $A_{(Fw)} + A_{(Fv)} - A_{(Fp)}$ , and the IPW can be expressed as:

$$IPW = \frac{A_{(Fw)} + A_{(Fv)} - A_{(Fp)}}{A_T} \quad (\text{Eq. 3-3})$$

Where  $A_{(Fw)}$  and  $A_{(Fv)}$  represent the area of the fractures formed before and during weathering process and void fractures in the weathering zone, respectively,  $A_{(Fp)}$  is the area of the fractures within the parent rock, and  $A_T$  is the area of the total inspected area.

The IPW in Equation (3-3) reflects the physical weathering degree and can be used to compare the physical weathering intensity for a specific rock type. However, the variation in the rock strength among different lithologies makes a quantitative comparison of the IPW impossible. To

---

solve this problem, one method is to normalize the IPW with the corresponding susceptibility to physical weathering for each type of rock. The susceptibility is represented by UCS.

As different types of physical weathering fractures exist, they should be normalized by their corresponding individual UCS. For basaltic and granitic rock, the UCS can be acquired with Equations (3-1) and (3-2), respectively. For the void fractures, the rock strength at the weathered sampling position is applied, which is expressed as  $UCS_w$ . However, as it is difficult to determine the specific CIA value while the fractures were formed, the rock strength that the fractures represent is represented by the average rock strength between the parent rock ( $UCS_p$ ) and the weathered sampling position ( $UCS_w$ ), which is defined as  $UCS_A$  and expressed as:

$$UCS_A = \frac{UCS_p + UCS_w}{2} \quad (\text{Eq. 3-4})$$

When the weathering profile is influenced by tectonic fractures, the normalization process can be divided into the following two situations:

i) Tectonic fractures preexisting or formed during chemical weathering

For preexisting tectonic fractures, their mineral filling is often related to successive processes, i.e., fluid flow and water–rock interaction during burial and uplift. This may include different generations of secondary minerals that are unstable and usually dissolve during uplift. As a consequence, the tectonic fractures experience the same process as the preexisting physical weathering fractures. When tectonic fractures form during the chemical weathering process, they would also experience the same process as fractures formed by physical weathering during the same period. The same process leads to the same fractures characteristics. Therefore, to normalize the IPW, first, for the stage before and during chemical weathering, the area of the fractures in the weathering zone ( $A_{(Fw)}$ ) should subtract the area of the fractures within the parent rock ( $A_{(Fp)}$ ), then divide the area of the total inspected area ( $A_T$ ) and normalized by  $UCS_A$ . The stage at the end of chemical weathering should be the sum of the area between the fractures overprinted by burial diagenesis and void fracture divided by the total inspected area ( $A_T$ ) and normalized by the rock strength of the sampled weathering part ( $UCS_w$ ). Therefore, the final IPWN can be expressed as:



$$IPW_N = \frac{A_{(Fw)} - A_{(Fp)}}{A_T} * UCS_A + \frac{A_{(Fb)} + A_{(Fv)}}{A_T} * UCS_w \quad (\text{Eq. 3-5})$$

ii) Tectonic fracture formed at the end of chemical weathering and/or during burial diagenesis

When tectonic fractures form at the end of the chemical weathering process or during burial diagenesis, they should be the fracture area formed at the end of the weathering process, which contains the void fractures, and the fractures overprinted by burial diagenesis subtract the fracture area in the parent rock ( $A_{(Fp)}$ ) and then normalize by  $UCS_w$ . Together with the fractures formed before and/or during chemical weathering, the IPWN can be expressed as:

$$PWI_N = \frac{A_{(Fw)}}{A_T} * UCS_A + \frac{A_{(Fb)} + A_{(Fv)} - A_{(Fp)}}{A_T} * UCS_w \quad (\text{Eq. 3-6})$$

### 3.5.5. Accounting for spatial heterogeneity

Due to the heterogeneity of fracture distribution in the thin section, one view may not be able to represent the physical weathering value over the whole thin section. To determine the most appropriate strategy for acquiring the representative IPWN value, tiles of 3\*3, 3\*5, 4\*5 over all areas of the thin section were applied. The results indicate that, the variation in the average value of the IPW approaches stable values after 15 visions independent of rock type. Therefore, a grid of 3\*5 is applied (Fig. 3-5).

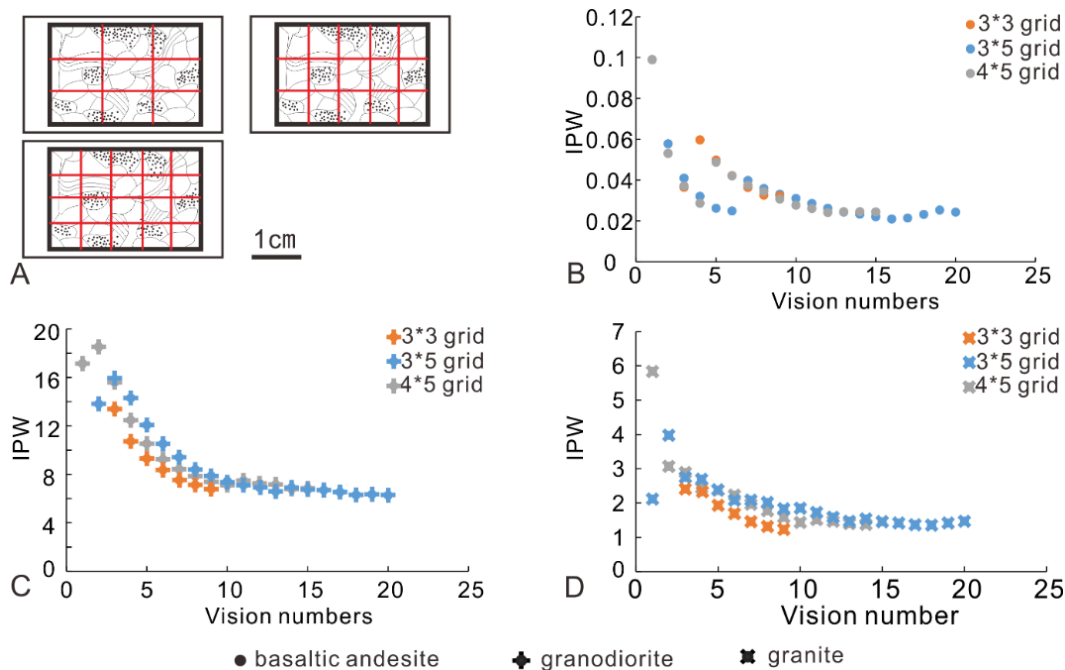


Fig. 3-5 The variation in the IPW with increasing view number and view distribution on thin sections from three different rock types in this case. A: view distribution strategy B: basaltic andesite; C: granodiorite; D: granite.

### 3.6. Chemical weathering index normalization

#### 3.6.1. Chemical weathering ability (CWA)

The quantification of chemical weathering has been well developed and widely applied (e.g. Nesbitt and Young 1982; Mclennan 1993; Fedo et al. 1995; Schoenborn and Fedo 2011; Babechuk et al. 2014). The common indices can be regarded as the absolute chemical weathering degree of a certain lithology. Furthermore, weathering rates for individual minerals, such as plagioclase, K-feldspar, biotite and hornblende have been quantified (e.g. Schott et al. 1981; Riebe et al. 2003). Previous studies have put much effort into determining weathering rates of fresh minerals in the laboratory (e.g. White et al. 2001b; Martinez et al. 2014). Mineral weathering in the natural environment, however, is a continuous process from fresh to weathered. White and Brantley (2003) concluded that the weathering rate of a mineral decreases with time. Based on an experiment with both fresh rock and weathered rock that lasted 6.2 years, they proposed an equation to depict the alteration rate ( $R/\text{mol m}^{-2} \text{s}^{-1}$ ) in the natural environment for different minerals:

$$R = 10^A * t^b \quad (\text{Eq. 3-7})$$

Table 3-1 Parameter values of different minerals for Eq. 3-7 (White and Brantley, 2003).

Minerals	A	b	r (coefficient)
K-feldspar	-12.49±0.32	-0.647 ± 0.076	0.83
Hornblende	-12.67±0.22	-0.623 ± 0.067	0.92
Biotite	-12.32±0.25	-0.603 ± 0.073	0.83
Plagioclase	-12.46±0.16	-0.564 ± 0.046	0.89

With the alteration rate among different minerals, this study develops an equation to depict the total weathering mass (TWM) between the times  $t_1$  and  $t_2$ , which corresponds to the integral function of the weathering rate:

$$\text{TWM} = \int_{t_2}^{t_1} R \quad (\text{Eq. 3-8})$$

---

Based on the TWM of mineral types and the mineralogical composition of a rock, its ability to weather chemically can be described as its chemical weathering ability (CWA). It is calculated as the sum of the TWM for each type of mineral with the coefficient of its proportions in a rock-type:

$$\text{CWA} = p_1 * \text{TWM}_1 + p_2 * \text{TWM}_2 + p_3 * \text{TWM}_3 \dots \dots \quad (\text{Eq. 3-9})$$

Where  $p$  is the proportion of each type of mineral within the rock, which can be acquired by XRD. The formula provides a measure that rocks with higher CWA are more easily to be weathered under the same natural environment. Therefore, the CWA can be applied to evaluate the susceptibility of different rock-types to chemical weathering. Due to this calculation, the sensitivity of CWA to “unweatherable minerals” is low. This study considers ‘unweatherable’ minerals as those showing a chemical weathering rate in natural environments lower than  $10^{-14.5}$  to  $10^{-15.1}$  mol m<sup>-2</sup> s<sup>-1</sup> (e.g. quartz), which is several orders of magnitude slower than for other primary silicate minerals (Schulz and White, 1999). The CWA of a certain rock type is mainly sensitive to “weatherable minerals”, such as plagioclase and biotite. Therefore, using the CWA in this study, the quartz proportion for different types of rock is excluded. Hence, the formula provides a measure that rocks with higher CWA are more easily weathered under the same natural environment. In conclusion, CWA can be applied to assess the susceptibility of different types of rock to chemical weathering.

### **3.6.2. Normalization of chemical weathering indices using CWA**

The CWA for different igneous parent rocks provides a chance to determine the relationship for the chemical weathering degree under the same weathering intensity. As the chemical weathering degree can be well quantified by chemical weathering indices, such as CIA, PIA and CIW, to compare the chemical weathering intensity among different rock types, the final purpose is to normalize a chemical weathering index and make the values among different lithologies comparable. To do that, an appropriate solution is to first set a reference rock, and evaluate the chemical index of alteration of the reference rock under the same weathering conditions of the rock to be normalized based on the CWA relationship (Fig. 3-6).

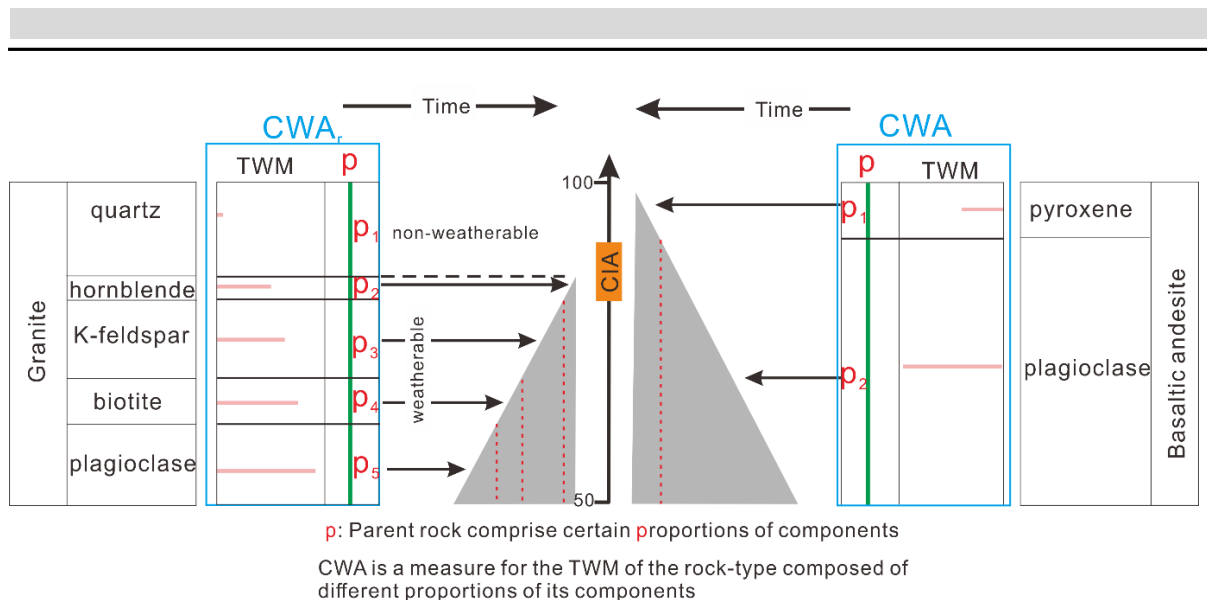


Fig. 3-6. Relationship and definition of total weathering mass (TWM) chemical weathering ability (CWA) and chemical index of alteration (CIA). The contribution to the weathering index CIA of each type of mineral is represented by the area of the gray part of the triangle (example based on granite and basaltic andesite in this case).

The methods for the quantification of the chemical index of alteration in previous studies are mainly based on the ratio between the sum of residual “mobile elements” (such as Na, Ca and K) and “immobile elements”(such as Al)(Fedo et al., 1995; Harnois, 1988; Nesbitt and Young, 1982). As Na, Ca, K and Al exist in most common weatherable rock-forming minerals (Deer et al., 2013), the classic chemical weathering index CIA (Nesbitt and Young, 1982), which contains all these elements, is taken as an example for the explanation of the chemical index of alteration normalization. The normalized values mirror the chemical weathering intensity among different lithologies. Therefore, the results can contribute to quantifying the climate variation even with lithologies that show intrinsically different susceptibilities to chemical weathering.

For the normalization of CIA values of the sampled rock, a reference rock is needed. The normalization process is divided into three steps:

i) First, the difference in the CIA values compared to fresh parent rock values is calculated (CIA<sub>f</sub>), this difference is called the deviation degree ( $\lambda$ ):

$$\lambda = \frac{CIA}{CIA_f} - 1 \quad (\text{Eq. 3-10})$$

The same formula is applied for the sampled rock. For the reference rock, the deviation of the CIA is defined as  $\lambda_r$ , and for the sampled rock to be normalized is defined as  $\lambda_s$ .

---

ii) Normalize the deviation range of CIA for the sampled rock type

By definition, the maximum CIA value is 100 if the mobile elements Na, Ca, and K are completely leached and only silicates are left over. However, for different minerals, the proportions of Na, Ca, K and Al within the silicate are different. As a result, the CIA values vary with rock types and mineral types, e.g. the CIA value for feldspars is 50; for biotite between 50 and 55, for hornblende 10 to 30 and for pyroxene between 0 and 20 (Mclennan, 1993; Nesbitt and Young, 1984). This means that chemically fresh mafic rocks dominantly composed of pyroxene or hornblende, show CIA values lower than those of felsic rocks, mainly consisting of feldspars and biotite.

Thus, a correction coefficient  $n$  is introduced to correct the variation range of CIA between the reference rock and the sampled rock, which is normalized to the same range:

$$n = \frac{CIA_{fr} * (100 - CIA_{fs})}{CIA_{fs} * (100 - CIA_{fr})} \quad (\text{Eq. 3-11})$$

Where  $CIA_{fs}$  refers to unweathered fresh part of the sampled rock and  $CIA_{fr}$  refers to the unweathered fresh part of the reference rock.

iii) Normalization of CIA for sampled rock type with CWA

With the correlation coefficient  $n$ , the variation range of CIA between the sampled rock and reference rock is corrected to the same range. However, due to the difference in the susceptibility to chemical weathering, the deviation degree should further consider the discrepancy in the CWA between the sampled rock and the reference rock. Therefore,  $\lambda_s$  should be normalized based on the CWA between the sampled rock ( $CWA_s$ ) and reference rock ( $CWA_r$ ) and the correction coefficient  $n$ . The result is defined as  $\lambda_N$ :

$$\lambda_N = \frac{\lambda_s * CWA_r}{n * CWA_s} \quad (\text{Eq. 3-12})$$

It is noticeable that the maximum CIA value for different types of rock is 100. To maintain the accuracy, it is better to also keep the CIA value of the sample with a CWA lower than 100 after normalization. Therefore, it is better to set the rock with a lower CWA as the reference rock.

Putting all calculation steps into a final formula, the CIA values of the sampled rock can be normalized ( $CIA_N$ ) using the CIA value of the fresh part of the reference rock ( $CIA_{fr}$ ) and  $\lambda_N$ .

---

$$CIA_N = CIA_{fr} * (1 + \lambda_N) \quad (\text{Eq. 3-13})$$

The CIAN represents the chemical index of alteration for the reference rock but under the same weathering conditions as the sampled rock. As the different types of rock are all normalized by the reference rock, the chemical weathering intensity can be compared. However, fresh rock needs different chemical weathering intensities to reach the same chemical index of alteration (CIA) value within the same time. This means that with a given CIA value, the shorter the weathering period is, the more intense the chemical weathering must be.

### 3.7. Integrative evaluation of weathering conditions

Previous studies on weathering degree in paleoenvironments emphasize the absolute chemical weathering degree mostly via CIA, CIA-K and  $\Sigma$  Bases/Al values (Fedon et al., 1995; Maynard, 1992; Retallack, 1999; Zhou et al., 2017). The characteristics formed by physical weathering are less considered.

This study pursues a twofold strategy to improve this deficit in paleoweathering studies: (i) petrographic analysis of physical weathering via fracture analysis and (ii) normalization of the CIA to rock types. The detailed workflow is depicted in Fig. 3-7.

For chemical weathering, the weathering index (CIA) for chemical weathering is first calculated. Second, the time scale of the supergene alteration and reference rock is evaluated. Then, the TWM and CWA can be calculated based on the time scale and the composition of the parent rock. After that, the deviation degree of the CWA ( $\lambda$ ) is acquired based on the reference rock. With these three parameters, the weathering indices can be normalized following Eq. 3-10 to Eq. 3-13 to quantitatively assess the chemical weathering intensity among different lithologies.

For physical weathering, the fractures under the microscope are analyzed. The ratio between the fracture area and total area and the index of physical weathering (IPW) are acquired. To normalize the IPW, the formation processes of the fractures are evaluated and normalized with the corresponding rock strength. The corresponding rock strength (UCS) is calculated based on the relationship between CIA values and UCS. Finally, the IPWN can be acquired as the sum of the product between the ratio of different stage fractures with the total area and the corresponding UCS (Eq. 3-

5& 3-6). With both, the physical and chemical weathering characteristics, the integrative weathering regime of the rock sample is quantitatively determined.

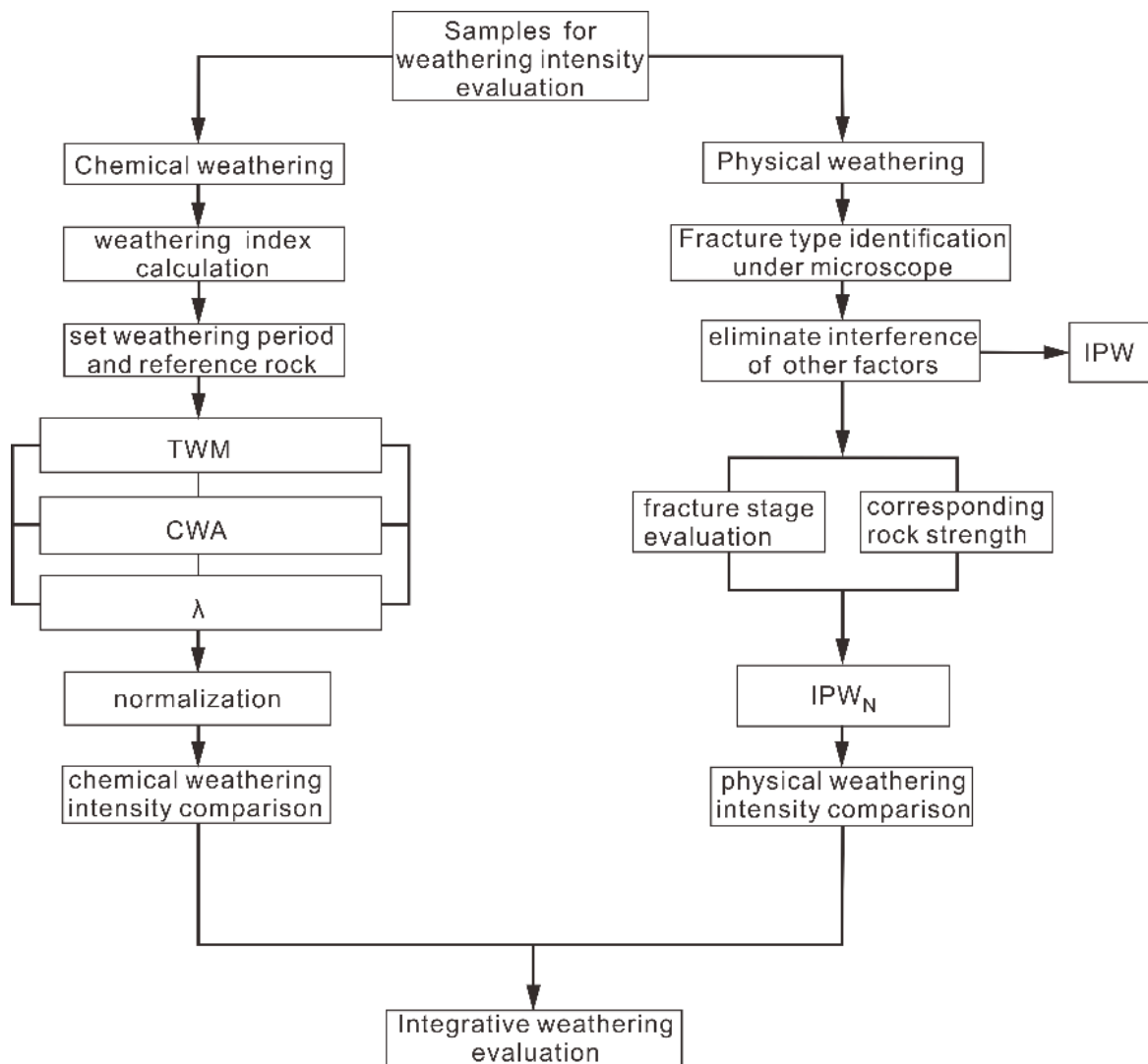


Fig. 3-7 Workflow for integrative weathering evaluation.

### 3.8. Case study

#### 3.8.1. Geological Setting

To apply and test the quantification of paleoweathering a widely developed paleoweathering surface was selected. For this attempt, a set of drill cores penetrating through the post-Variscan non-conformity in Central Europe were chosen. For the selection of drill cores, the imprints by modern weathering were avoided.

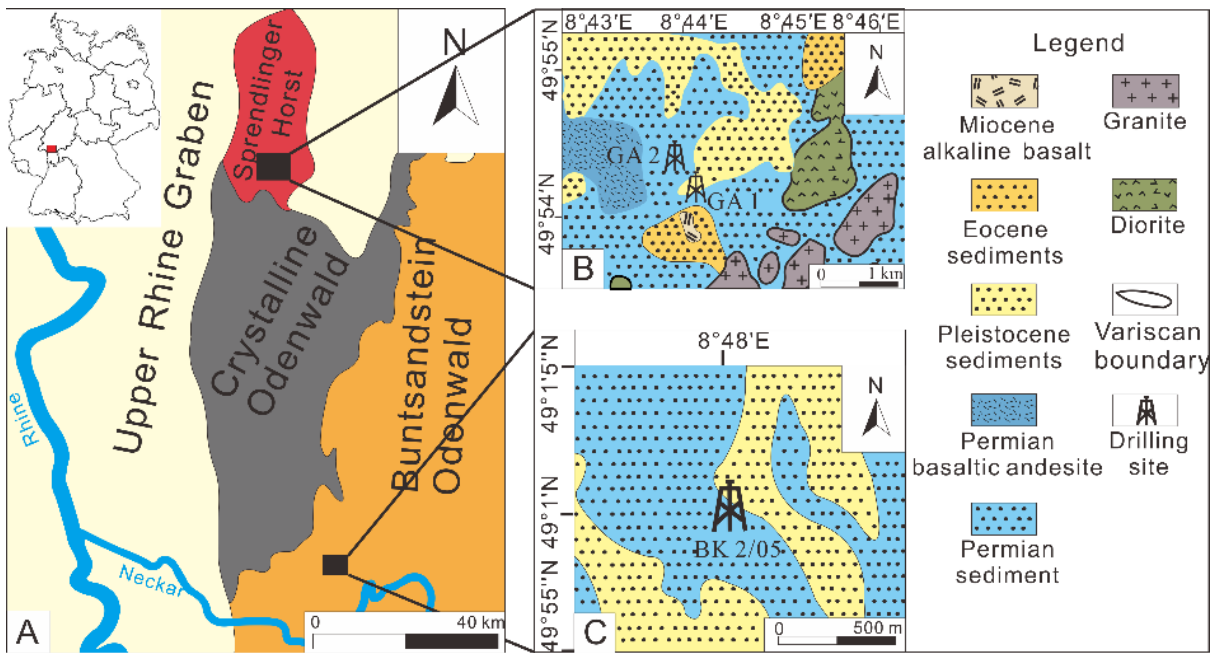


Fig. 3-8 Location and geology of the research area in S-Hessia (SW-Germany, central Europe). Solid black lines within the map of Germany (upper left corner) are federal political boundaries. (A) Tectonic units in the research area and research locations. The upper rectangle corresponds to Fig. 3-8B, and the lower rectangle corresponds to Fig. 3-8C; (B) Lithologic composition of the research area on the Spredlinger Horst. (C) Lithologic composition of the research area in Langenthal.

The weathered crystalline basement of the Variscan nonconformity belongs to the so called Mid-German Crystalline Zone (MGCZ) formed during the Variscan orogeny from ca. 360 to 320 Ma (Kroner et al., 2007a). After the Variscan orogeny, the MGCZ was a highland, which was continuously weathered and eroded until the Permo-Carboniferous (Willner et al., 1991; Zeh and Brätz, 2004). In the study area, sedimentation started in the early Permian, which can be concluded from contemporary volcanic rocks in the Saar Nahe Basin that are dated to approximately  $290 \pm 6$  Ma (Lippolt and Hess, 1983). At this time, the basement became covered by bimodal volcanic rocks that interfinger with Rotliegend sediments and are overlain by coarse-grained, arkosic alluvial fan to fluvial deposits (Becker et al., 2012a). These rocks belong to the Rotliegend Group. Between the youngest basement rocks and the basal Rotliegend a time gap of ca. 30 Myr exists during which weathering must have taken place (McCann et al., 2006; Opluštil and Cleal, 2007). From the late Carboniferous to early Permian, the climate gradually changed from humid-ever wet to a progressively enhanced seasonal and arid climate in central Europe (Izart et al., 2006; Michel et al., 2015).



The trend was interrupted by several deglaciation events that converted the climate to relatively more humid conditions (Roscher and Schneider, 2006). After a roughly concordant hiatus in the mid-Permian, the region was flooded by a saline, epicontinental sea, the so-called Zechstein, at approximately 257 Ma (Hagdorn and Mutter, 2011; Stolz et al., 2013). The study area was at the southern margin of an embayment of the basin's center in the north (South Permian Basin) and only thin dolomitic and marly sediments were deposited (Becker et al., 2012a). Around the Permian–Triassic Boundary, the deposition of several hundred meter-thick fluvial, lacustrine to aeolian red-beds of the Buntsandstein started. From the Middle Triassic to Jurassic, the sediments mainly consisted of clastic rock, carbonate and evaporites (Ziegler, 1982; Ziegler and Dèzes, 2005). Since the Eocene, the Upper Rhine Graben has been formed and filled with various fluvial, lacustrine and marine sediments (Schwarz and Henk 2005).

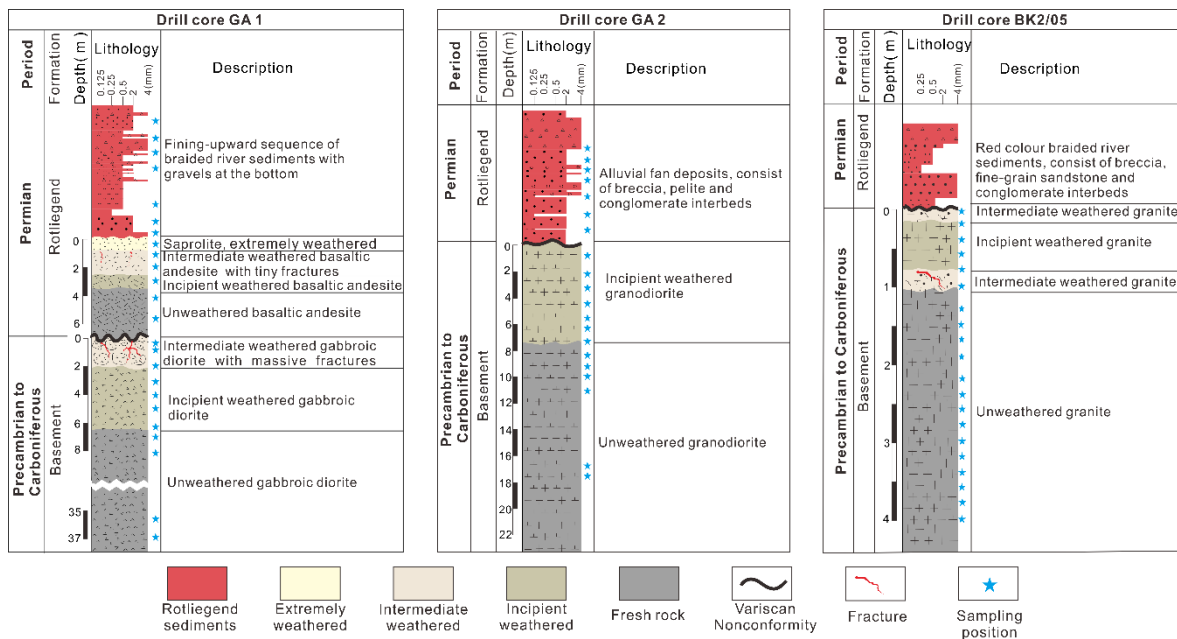


Fig. 3-9 Lithological section of the GA1, GA2 and BK2/05 drill cores with emphasis on the weathered interval. Blue stars indicate the sampling locations. Note, the weathering degree : “extremely weathered, intermediate weathered, incipient weathered and fresh” is based on Fedo et al. (1995).

Three drill cores for this study that fulfil the following criteria were selected: a) penetration through the Variscan nonconformity at a depth of at least 13 m to rule out modern weathering (Liang et al., 2021), and b) the basement rock should be different for each drilling. The selected drill cores were from north and south of the MGCZ. Two drill cores were from the north and were

---

located on the Spendlinger Horst. Its basement rocks belonged to the northern extension of the Bergsträsser Odenwald and were mainly composed of felsic plutonic rocks. On the uplifted fault block of the Spendlinger Horst, a succession of Rotliegend of up to 250 m was conserved (Marell, 1989). All younger sediments were eroded during exhumation (Matte, 1991; McCann, 1999) (Fig. 3-8). According to thermochronologic studies, the maximum subsidence depth was achieved in the Lower Cretaceous, which makes it probable that some Cretaceous deposits were also present (Cloetingh et al., 2006; Ziegler et al., 2004).

The Rotliegend sediments in this area are divided into the Moret and Langen Formations. The latter contains volcanic rocks (Menning et al., 2005). Previous studies assigned the Rotliegend sediment of the two drill cores GA2 and GA1 to the Moret Formation and the Langen Formation with basaltic andesite, respectively (Liang et al., 2021). The weathering depth in the basaltic andesite is approximately 6 m, in the gabbroic diorite basement is approximately 6.5 m, and in the GA1 drill core, the weathering depth in the GA2 basement is approximately 8.2 m.

Drill core BK2/05 is located on a valley floor in the southernmost part of Odenwald, where the Variscan basement is composed of Heidelberg Granite and the weathering depth is approximately 2 m. The Rotliegend sediments overlying the granite in BK2/05 belong to the Michelbach Formation, for which an age between 290 and 280 Ma is assigned (Edgar and Hubert, 2009) (Fig. 3-9). The Rotliegend is followed by 30 m thick Zechstein deposits and then 6 m of basal Buntsandstein. Xenoliths in a Late Cretaceous volcanic pipe approximately 15 km east of the drill site prove a sediment succession up to the Middle Jurassic, which is eroded down to the upper Buntsandstein (Geyer and Nitsch, 2011). It is estimated that approximately 650 m of sediments are missing, which sums up to a total maximum sediment cover of approximately 1000 m in the south (Geyer and Nitsch, 2011; Menning et al., 2005).

### **3.8.2. Analytical Methods**

In total, 52 samples were collected around the nonconformity. In detail:

---

Seventeen samples were from the GA1 drill core, which were split into 6 from the weathering profile of basaltic andesites (5 paleosol, 1 bedrock) and 11 gabbroic diorites (5 paleosol, 6 bedrock).

Thirteen samples were from the weathering profile of granodiorite in GA2 (6 paleosol, 7 bedrock).

Twenty-two samples were from the weathering profile of granite in BK2/05 (7 paleosol, 15 bedrock).

All these samples were collected from paleosols in the top to fresh parent rock in the bottom for each weathering profile. The sampling interval was approximately 1 m for the samples from basaltic andesite and the GA1 and GA2 basement. To acquire the detailed variation in weathering characteristics, the interval was reduced to 40 cm at the topmost part. Due to the low weathering degree of BK2/05 and to express trends of weathering at a more precise scale, the interval was reduced to approximately 20 cm.

Thin sections were made to analyze the petrological features of the samples under a polarizing microscope (PM) and scanning electron microscope (SEM). Another part was milled into powder with an achate mill and analyzed for major and trace elements as well for mineral composition. Geochemical analysis including major and trace elements and C and O isotopes of the carbonate within the samples, was performed at the State Key Laboratory of Isotope Geochemistry, Guangzhou Institute of Geochemistry, Chinese Academy of Science. The detailed processes for the measurement of major and trace elements are documented in Liang et al. (2021). For the measurement of C and O isotopes, the powder was first roasted in vacuum at 400 °C for 4 hours to remove organic contaminants. The roasted powder was then reacted with 100% phosphoric acid ( $\text{H}_3\text{PO}_4$ ) at 25 °C. For the samples containing both calcite and dolomite, the  $\text{CO}_2$  released during the first 30 min after a reaction was assumed to have come from the calcite part, and the  $\text{CO}_2$  gas evolved from 30 min to 72 h and was collected as the dolomite part. The gas was measured by a MultiPrep-GV Isoprime II mass spectrometer. Both the  $\delta^{13}\text{C}$  and  $\delta^{18}\text{O}$  are expressed in per mil (‰) relative to the PDB standard. The international reference material NBS-19 was applied for the calibration, and the analytical precision for C was better than 0.2‰, and for O was 0.3‰.

---

Bulk powder was analyzed by XRD at Goethe University Frankfurt. The powder was carefully back-loaded to reduce the preferred orientation and analyzed by a PANalytical X'Pert diffractometer equipped with a Bragg–Brentano goniometer (copper beam). The mineral-phase proportions were estimated by weighted XRD peak intensities after conversion with their typical reference intensity ratios (RIRs), as found in the powder diffraction file (PDF-2 and PDF-4 of the International Centre of Diffraction Data) with MacDiff software (Petschick et al., 1996).

As the fracture data were collected from drill cores, it was difficult to measure the fracture orientations. Alternatively, the angle within the fractures can act as a useful tool to assess the tectonic fractures, as they indicate a preferential angle with a smooth fracture surface, while the fractures formed due to weathering show random angles (Caspari et al., 2020; Feng et al., 2021; Scarpato, 2013). In this study, fracture angles were measured clockwise and started from the horizontal direction. The results were analyzed by rose diagram to document whether the fractures have preferential directions.

### **3.8.3. Results**

#### *Petrological and mineral characteristics*

The lithologies among the three drill cores include four rock types: gabbroic diorite, basaltic andesite in GA1, granodiorite in GA2 and granite in BK2/05. To better illustrate the variations in the weathering profile, the petrological characteristics acquired from microscopy and mineral compositions from XRD are depicted together.

Gabbroic diorite (GA1): The fresh part of the granodioritic basement in GA1 at 6 m depth below the nonconformity is coarse-grained (~ 6 mm) and consists of plagioclase (43%), amphibole (19%), biotite (23%) and quartz (15%). Fractures are fairly scarce and are all closed (Fig. 3-10A1). Toward the nonconformity, the density and width of the fractures and the ratio of the secondary minerals all increase at the expense of the primary minerals. For example, at a depth of 2.9 m, the density of the fractures increases significantly and the average width of the fractures increases to approximately 25 µm. The fractures are filled by clay minerals and calcite, accompanied by a small proportion of void fractures. In addition, weatherable primary minerals such as plagioclase and

biotite are altered and partly replaced by secondary minerals, such as clay minerals and carbonate minerals (Fig. 3-10A2). In the topmost part, at a depth of 0-0.9 m below the nonconformity, the fractures are ubiquitous with a width between 5 and 100  $\mu\text{m}$  (Fig. 3-10A3). The proportions of plagioclase and biotite decrease to approximately 7% and 10%, respectively, with secondary minerals increasing to approximately in total 75% (Fig. 3-8). Most fractures are filled by carbonate, some by clay minerals, and a minority are void (Fig. 3-10A3).

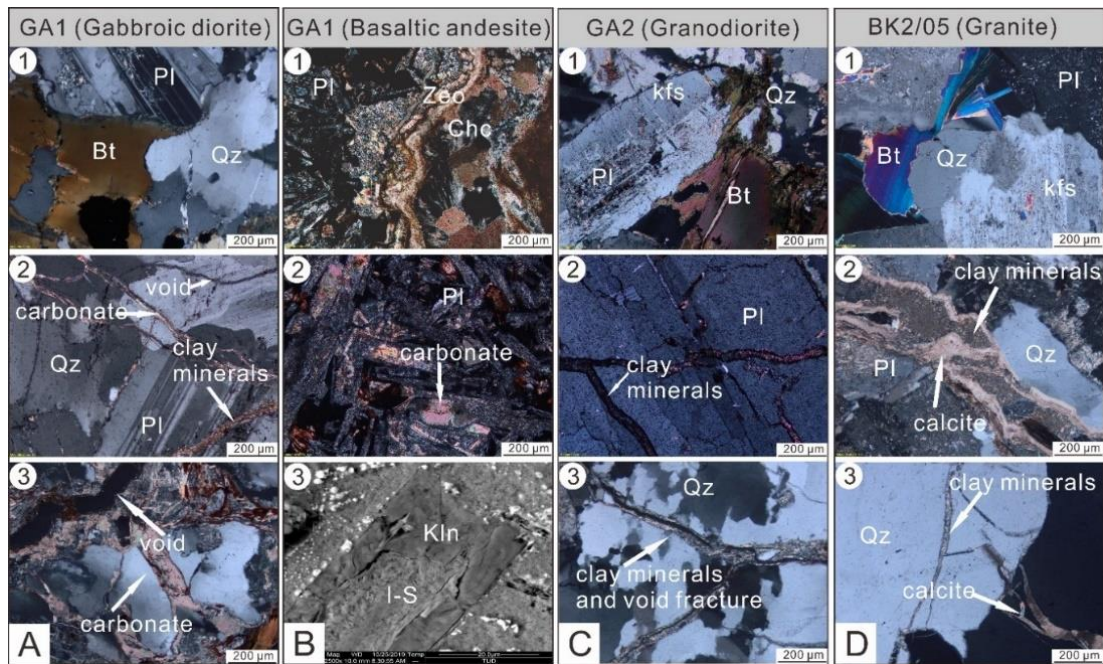


Fig. 3-10 Petrographic characteristics of the basement and the overlying volcanic rock in the GA1 and GA2 drill cores: (A): 1) fresh gabbroic diorite (30 m); 2) gabbroic diorite (3 m), fractured feldspar grain filled by clay and carbonate minerals and void fracture; 3) gabbroic diorite (0 m), fractured quartz grains filled by calcite and void fractures; (B): 1) fresh basaltic andesite (5.4 m); 2) basaltic andesite (0.4 m), fractures are rare; 3) basaltic andesite (0 m), completely weathered feldspar grains with intact shape; (C): 1) fresh granodiorite (17.6 m); 2) monzogabbro (2.6 m), slightly weathered plagioclase; 3) granodiorite (0 m), fractures filled by clay minerals and void fractures in the middle of earlier fractures; (D): 1) fresh granite (10.9 m); 2) granite (0.8 m), highly weathered, fracture filled by carbonate and clay minerals; 3) granite (0 m), fractures filled by calcite and clay minerals. Abbreviations used in the figure and caption are as follows: Kln – kaolinite, Bt – biotite, Pl – plagioclase, Zeo – zeolite, Chc – chalcedony, kfs – K-feldspar and Qz – quartz.

Basaltic andesite (GA1): For basaltic andesite, the fresh part at a depth of 5.4 m shows an amygdaloid texture. The matrix contains plagioclase crystals, whereas the amygdaloid is filled with calcite, zeolite and chalcedony. Fractures in this part are rare (Fig. 3-10B1). Toward the surface, such

as at approximately 0.4 m, the primary minerals which are mainly plagioclase, are gradually altered and transferred to clay minerals, the content of the primary minerals gradually decreases from 81.5% at 5.4 m to 72.5% at 0.4 m below the weathering surface (Fig. 3-11), and fractures are very limited (Fig. 3-10B2). In the topmost part of the basaltic andesite (13.9 m) which is in the weathering surface, nearly all primary minerals are transferred into secondary minerals, the shape of the primary mineral grains is well preserved, the density of the fractures is still limited, all the fractures are void and the width of the average fractures is approximately 30  $\mu\text{m}$  (Fig. 3-10B3).

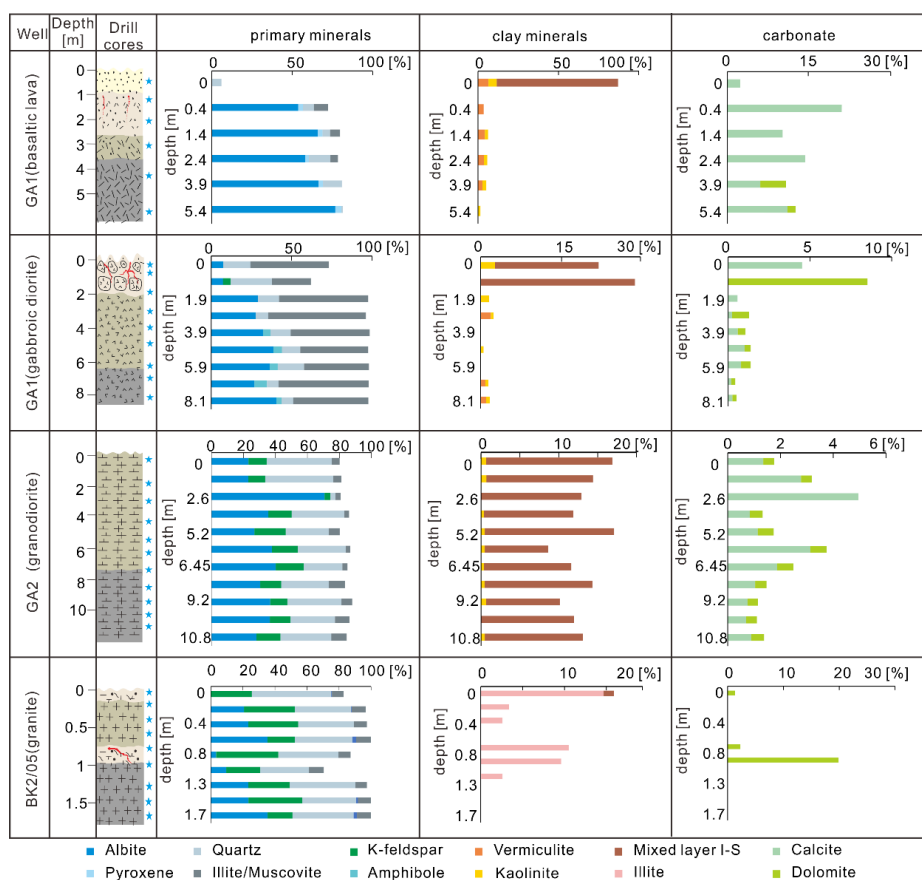


Fig. 3-11 Mineral characteristics along the drill core profiles; the lithology legend refers to Fig. 3-9

Granodiorite (GA2): The fresh granodiorite in GA2 at a depth of 17.6 m is coarse-grained (approximately 5 mm) and consists of plagioclase (35%), biotite (10%), K-feldspar (15%), quartz (30%) and 10% other minerals (Fig. 3-11). From bottom to top, the primary minerals have an overall decreasing trend while the secondary minerals such as the mixed layer I-S and carbonate increase

---

(Fig. 3-11). Toward the surface of the basement, the density and width of fractures also increase. In the fresh part of the granodiorite, the fractures are very limited (Fig. 3-10C1). At 5.8 m, fractures are frequent with widths of approximately 10  $\mu\text{m}$ , and most of the fractures are filled by clay minerals, with a minority of fractures filled by carbonate (Fig. 3-10C2). In the topmost part of GA2, fractures are more frequent with a width of approximately 25  $\mu\text{m}$ . The fractures are mainly filled by clay minerals, accompanied by a small proportion of void fractures and only a minority of fractures are filled by carbonate minerals (Fig. 3-10C3).

Granite (BK2/05): The fresh granite in the BK2/05 drill core is coarse-grained (approximately 1 cm) and mainly consists of K-feldspar (20%), plagioclase (30%), biotite (8%), amphibole (2%) and quartz (40%). The primary minerals fluctuate between 1.5 m and 0 m below the weathering surface, and the secondary minerals are mainly illite (Fig. 3-11). In the bottom part, no fracture is found (Fig. 3-10D1). At the position 0.5 meters above the fresh part, there is one fracture throughout the thin section with a width of approximately 100  $\mu\text{m}$ . The fracture is filled by clay minerals, carbonate and voids along the edge. The widths of the other fractures are approximately 8  $\mu\text{m}$  and filled by clay minerals (Fig. 3-10D2). In the topmost part of the granite, fractures are frequent and have an average width of 15  $\mu\text{m}$ , some as low as 5  $\mu\text{m}$ . All the fractures are mainly filled by clay and carbonate minerals. Primary minerals, such as plagioclase and biotite, are highly altered and accompanied by secondary clay minerals. (Fig. 3-10D3).

#### *Fracture characteristics and IPW*

The detailed fracture angle and fracture area under microscale data are given in Appendix III-I (Tables A2 and A3, respectively). In total, 162 fractures along three drill cores are recognized and analyzed, among which 59 are for the basaltic andesite part of GA1, 64 are for the gabbroic diorite part of GA1, 37 are for GA2 and 2 are for BK2/05. The statistics of the fracture angle orientation are illustrated in Fig. 3-12. Fractures along the entire drill cores indicate a random distribution of angles. A preferential angle distribution does not exist. This indicates that the fractures along the three drill cores all formed due to physical weathering. The contribution of other factors is insignificant (Scarpato, 2013).

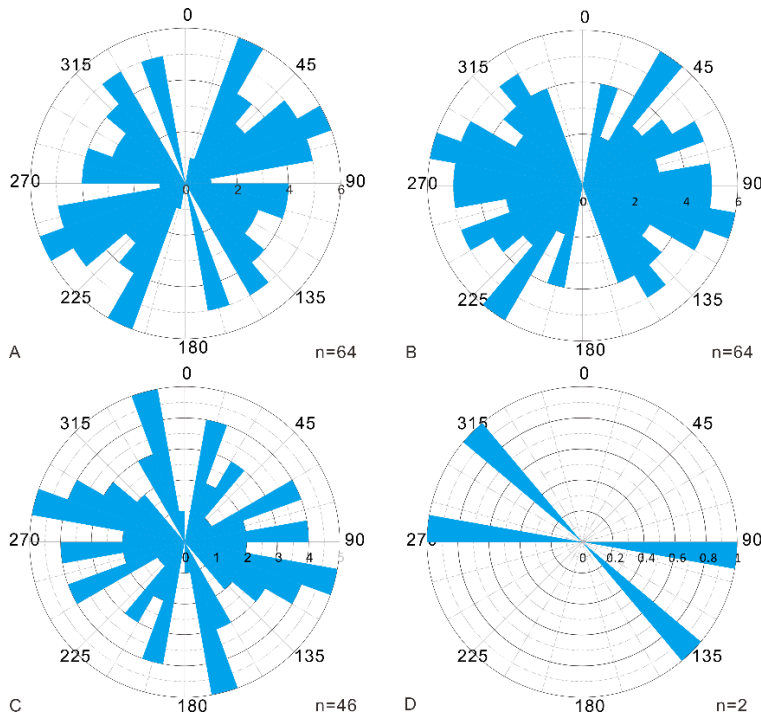


Figure 3-12. Rose diagram of fracture angle, (A) basaltic andesite part of GA1; (B) gabbroic diorite basement of GA1; (C) granodiorite basement of GA2; (D) granite basement of BK2/05

The ratio between the average values of the fracture areas and the total area of the pictures are visualized in Fig. 3-13. The fracture area ratio (IPW) values are represented by the average of 15 values from each thin section. In the gabbroic diorite, the physical weathering depth is 6.5 m, the area of void fractures is limited to the upper part (0–2.9 m), and the proportion of void fractures at 2.9 m is 0.83 %, increases to 2.0% at 0.9 m and decreases to 0.18% at the surface. The proportion of fractures filled by carbonate increases rapidly from 0% at a depth of 4.9 m to 13.0% in the topmost part. The proportion of fractures filled by clay minerals gradually increases from 0.16% at 6.5 m to 5.4% in the topmost part, and in the fresh part, no open fractures exist. In basaltic andesite the physical weathering depth is limited in the top part which is from 0 to 0.4 m and only void fractures are observed. Their measured area shows an overall increasing trend toward the top with a sharp increase at the topmost part.

Along the GA2 drill core, the physical weathering depth is approximately 10.8 m below the paleo-surface, and the void fractures are limited to the topmost part with a proportion of 0.78% of all observed fractures in this part. The fractures filled by carbonate are only observed at a depth of 2.6 m, which yields a value of 3.5%, while the fractures filled by clay minerals exhibit a trend from



0.27% at the bottom (9.2 m) to 4.6% at the top. All types of fractures are not found in the fresh part (17.6 m). In the BK2/05 drill core, the physical weathering depth from 0 to 0.8 m is documented, and the void fractures are also observed only in the topmost part, with a value of 0.31%. The area of the fractures filled by carbonate yields a value of 0.79% at 0.8 m and 4.72% at the topmost surface. The fractures filled by clay minerals decrease from 0.97% at 0.8 m to 0.28% at 0.2 m and increase to 1.02% at the topmost part. In the fresh part (10.8 m), fractures also do not exist.

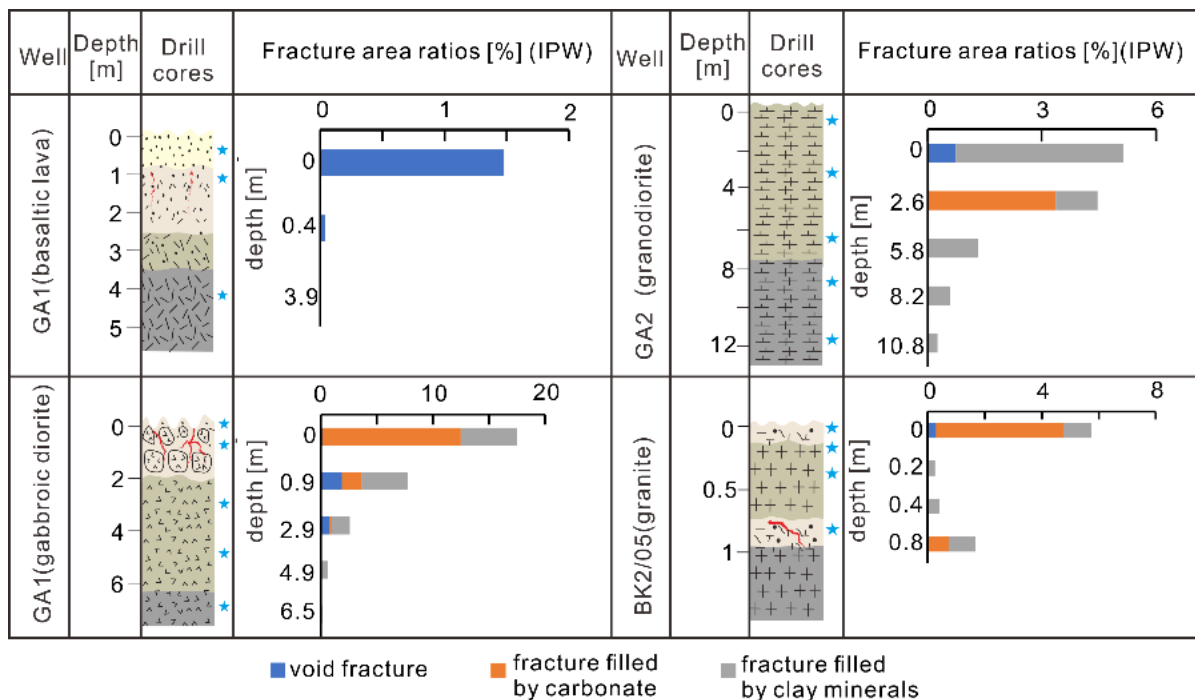


Fig. 3-13 Fracture distribution and IPW values along the profiles; the lithology legend refers to Fig. 3-9.

In the basaltic lava part of GA1, the IPW<sub>A</sub> values increase from the bottom to the top, with a dramatic increase to 1.56 in the topmost part. Both the gabbroic diorite and granodiorite basement in GA1 and GA2 show a gradual increasing trend of IPW from bottom to top, while in BK2/05 between 0 and 1.8 m the IPW values fluctuate from bottom to top.

However, thin sections from the fresh rocks at all drillings do not show fractures. Therefore, the ratios between the total area of the fractures and the view area in this case can be considered as the true value of IPW, i.e. all observed microfractures are caused by physical weathering.

---

### Determining the $IPW_N$

The fractures among the investigated drill cores consist of three types: fractures filled by clay minerals, fractures filled by carbonate and void fractures. To evaluate the  $IPW_N$  values, the key point is to determine the fractures formed during chemical weathering to calculate the corresponding UCS for each fracture type. The UCS for fractures filled by clay minerals is represented by the average UCS value between the unweathered and the sampling position. For the void fractures, the UCS at the sampling position is applied. The UCS for basaltic (basaltic andesite) and granitic (granodiorite and granite) rock under different weathering degrees (CIA value) can be calculated based on Eq. 3-1 and Eq.3-2.

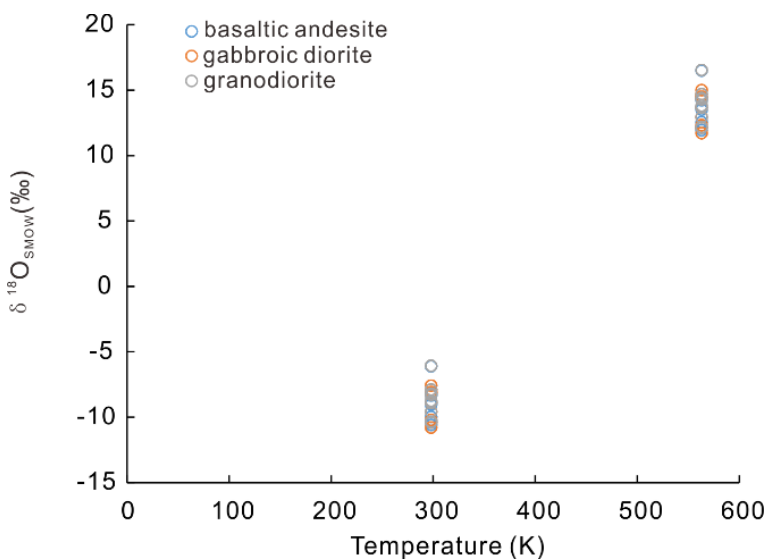


Fig. 3-14 Calculated  $\delta^{18}O$  values versus estimated temperatures of formation waters for GA1 and GA2 based on Equation (14) (Friedman and O'Neil, 1977).

Since the nonconformity experienced burial diagenesis, for the fractures filled by carbonate, it is important to decide whether the carbonate was formed during the weathering stage or the burial stage. The fractures filled by carbonate formed during the weathering process should be treated similarly to fractures filled by clay minerals. Fractures filled by carbonate formed during burial diagenesis should be treated as void fractures.

To distinguish the source of the carbonate, the C and O isotope compositions of the carbonate within the fractures are analyzed (Fig. 3-14). The  $\delta^{18}O$  composition of carbonate-forming fluid was determined based on the method proposed by Michel and Tabor (2016) to assess the influence of

---

the overprint of burial diagenesis. Based on the fluid composition, the isotope fractionation between calcite and water is calculated after Friedman and O'Neil (1977):

$$10^3 \ln \alpha_{cc-w} = 2.78(10^6 T^{-2}) - 2.89 \quad (\text{Eq. 3-14})$$

In Eq. 3-14, T refers to the temperature on the Kelvin scale.  $\ln \alpha_{cc-w}$  equals  $\ln[(\delta^{18}O_{cc}+1000)/(\delta^{18}O_w+1000)]$ ,  $\delta^{18}O_{cc}$  refers to the measured  $\delta^{18}O$  value of calcite, and  $\delta^{18}O_w$  is the  $\delta^{18}O$  value of coexisting water. As all  $\delta^{18}O$  in Eq. 3-14 are related to SMOW (Craig, 2013), the  $\delta^{18}O$  (PDB) acquired from the measurement is transformed to the SMOW standard after Eq. 3-15 based on Friedman and O'Neil (1977):

$$\delta^{18}O_{SMOW} = 1.03086 * \delta^{18}O_{PDB} + 30.86 \quad (\text{Eq. 3-15})$$

The results are listed in Appendix III-I (Table A5) and visualized in Fig. 3-14.

If all the calcite within the weathering profile of GA1 and GA2 was formed during surface weathering under the temperature of 25 °C, the estimated  $\delta^{18}O_{SMOW}$  of the calcite-water yield values between -10.8‰ and -6.08‰. However, the presence of coexisting authigenic minerals, such as dolomite and quartz, indicate the weathering profile should be overprinted by a higher temperature. Previous studies indicates that the weathering profile experienced a maximum temperature up to approximately 290 °C (Burisch et al., 2017; Wagner et al., 1990). Under this temperature, the estimated  $\delta^{18}O_{SMOW}$  values range between 12.73‰ and 16.50‰. The value range is clearly higher than that of the meteoric water but is highly likely for geothermal and/or hydrothermal fluids (Ruddiman, 2008; Stataude et al., 2012; White, 2009). Therefore, the calcite within GA1 and GA2 should all have formed during burial diagenesis rather than chemical weathering. In addition, dolomite is a typical mineral that precipitated during burial diagenesis (Stimac et al., 2015). The fractures filled by carbonate (calcite and dolomite) should be originally void and should be treated as void fracture and normalized by the UCS under the present chemical index of alteration.

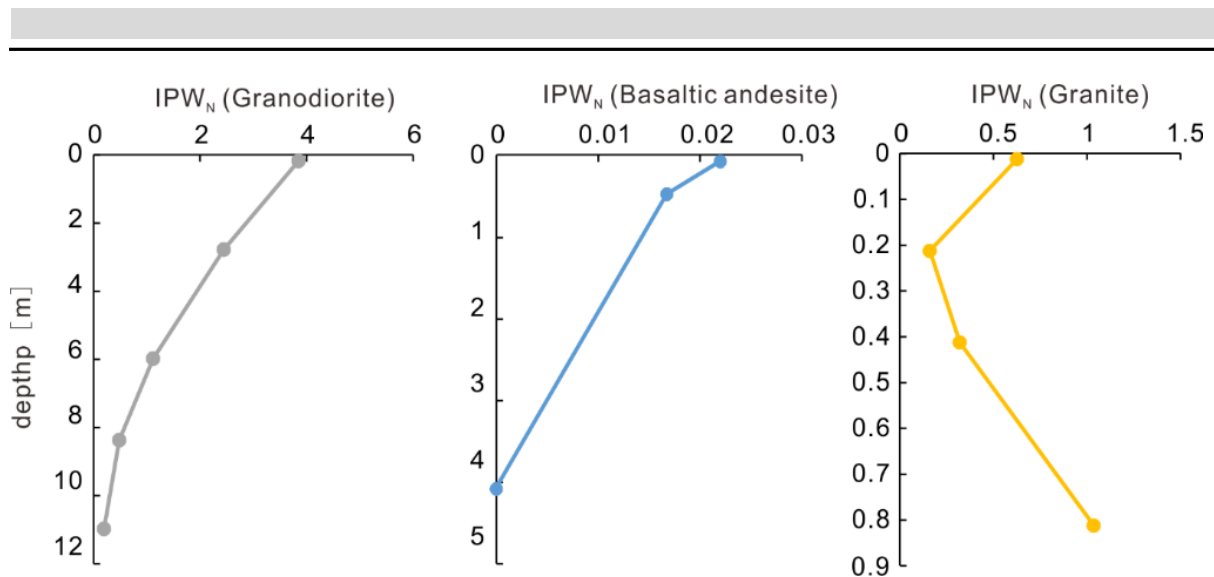


Fig. 3-15 IPW<sub>N</sub> along the granodiorite in GA2, basaltic lava in GA1 and granite in BK2/05 drill core profiles.

The normalized index of physical weathering (IPW<sub>N</sub>) is visualized in Fig. 3-15. The IPW<sub>N</sub> values of the granodiorite in the GA2 drill core increase from 0.22 at the bottom to 3.85 at the top. The physical weathering trend is mainly controlled by fractures filled by clay minerals. An exception is the sample from 2.6 m, where fractures are mainly filled with carbonate. Based on the characteristics of the thin section, the lithology in this position is close to gabbro. The CIA value for the fresh gabbroic rock is approximately 35 (Fritz, 1988), and the CIA of this sample yields a value of 45.1. Using the results of the fracture analysis and mineral characteristics (Fig. 3-10C2 & Fig. 3-11), the sample was slightly weathered. For the slightly weathered gabbroic rock or the slightly weathered gabbroic rock previous studies using 26 samples indicate a UCS between 36.6 and 69.6 (Aggisttalis et al., 1996). Here, the arithmetic average value of 43.1 was applied. The results show a gradually decreasing trend of physical weathering from top to bottom.

In the basaltic andesite part of the GA1 drill core, only tiny void fractures were observed. Here, the IPW<sub>N</sub> values range from 0 to 0.022 from bottom to top, which indicates low physical weathering intensity.

The IPW<sub>N</sub> values of the granite in BK2/05 range from 0.16 to 1.04. From 1.8 m below the weathering surface the IPW<sub>N</sub> values first decrease from 1.04 to 0.16 at 0.2 m and then increase to 0.63 at the topmost surface.

### Characteristics of major elements

The results of bulk major element concentrations are listed in Appendix III-I (Table A1), and the representative elements and CIA values along the profile are visualized in Fig. 3-16.

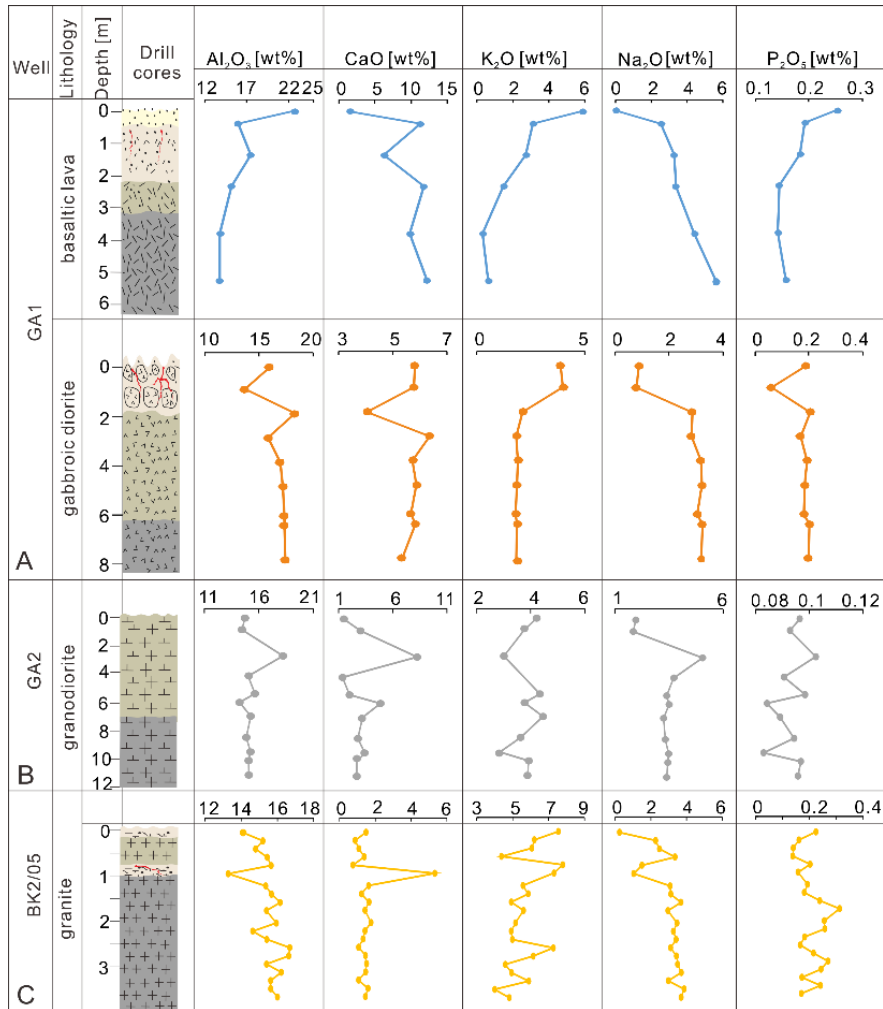


Fig. 3-16 Major elements and CIA values along the GA1, GA2 and BK2/05 profiles; the lithology legend refers to Fig. 3-9

For the basaltic andesite in the GA1 drill core, element concentrations of Al, K and P have a decreasing trend from top to bottom, while Ca and Na increase. In the gabbroic diorite part, the element concentrations of Al and P fluctuate in the top part (0–0.9 m) but display an overall increasing trend from top to bottom. Both K and Na indicate a significant shift between the top part (0–0.9 m) and the lower part (1.9–7.9 m), while the concentration of K decreases from top to bottom and Na increases from top to bottom.

---

For the GA2 drill core, except for the samples from 2.6 m and 5.8 m, the concentration of Al is almost constant. In contrast, Na and Ca show an overall increasing trend from top to bottom, whereas K decreases.

The results from BK2/05 indicate that the concentrations of Al and Ca increase from top to bottom, while Ca is almost constant and K has a decreasing trend. All the elements have an abnormal value in the sample at 1 m below the weathering surface, with the relative content values of Al and Na being lower and Ca and K being higher than any other position along the drill core.

#### *Determining and normalizing of the chemical index of alteration*

The results acquired by Liang et al (2021) indicate that the weathering profile in the area was overprinted by K-metasomatism. This affects chemical weathering indices such as CIA (Fedo et al., 1995; Zhou et al., 2017; Fàbrega et al., 2019). Previous studies proposed several methods to eliminate the effect of K-metamorphism (e.g. Harnois 1988; Maynard 1992; Panahi et al. 2000). Both Harnois (1988) and Maynard (1992) eliminated the inconsistent behavior and/or the metasomatism of K by removing  $K_2O$  from the CIA equation directly. The elimination of the K component does not account for the associated aluminum; hence, the method works well for evaluating the chemical index of alteration of plagioclase. However, it is not appropriate to evaluate the weathering degree of the parent lithologies that contain K-feldspar and/or biotite, especially when the parent rock is not completely weathered. Since the samples in this study include granite (BK2/05) and granodiorite (GA2), the A–CN–K diagram was applied to assess the chemical index of alteration under K-metamorphism (Nesbitt and Young, 1984) (Fig. 3-17). Previous studies indicate that the weathering trend for the upper continental crust should be in accordance with the A–CN axis given the depletion rate among Ca, Na and K (Nesbitt and Young, 1984). However, while the weathering profile was overprinted by K-enrichment diagenetic fluids (so-called K-metamorphism), the weathering trend was shifted to the K-apex (Fedo et al., 1995). As shown in Fig. 3-17A, the weathering trend for all three drill cores extends to the K apex. Similar results were found by Schmidt et al. (2021).

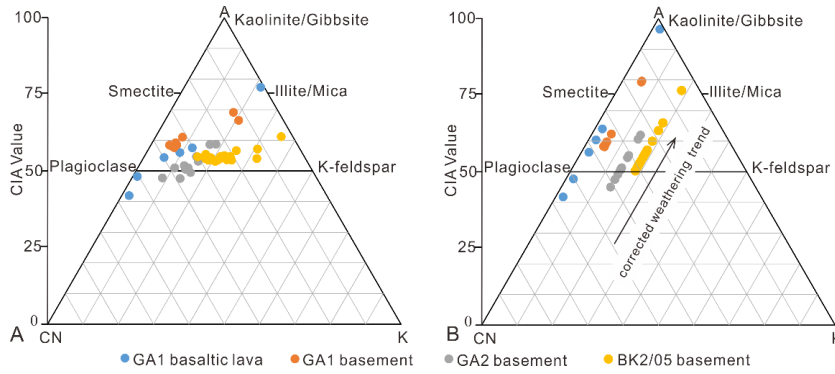


Fig. 3-17 A–CN–K diagram of the samples from GA1, GA2 and BK2/05 before (A) and after (B) K correction based on Nesbitt and Markovics (1997).

To correct the K content within the weathering profiles, the method proposed by Panahi et al. (2000) was applied. The detailed method is expressed as follows:

$$K_2O_{\text{corr}} = \frac{m \cdot A_w + m \cdot CN_w}{1 - m} \quad (\text{Eq. 3-16})$$

$A_w$  and  $CN_w$  refer to the  $Al_2O_3$  and  $(CaO^* + Na_2O)$  contents in the weathering zone, respectively, while

$$m = \frac{K}{A + CN + K} \quad (\text{Eq. 3-17})$$

In Eq. 3-17, the K, A and CN values for m are from the unweathered parent rock sample.

With the correction, the weathering trend for all the drill cores was parallel to the A-CN joint, and the effects for CIA values from the burial diagenesis were removed.

The age of the weathering surface may be younger than the exposure age of the basement, as the weathering surface will be renewed by continuous erosion (Riebe et al., 2003). The post-Variscan nonconformity represents a diachronous time gap between tens and hundreds of millions of years in central Europe (Kroner et al., 2007b; Zeh and Brätz, 2004). However, a precise chemical weathering scale is uncertain due to the effect of erosion. Therefore, a wide range for the duration of weathering from ten thousand to one million years was applied. This assumption also enabled the determination of the  $CIA_N$  variations for a certain rock type under different weathering intensities. The TWMs produced in these time periods for plagioclase, K-feldspar, hornblende and biotite are calculated with Eq. 3-7. For the weathering rate of pyroxene, Franke (2009) indicated that the weathering ratio between pyroxene and hornblende is 1:1.5, and Hausrath et al. (2008) suggests

that the weathering rates between pyroxene and plagioclase is 1:5. Applying Eq. 3-6, these two results match perfectly with each other. The corresponding CWA for different types of rock is calculated by Eq. 3-9, based on the mineral proportions in the fresh part. Due to the lack of mineral proportions of the fresh rock for the sample at 2.6 m below the weathering surface (58.3 m) in the GA2 drill core, the result for this sample is ruled out. To normalize the CIA value and make weathering intensity over all rock types comparable, fresh granite samples from drill core BK2/05 are set as the reference lithology. This is because the CWA of the granite is moderate compared to the other three lithologies. After normalization, the  $CIA_N$  range for other lithologies will not exceed 100. With the parameters  $\lambda$ ,  $n$  and  $\lambda_N$ , the original CIA was normalized to  $CIA_S$  and  $CIA_N$ . All the relevant parameters and results are listed in Appendix III-I (Table A4) and the original CIA, CIA corrected by  $n$  ( $CIA_S$ ), and  $CIA_N$  values are visualized in Fig. 3-18. For all three lithologies, after normalization to the granite from BK2/05, all the normalized CIA values show an overall similar trend to the original values. As the CIA,  $CIA_S$  and  $CIA_N$  from all the drill cores show an overall decreasing trend, the chemical weathering depth changed from 6.45 m, 3.9 m, 5.4 m and 2.1 m in the GA2, gabbroic diorite and basaltic andesite parts of the GA1 and BK2/05 drill cores.

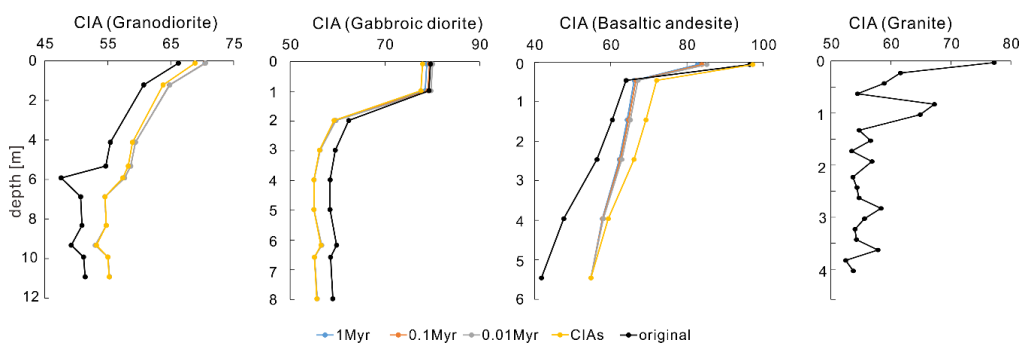


Fig. 3-18 Characteristics of the original CIA values and normalized CIA values of granodiorite, basaltic andesite and gabbroic diorite based on granite along drill core profiles GA2, GA1 and BK2/05.

### 3.9. Discussion

#### 3.9.1. Integrative weathering evaluation in the research area

The post-Variscan nonconformity in central Europe represents a time gap of millions years (Opluštil and Cleal, 2007). It was formed after the Variscan orogenesis and was successively buried by continental and marine sediments due to the onset of basin formation at approximately 320



---

Ma and ongoing subsidence up to the Triassic period. The alteration at this first order nonconformity was studied only locally with a focus on petrophysical properties. Littke et al. (2000) pointed out that porosities and permeabilities increased due to supergene alteration. This is confirmed by hydrothermal and geothermal studies, but the authors found significant heterogeneity (Bons et al., 2014; Schäffer et al., 2021). To date, this has been not linked to specific rock types as addressed in this paper. In our research area, the nonconformity crops out and different Variscan crystalline rocks underlie lower Permian basaltic rocks, as well as proximal immature clastic rocks. A series of cored drillings hit the nonconformity at depths of 13 to 62 meters which guaranteed that recent alteration was negligible.

Fig. 3-19 summarizes trends of corrected CIA and IPW for the basement beneath the first-order post-Variscan nonconformity, as well as for an intra-Permian lower-order unconformity of the basaltic to andesitic lava flow. The first-order nonconformity was represented by the weathering surface of the gabbroic diorite basement in GA1, granodiorite basement in GA2 and granite basement in BK2/05. As expected IPW and  $CIA_N$  all show a decreasing trend with depth, i.e., physical and chemical weathering intensity decreases with depth. The normalized  $IPW_N$ , however, shows opposite trends for the granite. This was probably due to the heterogeneity in the weathering profile.

The granodiorite at GA2 (Fig. 3-19A) shows decreasing values with depth for IPW and  $IPW_N$  values. The fractures were mainly filled by clay minerals except at 2.6 m depth where diagenetic carbonate fills the void (see also Fig. 3-10). After the normalization of IPW, the gradually decreasing  $IPW_N$  values from top to bottom suggest that the physical weathering intensity decreased with increasing depth.  $CIA_N$  also decreased with depth from approximately 70 to 50 depending on the age model.

For the gabbroic diorite in the GA1 drill core (Fig. 3-19B), only the IPW was calculated because this rock type does not belong to either granitic rock and or basaltic rock. Thus, the relationships between CIA and UCS in this case are not suitable for the rock type in GA1. The IPW again decreases with depth. It has the highest values of all basement rocks which means strong fracturing.

The  $CIA_N$  decreases from approximately 80 to 55. Compared to the granodiorite the decrease is not gradual, but shows an abrupt decrease to less weathered rock at a depth of approximately 2 m. The intraformational basaltic andesite in the GA1 section (Fig. 3-19C) over the post-Variscan nonconformity shows much lower physical weathering indicated by IPW and  $IPW_N$ . Fractures are voids, which indicates that the fractures were formed during the very latest stage of chemical weathering and that the physical weathering intensity is very limited. The  $CIA_N$ , however, is very high at the top which reflects the higher weatherability of the aphanitic volcanic rock. It drops abruptly at a depth of 0.4 m. This shows the shorter time interval for weathering of the lava flow compared to basement rocks at the post-Variscan nonconformity.

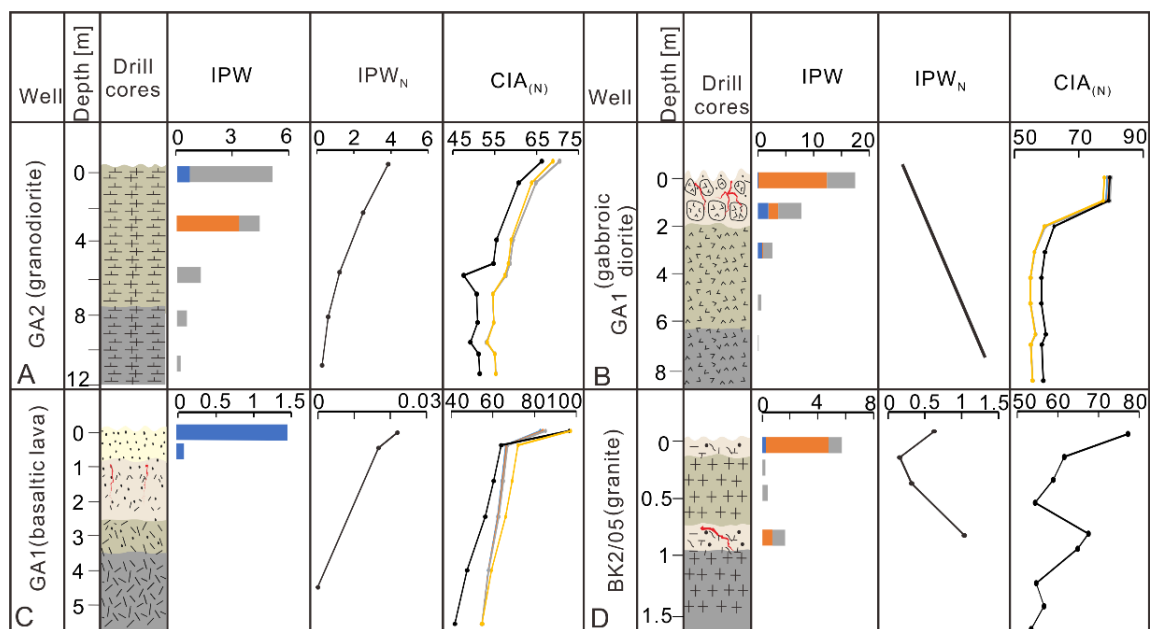


Fig. 3-19 Comprehensive weathering characteristics for GA2, GA1 and BK2/05; note that A to D are based on chronological order. Numbers are ratios of indices. The legend refers to Fig. 3-9 and 3-17.

The granite in drill core BK2/05 shows relatively little weathering which penetrates only some decimetres. Fractures are mainly filled during burial diagenesis with calcite and dolomite. Clay minerals are almost absent. Weak chemical weathering is confirmed by the  $CIA_N$  which declines from approximately 78 to 55 at a depth of 0.4 m.

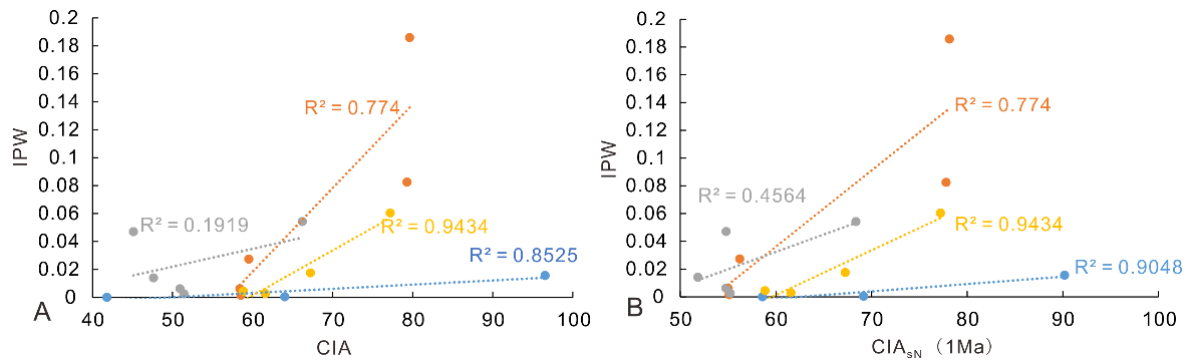


Fig. 3-20 Relationship between the IPW and CIA and CIA<sub>sN</sub>. Legend refers to Fig.3-17

Fig. 3-20 shows the relationship between the physical and chemical weathering indices. Although in all cases a positive correlation can be observed, the inclination of the regression line is different for each rock type. This means that the balance of physical vs. chemical weathering is clearly rock dependent. Fig. 3-20B shows that the positive relationship enhanced after normalization, particularly for basaltic andesite and granite. As expected, this indicates that the physical weathering process will enhance the chemical weathering intensity due to the fractures formed under physical weathering. The process increases the specific surface area of the rock and provides pathways for meteoric water (Migoń and Lidmar-Bergström, 2002).

### 3.9.2. Implications for paleoclimate research and for heterogeneity assessment of nonconformity reservoirs

The results gained with the methods introduced in this study can be related to paleoclimate data, such as the mean annual temperature (MAT) and mean annual precipitation (MAP), which offers additional fields of applications and quantitative comparisons in paleoclimate research. Previous studies indicate that the physical weathering process refers to an arid climate, while under a humid climate, the chemical weathering process dominates (Bland and Rolls, 1998). The results of this study show that the overall physical weathering intensity shows a decreasing trend and then increases from granodiorite (GA2) and basaltic andesite (GA1) to granite (BK2/05), while the chemical weathering intensity shows the opposite trend. Hence, it can be stated that the climate exhibits a gradual trend toward more humid conditions reflected by the increase in chemical weathering intensity accompanied by the decrease in physical weathering intensity.

---

However, to extend the field of applications and to show the robustness of the methods and results proposed in this study, the major elements employed in this case study are used to apply the methods proposed by Retallack (2006) and Sheldon (2006). The methods make use of the CIA-K and the “clayness (C)”, which is expressed as the ratio between Al and Si in the mole fraction. This ratio is directly correlated with paleoclimate conditions indicated by the B-horizon of the soil profile. (Retallack, 2006; Sheldon, 2006; Sheldon and Tabor, 2009). While the CIA-K can be applied to assess the mean annual precipitation (MAP), the “clayness (C)” is a useful tool for the estimation of mean annual temperature (MAT):

$$\text{MAP}(\text{mmyr}^{-1}) = 221.2e^{0.0197(\text{CIA-K})} \quad (\text{Eq. 3-18})$$

$$\text{MAT}(\text{°C}) = 46.94 * C + 3.99 \quad (\text{Eq. 3-19})$$

In addition to Eq. 3-18 and 3-19, a data-driven paleosol-paleoclimate model (PPM) was proposed by Stinchcomb et al. (2016). Their model was developed based on 685 samples from the B horizon from different soil profiles. The investigated elements comprised K, Al, Si, Ca, Na, Al, Ca, Na, Fe, Mg, Mn, Ti and Zr, which were analyzed by combining partial least squares regression (PLSR) and nonlinear spline. The output results of this model include both MAP and MAT. However, the model does not consider the overprint of burial diagenesis. Thus, to apply this model to weathering profiles influenced by burial diagenesis, elements that are preferentially affected such as Ca and K should be corrected.

To apply the PPM model of Stinchcomb et al. (2016), paleosol samples from the topmost part of the weathering profile, with the parent rock of basaltic andesite and gabbroic diorite in GA1, granodiorite in GA2 and granite in BK2/05 were selected. For both methods, the CaO was corrected based on McLennan (1993). The K<sub>2</sub>O content for PPM is corrected based on Panahi et al. (2000). The comparison of the results from these two studies and the method proposed in this study is listed in Table 3-2.

Using the PPM of Lukens et al. (2016) rock types comprising granodiorite (GA2), gabbroic diorite (GA1), basaltic andesite (GA1), and granite (BK2/05), the MAP shows an increasing trend

from 542 to 1522 mm/yr followed by a decreasing trend to 1109 mm/yr. The MAT gradually increases from 10.3 to 21.3 °C and then decreases to 10.3 °C. Overall, these trends in MAP and MAT coincide well with the trends of IPWN and CIAN in this study. Hence one can make use of this quantitative relationship to additionally assess MAP and MAT with the same database as used for the methods suggested in this study.

Table 3-2. Results from the methods proposed by Sheldon (2006), Lukens et al. (2016) and this study, note the unit for MAP is mm and MAT is °C.

Samples	Sheldon (2006)		Lukens et al. (2016)			This study				
	MAP	MAT	Low MAP	Best MAP	High MAP	Low MAT	Best MAT	High MAT	CIAN	IPWN
GA2 granodiorite	912.67	10.14	208	542	877	7.6	10.3	13	70	3.85
GA1 gabbroic diorite	1163.33	12.53	1158	1442	1727	11.6	13.6	15.7	78	—
GA1 basaltic andesite	1544.22	17.32	1127	1522	1917	17.8	21.3	24.8	82	0.02
BK2/05 granite	1427.73	9.82	723	1109	1495	7.4	10.3	13.2	77	0.16

For the results calculated based on the PPM proposed by Sheldon (2006), the MAT shows a similar trend as the weathering intensity from this study. The MAP of the paleosols weathered from basaltic andesite and gabbroic diorite fits well with the model of Lukens et al. (2016) and with the chemical weathering intensity. However, the samples from the other two drill cores, especially the paleosols weathered from granite in BK2/05, show a clearly higher MAP close to basaltic andesite. The value of CIA-K is 94.7, while the petrographic and mineralogical characteristics indicate that the sample is only moderately weathered (Fig. 3-7D & 3-8). An explanation is that the parent rock (granodiorite and granite) of the samples contains K-feldspar, which leads to a higher value of CIA-K compared to its actual chemical index of alteration (Fedo et al., 1995). Nevertheless, our results still show a positive correlation with the variation in both MAP and MAT.

In conclusion, both models coincide with CIA<sub>N</sub> and IPW<sub>N</sub> trends, meaning that the increases in precipitation and temperature indicate a warm and humid climate. Subsequently, a more intense

---

chemical weathering environment with a relatively lower rate of physical weathering processes appears.

In addition to paleoclimate evaluation, the  $CIA_N$  and  $IPW_N$  may also be applied for the evaluation of the heterogeneity of nonconformity reservoirs. With the alteration of the meteoric environment, the petrophysical properties of the weathering zone along the basement rock change (Gardner, 1940; Walter et al., 2018). Note that both physical and chemical weathering are sensitive to different lithologies, which causes a specific response of petrophysical properties. Therefore, when working on a weathered basement comprising different lithologies, the weathering intensity ( $IPW_N$  and  $CIA_N$ ) should be calculated as suggested in this study. Then, on a regional scale, the weathering intensity and the weathering degree of different lithologies distributed along the nonconformity can be assessed to find suitable assets in terms of reservoir quality. In addition, based on the relationship between the weathering degree and petrophysical characteristics (Walter et al., 2018; Wu et al., 2013) the heterogeneity of the nonconformity reservoir can be evaluated.

### **3.10. Perspectives**

The suggested theoretical and practical concept for the rock-specific quantification of physical and chemical weathering in this paper opens new avenues to study the complex processes at nonconformities but also for paleosols in the sedimentary stratigraphic record. A high applicability is given because it is designed for studies on drill cores and at the microscale. However, there is still a potential for improvements. First, the relationship between UCS and CIA values for more rock types could be developed in the future. With these relationships, the physical weathering intensity for more rock types could be compared. Second, the strategy for sampling could be restricted, e.g., all the samples should avoid macro/mesoscale fractures along drill cores. While the samples are more unified, the weathering degree results should be more representative. Last, the effect of the weathering intensity on the petrophysical characteristics of different types of rock is only weakly discussed here. The influences of both physical and chemical weathering intensity on the porosity and permeability of different rocks are still uncertain. Relevant work, such as the petrophysical

---

characteristics of different igneous rocks under a variety of weathering intensities, could be measured in the future. With the results, the heterogeneities of the nonconformity reservoir may be quantified and the results may contribute to reservoir quality assessment.

### **3.11. Summary and conclusions**

Both physical and chemical weathering are significant processes on the surface of the earth. This study suggested a new index of physical weathering (IPW) to quantify physical weathering in paleoweathering profiles at the microscale. Using the IPW, an integrated concept to quantify the weathering intensity for both physical and chemical weathering is proposed. The suggested quantification method is designed for drill core investigations using petrographic and computer-aided textural thin section analysis, combined with standard mineralogical XRD, as well as geochemical XRF and ICP-MS analyses. This study also introduces a normalization procedure for physical weathering, the IPW<sub>N</sub>, as well as a procedure to normalize the CIA to rock types expressed by the CIA<sub>N</sub>.

The introduction of the new indices IPW<sub>N</sub> and CIA<sub>N</sub> and its corresponding workflow allows for the first time the simultaneous quantification of the physical and chemical weathering intensity at subaerial paleo-surfaces in the geological record. This makes the effects of weathering comparable at the regional scale regardless of rock type in terms of paleoclimate and heterogeneity assessment, as well as alteration of petrophysical properties.

As a case study, three drill cores from the first-order post-Variscan nonconformity in southwestern Germany were taken hitting the nonconformity in several tens of meters, which excludes the overprint of recent weathering. At the nonconformity, Precambrian to Paleozoic magmatic rocks (granodiorite, gabbroic diorite and granite) were weathered and diagenetically altered and overlain by Permo-Carboniferous volcanic and sedimentary rocks. A basaltic andesite lava flow within the Rotliegend also shows weathering at the top which has been investigated in addition. The calculated IPW<sub>N</sub> and CIA<sub>N</sub> trends of these sections coincide well with trends of paleosol-paleoclimate models revealing mean annual temperature (MAT) and mean annual precipitation (MAP), which illustrate the potential to synchronize the suggested indices with other paleoclimate proxies. This

---

offers a completely new spectrum of possibilities to quantitatively compare weathering and climatic conditions at the regional scale, regardless of lithologic constraints.

### **3.12. Acknowledgement**

Geochemical analysis for this work was co-funded by “University Scientific Research Program of Xinjiang Uygur Autonomous Region Education Department (grant no. XJEDU2019Y070)” and China Scholarship Council (CSC) (grant no. 201806400006). The authors would like to thank the Senckenberg Research Station of Grube Messel, Dr. Sonja Wedmann and Mr. Bruno Behr who provided drill cores for this work and Mr. Reimund Rosmann who provided much help.



---

## 4. Palaeo-weathering of different basement rocks along a first order nonconformity - case study at the post-Variscan nonconformity (Germany)

---

Liang Fei<sup>1</sup>, Matthias Hinderer<sup>1</sup> Jens Hornung<sup>1</sup>

<sup>1</sup>Material and Geosciences, Institute of Applied Geosciences, Technical University of Darmstadt, Darmstadt 64287, Germany

\* Correspondence. Liang Fei. Email: liang@geo.tu-darmstadt.de;

*Received at Editorial Office: 12 Sep 2022 – Article revised: 26 Feb 2023 – Article accepted for publication: 6 Mar 2023*

*(<https://authors.elsevier.com/tracking/article/details.do?aid=107070&jid=CATENA&surname=Liang>)*

### 4.1. Author contributions

(i) Fei Liang as the first author collected and prepared all the samples, conceptualized and prepared the paper.

(ii) Matthias Hinderer helped conceptualized and supervised this research.

(iii) Jens Hornung helped revise and polish the manuscript.

**Abstract:** Intracratonic sedimentary basins develop on first-order nonconformities. Although the evolution of such basins has been the focus of many studies, the formation of the basement surfaces has rarely been considered. In this paper, we investigated the physical and chemical paleoweathering of different basement rocks at the post-Variscan nonconformity in Central Europe. We used a comprehensive approach by accounting for different scales and integrating physical and chemical weathering. Physical weathering was qualitatively classified at the macro/mesoscale and quantitatively classified at the microscale using thin sections and through measuring fracture areas by image analysis. Chemical weathering was quantified by distinguishing the mineralogical and geochemical characteristics measured by X-ray diffractometry (XRD), X-ray fluorescence (XRF) and inductively coupled plasma mass spectrometry (ICP-MS). Compared to previous studies, common physical and chemical weathering indices were normalized to the rock types to improve the weathering intensity comparison. Clay transfor-

---

mation and carbonate/dolomite precipitation in the paleoweathering sections indicate a temperature interval of 100 to 300 °C for the circulating fluids during burial. The maximum chemical weathering intensity was found at the top surface of the basaltic andesite with a  $CIA_N$  (normalized chemical index of alteration) value of 83, whereas the  $IPW_N$  (normalized index of physical weathering) was less than 0.1. The gabbroic diorite and granite had a  $CIA_N$  value of 78, whereas the physical weathering intensity was approximately 0.6. The lowest chemical weathering intensity was observed at the top of the granodiorite and tonalite at 71, and both rock types showed the highest physical weathering intensity of approximately 4. Because of the normalization procedure, the differences in the ratio of chemical versus physical weathering can be directly linked to aridity-humidity changes in the lower Permian paleoclimate. The concept and results of this work can be used for future studies on continental paleoclimate as well as for reservoir modeling.

**Key words:** weathering; macro/mesoscale characteristics; major and trace elements, post-Variscan; SW Germany

## 4.2. Introduction

A nonconformity refers to a geological surface between weathered and eroded crystalline rock and overlying sediments, representing a significant gap in the geological record (Catuneanu, 1996). Such surfaces also play an important role in the subdivision and correlation of stratigraphic successions as well as in establishing boundaries in reservoir models (Catuneanu, 2006). Nonconformities are diachronous and form over long time intervals driven by tectonic cyclicity. This process involves uplift, weathering, erosion, and burial by sediments when uplift ceases and subsidence takes place.

Nonconformities are prime features of continental sedimentary basins and are formed at the transition from mountain-building processes to postorogenic subsidence (Geissman and Harlan, 2002). Prominent examples are the “Great unconformity” on the Colorado Plateau in North America, the widespread Cambro-Ordovician cover over the Pan-African basement in Africa, and

---

the Permo-Carboniferous cover of the Variscan orogen running over large parts of western, southern and central Europe (Avigad et al., 2017; Malek-Mahmoudi et al., 2017). We selected the post-Variscan nonconformity in the central part of the Variscan Orogen, where the basement is formed from high grade metamorphic and plutonic rocks. In particular, this study focused on the cover-basement interface of the Odenwald crystalline basement complex (OCC), the largest basement window of the Mid-German Crystalline Zone (MGCZ) belonging to the Saxo-Thuringian realm (Dörr and Stein, 2019a; Willner et al., 1991). This interface is characterized by multiple types of magmatic and metamorphic rocks of late Neoproterozoic to Carboniferous age (Dörr and Stein, 2019b). This basement is a typical Variscan basement and can be correlated with the northern Armorican Massif in France and the Ossa-Morena Zone in southwest Spain (Martinez-Catalan 2020). Moreover, similar Variscan basement rocks stretch from the Iberian Massif in central Spain over the Massif Central in France, to the Bohemian Massif. Variscan basement units are also widespread in the Mediterranean and the Alps; i.e., the sections studied herein are representative of large parts of this nonconformity in Europe (Maino et al., 2019; von Raumer et al., 2013).

Previous studies on the post-Variscan nonconformity have focused mainly on its tectonic evolution (Funedda, 2009; Kroner et al., 2007; Willner et al., 1991). The basement alteration along the nonconformity has been studied, e.g., by Parcerisa et al., (2010) in the Morvan Massif (France) and by Fàbrega et al. (2019) in NE Spain. They observed thermal diagenetic overprinting, such as the albitization of plagioclase, but did not attempt to disentangle paleoweathering from burial diagenesis. The modern weathering characteristics of Variscan crystalline rocks have been systematically studied in the Sila Massif (Italy) based on both field studies and geochemical characteristics (Scarciglia et al., 2016). The influence of hydrothermal alteration before the weathering process has been carefully described, but the weathering intensity differences among different rock types have rarely been mentioned.

Along nonconformities repeated alteration processes take place. During uplift, the crystalline basement is exposed to the surface and undergoes physical and chemical weathering. The extent

---

of both these weathering processes depends on the climatic conditions (Joo et al., 2016). During this so-called supergene process, the basement rock is gradually broken and dissolved, and pedogenetic processes lead to the transformation and translocation of matter (McLennan, 1993). Soil types depend on the continental climatic conditions, relief, time, biological activities and parent materials and can serve as preferred paleoclimatic archives in continental realms (Cissé et al., 2023; Sreedevi et al., 2022).

The chemical weathering of silicates is incongruent, and primary minerals such as feldspar and biotite are only partly dissolved and gradually decompose to secondary minerals such as smectite and illite and eventually into kaolinite and gibbsite. Geochemically, this means that mobile elements such as Na, K and Ca are depleted (Nesbitt and Young, 1989a). As the chemical weathering process continues, the porosity increases, micro-channels (spaces formed due to the shape of the secondary minerals) may form within the minerals due to the loss of materials, and the rock strength decreases (Moon and Jayawardane, 2004; Santos et al., 2018). Loose material can be liberated by flowing water or wind. Water transports the material downhill, where it accumulates as a proximal alluvial fan that develops into a river system further downstream. In the case of ongoing subsidence, sedimentation retrogrades and the weathered basement surface becomes successively covered by sediments, causing a so-called nonconformity to form. With ongoing subsidence, the weathering profile is realtered by increasing hypergene processes, e.g., increased pressure, temperature, and throughflow of diagenetic fluids (Sandler et al., 2012). All this information stored in paleoweathering profiles provides an ideal opportunity for paleoclimate reconstruction, when disentangled from hypergene processes (Nesbitt and Young, 1982),

In addition, alterations at the site of a nonconformity change the petrophysical characteristics of the rocks and usually increase their porosity and permeability, leading to the transformation of solid basement rocks into potential reservoirs for petroleum and water (Halbouty, 1972). This can also have implications for ore-forming processes. At the Variscan nonconformity,

---

hydrothermal mineralizations are known from the Spessart region ca. 50 km east of the Odenwald region (Fusswinkel et al. 2014).

Liang et al. (2021) studied drill cores penetrating the post-Variscan nonconformity in the northernmost Odenwald region. In their case study, supergene and hypogene alterations were distinguished by correcting for element shifts and taking into account feldspar – clay mineral reactions. The K-metasomatism and the overprint of hydrothermal fluids were also documented. In Liang et al. (2022), physical weathering was additionally considered, and an integrated workflow for the quantification of both physical and chemical paleoweathering was presented. Physical weathering was quantified using the ratio between the area of microfractures in the thin sections and those of the unaltered rock and by considering the rock strength. The chemical weathering degree was normalized for different rock types by the chemical weathering ability (CWA)(Liang et al., 2022). In both cases, observed and/or measured data were corrected for either chemical or tectonic overprinting during burial.

In this paper, the workflow of Liang et al. (2022) is applied to additional drill cores obtained at the post-Variscan nonconformity in the Odenwald region, focusing on the paleoweathering characteristics of different rock types and a combination of macro/mesoscale, microscale, mineralogical and geochemical characteristics. The aim of this study is to extend our quantitative approach of paleoweathering to more rock types and more settings at the prominent post-Variscan nonconformity. This requires (i) considering chemical and physical weathering, (ii) setting up the relationships among weathering characteristics at different scales and combining different analytical tools, and (iii) comparing weathering characteristics among different lithologies but under similar climatic conditions. Moreover, in this study, we expect to detect a predominantly arid to semiarid climate after the Variscan Orogeny (Roscher and Schneider, 2006), along with relatively short humid intervals, as was revealed by Liang et al., (2021). The basement of the Odenwald region experienced a uniform burial history; e.g., the hypogene processes are expected to have been similar at all locations, and the same correction is applied herein as was applied in Liang et al., (2021).

---

### 4.3. Geological setting

The prominent post-Variscan nonconformity offers an ideal case for studying paleoweathering. It was formed after the Variscan Orogeny during the late Carboniferous to the early Permian. We selected four drillings penetrating through the post-Variscan nonconformity where the basement was always covered with sediments or volcanic rocks of the Rotliegend age; i.e., the age of paleoweathering can be assumed to be highly comparable among the drilling sites (Fig. 4-1). The basement rocks underneath the nonconformity provide a wide spectrum of common magmatic rocks ranging from gabbroic diorite, tonalite, and granodiorite to granite. At one site, the basement is overlain by an early Permian lava flow, which is classified as basaltic andesite according to geochemical analysis (Liang et al. 2021). This lava flow was considered in this study to analyze the effects of different textures (aphanitic vs. phaneritic), although its chemical composition is similar to that of gabbroic diorite.

All basement rocks belong to the MGCZ in the center of the Variscan Orogen, which was formed as a magmatic arc during the Lower Carboniferous Variscan Orogeny and most likely contains the Rhenic Suture (Stein 2001, Zeh and Gerdes, 2010, Stein et al. 2019). U–Pb zircon dating of these magmatic rocks yielded ages between 354 and 332 Ma (Stein et al. 2022). On the Spredlinger Horst, however, Neoproterozoic/early Cambrian magmatic rocks were also discovered recently, with an age of  $540 \pm 8$  Ma (Dörr & Stein 2019). In the upper Carboniferous, the MGCZ fragmented during orogenic collapse and postorogenic transtensional tectonics into intramontaneous basins and highs that were filled by alluvial, fluvial and lacustrine sediments. One of these highs was the OCC, which today is framed by the Kraichgau Basin in the south and the eastern termination of the Saar-Nahe Basin. In the Cenozoic, the Saar-Nahe Basin was tectonically fragmented due to the formation of the Upper Rhine Graben, the eastern shoulder of which in the northern region is the Spredlinger Horst. The basements of the selected drillings all belong to the OCC and are all in a marginal position with respect to the Kraichgau Basin and the Saar-Nahe Basin. Sedimentation began in the earliest Permian at approximately 295 Ma. A time gap of at least 350 million years exists at the nonconformity, during which plutonic rocks were exhumed and exposed by erosion.

---

The overlying Rotliegend deposits reach a thickness up to 250 m and are composed of weakly sorted alluvial sediments graded into braided, meandering fluvial sediments as well as playa sediments to the top (Marell, 1989). At the base, bimodal felsic and mafic volcanic rocks are intercalated regionally.

During the mid-Permian, the Saar-Nahe Basin was inverted and uplifted. Farther west of the study area, Henk (1992) estimated a maximum overburden of upper Carboniferous and Permian sediments of 2400 m based on mudstone compaction; these sediments had already been eroded in the mid-Permian. In the late Permian, the relief became smoother, and the area was flooded by the epicontinental Zechstein Sea. Continuing subsidence led to the deposition of Triassic and Jurassic sediments with a total maximum thickness of 1500 m. Maximum burial and heating prevailed during the upper Jurassic to lower Cretaceous, as evidenced by fission track dating (Wagner et al., 1990). Since the Cenozoic, repeated faulting accompanied by graben formation (including in the Upper Rhine Graben) and horst uplift have led to the removal of the complete Mesozoic sediment cover at the investigated sites (Cloetingh et al., 2006).

The Spredlinger Horst, where the northernmost three wells are located, contains a relatively thin cover of Rotliegend sediments intercalated by basaltic lava flows. The stratigraphy in this area includes the Moret Formation and the Lower and Upper Langen Formations (Moret, 1989; Becker et al., 2012), among which the Lower Langen Formation contains volcanic lava. This volcanic lava can be correlated to a stratigraphically similar volcanic episode in the Saar-Nahe Basin, which yielded an age of  $290 \pm 6$  Ma (Lippolt and Hess, 1983). The southernmost drilling belongs to the 337-Ma Variscan Heidelberg Granite, which is overlain by the Michelbach Formation of the Rotliegend and the Zechstein Dolomite Formation and Langenthal Formation (Hug and Gaupp, 2006). The thickness of the Michelbach Formation is approximately 8 m and its age is estimated to be between 290 and 280 Ma (Edgar and Hubert, 2009).

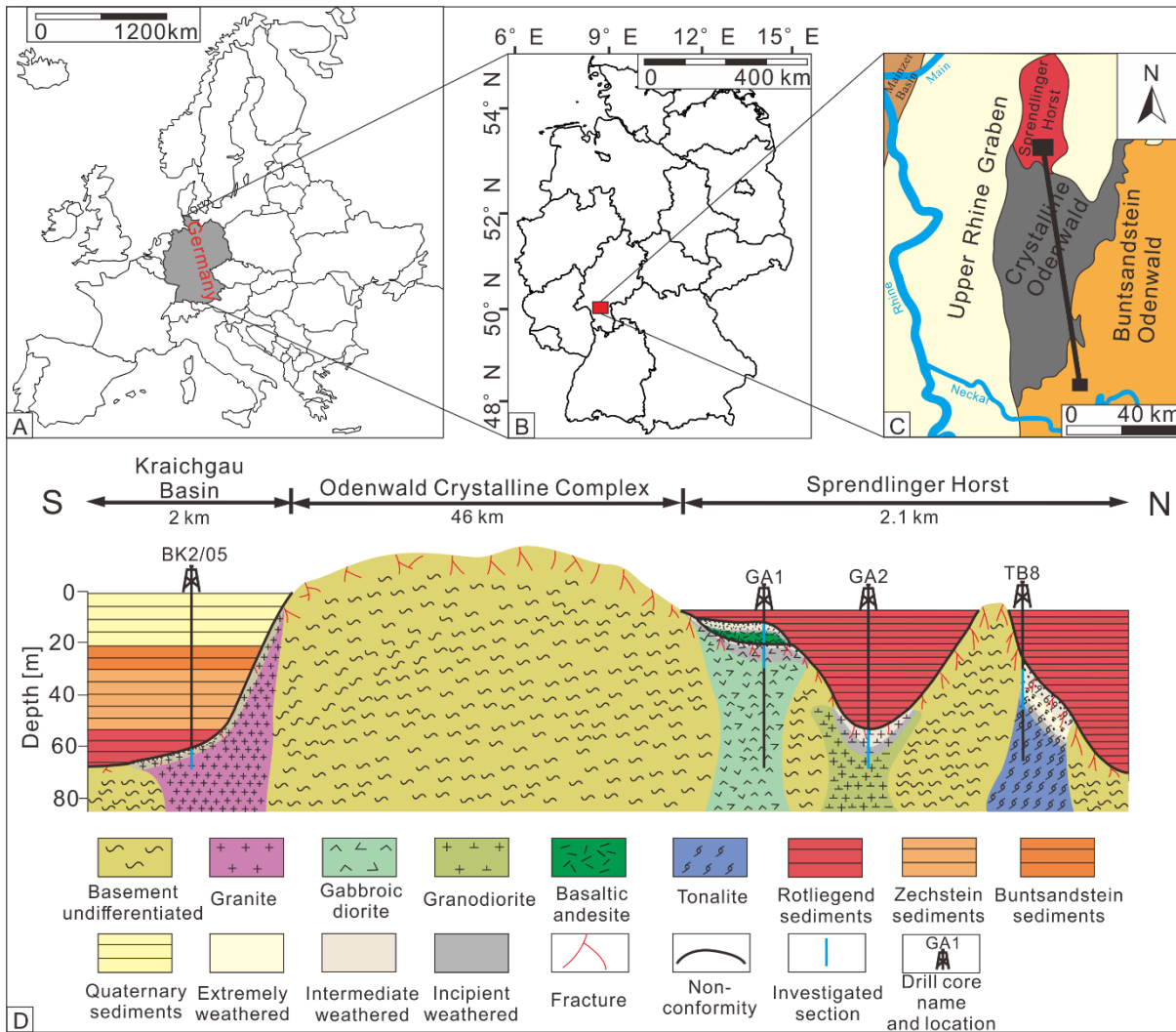


Fig. 4-1. Location maps and schematic cross section from the Kraichgau Basin through the Odenwald Crystalline Complex to the Spredlinger Horst. Locations and geologic context of the drill cores used in this study are shown.

#### 4.4. Materials and Methods

Four drill cores with different lithologies were selected for this study, three of which were from the Spredlinger Horst, i.e., from the former eastern margin of the Saar-Nahe Basin (GA1, GA2, and TB8) and one of which was from the northern margin of the Kraichgau Basin (BK2/05). All core sections consist of basement rock and overlying sediments. The nonconformity penetrates to depths of 20 to 60 m and avoids overprinting by modern weathering (see Fig. 1). In the GA1 drill core, the basement is overlain by a basaltic andesite, and in all other drill cores, the basement is overlain by alluvial Rotliegend sediments. The lithologies of the basement rocks in the GA1, GA2, TB8 and BK2/05 cores are gabbroic diorite, granodiorite, tonalite and granite, respectively. The



---

sediments and basaltic andesite in GA1 belong to the Lower Langen Formation (Menning et al., 2005), while the sediments in GA2 and TB8 belong to the Moret Formation (Liang et al., 2021), and those in BK2/05 belong to the Michelbach Formation (Edgar and Hubert, 2009). Paleoweathering of the basement sections in GA1, GA2, and BK2/05 were analyzed with respect to petrology, mineralogy, and geochemistry using thin sections, X-ray fluorescence (XRF), inductively coupled plasma mass spectrometry (ICP–MS), and X-ray diffraction (XRD) (Liang et al., 2022, 2021). Both chemical and physical weathering were corrected and quantified. In this paper, we add a tonalite in TB8 as a further rock type and extend the weathering analyses of all drillings to the macro/mesoscale, i.e., by performing visual classifications of the weathering degrees in the drill cores. In this work, we intend to link sophisticated thin section analysis and analytical methods to perform rapid core inspections that can be performed immediately onsite after drilling.

#### **4.4.1. Physical and chemical weathering degree evaluation**

The weathering assessment was performed at two scales (Fig. 2): (i) at the macro- to mesoscopic visual scale using a hammer, HCl and lenses and (ii) at the microscopic scale using thin section analysis; in addition, (iii) instrumental analytics of the geochemistry and mineralogy were performed using XRF, ICP–MS, and XRD. With the results from all three aspects, the relationships between the analytics and visual scale were acquired, and a comprehensive evaluation of weathering was developed (Fig. 4-2).

##### *Macro- to mesoscale classification*

For the macro- to mesoscale scale analysis, weathering characteristics were described with respect to the texture and structure, rock strength, and color of the drill cores based on the Rock Weathering Classification Diagram (Aggisttalis et al., 1996; Borrelli et al., 2014). According to this classification scheme, the texture analysis of the rock focused mainly on the crystallinity, while the structure analysis included both original and secondary structures (e.g., fractures).

The rock strength was specified in terms of the uniaxial tensile strength (UTS), uniaxial compressive strength (UCS), shear strength, and impact strength. The formation of fractures during weathering is more related to the UTS than to the UCS (Aadnøy and Looyeh, 2019). These two parameters can be measured and calculated. In contrast, in the macro/mesoscale analysis, the rock strength was qualitatively described with tactile sensations using a geological hammer, hands and water (Aggisttalis et al., 1996; Borrelli et al., 2014). Based on the diagram, the weathering degree was divided into five degrees: fresh, slightly weathered, moderately weathered, highly weathered and completely weathered (e.g. Arel and Tugrul, 2001).

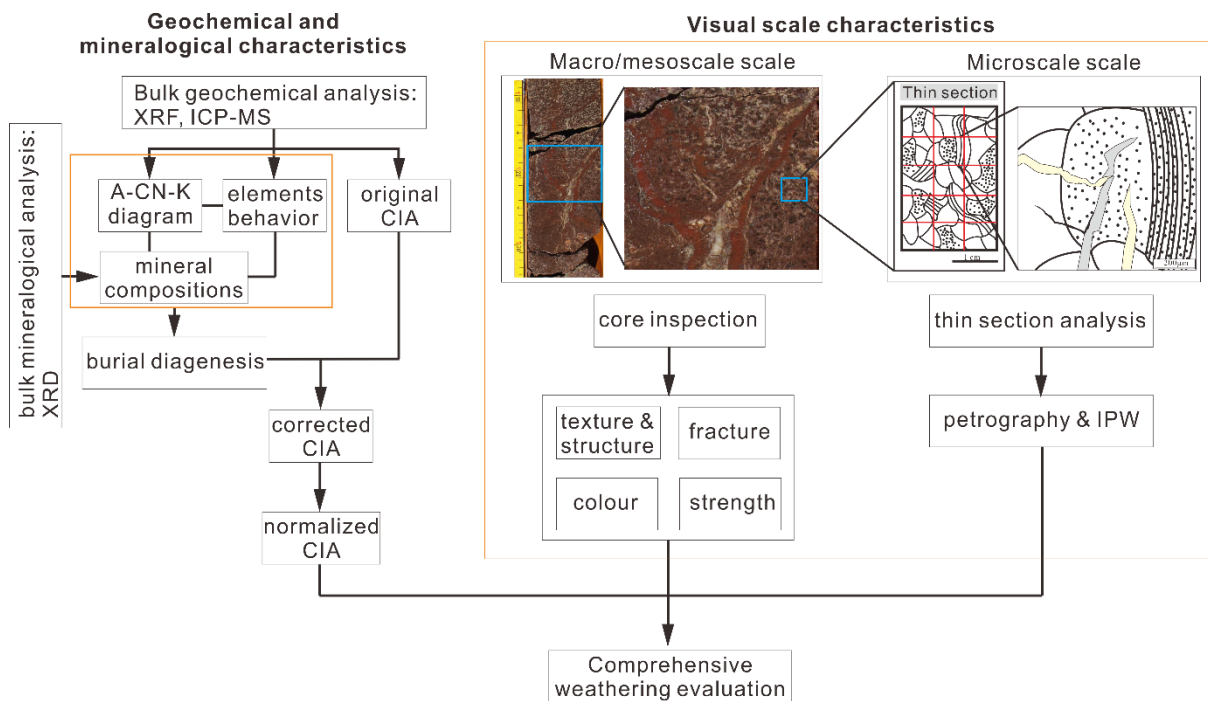


Fig. 4-2. Integrated work flow to evaluate the weathering degree. Procedure for evaluation of burial diagenesis is in the red frame and described in Liang et al. 2021). CIA = Chemical index of alteration, IPW = Index of physical weathering.

#### Physical weathering quantification

The physical weathering degree was quantified at the microscale using the index of physical weathering (IPW) based on the microfractures within the thin sections under a polarizing microscope (Liang et al., 2022). The IPW is equal to the ratio between the fracture area and the total detected area under the microscope. Representative cut-outs at 3 to 5 levels in the weathering zone were selected to prepare the thin sections. This microscale inspection was not

practicable for cases of specimens that were intensively fractured or decomposed. The fractures were categorized into clay-filled, calcite-filled, and void fractures. For each thin section, 15 visual evenly distributed areas within the thin section were analyzed, and the mean ratios were determined. This analysis provided the apparent IPW. In such research, the IPW may need to be corrected if the research area is affected by tectonic movement. To account for this, the fracture-to-matrix ratio of the unweathered rock at a depth of at least two meters below the fresh zone was defined as the background reference value. Then, the background fracture values were subtracted from each fracture area measurement value prior to normalization by the total detective area values as follows:

$$IPW_{\text{corr}} = \frac{A_{(\text{Fw})} - A_{(\text{Ff})}}{A_T} \quad (4-1)$$

Where  $IPW_{\text{corr}}$  refers to the corrected physical weathering degree,  $A_{(\text{Fw})}$  is the fracture area in the weathering zone,  $A_{(\text{Ff})}$  is the background fracture that is represented by the fractures in the fresh zone, and  $A_T$  is the total detected area. Drill cores GA1, GA2 and BK2/05 were not affected by tectonic fractures, i.e.,  $IPW_{\text{corr}}$  was equal to IPW.

The IPW should be normalized by the susceptibility to physical weathering to acquire  $IPW_N$ . With the  $IPW_N$ , the physical weathering intensity can be compared. Because the  $IPW_{\text{corr}}$  depends on rock strength and thus on rock variety (e.g. Ceryan et al., 2008), the susceptibility to physical weathering is represented by the rock strength (Chiu and Ng, 2014; Thomson et al., 2014). The accurate rock strength is represented by the uniaxial compressive strength (UCS), which was calculated based on the relationship between the UCS and CIA for basaltic and granitic rocks (Liang et al., 2023). Based on the specific UCS along the weathering profile, the final  $IPW_N$  was acquired (see Appendix IV-II) (Liang et al., 2022).

#### *Chemical weathering quantification*

The chemical weathering degree was quantified by the chemical index of alteration (CIA) (Nesbitt and Young, 1982), which can be expressed as follows :

$$CIA = \frac{Al_2O_3}{Al_2O_3 + Na_2O + K_2O + CaO} * 100 \quad (4-2)$$

Where  $\text{CaO}^*$  refers to the Ca within the silicate only. For the Ca correction, the method proposed by McLennan (1993) was applied:  $\text{CaO}_{\text{rest}} = \text{CaO} - 10/3 \cdot \text{P}_2\text{O}_5$ , where  $\text{P}_2\text{O}_5$  relates to apatite, and  $\text{CaO}^* = \text{CaO}_{\text{rest}}$  when  $\text{CaO}_{\text{rest}} \leq \text{Na}_2\text{O}$ ; otherwise,  $\text{CaO}^* = \text{Na}_2\text{O}$ .

As up to 2400 m of former overburden has been estimated in the study area (Henk, 1993), the geochemical data need to be corrected for hypogene alteration. Liang et al. (2021) demonstrated that K enrichment is the prime concern resulting in decrease in the apparent CIA value. For the K correction, the method proposed by Panahi et al. (2000) was applied:

$$\text{K}_2\text{O}_{\text{corr}} = \frac{m \cdot A_w + m \cdot \text{CN}_w}{1 - m} \quad (4-3)$$

Where  $A_w$  and  $\text{CN}_w$  refer to the  $\text{Al}_2\text{O}_3$  and  $(\text{CaO}^* + \text{Na}_2\text{O})$  contents in the weathering zone, respectively, and

$$m = \frac{K}{A + \text{CN} + K} \quad (4-4)$$

where the K, A and CN values relate to the fresh protolith sample.

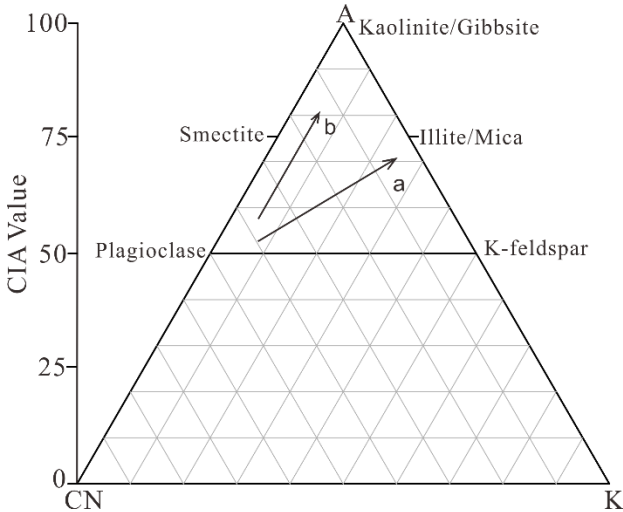


Fig. 4-3 the A-CN-K diagram with the ideal weathering trend (b) and K- metasomatism weathering trend (a)

Additionally, K-metasomatism can be visualized and corrected using an A-CN-K diagram (Fedotkin et al., 1995; Liang et al., 2021). The ideal weathering trend in the A-CN-K diagram should be parallel to the A-CN axis due to depletion-rate among Na, Ca and K (Nesbitt and Young, 1984). This trend extends to the K apex in the case of K metasomatism (Fig. 4-3).

---

Similar to physical weathering, the susceptibility to chemical weathering also varies among rock types due to chemical composition and textures differences (Martinez et al., 2014; Middelburg et al., 1988; Patino et al., 2003). To compare the chemical weathering intensity among different lithologies, the CIA value should also be normalized. Although the CIA value of all types of completely weathered rock is 100, the initial values vary for different protolith rocks (Fedó et al., 1995; Mclennan, 1993). To normalize the CIA of the rock types, first, a reference rock is needed ( $CIA_R$ ). For each rock type, the CIA range from the protolith to a completely weathered state, i.e., 100, was normalized to the range of the reference rock. Second, the susceptibility to chemical weathering of the protolith rock was taken into account, and expressed as the chemical weathering ability (CWA); the CWA is the integral function of the weathering rate with time for different minerals making up the rock (Liang et al., 2022) (see also in the Appendix IV-II). With the CWA, the final  $CIA_N$  can be acquired.

#### **4.4.2. Sampling and analytical methods**

Based on the macro/mesoscale characteristics measured along the drill cores, representative samples were selected and prepared for thin section analysis. Three thin sections were taken along the basaltic andesite section, six from the gabbroic diorite in GA1, six from the granodiorite in GA2, six from the tonalite in TB8 and five from the granite in BK2/05. The thin sections were observed by polarizing microscopy to acquire microscale visual characteristics. For the analyses of mineralogical and geochemical characteristics, in total, 69 samples were collected, among which 17 samples were from GA1 (6 basaltic andesite and 11 gabbroic diorite samples), 13 granodiorite samples were from GA2, 17 tonalite samples were from TB8, and 22 granite samples were from BK2/05. The sampling intervals at GA1, GA2, and TB8 were approximately 1 m, and samples were more closely spaced in the top part to accurately document the weathering profile. Due to the low weathering degree, the sampling intervals in BK2/05 were set to approximately 20 cm to acquire more detailed weathering information. Rocks were crushed, and veins with widths exceeding 1 mm were removed to avoid artifacts. After milling, the powder samples were divided into three groups, and two were used for major and trace element measurements with

---

XRF and ICP–MS, respectively, while the third was used for XRD analysis. The measurements of major and trace elements were performed in the State Key Laboratory of Isotope Geochemistry, Guangzhou Institute of Geochemistry, Chinese Academy of Sciences. Major elements were measured by a ZSX Primus IV XRF, and the samples were first weighed and then ignited at 900 °C for 3 h, after which the samples were weighed again to measure the loss on ignition (LOI). Then, 0.51–0.53 g of each sample was weighed and mixed with  $\text{Li}_2\text{B}_4\text{O}_7$  at a ratio of 1:8. The mixture for each sample was then fused at 1150 °C in a Pt crucible to make a glass disk for XRF analysis.

Trace elements were measured by a Thermo X Series 2 ICP–MS. First, 40 mg powder for each sample was weighed and mixed with 0.8 mL 1:1  $\text{HNO}_3$ , 0.8 mL HF and 0.5 mL 3 N  $\text{HClO}_4$  in high-pressure-resistant Savillex Teflon beakers. The mixture was heated at 100 °C for 48 h to evaporate all the liquid. Second, the residue in the beaker was added to 0.8 mL 1:1  $\text{HNO}_3$  and heated at 100 °C for 12 h. Third, the beakers were sealed before 0.8 mL HF and 0.5 mL 3 N  $\text{HClO}_4$  were added. These beakers were then moved into an oven and heated at 190 °C for 48 h to ensure that all the sample powder was completely dissolved. Fourth, the beakers were opened to evaporate all the liquids, sealed again after adding 4 mL 4 N  $\text{HNO}_3$  to each and moved into an oven for 4 h at 170 °C. Finally, the solution in the beakers was diluted with 3%  $\text{HNO}_3$  until the weight of the solution was 250 times that of powder sample. A 0.25 g solution was taken and diluted with 3%  $\text{HNO}_3$  to 2.00 g and mixed with 2.00 g Rh-Re standard solution. The mixed solution was examined by ICP–MS to acquire the trace element contents. To monitor the analytical quality of both major and trace elements, international standard samples of GSR-1 (granite), GSR-2 (andesite) and GSR-3 (basaltic andesite) were applied.

The mineral compositions were measured by XRD. The whole rock powder samples were prepared by back-loading to reduce the preferred orientation. The prepared samples were measured by a PANalytical X'Pert diffractometer equipped with a Bragg–Brentano goniometer (copper beam) at the University of Frankfurt. All samples were scanned at 40 kV and 30 mA for 2 h, and the time for each step was 50 s with a step size of  $0.008^\circ$  starting at an angle of  $2.5^\circ$  and ending at  $70^\circ$ . The mineral phase proportions were estimated by weighted XRD peak intensities

after conversion with their typical reference intensity ratios (RIR) as found in PDF-2 and PDF-4 with the software MacDiff (Petschick et al., 1996).

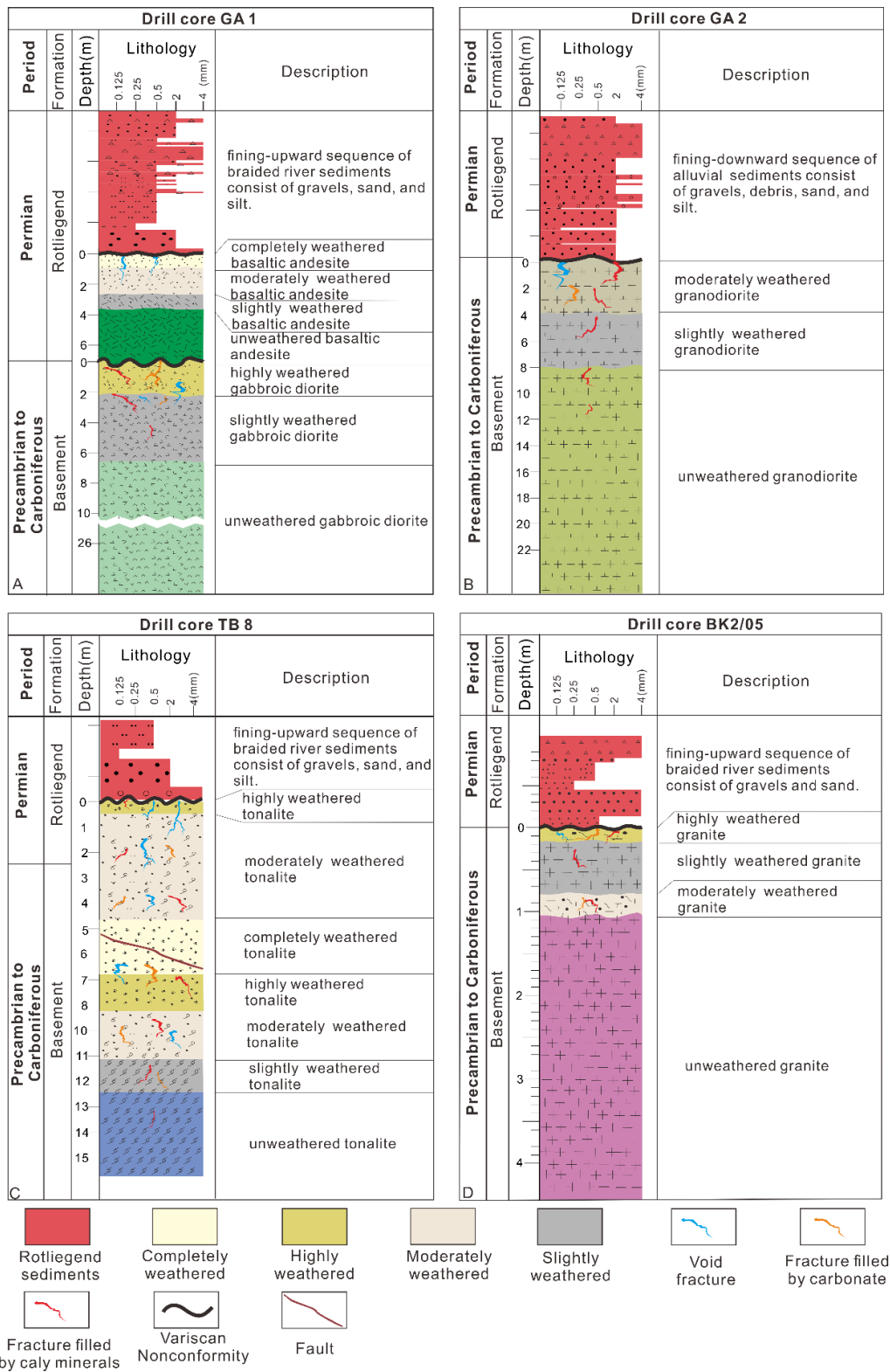


Fig. 4-4. Macro to meso-scale visual characteristics of the drill cores. Weathering degree according to Aggisttalis et al. (1996) and Borrelli et al. (2014). Further explanation see text.

---

## 4.5. Results

### 4.5.1. Macro- to mesoscale visual weathering characteristics

Based on the drill core observations, the macro- to mesoscale weathering characteristics were logged. Fig. 4-4 summarizes the general features, and Fig. 4-5a to Fig. 4-5b give a detailed description of the texture, structure, rock strength and color of each core sample; these characteristics were used to assess the fresh rock and four qualitative weathering degrees following Aggisttalis et al. (1996) and Borrelli et al. (2014): slightly, moderately, highly and completely weathered.

GA1: The weathering degree of the overlying early Permian basaltic andesite, shows a rapidly decreasing trend from top to bottom (Fig. 4-4A). The top 0.3 m consists of saprolite. In this part, the original texture can hardly be observed, but the fracture structure is well-preserved and filled by whitish-gray minerals; the strength of the weathered rock is weak, it is easily broken by hand, and the lost material is easily dispersed in water. The color is secondary and dark red. Based on the Rock Weathering Classification diagram of Aggisttalis et al. (1996), this section can be defined as completely weathered. From 0.3 to 2.4 m, the width of the fractures is approximately 2 mm, and the fractures are filled by secondary minerals; however, the density of the fractures is reduced. The original texture is recognizable. Compared to the top 0.3 m, the rock strength is increased, but the surface of the rock can still be scratched by a geological hammer, and secondary colors still dominate. This section is defined as moderately weathered. From 2.4 to 3.9 m, the original aphanitic texture is well-preserved, fractures are absent, the strength is very close to that of the fresh rock, and the original color is only slightly faded. This stage is defined as slightly weathered. The fresh part (3.9-5.4 m) shows an aphanitic texture and is dominated by a fresh gray color with some yellowish Fe-oxide staining the interface between the amygdules and matrix.

The gabbroic diorite also shows a clear declining weathering trend with depth; however, in contrast from the basaltic andesite, the fracturing is pervasively distributed. Down to a 1.9-m depth, fractures reach widths up to 1 cm and are filled with dark-red, fine-grained minerals, most likely clay minerals. The original phaneritic texture is locally preserved, the strength is



substantially reduced compared to the fresh rock, and the sample can be easily broken with a geological hammer. The original color is nearly completely faded, and the matrix is dominated by a whitish-gray color disturbed by the filled fractures. This section is defined as highly weathered. From 1.9 to 6.1 m, the original phaneritic texture is well-preserved, fracturing is very rare, the strength is comparable to that of fresh rock, and the original color is recognized as a mix of black and white with slight reddish stains. This part is defined as slightly weathered. From 6.1 m down, fresh gabbroic diorite occurs, fractures are absent and the color is spotted with black and white minerals (Fig. 4-5a).

well	depth [m]	drill core	weathering degree	drill core photo	texture and structure	strength	color
GA1	0		completely weathered		original aphanitic texture and amygdaloidal structure faintly conserved; fracture is rare, width is around 2 mm and filled by secondary minerals	large pieces can be easily broken by hand and slake in water; point of geological pick indents the rock deeply.	original color (grey) completely faded, and dominated by secondary penetrative dark red.
	2		moderately weathered		original aphanitic texture and amygdaloidal structure still preserved; fracture is rare, width is around 2 mm and filled by secondary minerals	comparable to the fresh rock but point of geological hammer can produce a scratch on the surface of the rock	original color pervasively faded, and can be found locally with secondary color (dark red and whitish grey) patchily distributed
	4		slightly weathered		original aphanitic texture and amygdaloidal structure well preserved; fractures are not found	comparable to the fresh rock	original color pervasively distributed, with small amount of secondary color (whitish grey) patchily distributed
	6		unweathered		original aphanitic texture and amygdaloidal structure; tiny fractures are very limited and filled by secondary minerals	no loss of strength	original color (grey), with some limonite-stained amygdaloid
GA1	0		highly weathered		original phaneritic texture partly preserved; fracture is ubiquitous; width between 0.5 and 1 cm and filled by red secondary minerals	substantially reduced, larger pieces can be easily broken by geological hammer, and do not slake in water	original color pervasively faded, and can be found locally with secondary color (dark red and whitish grey) widely distributed
	4		slightly weathered		original phaneritic texture well preserved; fracture is rare, width around 2 mm and filled by secondary minerals	comparable to the fresh rock	original color pervasively stained by dark red
	8		unweathered		original phaneritic texture; fracture is not found	no loss of strength	original color (mix of black and white)
GA2	0		moderately weathered		original phaneritic texture well preserved; tiny fracture is common, width less than 1 mm and stained by Fe-oxide	comparable to the fresh rock, point of geological hammer can produce a scratch on the surface of the rock	original color pervasively faded, and dominated by whitish grey with Fe-oxide stained the ubiquitous tiny fractures
	4		slightly weathered		original phaneritic texture well preserved; fracture is rare, width less than 1 mm and stained by Fe-oxide	comparable to the fresh rock	original color slightly faded and dominated with red color Fe-oxide stains the fracture
	8		unweathered		original phaneritic texture; fracture is not found	no loss of strength	original color (mix of dark red, black spot and grey)
	12		unweathered		original phaneritic texture; fracture is not found	no loss of strength	original color (mix of dark red, black spot and grey)
	16		unweathered		original phaneritic texture; fracture is not found	no loss of strength	original color (mix of dark red, black spot and grey)

Fig. 4-5a. Macro- to mesoscale visual characteristics of GA1 and GA2 drill cores. Legend for lithological logs see Fig. 4-4.

---

GA2: The original phaneritic texture is well-preserved along the whole basement section. In the top 4.1 m, tiny fractures less than 1-mm wide are widely distributed and stained by dark red Fe-oxide. The strength of this section is almost comparable to that of fresh rock, but this section can be scratched by a geological hammer. This part is defined as moderately weathered. From 4.1 to 8.2 m, the density of fractures is reduced, the color is stained by dark-red Fe-oxide, and the strength is comparable to that of fresh rock. This part is defined as slightly weathered. From 8.2 m downward, fresh granodiorite is observed with spotted dark red, black, gray and white minerals (Fig. 4-5a).

TB8: Within the top 0.5-m section, the original texture is conserved in relicts, fractures are not recognizable, and the rock can be easily broken by a geological hammer, but the material does not slake in water. The original color is not recognizable, and the color is dominated by whitish-gray stained with dark red. This part is defined as highly weathered. From 0.5 to 4.5 m, the aphanitic texture is fairly preserved, with fractures pervasively distributed and filled by secondary minerals. The strength is reduced, and the rock can be easily scratched by the hammer. The original color is patchily faded and spotted by white patches. This part is defined as moderately weathered. From 4.5 to 7.1 m, fracturing is pervasive, and a fault crosses the core between 5.7 and 7.1 m. The original texture is still preserved, larger pieces can be broken by hand, and the materials easily slakes in water. The original color is widely faded with white spots. This part is defined as completely weathered. From 7.1 to 8.2 m, the fracture density is reduced, the rock strength increases but can still be scratched by the geological hammer, and the original color pervasively fades. This part is defined as highly weathered. From 8.2 to 10.2 m, the original aphanitic texture is well-preserved with few fractures stained by Fe-oxide. The strength is comparable to that of fresh rock, the geological hammer can produce only slight scratches on the surface; the original color is well-preserved. This part is defined as moderately weathered. From 10.2 to 11.8 m, the original texture is perfectly preserved, but tiny fractures are widely distributed and stained by Fe-oxide. The strength is comparable to that of fresh rock, and the general color is very close to that

of fresh rock. This part is defined as slightly weathered. Below 11.8 m, the core consists of fresh rock with a phaneritic texture and a grayish color (Fig. 4-5b).

well	depth [m]	drill core	weathering degree	drill core photo	texture and structure	strength	color
TB8	0		highly weathered		original texture and structure are present in relict form; fracture is not recognizable	large pieces can be easily broken by geological hammer and do not slake in water.	original color (pewter) pervasively faded, and stained by penetratively dark red.
	2		moderately weathered		original aphanitic texture preserved fairly well; fracture width is around 5 mm and filled by secondary minerals	comparable to the fresh rock but point of geological hammer can produce a scratch on the surface of the rock	original color (pewter) patchily faded, and mix with secondary offwhite color
	4		completely weathered		original aphanitic texture faintly preserved; fracture is pervasive, width is around 2 mm and filled by secondary minerals	large pieces can be easily broken by hand, point of geological hammer indents the rock deeply	original color (pewter) widely faded, and mix with secondary white color tiny spot
	6		highly weathered		original aphanitic texture still preserved; fracture is limited	large pieces can be easily broken by geological hammer and do not slake in water	original color (pewter) widely faded, and replaced by the mixture of dark grey and offwhite
	8		moderately weathered		original aphanitic texture well preserved; fracture width is less than 1 mm and stained by red-colored Fe-oxide	comparable to the fresh rock, point of geological hammer can produce a scratch on the surface of the rock	original color (pewter) well preserved, with much less distributed secondary offwhite
	10		slightly weathered		original phaneritic texture perfectly preserved; fracture is widely distributed, width less than 1 mm	comparable to the fresh rock	close to original color (pewter)
	12		unweathered		original phaneritic texture	no loss of strength	original color (pewter)
BK2/05	0		highly weathered		original porphyritic texture preserved fairly well; fracture width is around 1 mm and filled by secondary minerals	rock strength substantially reduced, larger pieces can be easily broken by geological hammer and do not slake in water	original color (pink white color with dark minerals) totally faded, with much less distributed secondary offwhite
	0.2		slightly weathered		original porphyritic texture perfectly preserved; fracture is not found	comparable to the fresh rock	close to original color (pink white color with dark minerals)
	0.8		moderately weathered		original porphyritic texture well preserved with a void fracture.	comparable to the fresh rock, point of geological hammer can produce a light scratch on the surface of the rock	close to original color (pink white color with dark minerals), but more pink
	2		unweathered		original porphyritic texture	no loss of strength	original color (pink white color with dark minerals)

Fig. 4-5b. Macro- to mesoscale visual characteristics of TB8 and BK2/05 drill cores. Legend for lithological logs see Fig. 4-4.

BK2/05: In the top 0.2 m, the original granular-porphyritic texture can be recognized. Fractures are rare, filled by secondary minerals, and do not exceed 1 mm in width. The strength is substantially reduced compared to that of fresh rock, and the geological hammer can indent the rock superficially. The original color is faded and dominated by a pervasively distributed reddish color. This part is defined as highly weathered. From 0.2 to 0.8 m, no fractures are found, and the

---

original granular-porphyratic texture is perfectly preserved. The strength is comparable to that of fresh rock, while the original color is only slightly faded. This part is defined as slightly weathered. From 0.8 to 1 m, the original texture is well preserved; however, a fracture runs throughout this part. The strength is comparable to the fresh part, and the color is more pinkish. This part is defined as moderately weathered. From 1 m downward, fresh granite can be observed with porphyritic pinkish feldspar in a black-whitish gray matrix (Fig. 4-5b).

#### **4.5.2. Microscale visual weathering characteristics**

For each macro- to mesoscale weathering degree, a microscale thin section analysis was carried out. Most characteristic features are shown in Fig. 4-6.

GA1: In the completely weathered part of the basaltic andesite, primary minerals are nearly all altered and transformed into clay minerals; however, the primary grain shape is preserved and can be easily recognized. The fractures are void with a width of 80  $\mu\text{m}$ , and some are stained by Fe-oxide; in the moderately weathered section, the primary minerals are intermediately weathered, and approximately half of the primary minerals are altered to secondary minerals. Fractures are rare and have an average width of approximately 40  $\mu\text{m}$ . Within the slightly weathered part, fractures are absent, and primary minerals have limited alteration traces. The fresh part consists of primary mineral grains without any fractures. (Fig.4-6a).

In the highly weathered upper part of the underlying gabbroic diorite, primary minerals such as feldspar are mostly weathered and transformed into clay minerals, and mineral shapes are distorted or fractured. The fracture widths are between 110 and 200  $\mu\text{m}$ , and the fractures are filled mainly with carbonates. Some are filled with clay minerals or are voids. Within the slightly weathered part, feldspar, biotite and amphibole are incipiently weathered, the primary grain shapes are much less distorted, and fractures are distributed mainly within feldspar and biotite with widths of approximately 10  $\mu\text{m}$  and 30  $\mu\text{m}$ , respectively. These fractures are filled mainly by clay minerals and carbonates. The fresh part consists of fresh feldspar, biotite, amphibole and quartz, the mineral grain shape is perfectly preserved, and fractures are not observed (Fig. 4-6a).

GA2: In the upper, moderately weathered part of the granodiorite, the primary minerals are intermediately weathered, with less than half of the minerals such as plagioclase being weathered and the grain shapes being fairly preserved. Fractures have a width of 90  $\mu\text{m}$ , are void in the center and are filled by clay minerals and carbonate at the fracture walls. The fracture density is reduced within the slightly weathered part, the fracture width is reduced to approximately 50  $\mu\text{m}$ , and fractures are mainly filled by clay minerals. The unweathered part consists of fresh minerals, but tiny fractures with widths less than 10  $\mu\text{m}$  filled with clay minerals still exist (Fig. 4-6a).

well	depth [m]	drill core	macro/meso-scale weathering degree	drill core photo	thin section	microscale description
GA1	0	①	completely weathered			primary minerals are nearly all weathered, primary grain shapes are well preserved, Fe-oxide surrounds the amygdaloid, and the fractures are all void and the width is around 80 $\mu\text{m}$ .
	2	②	moderately weathered			primary minerals are intermediately weathered, primary grain shapes are well preserved, Fe-oxide is missing, the fractures are all void with a width around 40 $\mu\text{m}$
	4	③	slightly weathered			primary minerals slightly weathered, and fractures are not found
	6	④	unweathered			primary minerals are well preserved, and fractures are not found
GA1	0	①	highly weathered			primary feldspar are in relict form, and transformed to clay minerals mostly, even quartz grains were fractured, which filled by carbonate, clay minerals and void fracture; the width is from 110 to around 200 $\mu\text{m}$
	4	②	slightly weathered			primary feldspar are slightly weathered, especially biotite is more weathered than feldspar; the width of fractures within biotite is around 30 $\mu\text{m}$ , while within the feldspar is less than 10 $\mu\text{m}$ ; fracture within both filled by carbonate, clay minerals and some void fractures
	8	③	unweathered			primary minerals are well preserved, and fractures are not found
GA2	0	①	moderately weathered			primary feldspar are moderately weathered and transformed to clay minerals; the width of fractures is around 90 $\mu\text{m}$ ; fracture within both filled by carbonate, clay minerals and some void fractures
	8	②	slightly weathered			primary feldspar are slightly weathered; the width of fractures is around 50 $\mu\text{m}$ and mainly filled by clay minerals with Fe-oxide stain in between with the primary mineral grains
	16	③	unweathered			primary minerals are well preserved, and the fractures are rare with a width less than 10 $\mu\text{m}$ , and mainly filled by clay minerals

Fig. 4-6a. Microscale visual characteristics of GA1 and GA2 drill cores. Legend for lithological logs see Fig. 4-4.

well	depth [m]	drill core	macro/meso-scale weathering degree	drill core photo	thin section	microscale description
TB8	0	①	highly weathered			primary minerals are in relict form, primary grain shapes no longer exist, the fractures are mainly void and the width is around 30 µm.
	2	②	moderately weathered			primary minerals are moderately weathered and transformed to clay minerals, fractures are void or filled by clay minerals and carbonate, the width is around 30 µm.
	4	③	completely weathered			primary minerals are in relict form and are weathered to clay minerals, fractures are void or filled by clay minerals and carbonate, the width is around 10 µm.
	6	④	moderately weathered			primary minerals are moderately weathered to clay minerals, fractures are mainly filled by clay minerals and stain by Fe-oxide, the width is from 10 to 20 µm.
	8	⑤	slightly weathered			primary minerals are slightly weathered, the fractures are filled by clay minerals and carbonate, the width is less than 10 µm.
	10	⑥	unweathered			primary minerals are well preserved, fractures are rare, with a width less than 10 µm.
BK2/05	0	①	highly weathered			primary minerals are moderately weathered and transformed into clay minerals; fractures are mainly filled by carbonate, the width is larger than 90 µm.
	0.5	②	slightly weathered			primary minerals are slightly weathered; fractures are very rare.
	1	③	moderately weathered			primary minerals are moderately weathered and transformed to clay minerals; tiny fractures with width less than 10 µm are common.
	1.5	④	unweathered			primary minerals are well preserved and fractures are not found
	2					

Fig. 4-6b. Microscale visual characteristics of TB8 and BK2/05 drill cores. Legend for lithological logs see Fig. 4-4.

TB8: The top 0.5 m of the tonalite is highly weathered, primary grain shapes cannot be recognized, and fractures are mainly void with a width of approximately 30 µm. From 0.5 to 4.5 m, the drill core is moderately weathered at the macro- to mesoscale. Under the microscope, the primary minerals are intermediately weathered, the primary grain shape is recognizable, and the width of the fractures is approximately 30 µm. From 4.5 to 7.1 m, the weathering degree increases again to completely weathered, the feldspar is nearly all weathered, and the fractures are void or filled by clay minerals with a width of 10 µm. From 8.2 to 10.2 m, the drill core is moderately weathered, the grain shapes are slightly distorted, and fractures have range in width from 10 to 20 µm and are mainly filled by clay minerals and stained by Fe-oxide. The minerals within the slightly

---

weathered part of the tonalite are only incipiently weathered, the fracture width is less than 10  $\mu\text{m}$ , and both are filled by clay minerals and carbonate. The fresh part consists exclusively of primary minerals, and fractures are absent (Fig. 4-6b).

BK2/05: The top 0.2 m of the granite is highly weathered. Approximately half of the primary minerals, such as feldspar and biotite, are altered to secondary minerals; however, the grain shapes are well-preserved. Within the mineral grains, the fractures are mainly filled by carbonates with a small number of void fractures. The part from 0.2 m to 0.8 m is slightly weathered, fractures are very rare, and feldspar is only slightly altered with a perfect grain shape. In the moderate section from 0.8 to 1 m, feldspar is intermediately weathered, and fractures are tiny and frequent but have widths less than 10  $\mu\text{m}$  and are filled mainly by clay minerals. From 1 m downward, the granite is unweathered, as confirmed by the presence of fresh feldspar, biotite and quartz (Fig. 4-6b).

#### **4.5.3. Mineralogical characteristics**

The proportions of minerals from XRD analysis are presented in Fig. 4-7 and documented in Appendix IV-I. The primary mineral types are determined by the mineral composition of the fresh parent rock and included quartz, plagioclase, K-feldspar, biotite, pyroxene and hornblende, while the secondary minerals are those occurring only in the weathering zone and consist mainly of mixed layers of illite, smectite, calcite and dolomite. The proportion of primary minerals shows vertical variations and reaches 100% at the bottom of the drill core except, for the basaltic andesite in GA1 and the granodiorite in GA2. In the top part of the weathering profiles, secondary minerals reach proportions up to 100% for the basaltic andesite, ca. 60% for the tonalite, 40% for the gabbroic diorite, and 20% for the granodiorite and granite. The gabbroic diorite and the granite show rapid declines, and their weathering horizons are less than 1 m deep. In contrast, the granodiorite and tonalite have weathering profiles deeper than 10 m. The weathering zone of basaltic andesite reaches 5.4 m. The most dominant secondary mineral is illite/smectite. In the weakly weathered granite, only illite/mica is observed. Dolomite and calcite occur in all drill cores as fracture-filling minerals. Anatase is detected by XRD mainly in basaltic andesite and

granodiorite in the GA1 and GA2 drill cores, with average contents of approximately 1% and 0.65%, respectively. Hematite could be identified from XRD along all drill cores except in the granite in BK2/05. The average hematite contents are approximately 2.5% in the basaltic andesite and less than 1% in the other drill cores.

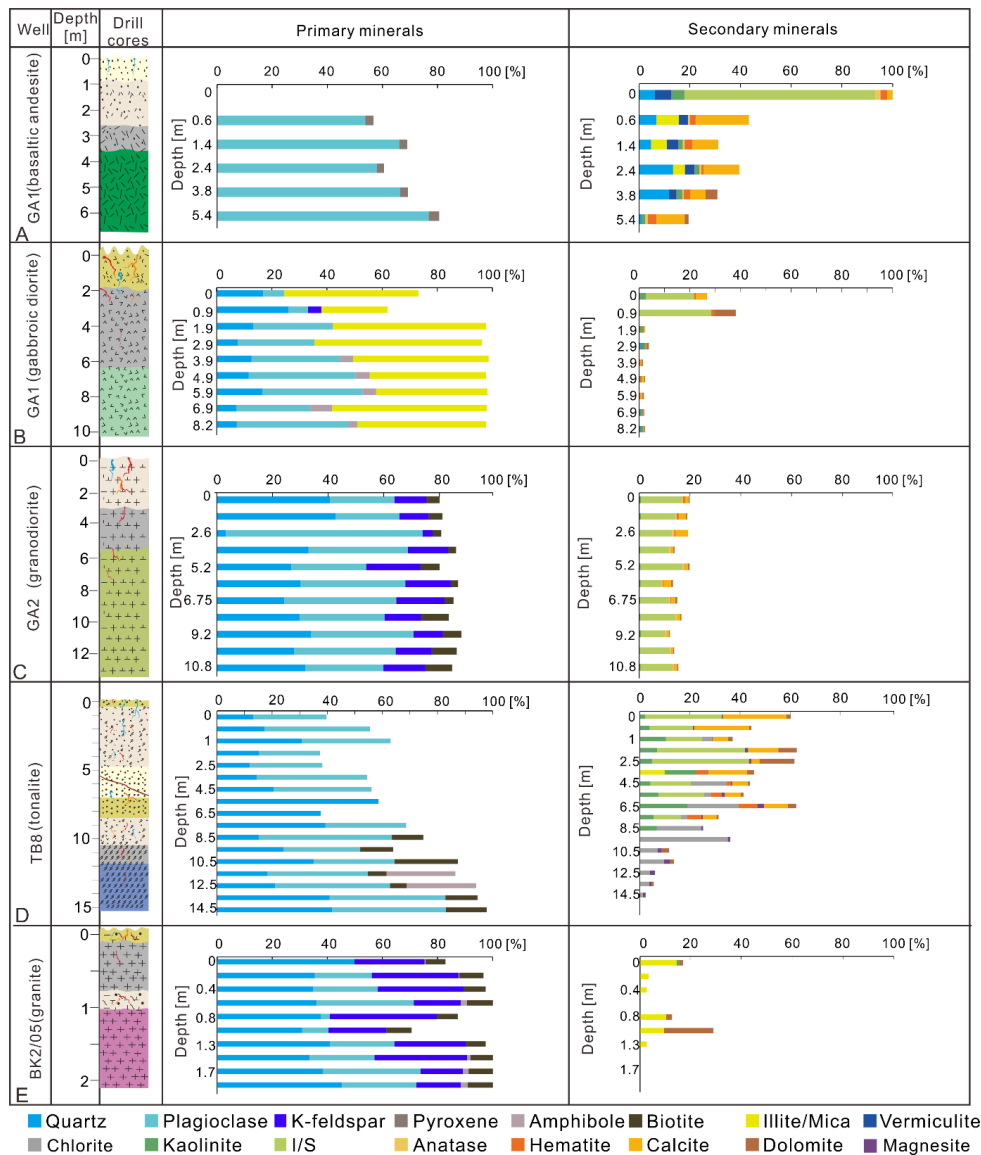


Fig. 4-7. Primary and secondary mineral characteristics of the drill cores according to XRD powder measurements. Legend for lithological logs see Fig. 4-4.

#### 4.5.4. Geochemical weathering characteristics

Along with mineralogical data, geochemical data are also provided in Appendix IV-I (Table S3). The enrichment or depletion of major and trace elements during weathering and burial diagenesis was quantified using the  $\tau$  value (Nesbitt, 1979).



### REE characteristics

The rare earth elements were divided into three groups: light rare earth elements (LREEs: La-Nd), middle rare earth elements (MREEs: Sm-Dy) and heavy rare earth elements (HREEs: Ho-Lu) (Johannesson and Lyons, 1995; Santos et al., 2019). The REE results are shown as chondrite-normalized patterns (Taylor and McLennan, 1985)(Fig. 4-8).

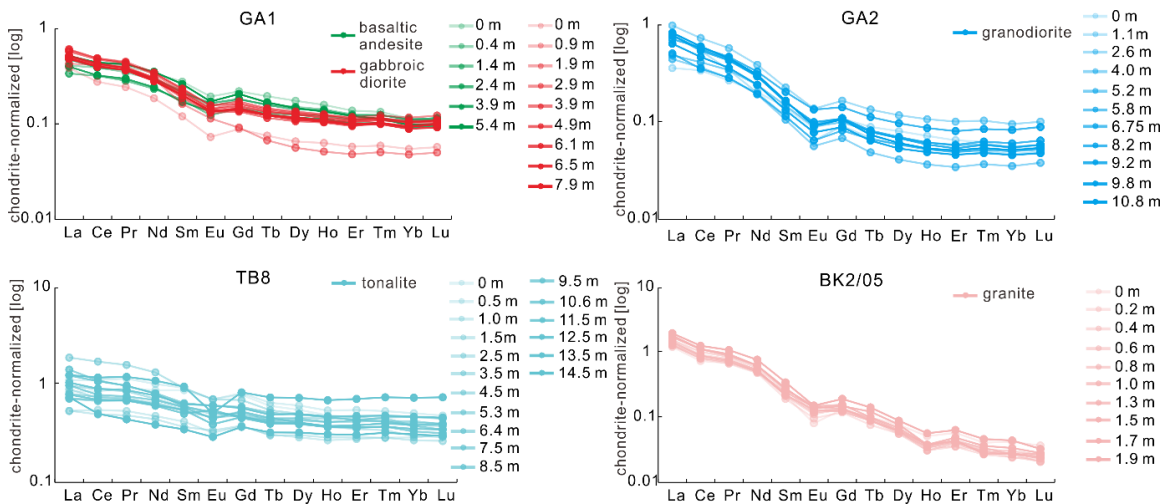


Fig. 4-8. Chondrite-normalized REE patterns.

The REE patterns of the basaltic andesite and gabbroic diorite in GA1, the granodiorite in GA2 and the granite in BK2/05 are invariant at different depths without a clear trend of enrichment and/or depletion. The element abundance decreases from LREE and MREE to HREE, showing a clear right-dipping REE trend. The steepness of this right-dipping trend is linked to the acidity of the rock and is most pronounced for felsic rocks such as granite and granodiorite. The tonalite in TB8 shows the flattest REE pattern.

### Quantification of element transfer by weathering

The depletion or enrichment of elements during the alteration process is quantified here by the method proposed by Nesbitt (1979), which is also known as the  $\tau$  value model:

$$\tau_X = (X_S/I_S)/(X_P/I_P) - 1 \quad (4-5)$$

where X refers to any elements in the sample (S) we need to quantify, I refers to the immobile elements, and P represents the fresh protolith. When  $\tau_X > 0$ , element X is enriched during

alteration; when  $\tau_x = 0$ , element X is immobile; when  $-1 < \tau_x < 0$ , element X is depleted; and when  $\tau_x = -1$ , element X is completely depleted. Commonly, Zr and Ti are selected as immobile reference elements in pedogenic studies. In the present case, Ti was adopted, and the results are shown in Fig. 4-9.

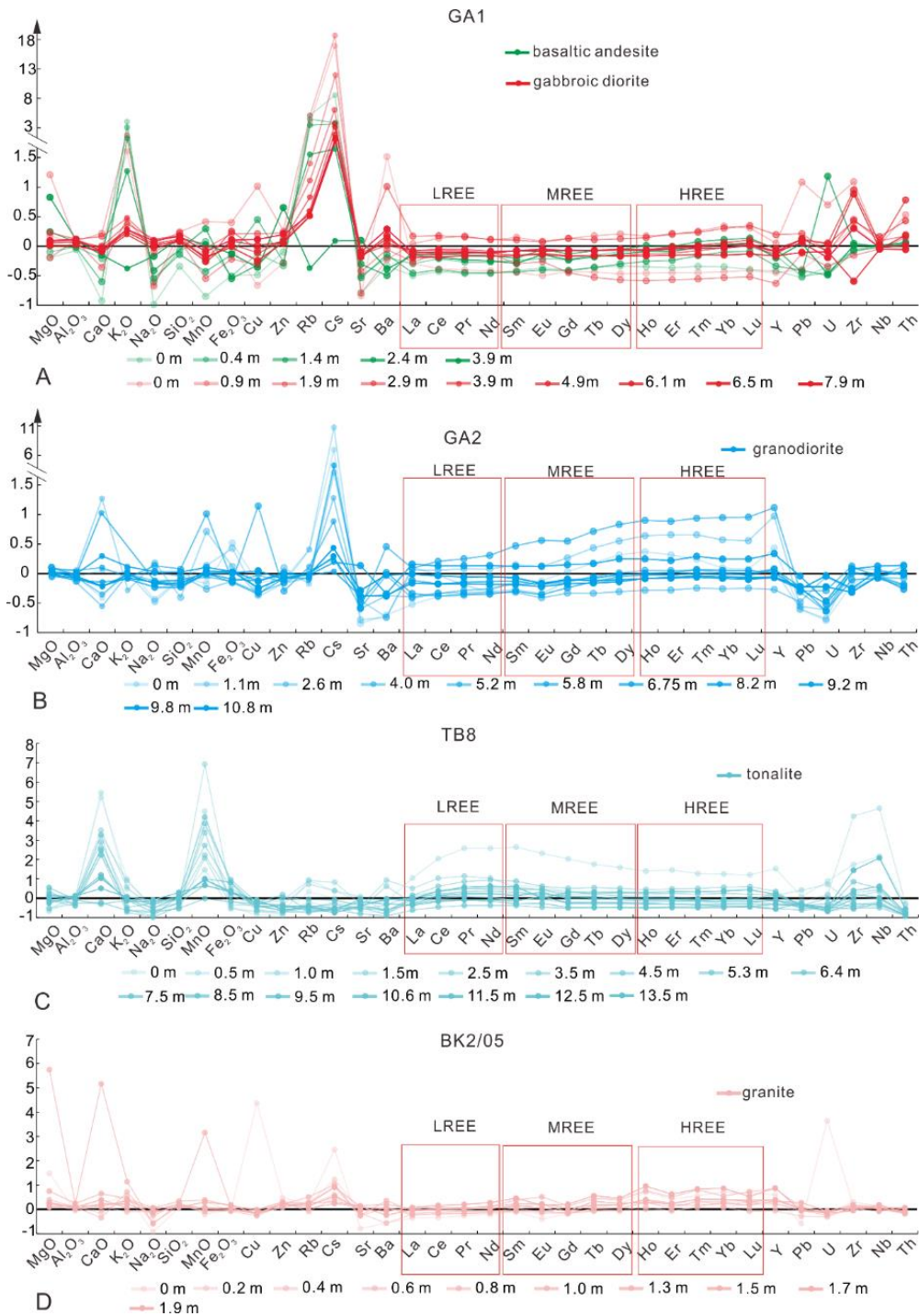


Fig. 4-9.  $\tau$  values according to Nesbitt (1979) of the weathering profiles GA1 (A), GA2 (B), TB8(C) and BK2/05(D)

---

The basaltic andesite in GA1 shows depletions in Na, Ca, Sr and Ba and strong enrichments in Cs, Rb, and K. The latter can be assigned to K metasomatism (Liang et al., 2021). The elemental patterns of Mg, Mn, Cu, Zn are scattered, and that of Al appears unchanged. The depletion degrees of Na, Ca, Sr and Ba decrease from top to bottom, while those of Cs, Rb and K increase. REEs tend to be depleted in the weathering zone, and the depletion degree decreases from LREEs and MREEs to HREEs. Pb and U are also depleted, probably due to an oxidized environment where they entered a soluble state ( $\text{Pb}^{6+}$  and  $\text{U}^{4+}$ ) (Prazeres et al., 2018; Richardson and King, 2018). Y, Zr, Nb and Th are nearly immobile. The basement part of GA1 shows slight depletions in Ca, Na, Mn, and Sr, and, again, strong enrichments in Cs and Rb, with a less pronounced K enrichment. The depletion degree of Na gradually decreases from bottom to top, that of Ca decreases from bottom to the mid-upper part, and the  $\tau_{\text{Ca}}$  values indicate Ca enrichment in the top part. Compared to the overlying basaltic andesite, the enrichment of K and Rb is relatively low, but that of Cs is higher. The REE pattern of the gabbroic diorite shows a stronger diverging trend from LREE and MREE to HREE at depths of 0 m, 0.9 m, 1.9 m and 2.9 m; this trend is interpreted to have been caused by physical fracturing and heterogeneous chemical alteration (Liang et al., 2021). U and Pb are enriched in the top part, and this might have been caused by element transfer from the overlying basaltic andesite. The  $\tau$  values of Zr and Th are relatively dispersed, probably due to the heterogeneous distribution of their carrier mineral zircon.

In the GA2 drill core, Na, Sr and Ba are all depleted in the weathering zone. Ca is scattered and is clearly enriched at 2.6 m and 5.8 m due to carbonate impregnation, as seen in the thin sections. The enrichment of K and Rb is limited, but, again, that of Cs is very pronounced, with a  $\tau$  value of approximately 11. REEs again show a diverging trend from LREE and MREE to HREE, and HREEs are enriched in the weathering zone. The elements of Y, Pb and U are significantly depleted, which again can be explained by oxidation. Zr, Nb and Th show relatively constant  $\tau$  values of approximately 0.

The tonalite of TB8 shows strong enrichment in Ca and Mn increasing from bottom to top; this trend is associated with the increase in carbonates in the thin sections. K, Rb, Cs and Ba are also

---

enriched in the top part. Na, Cu, and Sr are depleted but show overall increasing trends from bottom to top. Other elements show only slight shifts. The REE pattern of the weathered tonalite shows a different trend than the other lithologies. LREEs are relatively enriched compared to MREEs and HREEs. Pb and U tend to be depleted, while the  $\tau$  values of Zr and Nb are scattered. The Zr and Nb enrichment within the weathering profile may be explained by the heterogeneity of the accessory-mineral spatial distribution (Kempe et al., 2015). Th also shows a depletion tendency, but this trend is less pronounced.

The top part of the granite in BK2/05 shows partly strong enrichments in Mg, Ca, K, Mn, Cu, Rb, and Cs. This can be assigned to carbonate impregnation and clay formation, as supported by the thin section observations. Na is the only major element that is depleted in the weathered zone, indicating plagioclase dissolution. The overall Sr and Ba trends indicate depletion, and the elements within several samples are enriched, which may have been caused by heterogeneous alteration. The REE pattern of the granite is similar to that of the granodiorite in GA1. Pb and U are scattered, with the latter showing strong enrichment in the uppermost section of the weathering profile, most likely due to oxidation.

#### **4.5.5. Weathering characteristics at the post-Variscan nonconformity**

Based on the method proposed by Liang et al., (2022)(see also Appendix IV-II), the intensities of both physical and chemical weathering undergone by the different rock types are analyzed. In both cases, corrections are needed to account for effects caused by processes other than weathering. This includes (i) a correction of the microfracture area in thin sections with respect to tectonic fracturing and the calculation of  $IPW_N$ , (ii) a correction of chemical data with respect to burial diagenesis and the calculation of  $CIA_N$ , and (iii) a correction for secondary minerals by using the A–CN–K diagram.

##### *Physical weathering quantification and normalization*

The results of the microscale assessment of the physical weathering index are displayed in Fig. 4-10, and details are documented in Appendix IV-I, Table A1.

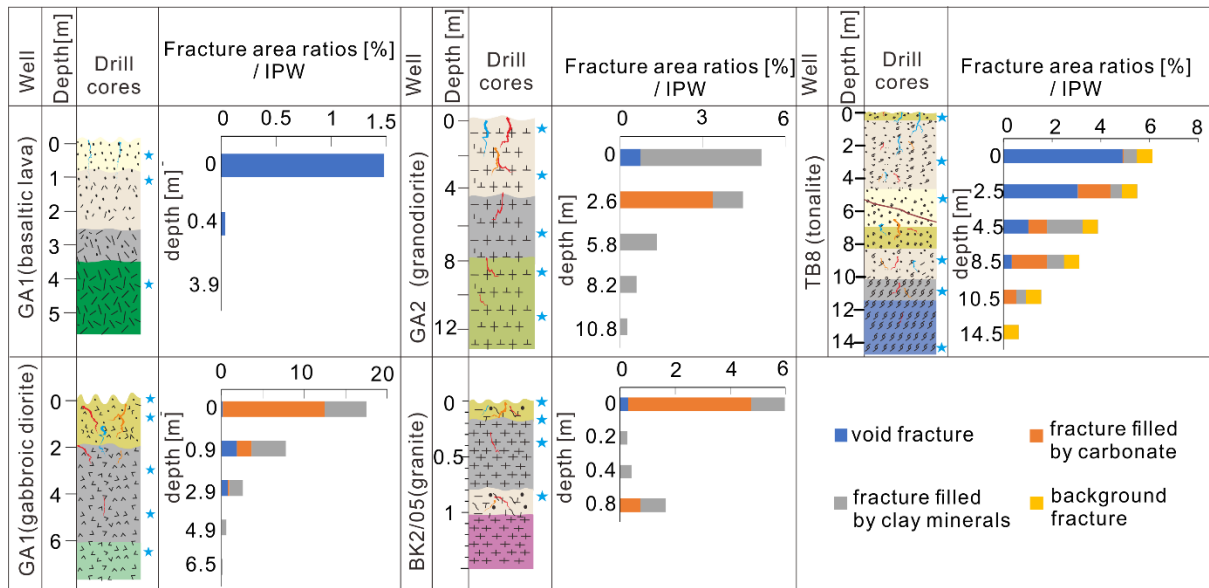


Fig. 4-10. Assessment of the index of physical weathering IPW from microfractures in thin sections for the drill cores according to the method of Liang et al., (2022). The fracture area ratio corresponds to the IPW before normalization.

The basaltic andesite part in GA1 shows only one void fracture. Therefore, the fracture area ratio strongly decreases from 0 m to 0.4 m and gradually decreases further to 0. In the underlying gabbroic diorite, the fracture area ratio decreases gradually from top to bottom from 18.6 to 0. Here, fractures are mostly filled by carbonates and clay minerals. The granodiorite in GA2 also shows a gradual decrease in the fracture area ratio down to a depth of approximately 10 m. Again, void fractures are rare, and most fractures are filled with clay or carbonates. TB8 also shows fractures at a depth of 14.5 m; these are interpreted as tectonic fractures and are shown in yellow as “background fractures” in Fig. 10. This finding is supported by the varying meso-/macroscale weathering degree along the core with a completely weathered interval at depths between 5 and 7 m. The fracture area ratio in the granite of BK2/05 is developed within a relatively small scale not deeper than 0.8 m and rapidly decreases. Due to heterogeneous fracturing, a higher value is again observed at a depth of 0.8 m before fractures become absent.

Fig. 4-11 presents the normalized  $IPW_N$  for the basaltic andesite in GA1, the granodiorite in GA2 and the granite in BK2/05; i.e., the IPW is normalized to the rock strength. This means that the values can be directly compared among different rock types. However, the UCS is not available for

gabbroic diorite or tonalite; i.e., these rock types could not be normalized and therefore are not shown in Fig. 4-11. The granodiorite and basaltic andesite in GA1 both show gradual  $IPW_N$  decreases from the top of the weathered zone to the bottom. The granite of BK2/05 deviates from this trend, which can be explained by the low weathering depth and the heterogeneity of the fracture distribution.

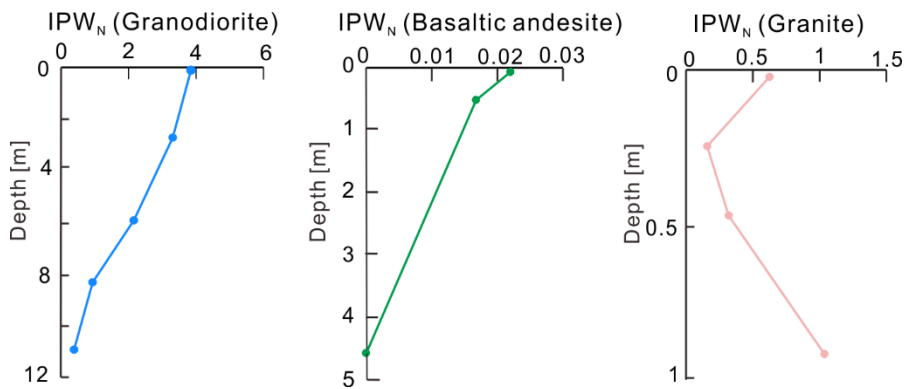


Fig. 4-11. Normalized index of physical weathering with respect to rock type and tectonic fractures.

#### *Chemical weathering quantification and normalization*

Fig. 4-12 shows the A–CN–K diagram alongside the measured data before and after the K metasomatism, Ca and K are corrected according to the procedure described in subsection 4.4.1, resulting in the  $CIA_{corr}$  results shown in Fig. 4-12B. For all drill cores, the  $CIA_{corr}$  values are higher than the original CIA values because of K-metasomatism. This tendency is more pronounced in the top part of the weathered sections because K metasomatism is more efficient in this part due to the relatively high porosity and permeability and the high contents of secondary minerals that absorb K (Jian et al., 2019).

In addition to the K correction, the A–CN–K diagram can also be applied to predict the alteration processes of minerals (Nesbitt and Young, 1989a, 1984; Zhou et al., 2017). For lithologies with limited K contents, such as basaltic andesite, gabbroic diorite and tonalite in this study, weathering trends are directed toward smectite and kaolinite, and illite is less expected (Nesbitt and Young, 1989a). According to the A–CN–K diagram (Fig. 4-12B), the weathering products of the basaltic andesite in the topmost part should be dominated by kaolinite accompanied by a

minor portion of smectite, while that in the lower part should be dominated by smectite (Liang et al., 2021). The gabbroic diorite in GA1 should be dominated by smectite and kaolinite as long as the CIA is high. However, the XRD analysis shows little kaolinite, which can be explained by the presence of remnant or transitional K-bearing clay minerals such as mixed layers of illite and smectite. This result is supported by the positive  $\tau_K$  trend.

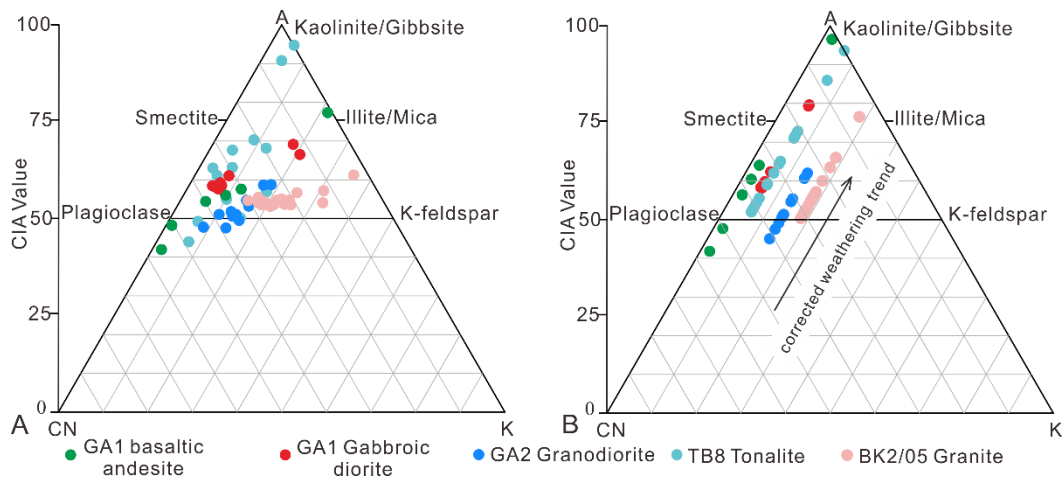


Fig. 4-12. The weathering profiles in the A-CN-K diagram before (A) and after (B) correction of Ca and K.

The tonalite in TB8 has a similar K content as the basaltic andesite and the gabbroic diorite in GA1; therefore, the initial weathering products should also be dominated by smectite and kaolinite according to the A-CN-K diagram. However, the XRD results again point to a transitional mixed layer of illite and smectite in the upper part (0-7.5 m) with a minority of kaolinite. In the lower part, K is depleted, and the XRD results show the dominance of chlorite. The transformation of smectite to chlorite takes place between 150 and 300 °C (Schmidt & Robinson, 1997; Robinson et al., 2002). This pattern at TB8 can be explained by the smectite that originated from chemical weathering being transformed to a mixed layer of illite and smectite in the upper part; due to the high content of clay minerals forming a barrier between the upper and lower parts, the lower part was not influenced by the chemical composition of the diagenetic fluid, while the temperature of the fluid promoted the transformation of smectite to chlorite (Eggleton and Banfield, 1985; Robinson et al., 2002).

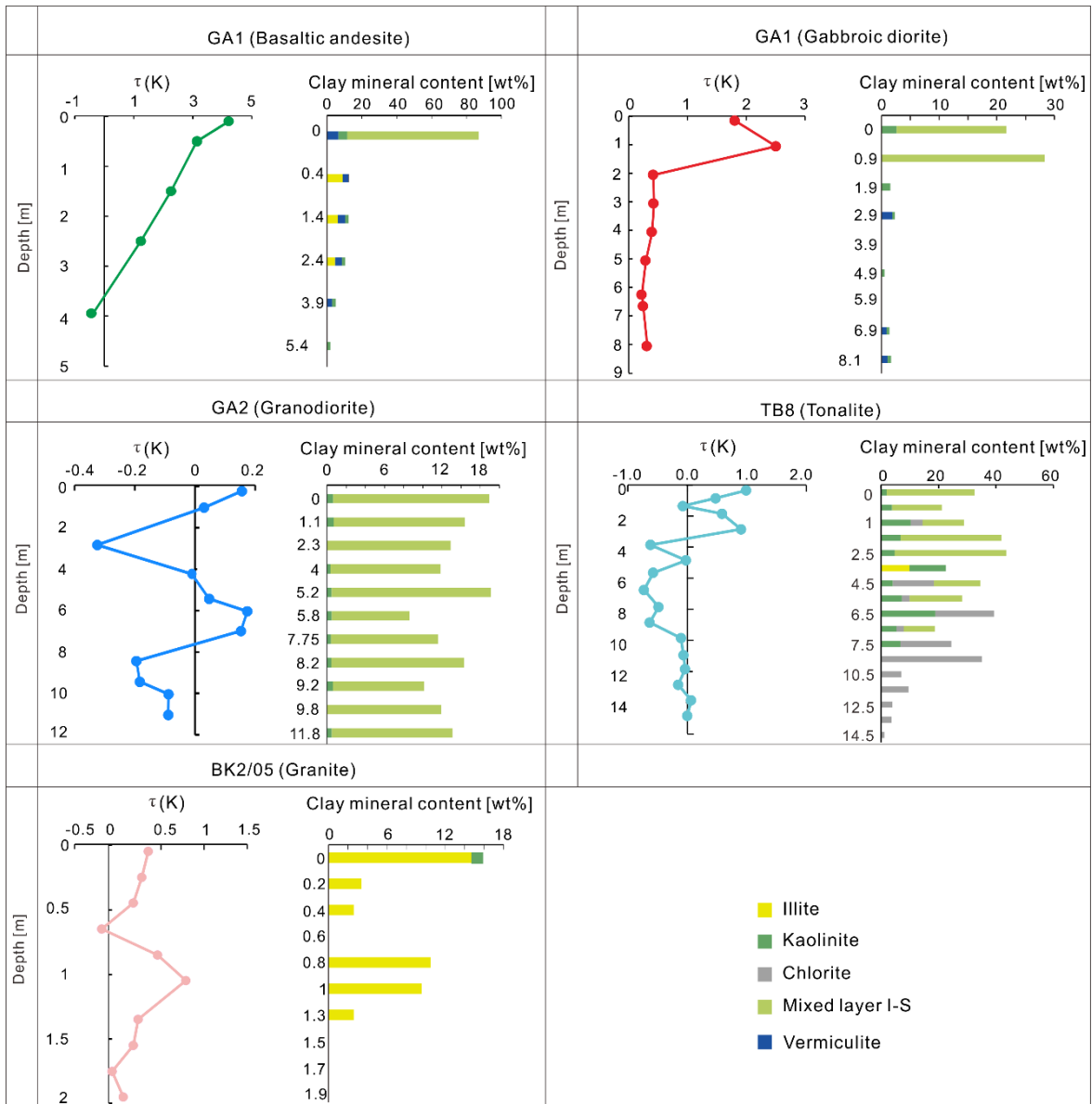


Fig. 4-13.  $\tau_K$  value and clay mineral characteristics from XRD measurements.

Compared to the basaltic andesite, the gabbroic diorite in GA1 and the tonalite in TB8, the K surpluses within the granodiorite in GA2 and the granite in BK2/05 were higher, according to the A-CN-K diagram. Theoretically, this enabled the formation of illite during chemical weathering. However, along drill core GA2, the clay minerals are also dominated by a mixed layer of illite and smectite, also indicating overprinting by K-rich diagenetic fluids. The initial weathering product along GA2 should also be mainly smectite. This indicates that the granodiorite in GA2 was weathered within a poorly drained system under arid climate conditions (Aoudjit et al., 1995; Jian et al., 2019). The same scenario can be applied to the granite in BK2/05, where illite likely



transformed from smectite during hypogene diagenesis, and the climate conditions should have also been arid. One noticeable issue is the coexistence of hematite with smectite in the weathering products of mafic to intermediate rocks. Earle (2015) summarized that under a poorly drained system, with the hydrolysis of ferromagnesian silicates such as pyroxene, amphibole and biotite, smectite was formed; meanwhile, the liberated  $\text{Fe}^{2+}$  was oxidized and converted to hematite due to the presence of oxygen.

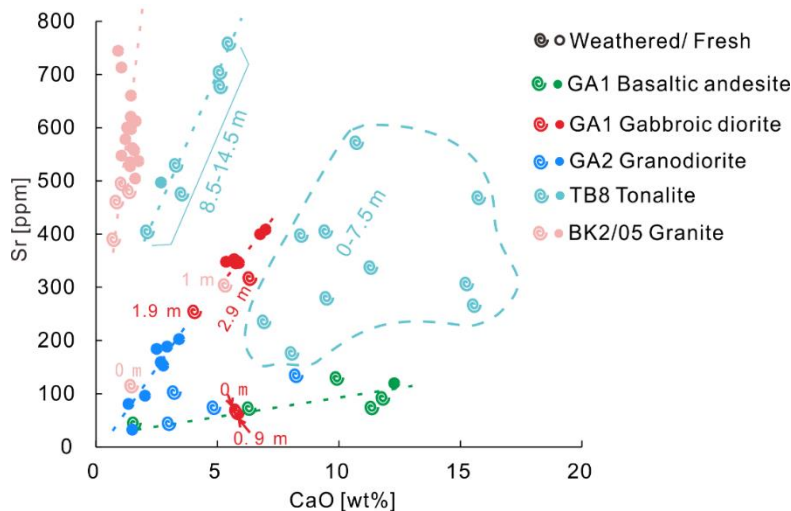


Fig. 4-14. Cross plot of Sr-CaO according to Brandstätter et al., (2018). Deviation from regression lines is interpreted as diagenetic overprint.

The Sr/CaO ratio can be applied as a parameter to distinguish among different phases of diagenetic fluid because scatter plots of fresh to altered rocks form a linear trend, the gradient of which is determined by the composition of the diagenetic fluid (Brandstätter et al., 2018). This effect is demonstrated in Fig. 4-14. In the Sr-CaO plot, the weathered rock types can be well-separated and show different trend lines with different gradients. For the basaltic andesite of GA1, the ratio between Sr and CaO in the fresh and weathered parts is nearly constant. For the gabbroic diorite of GA1, however, the samples from 0 and 0.9 m clearly deviate from the trend in the lower part, which corresponds well to the basaltic andesite. Liang et al. (2021) showed that the Ca in the basaltic andesite is original, and the topmost part of the gabbroic diorite in GA1 is overprinted by fluids from the overlying basaltic andesite. For the granodiorite in GA2, the data from the topmost weathering zone again deviate from the lower part. Along the TB8 drill core, the Sr/CaO ratio

shows two trend lines: one from 0 to 7.5 m and the other from 8.5 to 14.5 m. The Sr/CaO ratios in the upper part are scattered, and no clear trend line is developed. The lower part, however, shows a good linear trend consistent with a gradual weathering trend. The separation of these two parts can be explained by the access of diagenetic fluids in the highly fractured upper part and the barrier effect of the fractures filled with clays at a depth of approximately 8 m. In the thin weathering zone of BK 2/05, the Sr/Ca ratios from 0 m and 1 m deviate from the lower part. Again, this points to diagenetic overprinting by diagenetic fluids that could easily infiltrate along the fractures up to a 1-m depth.

Table 4-1. Difference of chemical weathering parameters for the selected lithologies according to Liang et al., (2022).

chemical weathering intensity	lithologies	CWA (1Myr)	CWA (0.1Myr)	CWA (0.01Myr)
71	granodiorite	1.51E-08	5.75E-09	2.20E-09
	tonalite	1.81E-08	6.77E-09	2.55E-09
78	gabbroic diorite	1.62E-08	6.02E-09	2.25E-09
	granite	1.68E-08	6.41E-09	2.46E-09
83	basaltic andesite	2.55E-08	9.35E-09	3.43E-09

*Normalization for different rock types*

To normalize the CIA among the rock types, the granite from BK2/05 is chosen as the reference rock ( $CIA_R$ ). The weathering rates of silicate minerals decrease with time because of kinetics. (White et al., 2001). This means that also the CWA is changing over time. Taking a time-dependent CWA and the CIA of the reference rock, the normalized  $CIA_N$  can be acquired. This process was documented by Liang et al., (2023) (see also in Appendix IV-II). Table 1 shows the CWA values on different time scales (0.01 ~ 1 Myr). As the post-Variscan nonconformity represents a diachronous time gap from tens to hundreds of million years in central Europe, a duration of one

million years was applied to normalize the chemical weathering degree. The original CIA, chemical weathering degree corrected for K and Ca ( $CIA_{corr}$ ),  $CIA_R$  normalized in reference to granite in BK2/05, and time-corrected  $CIA_N$  (1 Myr) are visualized in Fig. 4-15.

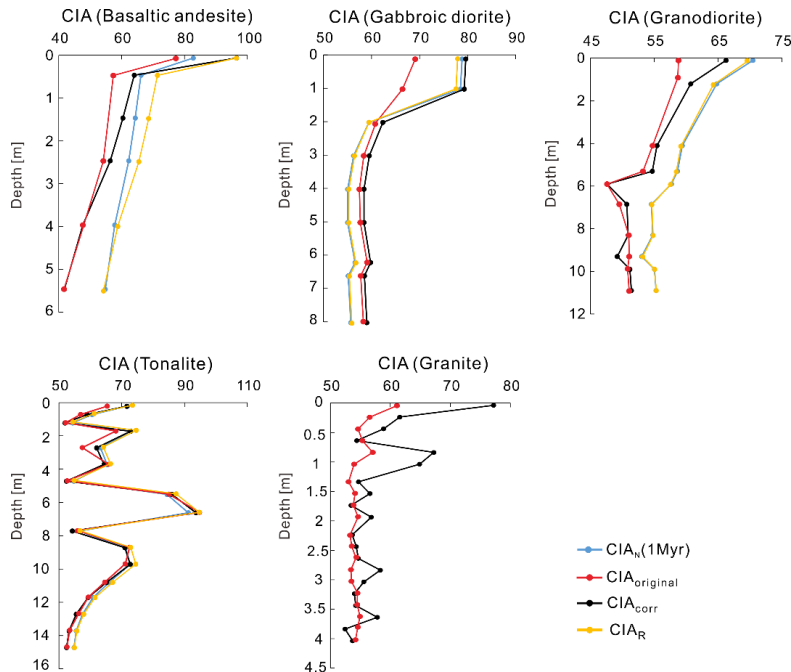


Fig.4-15. Original  $CIA_{original}$ , corrected  $CIA_{corr}$  for Ca and K, normalized  $CIA_R$  based on granite in BK2/05 and time-normalized  $CIA_N$  along the drill core profiles.

The  $CIA_{corr}$  values are all higher than the original CIA values, and the difference between these two values is due to the overprint of K and Ca. With increasing depth, these two values gradually become consistent (Nesbitt et al., 1980; Wu et al., 2021). This finding corresponds well with the trends in the A–CN–K diagram. The normalization of  $CIA_{corr}$  to the granite in BK2/05 leads to the  $CIA_R$ , meaning that the CIA values of other rocks were normalized to the same range (minimum to maximum values) as the granite in BK2/05. Therefore, for rocks with minimum  $CIA_{corr}$  values smaller than that of granite, the overall  $CIA_R$  values along the weathering profile are higher, such as for the basaltic andesite in GA1, the granodiorite in GA2 and the tonalite in TB8. In contrast, if the minimum  $CIA_{corr}$  values are higher than the  $CIA_R$  values, the overall  $CIA_R$  values are lower than the  $CIA_{corr}$  values, as in the case for the gabbroic diorite in GA1. As the maximum CIA value for all rock types is 100, the  $CIA_{corr}$  values gradually approach the  $CIA_R$  values. A relatively high CWA value indicates that the rock is more easily chemically weathered. Therefore, rocks with higher

---

CWA values than the reference rock (granite in BK2/05) result in lower  $CIA_N$  values than the  $CIA_R$ , as is the case for the basaltic andesite in GA1 and the tonalite in TB8. Otherwise, the opposite trend is observed, such as for the gabbroic diorite and granodiorite in GA1 and GA2, respectively (Liang et al., 2022).

## 4.6. Discussion

### 4.6.1. Implications for the integrative weathering degree

The weathering characteristics under similar weathering conditions depend on the texture and mineral compositions of different rock types (Górska et al., 2022). For rocks with similar textures, rock types with lower strength and more unstable minerals weather relatively easily, both physically and chemically, as is the case for gabbroic diorite and granite in this study. Although these two lithologies weathered under the same environmental conditions, the  $CIA_{corr}$  values in the weathering zone for the gabbroic diorite are much higher than those for the granite, and the value difference even reaches to approximately 18. Similar results are also acquired by, e.g., Nesbitt and Young (1984) and Jiménez-Espinosa et al. (2007). Nevertheless, to better reflect the weathering conditions among different lithologies, the common indices related to the duration of weathering are further normalized in this case.

For the physical weathering conditions, the fractures at the microscale and the rock strength (UCS) are considered. The results show that even if the weathering conditions and textures are similar, the  $IPW_{corr}$  values are higher for rocks with lower rock strengths (e.g., gabbroic diorite), which have relatively high fracture densities. If the rock strengths are similar, the  $IPW_{corr}$  value is also similar regardless of differences in mineral composition, e.g., between granodiorite and the tonalite in this case. Similar results were also reported by Ceryan et al. (2008b), Tuğrul (1997) and Ündül and Tuğrul (2016) for granitoids, basaltic rock, dunites and diorite. The fracture density and width both have a negative relationship with the rock strength.

The  $CIA_N$  values show that the rock-type-specific  $CIA_N$  value deviates most from the  $CIA_{corr}$  value of basaltic andesite, and the difference yields a value of 14 in the topmost part, although the

---

weathering environment is similar (Fig. 15). One reason for this is that the weatherable mineral composition of basaltic andesite is significantly higher (in this case, it is approximately 80%) than those of the other rocks, mainly consisting of plagioclase and pyroxene (Fig. 4-7). In addition, the aphanitic texture and amygdaloidal structure may also promote the chemical weathering process and enhance the geochemical contrast (Borrelli et al., 2012). For rocks with phaneritic textures and weatherable mineral content between 50% and 60% (mainly plagioclase, K-feldspar and biotite) (Fig. 4-6), the deviation is significantly lower (Fig. 4-15). This trend is clearly opposite to the physical weathering trend and fits well with common expectations; that is, as the climate trends towards more humid conditions, the chemical weathering process will gradually dominate, and the physical weathering process weaken.

While the normalization of both physical and chemical weathering indices depicts the weathering intensity, analysis of the correlations of weathering characteristics among macro/meso-scale, microscale, mineralogical and geochemical characteristics can provide integrative results for weathering conditions. Comparisons of these multiple indices enable cross-validations and ensure the accuracy of the final interpretation results. For example, the physical weathering degree classified at the macro/mesoscale is well-linked to the fracture area proportion observed at the microscale. Macro/mesoscale rock characteristics such as the strength, color and texture also correspond well to the variations in secondary mineral contents and the chemical weathering degree determined from analytical data (Arias et al., 2016; Jian et al., 2019).

However, visual observations at the macro/mesoscale do not precisely reflect physical weathering, especially for drill cores that are interrupted by extra structures such as tectonic fractures and faults. This is the case along drill core TB8, where the fracture density under the macro/meso-scale has an exceptional increasing trend near the fault zone. Similar results were also observed by e.g. George et al. (2001), who found much denser fracture networks near a fault zone in the field. Observations at the microscale, however, still exhibit a gradually decreasing trend from top to bottom, as long as the samples in the fault zone are taken from the matrix at least 0.1 m away from the fault. In this case, microfractures can be regarded as having formed

---

through physical weathering and not by tectonic influence. Anders et al. (2014) found similar results for granitoids; the density of microfractures was concentrated within 0.1 m of tectonic faults, and the microfracture density rapidly decreased with distance to a fault. This study confirms that the physical weathering degree can still be determined for tectonically fractured rocks if samples are taken at least 0.1 m away from fault planes.

#### **4.6.2. Disentangling weathering from hypogene diagenesis and tectonic preconditioning**

Hypogene diagenesis refers to diagenesis promoted by ascending solutions, which may result in metasomatism and/or mineralization (Dill, 2010; Dill et al., 2012). Previous studies have indicated that multistage hypogene diagenesis was overprinted in the Permian to Mesozoic platform sediments in SW Germany (e.g., Staude et al., 2011). Hypogene overprinting has also been reported from the Permo-Carboniferous nonconformity at the basis of the analyzed platform sequence (Fusswinkel et al., 2014). Using the A–CN–K diagram, metasomatism in the weathering zone and the additional input of K from diagenetic fluids can be demonstrated. Correlation plots provide further evidence for the addition of Cs and Rb. The enrichment of these elements is consistent with the neoformation of clay minerals (Nesbitt and Young, 1989a, 1989b). The transformation of smectite to chlorite requires temperatures between 150 and 300 °C (Schmidt & Robinson, 1997; Robinson et al., 2002) and can be observed in the tonalite section of TB8. Further indicators of hypogene diagenesis are provided by calcite and dolomite, which mainly fill the fractures. Calcite and especially dolomite are typical minerals that form at temperatures between 100 and 200 °C (Chang et al., 2020). In this temperature range, minerals such as quartz, chalcedony and adularia can also be formed.

Fractures formed by tectonic activity or weathering are preferential pathways for diagenetic fluids. Fractures are not present in the chemically fresh bottom part of the cores analyzed herein except in the tonalite in TB8. To assess the formation of these fractures, the fracture characteristics were further studied with SEM imaging (Fig. 4-16A). As the rim walls of the fractures are angular, traces of corrosion are fairly rare, and the clay minerals are chaotically

oriented. We interpret this as the result of the infiltration of clay particles formed in the highly weathered upper zone. This process was also described by Santos et al. (2018), who categorized fractures and recognized clay in fractures as “transported clay”, including clay infillings and clay coatings. The extinction phenomena of these clay minerals under a polarizing microscope hint at the collapse of the original weathering structures followed by clay coating in secondary pores. In the weathered parts, the rim walls of the fractured minerals are mainly dissolved, showing a roundish shape (Fig. 4-16B). Therefore, the fractures at the bottom of TB8 should have formed before the weathering process occurred, and the fractures are well-preserved by filling with clay minerals. The fractures in the fresh part of TB8 are recognized as tectonic fractures; thus, to normalize the  $IPW_{corr}$  values, fractures filled by clay minerals should be first corrected for tectonic fractures before being normalized by the corresponding rock strength. In TB8, prominent tectonic fractures could also be observed in the weathering zone. The drill cores of GA1, GA2 and BK2/05, however, did not show tectonic fractures. This may be explained by the fact that the TB8 drill site is located near a fault, representing a relatively unstable tectonic environment (Greiling and Verma, 2001)

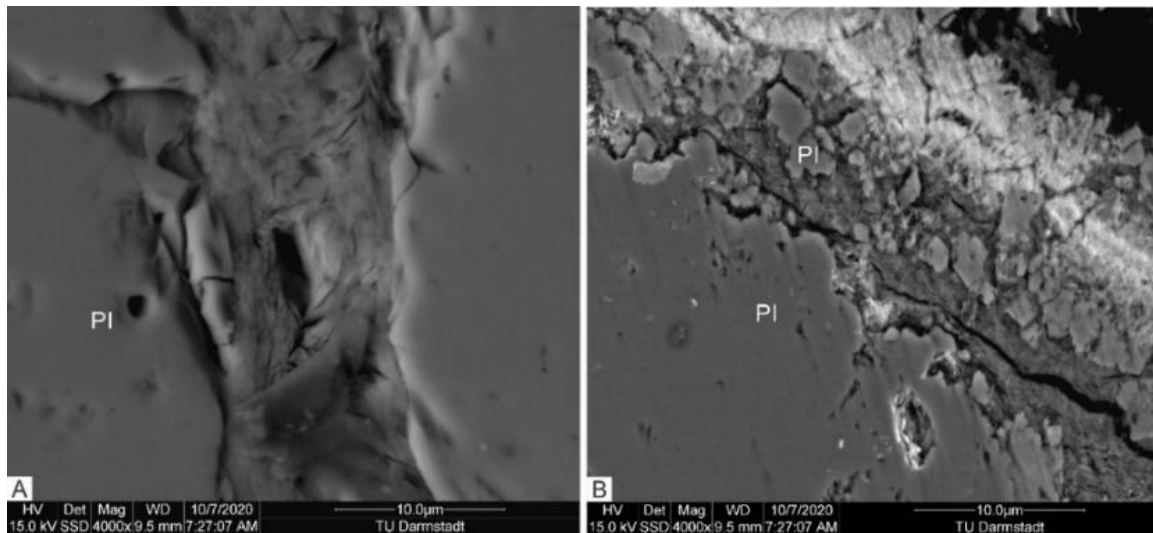


Fig. 4-16. (A) Angular rim of the fracture filled by clay minerals (TB8, z=14.5 m, SEM). (B) dissolved rim of the fracture filled by clay minerals (TB8, z=6.4 m, SEM), the abbreviations used in the figure and caption are as follows: z – depth, PI – plagioclase.

---

### 4.6.3. Multiscale weathering characteristics

Fig. 4-17 summarizes the depth trends of the weathering indices used in this study. The variation in LREE/HREE is also incorporated in Fig. 4-17. This is because the LREE/HREE ratio is commonly employed as another weathering index and compared to the CIA variations (Santos et al., 2019). Our qualitative assessment of the fracture density shows consistent trends at both the macroscale and mesoscale as well as for the microscale; however, microfractures can be observed at greater depths than fractures at other scales. This is most evident for the gabbroic diorite and the granodiorite. Similar observations were reported by Jian et al. (2019), who illustrated the paleoweathering characteristics of granodioritic basement in the Qaidam Basin. They observed microfractures under a polarizing microscope in the slightly weathered to fresh part of the basement, which was devoid of macro/mesoscale fractures.

Fig. 4-17 further shows the presence of clay minerals and carbonates. Generally, the clay mineral abundance is correlated with the chemical weathering indices, whereas the proportion of calcite is concordant with the physical weathering indices. This is caused by the filling of fractures by calcite, which is largely absent in the matrix except in the basaltic andesite. In contrast, clay minerals mostly reflect the alteration of feldspars, and neoformation is less dominant (Nesbitt et al., 1980). Previous studies indicate that the ratio between LREE and HREE may have a positive relationship with the chemical weathering degree, as LREEs can be absorbed especially by illite and Fe-oxide (e.g., Santos et al., 2019). However, in our case, the LREE/HREE ratio does not show a clear trend or is even inverse to the amount of clay minerals and the CIA. An explanation could be that the original weathering products were dominated by smectite that formed within an arid, poorly drained environment (Santos et al., 2022b; Jian et al., 2019; Santos et al., 2017); i.e., the behavior of REEs was dominated by the leaching process, and the LREEs were dissolved by acidic meteoric water, whereas the HREEs remained immobile (H. Wayne Nesbitt, 1979; Yang et al., 2019). This conclusion also supported by the  $\tau$  values of the REEs, which mostly indicate the depletion of the LREEs (Fig. 4-8).



---

The depth of physical and chemical weathering shows high variability from approximately 1 to 15 m for different rock types. For basaltic andesite, the chemical weathering depth is deeper than the physical weathering depth. By analyzing the weathering process of basalt, Nguetnkam et al., (2020) proposed that the aphanitic-amygdaloid texture is favorable for enhancing chemical alteration. For lithologies with phaneritic textures, physical weathering occurs more deeply than chemical weathering, as seen for the gabbroic diorite in GA1 and the granodiorite in GA2. Jian et al., (2019) observed similar characteristics in a granodiorite under arid climate conditions. In contrast, Braga et al. (2002) studied the weathering process of granitic rock under a relatively humid climate and found that physical weathering occurred less deeply than chemical weathering. This indicates that the physical and chemical weathering depths of phaneritic-textured rocks mostly rely on climate conditions. In our study, the phaneritic tonalite in TB8 and the granite in BK2/05 showed the opposite trend; physical weathering reached deeper than chemical weathering. This can be explained by tectonic faulting. Hayes et al., (2020) analyzed the factors controlling weathering fronts and found that tectonic faulting and decompression fracturing enable chemical weathering to prograde more deeply but still lag behind physical fracturing.

The  $IPW_{corr}$  values along all drill cores show a more abrupt decreasing trend between the topmost and the lower part compared to the  $IPW_N$  trend. Chiu and Ng (2014) studied the relationship between the chemical weathering degree and rock strength and proposed that the rock strength decreased drastically with increasing chemical weathering, especially under high grades of chemical weathering. Therefore, the incongruity between the topmost and the lower parts can be explained by the mutually reinforcing effect of physical and chemical weathering: a higher chemical weathering degree indicates a lower rock strength, as was considered here by normalization. After normalization, the  $IPW_N$  eliminates the effect of chemical weathering and normalizes the physical weathering degree among different lithologies. Consequently, the  $IPW_N$  trend shows a gradual decrease from top to bottom.

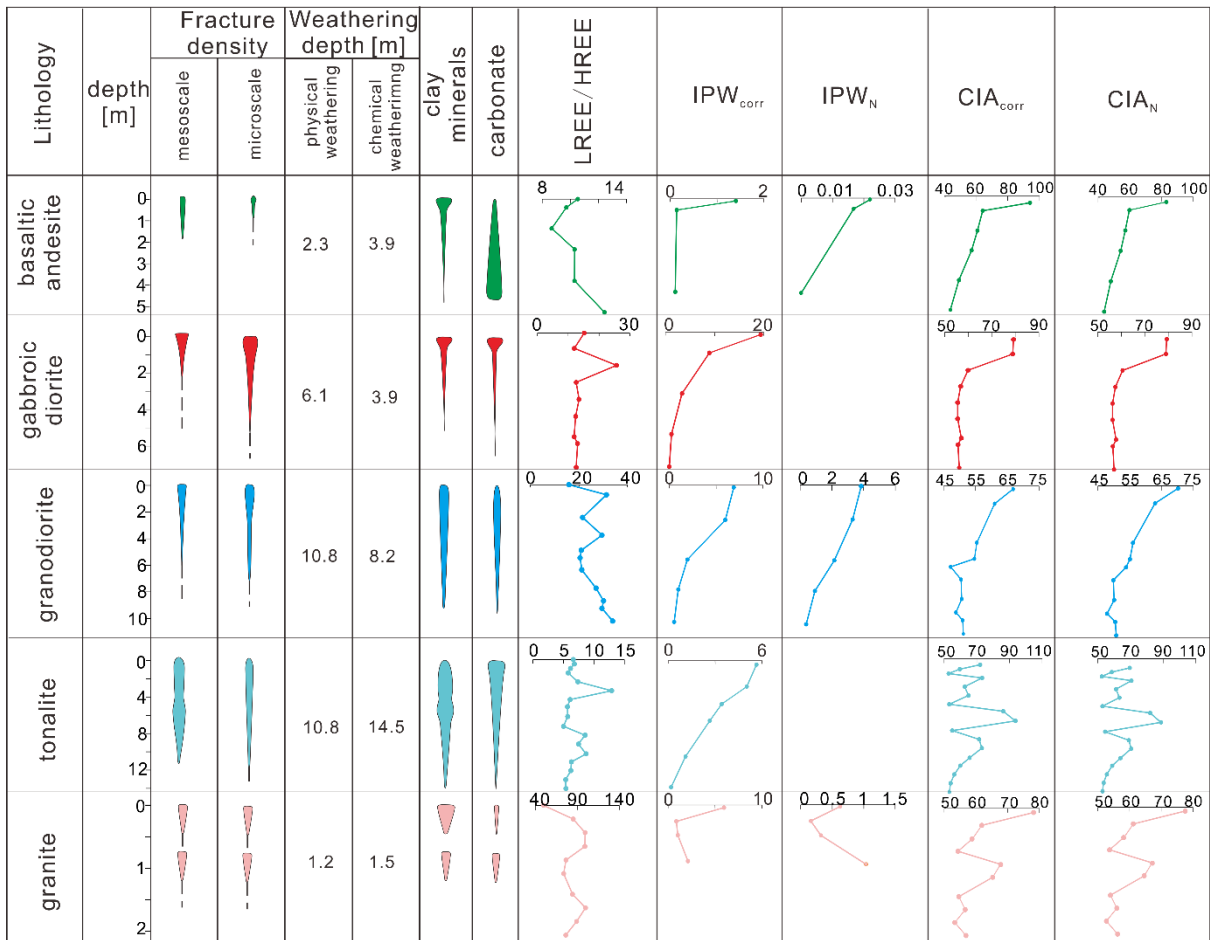


Fig. 4-17. Comprehensive weathering characteristics along the drill core profiles.

The CIA<sub>corr</sub> trend is similar to that of the normalized CIA<sub>N</sub>. For lithologies composed of higher weatherable mineral contents, such as basaltic andesite, the difference is more evident. Both values correspond well to the absolute physical weathering degree IPW<sub>corr</sub> except that of tonalite, which was influenced by tectonic faulting under conditions where physical and chemical weathering processes promote each other.

In summary, our integrated approach provides deeper insight into paleoweathering dynamics. Visual characteristic analysis (macro/mesoscale and microscale) provides a qualitative assessment of the weathering intensity, whereas mineralogical and chemical characteristic analyses allow for quantifications and uncover subtle changes in rock composition, such as element depletions or enrichments and mineral transformations ( Nesbitt, 1979; Tripathi and

---

Rajamani, 1999). The combination of these characteristic analyses not only provides an integrated weathering status but also helps eliminate the effects of nonweathering processes.

Weathering profiles along nonconformities are also an important topic for reservoir geology. Nonconformities are first- or second-order elements in stratigraphy and commonly form the bases of sedimentary basins. On the one hand, weathering characteristics increase the permeability of basinal fluids; on the other hand, the gradual disappearance of these features leads to hydraulic barriers (e.g., Gardner, 1940; Walter et al., 2018). Hence, the thickness of the weathered zone and the mode of weathering process play an important role. This study contributes to additional constraints about the roles of different lithologies controlling both.

#### **4.6.4. Implications of the reconstructed weathering degree for the Permian land surface**

As the  $IPW_N$  and  $CIA_N$  results obtained in this study were normalized based on the susceptibility of the rock types to weathering, the integrated information of both these terms can be taken to reconstruct paleoclimate conditions at the post-Variscan nonconformity. During the early Permian, an arid to semiarid climate with some humid intervals was reconstructed (Roscher & Schneider, 2016). The age of the rock surfaces can be estimated by obtaining the age of the overlying sediments and volcanic rocks. In the Sprendlinger Horst, the oldest sediment record is the Moret Formation, which overlies the GA2 and TB8 basements. Above the Moret Formation is the Lower Langen Formation, which contains the basaltic andesite found in GA1, for which an age of approximately  $290 \pm 6$  Ma can be assigned from similar volcanic rocks in the surrounding area (Lippolt and Hess, 1983). The Rotliegend sediments in BK2/05 are between 290 and 280 Ma (Edgar and Hubert, 2009). According to this information, the age of the weathering surfaces can be divided into four phases from old to young: the granodiorite and tonalite in GA2 and TB8 are ca. 300 Ma, the gabbroic diorite in GA1 is ca. 295 Ma, and the basaltic andesite in GA1 is ca. 290 Ma, while the granite in BK2/05 may be younger. Based on the climate curve of Roscher & Schneider (2016), the first-phase weathering period occurred under arid climate conditions; for

---

the second phase, the climate gradually changed to humid, and for the third phase, the climate was humid. After 290 Ma, aridization took over again.

The relationship between the physical (here expressed as  $IPW_N$ ) and chemical weathering intensities (here expressed as  $CIA_N$ ) can well reflect the climate conditions (Dill et al., 2014; Ruddiman, 2008). Under an arid environment, physical weathering dominates which should be reflected by a high  $IPW_N$  value and a low  $CIA_N$  value. Increasing humidity should be mirrored by a decreasing  $IPW_N$  value and increasing  $CIA_N$  value. This can also be verified by the secondary mineral characteristics within the weathering profiles of the granodiorite and granite in GA2 and BK2/05, respectively. The presence of smectite, as a 2:1 clay mineral, indicates a semiarid climate, while kaolinite, as a 1:1 clay mineral indicates strong leaching under a humid climate (dos Santos et al., 2022b, 2022a; Raucsik and Varga, 2008). The latter is the case for the topmost basaltic andesite section analyzed herein (Fig. 4-12B).

Comparing the hypothetical climate from the curve of Roscher and Schneider (2006), the general climate trend is tentatively confirmed by the ratio of  $IPW_N$  to  $CIA_N$ . The weathering surface of the first phase at approximately 300 Ma at GA2 and TB8 yields a  $CIA_N$  value of approximately 71 and an  $IPW_N$  value of approximately 4, indicating intensive physical weathering and thus arid conditions. This is supported by the presence of smectite as the primary weathering product (Aoudjit et al., 1995; dos Santos et al., 2022b). During deglaciation cycle III (DGC III, between 299 and 295.5 Ma), relatively humid conditions were promoted (Roscher and Schneider, 2006). Phase 2 at approximately 295 Ma in GA1 shows an increased  $CIA_N$  value of approximately 79 accompanied by an  $IPW_N$  value of 0.63. This indicates semiarid conditions fitting to the trend curve of Roscher and Schneider (2006). The weathering surface of the basaltic andesite shows maximum  $IPW_N$  and  $CIA_N$  values of 0.02 and 83, respectively, indicating a rather humid climate at approximately 290 Ma. This is in line with the dominance of kaolinite in the topmost part according to the A–CN–K diagram (Fig. 12B). In particular, this humid phase can be attributed to the early upper Rotliegend I wet phase (291 to 287 Ma during DGC IV of the Permo-Carboniferous glaciation (Fielding et al. 2007). For the weathering surface of BK2/05, the  $IPW_N$  and  $CIA_N$  values

---

are 0.6 and 77, respectively, again indicating relatively arid conditions. The weathering products in the topmost part are dominated by smectite with a minor kaolinite presence. The results are similar to those obtained for the gabbroic diorite in GA1, which also indicate a semiarid climate. The drying trend may be linked to the end of the DGC IV phase (291 to 287 Ma) and the Pietermaritzburg Transgression (PM-T, between 283.5 to 281 Ma).

#### **4.7. Conclusion**

In this paper, we aimed to evaluate the paleoweathering of different basement rocks at a first-order nonconformity. As a case study, the post-Variscan unconformity in the center of the late Paleozoic Variscan orogen in Central Europe was chosen. The basement surface was exposed under arid to subhumid climate conditions during the late Carboniferous and early Permian over 30 to 40 Ma and is now covered by alluvial Rotliegend sediments and, in one case, by a time-equivalent lava flow. All weathering sections were studied in drill cores with a minimum depth of 20 m, minimizing the modern weathering effect.

We used a new approach by accounting for different scales and integrating physical and chemical weathering. First, the weathering characteristics of the cores were described at the macro/microscale following existing classification schemes. Second, samples were taken for microscopic analysis of thin sections to quantify the physical weathering from the fracture area. Third, these samples were prepared for mineralogical and geochemical analysis using XRD, XRF, and ICP-MS to quantify chemical weathering. For physical weathering, a new index based on the fracture area in the thin section was applied; this index included a correction for tectonic fracturing. For chemical weathering, a modified CIA was used, which was corrected for diagenetic/hypogene overprinting, rock type, and time of exposure.

The maximum chemical weathering intensity was found at the top surface of the basaltic andesite with a  $CIA_N$  value of 83, whereas the physical weathering intensity  $IPW_N$  was less than 0.1. The gabbroic diorite and granite had  $CIA_N$  values of 78, whereas the physical weathering intensity was approximately 0.6. The lowest chemical weathering intensity was observed at the top of the

---

granodiorite and tonalite at 71, both showing the highest physical weathering intensity of approximately 4. Because of the normalization procedure, the differences in the ratio of chemical versus physical weathering are not rock-specific but can be directly linked to aridity-humidity changes in the lower Permian paleoclimate. The concept and results of this work can be used for studies on continental paleoclimate as well as for reservoir modeling.

#### **4.8. Acknowledgement**

The authors would like to thank Dr. Rainer Petschick for XRD analysis at the University of Frankfurt. Dr. Sonja Wedmann and Mr. Bruno Behr from the Senckenberg Research Station of Grube Messel gave access to the drill cores GA1, GA2, and TB8. BK2/05 was sampled in the core store of the Hessisches Landesamt für Natur, Umwelt und Naturschutz (HLNUG) at Wiesbaden. Reimund Rosmann gave manifold technical assistance.

**Funding:** This work was supported by the China Scholarship Council [grant numbers 201806400006]; Natural Science Foundation of Xinjiang Uygur Autonomous Region [grant number 2022D01F59]; the University Scientific Research Program of Xinjiang Uygur Autonomous Region Education Department [grant number XJEDU2019Y070].

---

## 5. Conclusion

---

In this section, the contribution of this thesis to the research of the weathering characteristics for both the modern and paleo-weathering profiles is summarized. In addition, the key weathering characteristics within the post-Variscan nonconformity in SW German are presented and discussed.

An integrated method is developed and validated by four representative drill cores. These case studies were concerned with the investigations of the distinguishing of hypogene and supergene alteration, mineral transformation, diagenetic environment accessing, and the difference of weathering characteristics among different lithologies in order to quantitatively compare them.

### 5.1. Contribution to the research about weathering

Aimed at the paleo-weathering profile, the methods for distinguishing supergene and hypogene alteration, and the elimination of the effect of hypogene overprint on supergene alteration were published by Liang et al. (2021) (the first publication). The alteration between the supergene and the hypogene process was distinguished according to comprehensive results. The results consider the mineral shapes under SEM, the weathering trend within the A-CN-K diagram, and the  $\tau$  values of the elements. The initial weathering products were restored based on the results from XRD, element behaviors, and the A-CN-K diagram. The CIA was chosen to quantify the chemical weathering degree, which was corrected by eliminating the effect of K- metasomatism and the enrichment of Ca due to the hypogene diagenesis.

For the paleo-weathering profile overprinted by hypogene diagenesis, the corrected CIA values can reflect the chemical weathering degree. However, for the rock composed of different types and proportions of minerals, even under the same environment, the weathering degree is variable. Therefore, the chemical weathering index such as CIA needs to be normalized by the susceptibility to chemical weathering for different types of rock. The result can reflect the chemical weathering intensity and enable the comparison of the chemical weathering characteristics among different lithologies. As discussed by Liang et al. (2022), the susceptibility to chemical weathering was represented by a new parameter CWA, which is calculated based on the weathering rate of different minerals in the natural environment. The rock with higher CWA tends to have a higher weathering degree with a higher proportion of the weathering products and more depletion of the mobile elements. After the normalization, the chemical weathering intensity can be acquired and compared to other locations.

The method for the quantification and normalization of physical weathering within a weathering profile was proposed in this thesis and published by Liang et al. (2022). The physical weathering quantification is represented by a new index physical weathering index (IPW). The index is based

---

on the ratio between the fracture and the total inspect area under the microscale. Based on the different minerals filled in the fractures, the index was normalized by the UCS, which was chosen to represent the susceptibility to physical weathering for different lithologies. With the index, the physical weathering degree and intensity of different types of rock can be evaluated.

## **5.2. Accounting for paleo-weathering profile**

The newly developed methods were applied by the post-Variscan nonconformity in Odenwald located in southwestern Germany. Based on the results, the depth of physical and chemical weathering shows a high variability from approximately 1 to 15 m for different rock types. For the basaltic andesite, the chemical weathering depth is deeper than the physical weathering due to the influence of the aphanitic-amygdaloid texture. For lithologies with phaneritic texture, physical weathering is deeper than chemical weathering as can be seen for the gabbroic diorite in GA1 and the granodiorite in GA2 due to the arid climate. The phaneritic tonalite in TB8 and granite in BK2/05 show the opposite trend whereas physical weathering reaches deeper than chemical weathering. This can be explained by tectonic faulting. One noticeable issue, in this case, is that the formation of the faults has a limited effect on the fractures under the microscale. Therefore, its influence on the evaluation of the physical weathering degree may be negligible. Detailed results were discussed by Liang et al. (2023).

All the weathering profile in the research area was influenced by the diagenetic fluids. In the A-CN-K diagram, the weathering trend is all excursion to the K-apex. Subsequently, the initial weathering production was all transformed to the K-bearing clay minerals, such as illite and the mix-layer of illite and smectite. After the correction of clay minerals measured by XRD, the weathering products in the research area should be dominated by smectite with the kaolinite in the part with a higher CIA value. What needs to be paid attention to is that the weathering products for different lithologies are diverse. For the rock with limited content of K, the illite as the weathering product is less expected, smectite should be dominated in the relatively lower chemical weathering degree regardless of the climate condition. Therefore, while accessing the climate condition with clay mineral types, the parent rock of the weathering products should be considered.

The chemical weathering process can improve the porosity and permeability of the rock. However, in the fault zone, the subsequently formed highly weathering zone with the weathering products may perform as a shield to prevent the diagenetic fluid from flowing downward as that indicated in the drill core TB8.

The element's behaviour based on the  $\tau$  values indicates the depletion degree during weathering process is decreasing from the LILE, REE to HFSE. The most depleted element is Na and followed



---

by Ca. The excepted-immobile elements REE show a differentiation of the depletion trend. From LREE, MREE to HREE, the depletion degree has a degreasing trend. The depletion degree of the elements corresponds well with the chemical weathering degree and is also influenced by the fractures. The elements such as REE and Ca are always enriched in the interface of the fracture and fracture-free zone.

The combination of physical and chemical weathering intensity can be applied to reflect the climate condition directly. A higher  $CIA_N$  accompanied by a relatively low  $IPW_N$  indicates domination of the chemical weathering process, which indicates a relatively humid climate, otherwise, the climate should be arid. This is verified by the clay mineral types. In the case study, the maximum physical and chemical weathering intensity are represented at the top surface of the weathering profile. The basaltic andesite yields a  $CIA_N$  value of 83, whereas the physical weathering intensity  $IPW_N$  is less than 0.1. The gabbroic diorite and granite followed with a  $CIA_N$  of 78, whereas the physical weathering intensity shows an  $IPW_N$  of 0.6. The lowest chemical weathering intensity was observed at the top of the granodiorite and tonalite with 71. However, both rock types show the highest  $IPW_N$  of approximately 4. The calculated  $IPW_N$  and  $CIA_N$  trends of these sections correspond well with trends of paleosol-paleoclimate models revealing mean annual temperature (MAT) and mean annual precipitation (MAP), which illustrate the potential to synchronize the suggested indices with other paleoclimate proxies. This offers a completely new spectrum of possibilities to quantitatively compare weathering and climatic conditions at the regional scale, regardless of lithologic constraints.

---

## 6. Perspectives

---

The methods proposed in this thesis for the evaluation of weathering characteristics provide fundamental logic and theoretical methods for the quantification of physical weathering, and quantification of physical and chemical weathering intensity. However, there is still a potential for improvements.

One of the improvements is the relationship between rock strength and chemical weathering indices. In this case, the relationship between UCS and CIA values is developed only for basaltic and granitic rock. For the evolution of the physical weathering degree over a large scale which also includes other lithologies, further investigation is needed. In addition, fracturing is also one of the fundamental parameters. Therefore, while the strength of the weathering profile is no longer able to support the stability of the primary physical weathering texture, such as residual soil, this method is also not applicable.

For the normalization of chemical weathering indices, it is noticeable that the fundamental data are the weathering rates for different minerals. Until present, previous studies for both lab and field only evaluated the weathering rate for plagioclase, hornblende, biotite, K-feldspar, and pyroxene (Franke, 2009; Hausrath et al., 2008; White and Brantley, 2003). In the future study, the investigation of the weathering rate for other minerals such as olivine in the field will be conducted. Another issue is that suitable methods to evaluate the weathering and denudation rate for the paleo weathering profile will also be developed to access a more accurate exposure time of the rock to alteration. With the accurate exposure time-to-alteration scale, a more precise weathering intensity will be performed.

Finally, for both the physical and chemical weathering normalization, the information which includes the geochemical and mineral compositions of the protolith is also needed. The evaluation of weathering intensity for both physical and chemical weathering provides a clear framework for the research about the nonconformity down to the meter scale. With more detailed information along the nonconformity, a meticulous depiction of the variables such as climate can be performed. Moreover, the quantified physical weathering together with CIA and  $CIA_N$  will give detailed information for the description and evaluation of nonconformity-type reservoirs, such as the relationship between physical weathering degrees and porosity and permeability. In addition, the quantified physical weathering degree, and physical and chemical weathering intensity also shed a light to quantify the influences between the physical and chemical weathering process.



---

---

## Reference

---

- Aadnøy, B. S. and Looyeh, R.: Rock Strength and Rock Failure, *Pet. Rock Mech.*, 145–163, doi:10.1016/b978-0-12-815903-3.00009-1, 2019.
- Aggittalis, G., Alivizatos, A., Stamoulis, D. and Stournaras, G.: Correlating uniaxial compressive strength with schimidt hardness, point load index Young's Modulus, and mineralogy of gabbros and basalts (Northern Greece), *Bull. Int. Assoc. Eng. Geol.*, (54), 191–193, doi:https://doi.org/10.1007/BF02600650, 1996.
- Anders, M. H., Laubach, S. E. and Scholz, C. H.: Microfractures: A review, *J. Struct. Geol.*, 69(PB), 377–394, doi:10.1016/j.jsg.2014.05.011, 2014.
- Anderson, S. P., Dietrich, W. E. and Brimhall, G. H.: Weathering profiles, mass-balance analysis, and rates of solute loss: Linkages between weathering and erosion in a small, steep catchment, *GSA Bull.*, 114(9), 1143–1158, doi:10.1130/0016-7606(2002)114<1143:wpmbaa>2.0.co;2, 2002.
- Aoudjit, H., Robert, M., Elsass, F. and Curmi, P.: Detailed study of smectite genesis in granitic saprolites by analytical electron microscopy, *Clay Miner.*, 1961, 135–147, doi:https://doi.org/10.1180/claymin.1995.030.2.05, 1995.
- Arel, E. and Tugrul, A.: Weathering and its relation to geomechanical properties of Cavusbasi granitic rocks in Northwestern Turkey, *Bull. Eng. Geol. Environ.*, 60(2), 123–133, doi:10.1007/s100640000091, 2001.
- Arias, D., Pando, L., López-fernández, C., Díaz-díaz, L. M. and Rubio-ordóñez, Á.: Deep weathering of granitic rocks: A case of tunnelling in NW Spain, *Catena*, 137, 572–580, doi:10.1016/j.catena.2015.10.026, 2016.
- Avigad, D., Morag, N., Abbo, A. and Gerdes, A.: Detrital rutile U-Pb perspective on the origin of the great Cambro-Ordovician sandstone of North Gondwana and its linkage to orogeny, *Gondwana Res.*, 51, 17–29, doi:10.1016/j.gr.2017.07.001, 2017.
- Babechuk, M. G., Widdowson, M. and Kamber, B. S.: Quantifying chemical weathering intensity and trace element release from two contrasting basalt profiles, Deccan Traps, India, *Chem. Geol.*, 363, 56–75, doi:10.1016/j.chemgeo.2013.10.027, 2014.

- 
- Babechuk, M. G., Widdowson, M., Murphy, M. and Kamber, B. S.: A combined Y/Ho, high field strength element (HFSE) and Nd isotope perspective on basalt weathering, Deccan Traps, India, *Chem. Geol.*, 396, 25–41, doi:10.1016/j.chemgeo.2014.12.017, 2015.
- Bauluz, B., Mayayo, M. J., Yuste, A. and González López, J. M.: Genesis of kaolinite from Albian sedimentary deposits of the Iberian Range (NE Spain): analysis by XRD, SEM and TEM, *Clay Miner.*, 43(3), 459–475, doi:10.1180/claymin.2008.043.3.10, 2008.
- Becker, A., Schwarz, M. and Schäfer, A.: Lithostratigraphic Correlation of the Rotliegend in the eastern Saar-Nahe Basin, *Jahresberichte und Mitteilungen des Oberrheinischen Geol. Vereins*, 94(April), 105–133, doi:10.1127/jmogv/94/2012/105, 2012a.
- Becker, A., Schwarz, M. and Schäfer, A.: Lithostratigraphische Korrelation des Rotliegend im östlichen Saar-Nahe-Becken Lithostratigraphic Correlation of the Rotliegend in the eastern Saar-Nahe Basin., 2012b.
- Behrmann, J. H., Ziegler, P. A., Schmid, S. M., Heck, B. and Granet, M.: The EUCOR-URGENT project. Upper Rhine Graben: Evolution and neotectonics, *Int. J. Earth Sci.*, 94(4), 505–506, doi:10.1007/s00531-005-0513-0, 2005.
- Beig, M. S. and Lüttge, A.: Albite dissolution kinetics as a function of distance from equilibrium: Implications for natural feldspar weathering, *Geochim. Cosmochim. Acta*, 70(6), 1402–1420, doi:10.1016/j.gca.2005.10.035, 2006.
- Berndt, M. E., Seyfried, W. E. and Beck, J. W.: Hydrothermal alteration processes at midocean ridges: experimental and theoretical constraints from Ca and Sr exchange reactions and Sr isotopic ratios, *J. Geophys. Res.*, 93(B5), 4573–4583, doi:10.1029/JB093iB05p04573, 1988.
- Berner, R. A.: Weathering, plants, and the long-term carbon cycle, *Geochim. Cosmochim. Acta*, 56(8), 3225–3231, doi:10.1016/0016-7037(92)90300-8, 1992.
- Berner, R. A. and Berner, E. K.: Silicate Weathering and Climate, in *Tectonic Uplift and Climate Change*, edited by W. F. Ruddiman, pp. 353–365, Springer US, Boston, MA., 1997.
- Bland, W. and Rolls, D.: *Weathering: An Introduction to the Scientific Principles*, Arnold. [online] Available from: [https://books.google.de/books?id=b%5C\\_Fa2SYM9CEC](https://books.google.de/books?id=b%5C_Fa2SYM9CEC), 1998.

---

Bons, P. D., Fusswinkel, T., Gomez-Rivas, E., Markl, G., Wagner, T. and Walter, B.: Fluid mixing from below in unconformity-related hydrothermal ore deposits, *Geology*, 42(12), 1035–1038, doi:10.1130/G35708.1, 2014.

Borrelli, L., Perri, F., Critelli, S. and Gullà, G.: Mineropetrographical features of weathering profiles in Calabria, southern Italy, *Catena*, 92, 196–207, doi:10.1016/j.catena.2012.01.003, 2012.

Borrelli, L., Perri, F., Critelli, S. and Gullà, G.: Characterization of granitoid and gneissic weathering profiles of the Mucone River basin (Calabria, southern Italy), *Catena*, 113, 325–340, doi:10.1016/j.catena.2013.08.014, 2014.

Brandstätter, J., Kurz, W., Richoz, S., Cooper, M. J. and Teagle, D. A. H.: The Origin of Carbonate Veins Within the Sedimentary Cover and Igneous Rocks of the Cocos Ridge: Results From IODP Hole U1414A, *Geochemistry, Geophys. Geosystems*, 19(10), 3721–3738, doi:10.1029/2018GC007729, 2018.

Breitkreuz, C., Käßner, A., Tichomirowa, M., Lapp, M., Huang, S. and Stanek, K.: The Late Carboniferous deeply eroded Tharandt Forest caldera–Niederbobritzsch granite complex: a post-Variscan long-lived magmatic system in central Europe, *Int. J. Earth Sci.*, 110(4), 1265–1292, doi:10.1007/s00531-021-02015-x, 2021.

Burisch, M., Gerdes, A., Walter, B. F., Neumann, U., Fettel, M. and Markl, G.: Methane and the origin of five-element veins: Mineralogy, age, fluid inclusion chemistry and ore forming processes in the Odenwald, SW Germany, *Ore Geol. Rev.*, 81, 42–61, doi:10.1016/j.oregeorev.2016.10.033, 2017.

Camuffo, D.: Physical weathering of stones, *Sci. Total Environ.*, 167(1–3), 1–14, doi:10.1016/0048-9697(95)04565-I, 1995.

Caspari, E., Greenwood, A., Baron, L., Egli, D., Toschini, E., Hu, K. and Holliger, K.: Characteristics of a fracture network surrounding a hydrothermally altered shear zone from geophysical borehole logs, *Solid Earth*, 11(3), 829–854, doi:10.5194/se-11-829-2020, 2020.

Catuneanu: Principles of sequence stratigraphy, 1st Editio., ELSEVIER SCIENCE & TECHNOLOGY, Oxford, United Kingdom., 1996.

- 
- Catuneanu, O.: Principles of Sequence Stratigraphy, Elsevier Science. [online] Available from: <https://books.google.de/books?id=8j-6UTXHmDkC>, 2006.
- Ceryan, S., Tudes, S. and Ceryan, N.: A new quantitative weathering classification for igneous rocks, *Environ. Geol.*, 55(6), 1319–1336, doi:10.1007/s00254-007-1080-4, 2008a.
- Ceryan, S., Tudes, S. and Ceryan, N.: Influence of weathering on the engineering properties of Harsit granitic rocks (NE Turkey), *Bull. Eng. Geol. Environ.*, 67(1), 97–104, doi:10.1007/s10064-007-0115-0, 2008b.
- Ceryan, S., Zorlu, K., Gokceoglu, C. and Temel, A.: The use of cation packing index for characterizing the weathering degree of granitic rocks, *Eng. Geol.*, 98(1–2), 60–74, doi:10.1016/j.enggeo.2008.01.007, 2008c.
- Ceryan, Ş.: New Chemical Weathering Indices for Estimating the Mechanical Properties of Rocks: A Case Study from the Kurtun Granodiorite, NE Turkey, *Turkish J. Earth Sci.*, 17(1), 187–207 [online] Available from: <https://journals.tubitak.gov.tr/earth/abstract.htm?id=9322>, 2008.
- Chang, B., Li, C., Liu, D., Foster, I., Tripathi, A., Lloyd, M. K. and Maradiaga, I.: Massive formation of early diagenetic dolomite in the Ediacaran ocean : Constraints on the “ dolomite problem ,” , 1–10, doi:10.1073/pnas.1916673117, 2020.
- Chen, P. Y., Wang, M. K. and Yang, D. S.: Mineralogy of dickite and nacrite from Northern Taiwan, *Clays Clay Miner.*, 49(6), 586–595, doi:10.1346/CCMN.2001.0490608, 2001.
- Chiu, C. F. and Charles W.W., N.: Relationships between chemical weathering indices and physical and mechanical properties of decomposed granite, *Eng. Geol.*, 179, 76–89, doi:10.1016/j.enggeo.2014.06.021, 2014.
- Chiu, C. F. and Ng, C. W. W.: Relationships between chemical weathering indices and physical and mechanical properties of decomposed granite, *Eng. Geol.*, 179, 76–89, doi:10.1016/j.enggeo.2014.06.021, 2014.
- Chou, L. and Wollast, R.: Steady-state kinetics and dissolution mechanisms of albite, *Am. J. Sci.*, 285, 963–993, 1985.

---

Chou, L. and Wollast, R.: Study of the weathering of albite at room temperature and pressure with a fluidized bed reactor, *Geochim. Cosmochim. Acta*, 48(11), 2205–2217, doi:10.1016/0016-7037(84)90217-5, 1984.

Cissé, G., Essi, M., Kedi, B., Nicolas, M. and Staunton, S.: Accumulation and vertical distribution of glomalin-related soil protein in French temperate forest soils as a function of tree type, climate and soil properties, *Catena*, 220(September 2022), doi:10.1016/j.catena.2022.106635, 2023.

Clift, P. D., Wan, S. and Blusztajn, J.: Reconstructing chemical weathering, physical erosion and monsoon intensity since 25Ma in the northern South China Sea: A review of competing proxies, *Earth-Science Rev.*, 130, 86–102, doi:10.1016/j.earscirev.2014.01.002, 2014.

Clive F., B.: Plate tectonics and the Himalayas, *Nature*, 239, 155–157, doi:https://doi.org/10.1038/239155a0, 1972.

Cloetingh, S., Cornu, T., Ziegler, P. A., Beekman, F., Ustaszewski, K., Schmid, S. M., Dèzes, P., Hinsch, R., Decker, K., Lopes Gardozo, G., Granet, M., Bertrand, G., Behrmann, J., van Balen, R., Michon, L., Pagnier, H., Rozsa, S., Heck, B., Tesauro, M., Kahle, H. G., Dewez, T., Carretier, S., Winter, T., Hardebol, N., Bada, G., Dost, B. and van Eck, T.: Neotectonics and intraplate continental topography of the northern Alpine Foreland, *Earth-Science Rev.*, 74(3–4), 127–196, doi:10.1016/j.earscirev.2005.06.001, 2006.

Craig, H.: Standard for Reporting Concentrations of Deuterium and Oxygen-18 in Natural Waters, *Science (80-. )*, 1(1958), 1833–1834, doi:10.1016/B978-0-08-052351-4.50022-4, 2013.

Cuccuru, S., Casini, L., Oggiano, G. and Cherchi, G. P.: Can weathering improve the toughness of a fractured rock? A case study using the San Giacomo granite, *Bull. Eng. Geol. Environ.*, 71(3), 557–567, doi:10.1007/s10064-012-0416-9, 2012.

Das, A., Krishnaswami, S., Sarin, M. M. and Pande, K.: Chemical weathering in the Krishna Basin and Western Ghats of the Deccan Traps, India: Rates of basalt weathering and their controls, *Geochim. Cosmochim. Acta*, 69(8), 2067–2084, doi:10.1016/j.gca.2004.10.014, 2005.

Deer, W. A., Howie, R. A. and Zussman, J.: *An Introduction to the Rock-Forming Minerals*, Third Edit., edited by F. W. A. DEER, R. A. HOWIE, and J. ZUSSMAN, The Mineralogical Society., 2013.



---

Dill, H. G.: Authigenic heavy minerals a clue to unravel supergene and hypogene alteration of marine and continental sediments of Triassic to Cretaceous age (SE Germany), *Sediment. Geol.*, 228(1–2), 61–76, doi:10.1016/j.sedgeo.2010.04.006, 2010.

Dill, H. G., Techmer, A., Botz, R., Dohrmann, R. and Kaufhold, S.: Hypogene and supergene alteration of the zeolite-bearing pyroclastic deposits at Tell Rimah , Jordan , and rift-related processes along the Dead-Sea-Transform Fault System during the Quaternary, *J. Volcanol. Geotherm. Res.*, 239–240, 49–68, doi:10.1016/j.jvolgeores.2012.05.018, 2012.

Dill, H. G., Balaban, S. I., Witt, B. and Wershofen, H.: Capturing digital data of rock magnetic, gamma-ray and IR spectrometry for in-situ quality control and for the study of the physical-chemical regime of residual kaolin deposits, SE Germany, *Ore Geol. Rev.*, 57, 172–190, doi:10.1016/j.oregeorev.2013.09.020, 2014.

Dill, H. G., Kaufhold, S., Ehling, A. and Bowitz, J.: Oxidized and reduced kaolin fan deposits: Their sedimentological-mineralogical facies and physical-chemical regime (North-Bavarian Kaolin Mining District, Germany), *Ore Geol. Rev.*, 72(P1), 459–484, doi:10.1016/j.oregeorev.2015.08.003, 2016.

Dörr, W. and Stein, E.: Precambrian basement in the Rhenic suture zone of the Central European Variscides (Odenwald), *Int. J. Earth Sci.*, 108(6), 1937–1957, doi:10.1007/s00531-019-01741-7, 2019a.

Dörr, W. and Stein, E.: Precambrian basement in the Rhenic suture zone of the Central European Variscides (Odenwald), *Int. J. Earth Sci.*, 108(6), 1937–1957, doi:10.1007/s00531-019-01741-7, 2019b.

Drever, J. I.: The effect of land plants on weathering rates of silicate minerals, *Geochim. Cosmochim. Acta*, 58(10), 2325–2332, doi:10.1016/0016-7037(94)90013-2, 1994.

Earle, S.: *Physical geology*, BCcampus, Victoria, B.C., 2015.

Edgar, N. and Hubert, Z.: *Beiträge zur Lithostratigraphie in Baden-Württemberg*, 2009.

Eggleton, R. A. and Banfield, J. F.: The alteration of granitic biotite to chlorite., *Am. Mineral.*, 70(9–10), 902–910, 1985.

---

Erişiş, S., Tuğrul, A., Selman, E. R. and Yılmaz, M.: The effect of composition and textural properties of basaltic rocks on their mechanical behaviour, *Jeol. Muhendisligi Derg.*, 43(2), 259–278, doi:10.24232/jmd.655348, 2019.

Erkoyun, H. and Kadir, S.: Mineralogy, micromorphology, geochemistry and genesis of a hydrothermal kaolinite deposit and altered Miocene host volcanites in the Hallaçlar area, Uşak, western Turkey, *Clay Miner.*, 46(3), 421–448, doi:10.1180/claymin.2011.046.3.421, 2011.

Fàbrega, C., Parcerisa, D., Thiry, M., Franke, C., Gurenko, A., Gòmez-Gras, D., Solé, J. and Travé, A.: Permian–Triassic red-stained albitized profiles in the granitic basement of NE Spain: evidence for deep alteration related to the Triassic palaeosurface, *Int. J. Earth Sci.*, 108(7), 2325–2347, doi:10.1007/s00531-019-01764-0, 2019.

Fedo, C. M., Eriksson, K. A. and Krogstad, E. J.: Geochemistry of shales from the Archean (~3.0 Ga) Buhwa Greenstone Belt, Zimbabwe: Implications for provenance and source-area weathering, 1996.

Fedo, C. M., Wayne Nesbitt, H. and Young, G. M.: Unraveling the effects of potassium metasomatism in sedimentary rocks and paleosols, with implications for paleoweathering conditions and provenance, *Geology*, 23(10), 921–924, doi:10.1130/0091-7613(1995)023<0921:uteopm>2.3.co;2, 1995.

Feng, J., Qu, J., Zhang, P. and Qin, F.: Development Characteristics and Quantitative Prediction of Multiperiod Fractures in Superdeep Thrust-Fold Belt, *Lithosphere*, 2021(1), 1–28, doi:10.2113/2021/8895823, 2021.

Fielding, C. R., Isbell, J. L., Birgenheier, L. P. and Rygel, M. C.: Late Paleozoic Deglaciation, *Geology*, 35(1), 87–92, 2007.

Di Figlia, M. G., Bellanca, A., Neri, R. and Stefansson, A.: Chemical weathering of volcanic rocks at the island of Pantelleria, Italy: Information from soil profile and soil solution investigations, *Chem. Geol.*, 246(1–2), 1–18, doi:10.1016/j.chemgeo.2007.07.025, 2007.

Franke, W. A.: The durability of rocks - Developing a test of rock resistance to chemical weathering, *Am. J. Sci.*, 309(8), 711–730, doi:10.2475/08.2009.04, 2009.

- 
- Friedman, I. and O'Neil, J. R.: Data of Data of Geochemistry Sixth Edition., 1977.
- Fritz, S. J.: A comparative study of gabbro and granite weathering, *Chem. Geol.*, 68(3–4), 275–290, doi:10.1016/0009-2541(88)90026-5, 1988.
- Funedda, A.: Foreland- and hinterland-verging structures in fold-and-thrust belt: An example from the Variscan foreland of Sardinia, *Int. J. Earth Sci.*, 98(7), 1625–1642, doi:10.1007/s00531-008-0327-y, 2009.
- Fusswinkel, T., Wagner, T., Wenzel, T., Wälle, M. and Lorenz, J.: Red bed and basement sourced fluids recorded in hydrothermal Mn-Fe-As veins, Sailauf (Germany): A LA-ICPMS fluid inclusion study, *Chem. Geol.*, 363, 22–39, doi:10.1016/j.chemgeo.2013.10.026, 2014.
- Gallagher, T. M. and Sheldon, N. D.: A new paleothermometer for forest paleosols and its implications for Cenozoic climate, *Geology*, 41(6), 647–650, doi:10.1130/G34074.1, 2013.
- Gardner, F. J.: Relationship of unconformities to oil and gas accumulation, *Am. Assoc. Pet. Geol. Bull.*, 24(11), 2022–2031, doi:https://doi.org/10.1306/3D933278-16B1-11D7-8645000102C1865D, 1940.
- Geissman, J. W. and Harlan, S. S.: Late Paleozoic remagnetization of Precambrian crystalline rocks along the Precambrian/Carboniferous nonconformity, Rocky Mountains: A relationship among deformation, remagnetization, and fluid migration, *Earth Planet. Sci. Lett.*, 203(3–4), 905–924, doi:10.1016/S0012-821X(02)00932-9, 2002.
- George E., H., J Ramon, A. and Lee, A.: Interaction between normal faults and fractures fault scarp morphology, , 28(19), 3777–3780, 2001.
- Geyer, M. and Nitsch, E.: *Geologie von Baden- Württemberg*, 2011.
- Gol'braykh, I. G., Zabaluyev, V. V. and Mirkin, G. R.: Tectonic analysis of megajointing: a promising method of investigating covered territories, *Int. Geol. Rev.*, 8(9), 1009–1016, doi:10.1080/00206816609474369, 1966.
- Goldich, S. S.: A STUDY IN ROCK-WEATHERING, *J. Geol.*, 46(1), 17–58, doi:https://doi.org/10.1086/624619, 1938.

- 
- Golodkovskaia, G. A., Krasilova, N. S., Ladygin, V. M. and Shaumian, L. V.: Factors controlling solid rock strength, *Bull. Int. Assoc. Eng. Geol.*, 11(1), 65–69, doi:10.1007/bf02635456, 1975.
- Górska, M. E., Woronko, B., Kossowski, T. M. and Pisarska-Jamroży, M.: Micro-scale frost-weathering simulation – Changes in grain-size composition and influencing factors, *CATENA*, 212, 106106, doi:https://doi.org/10.1016/j.catena.2022.106106, 2022.
- Greiling, R. O. and Verma, P. K.: Strike-slip tectonics and granitoid emplacement: An AMS fabric study from the Odenwald Crystalline Complex, SW Germany, *Mineral. Petrol.*, 72(1–3), 165–184, doi:10.1007/s007100170032, 2001.
- Gupta, A. S. and Rao, S. K.: Weathering indices and their applicability for crystalline rocks, *Bull. Eng. Geol. Environ.*, 60(3), 201–221, doi:10.1007/s100640100113, 2001.
- Hagdorn, H. and Mutter, R. J.: The vertebrate fauna of the Lower Keuper Albertibank ( Erfurt Formation , Middle Triassic ) in the vicinity of Schwäbisch Hall (Baden-Württemberg, Germany), *Paleodiversity*, 4(December), 223–243, 2011.
- Halbouty, M. T.: Rationale for Deliberate Pursuit of Stratigraphic, Unconformity, and Paleogeomorphic Traps<sup>1</sup>, *Am. Assoc. Pet. Geol. Bull.*, 56(3), 537–541, doi:10.1306/819A3E80-16C5-11D7-8645000102C1865D, 1972.
- Harnois, L.: The CIW index: A new chemical index of weathering, *Sediment. Geol.*, 55(3–4), 319–322, doi:10.1016/0037-0738(88)90137-6, 1988.
- Harriss, R. C. and Adams, J. A. S.: Geochemical and mineralogical studies on the weathering of granitic rocks, *Am. J. Sci.*, 264(2), 146–173, doi:10.2475/ajs.264.2.146, 1966.
- Hausrath, E. M., Navarre-Sitchler, A. K., Sak, P. B., Steefel, C. I. and Brantley, S. L.: Basalt weathering rates on Earth and the duration of liquid water on the plains of Gusev Crater, Mars, *Geology*, 36(1), 67–70, doi:10.1130/G24238A.1, 2008.
- Hayes, N. R., Buss, H. L., Moore, O. W., Krám, P. and Pancost, R. D.: Controls on granitic weathering fronts in contrasting climates, *Chem. Geol.*, 535, 119450, doi:10.1016/j.chemgeo.2019.119450, 2020.

---

Henk, A.: Subsidenz und Tektonik des Saar-Nahe-Beckens (SW-Deutschland), *Geol Rundsch*, 82, 3–19, 1993.

Henk, R. A.: Late Variscan exhumation histories of the southern Rhenohercynian Zone and western Mid-German Crystalline Rise: results from thermal modeling, 1995.

Hug, N. and Gaupp, R.: Palaeogeographic reconstruction in red beds by means of genetically related correlation: results from the upper Zechstein (Late Permian), *Zeitschrift der Dtsch. Gesellschaft für Geowissenschaften*, 157(1), 107–120, doi:10.1127/1860-1804/2006/0157-0107, 2006.

Hug, N. and Vero, G.: Ein vollständiges Zechsteinprofil im südlichen Odenwald: die hydrogeologische Erkundungsbohrung Langenthal BK2/05 Kurzfassung, *Geol.Jb.Hessen*, 135, 25–45, 2008.

Huh, Y.: Chemical weathering and climate - A global experiment: A review, *Geosci. J.*, 7(3), 277–288, doi:10.1007/BF02910294, 2003.

Izart, A., Sachsenhofer, R. F., Privalov, V. A., Elie, M., Panova, E. A., Antsiferov, V. A., Alsaab, D., Rainer, T., Sotirov, A., Zdravkov, A. and Zhykalyak, M. V.: Stratigraphic distribution of macerals and biomarkers in the Donets Basin: Implications for paleoecology, paleoclimatology and eustacy, *Int. J. Coal Geol.*, 66(1–2), 69–107, doi:10.1016/j.coal.2005.07.002, 2006.

Jayawardena, U. de S. and Izawa, E.: A new chemical index of weathering for metamorphic silicate rocks in tropical regions: A study from Sri Lanka, *Eng. Geol.*, 36(3–4), 303–310, doi:10.1016/0013-7952(94)90011-6, 1994.

Jian, X., Zhang, W., Liang, H., Guan, P. and Fu, L.: Mineralogy, petrography and geochemistry of an early Eocene weathering profile on basement granodiorite of Qaidam basin, northern Tibet: Tectonic and paleoclimatic implications, *Catena*, 172, 54–64, doi:10.1016/j.catena.2018.07.029, 2019.

Jiménez-Espinosa, R., Vázquez, M. and Jiménez-Millán, J.: Differential weathering of granitic stocks and landscape effects in a Mediterranean climate, Southern Iberian Massif (Spain), *CATENA*, 70(2), 243–252, doi:https://doi.org/10.1016/j.catena.2006.09.001, 2007.

- 
- Johannesson, K. H. and Lyons, W. B.: Rare-earth element geochemistry of Colour Lake, an acidic freshwater lake on Axel Heiberg Island, Northwest Territories, Canada, *Chem. Geol.*, 119(1–4), 209–223, doi:10.1016/0009-2541(94)00099-T, 1995.
- Joo, Y. J., Madden, M. E. E. and Soreghan, G. S.: Chemical and physical weathering in a hot-arid, tectonically active alluvial system of anza borrego desert, california, *Sedimentology*, 63(5), 1065–1083, doi:10.1111/sed.12249, 2016.
- Kempe, U., Möckel, R., Graupner, T., Kynicky, J. and Dombon, E.: The genesis of Zr-Nb-REE mineralisation at Khalzan Buregte (Western Mongolia) reconsidered, *Ore Geol. Rev.*, 64, 602–625, doi:10.1016/j.oregeorev.2014.05.003, 2015.
- Khanlari, G. R., Heidari, M. and Momeni, A. A.: Assessment of weathering processes effect on engineering properties of Alvand granitic rocks (west of Iran), based on weathering indices, *Environ. Earth Sci.*, 67(3), 713–725, doi:10.1007/s12665-011-1518-6, 2012.
- Kiehl, J. T. and Shields, C. A.: Climate simulation of the latest Permian: Implications for mass extinction, *Geology*, 33(9), 757–760, doi:10.1130/G21654.1, 2005.
- Kirsch, H., Kober, B. and Lippolt, H. J.: Age of intrusion and rapid cooling of the Frankenstein gabbro (Odenwald, SW-Germany) evidenced by  $^{40}\text{Ar}/^{39}\text{Ar}$  and single-zircon  $^{207}\text{Pb}/^{206}\text{Pb}$  measurements, *Geol. Rundschau*, 77(3), 693–711, doi:10.1007/BF01830178, 1988.
- Korkanç, M., Tuğrul, A., Savran, A. and Özgür, F. Z.: Structural–geological problems in Gümüşler archeological site and monastery, *Environ. Earth Sci.*, 73(8), 4525–4540, doi:10.1007/s12665-014-3739-y, 2015.
- Korsch, R. J. and Schäfer, A.: Geological interpretation of DEKORP deep seismic reflection profiles 1C and 9N across the variscan Saar-Nahe Basin southwest Germany, *Tectonophysics*, 191(1–2), 127–146, doi:10.1016/0040-1951(91)90236-L, 1991.
- Kowalczyk, G.: Permokarbon des Sprendlinger Horstes und der westlichen Wetterau (Exkursion I am 20. April 2001), *Jahresberichte und Mitteilungen des Oberrheinischen Geol. Vereins*, 83(April 2001), 211–236, doi:10.1127/jmogv/83/2001/211, 2001.

---

Kroner, U., Hahn, T., Romer, R. L. and Linnemann, U.: The variscan orogeny in the saxo-thuringian zone - Heterogenous overprint of Cadomian/Paleozoic Peri-Gondwana crust, *Spec. Pap. Geol. Soc. Am.*, 423, 153–172, doi:10.1130/2007.2423(06), 2007a.

Kroner, U., Hahn, T., Romer, R. L. and Linnemann, U.: The variscan orogeny in the saxo-thuringian zone - Heterogenous overprint of Cadomian/Paleozoic Peri-Gondwana crust, in *Special Paper of the Geological Society of America*, vol. 423, pp. 153–172, Geological Society of America., 2007b.

Lang, S.: Die geologische Entwicklung der Hanau-Seligenstädter Senke (Hessen, Bayern), *Naturwissenschaften* [online] Available from: <http://tuprints.ulb.tu-darmstadt.de/782/>, 2007.

Liang, F., Niu, J., Linsel, A., Hinderer, M., Scheuven, D. and Petschick, R.: Rock alteration at the post-Variscan nonconformity: implications for Carboniferous-Permian surface weathering versus burial diagenesis and paleoclimate evaluation, *Solid Earth*, (12), 1165–1184, doi:10.5194/se-12-1165-2021, 2021.

Liang, F., Hinderer, M. and Hornung, J.: Quantification of Physical and Chemical Palaeoweathering at the Microscale - A New Concept, *Int. J. Earth Sci.*, (0123456789), doi:10.1007/s00531-022-02281-3, 2022.

Liang, F., Hinderer, M. and Hornung, J.: Quantification of Physical and Chemical Paleoweathering at the Microscale - A New Concept, *Int. J. Earth Sci.*, 2023.

Lippolt, H. J. and Hess, J. C.: Isotopic evidence for the stratigraphic position of the Saar-Nahe Rotliegend volcanism I.  $^{40}\text{Ar}/^{40}\text{K}$  and  $^{40}\text{Ar}/^{39}\text{Ar}$  investigations, *Neues Jahrb. für Geol. und Paläontologie - Monatshefte*, 1983(12), 713–730, doi:10.1127/njgpm/1983/1983/713, 1983.

Maino, M., Gaggero, L., Langone, A., Seno, S. and Fanning, M.: Cambro-Silurian magmatism at the northern Gondwana margin (Penninic basement of the Ligurian Alps), *Geosci. Front.*, 10(1), 315–330, doi:10.1016/j.gsf.2018.01.003, 2019.

Malek-Mahmoudi, F., Reza Davoudian, A., Shabaniyan, N., Azizi, H., Asahara, Y., Neubauer, F. and Dong, Y.: Geochemistry of metabasites from the North Shahrekord metamorphic complex, Sanandaj-Sirjan Zone: Geodynamic implications for the Pan-African basement in Iran, *Precambrian Res.*, 293, 56–72, doi:10.1016/j.precamres.2017.03.003, 2017.

---

Marell, D.: Das Rotliegende zwischen Odenwald und Taunus, , 128 p. [online] Available from: <file://catalog.hathitrust.org/Record/102424593>, 1989.

Martinez, R. E., Weber, S. and Bucher, K.: Quantifying the kinetics of olivine dissolution in partially closed and closed batch reactor systems, *Chem. Geol.*, 367, 1–12, doi:10.1016/j.chemgeo.2013.12.017, 2014.

Matsuoka, N.: Rock weathering processes and landform development in the Sør Rondane Mountains, Antarctica, *Geomorphology*, 12(4), 323–339, doi:10.1016/0169-555X(95)00013-U, 1995.

Matsuoka, N., Moriwaki, K. and Hirakawa, K.: Field experiments on physical weathering and wind erosion in an antarctic cold desert, *Earth Surf. Process. Landforms*, 21(8), 687–699, doi:10.1002/(SICI)1096-9837(199608)21:8<687::AID-ESP614>3.0.CO;2-J, 1996.

Matte, P.: Accretionary history and crustal evolution of the Variscan belt in Western Europe, *Tectonophysics*, 196(3–4), 309–337, doi:10.1016/0040-1951(91)90328-P, 1991.

Maynard, J. B.: Chemistry of modern soils as a guide to interpreting Precambrian paleosols, *J. Geol.*, 100(3), 279–289, doi:10.1086/629632, 1992.

McCann, T.: The tectonosedimentary evolution of the northern margin of the Carboniferous foreland basin of NE Germany, *Tectonophysics*, 313(1–2), 119–144, doi:10.1016/S0040-1951(99)00193-6, 1999.

McCann, T., Pascal, C., Timmerman, M. J., Krzywiec, P., López-Gómez, J., Wetzel, A., Krawczyk, C. M., Rieke, H. and Lamarche, J.: Post-Variscan (end Carboniferous-Early Permian) basin evolution in Western and Central Europe, *Geol. Soc. Mem.*, 32, 355–388, doi:10.1144/GSL.MEM.2006.032.01.22, 2006.

McDonough, W. F. and Sun, S. s.: The composition of the Earth, *Chem. Geol.*, 120(3–4), 223–253, doi:10.1016/0009-2541(94)00140-4, 1995.

McFadden, L. D., Eppes, M. C., Gillespie, A. R. and Hallet, B.: Physical weathering in arid landscapes due to diurnal variation in the direction of solar heating, *Bull. Geol. Soc. Am.*, 117(1–2), 161–173, doi:10.1130/B25508.1, 2005.



---

Mclennan, S. M.: Weathering and Global Denudation, *J. Geol.*, 101, 295–303, doi:<https://doi.org/10.1086/648222>, 1993.

Menning, M., Gast, R., Hagdorn, H., Käding, K. C., Simon, T., Szurlies, M. and Nitsch, E.: Zeitskala für Perm und Trias in der Stratigraphischen Tabelle von Deutschland 2002, zyklusstratigraphische Kalibrierung der höheren Dyas und Germanischen Trias und das Alter der Stufen Roadium bis Rhaetium 2005, *Newsletters Stratigr.*, 41(3), 173–210, doi:10.1127/0078-0421/2005/0041-0173, 2005.

Mert, E.: An Artificial Neural Network Approach to Assess the Weathering Properties of Sancaktepe Granite, *Geotech. Geol. Eng.*, 32(4), 1109–1121, doi:10.1007/s10706-014-9785-0, 2014.

Mezger, J. E., Felder, M. and Harms, F. J.: Kristallingesteine in den maarablagerungen von Messel: Schlüssel zum verständnis der geometrien der messel-störungszone und des vulkanschlots und der posteruptiven beckenentwicklung, *Zeitschrift der Dtsch. Gesellschaft für Geowissenschaften*, 164(4), 639–662, doi:10.1127/1860-1804/2013/0034, 2013.

Michel, L. A. and Tabor, N. J.: Paleosol diagenesis and its deep-time paleoenvironment implications, Pennsylvanian-Permian Lodeve basin, France, *J. Sediment. Res.*, 86(July), 813–829, 2016.

Michel, L. A., Tabor, N. J., Montañez, I. P., Schmitz, M. D. and Davydov, V. I.: Chronostratigraphy and paleoclimatology of the lodève Basin, France: Evidence for a pan-tropical aridification event across the carboniferous-permian boundary, *Palaeogeogr. Palaeoclimatol. Palaeoecol.*, 430, 118–131, doi:10.1016/j.palaeo.2015.03.020, 2015.

Middelburg, J. J., van der Weijden, C. H. and Woittiez, J. R. W.: Chemical processes affecting the mobility of major, minor and trace elements during weathering of granitic rocks, *Chem. Geol.*, 68(3–4), 253–273, doi:10.1016/0009-2541(88)90025-3, 1988.

Middlemost, E. A. K.: Naming materials in the magma/igneous rock system, *Earth Sci. Rev.*, 37(3–4), 215–224, doi:10.1016/0012-8252(94)90029-9, 1994.

---

Migoń, P. and Lidmar-Bergström, K.: Deep weathering through time in central and northwestern Europe: Problems of dating and interpretation of geological record, *Catena*, 49(1–2), 25–40, doi:10.1016/S0341-8162(02)00015-2, 2002.

Molenaar, N., Felder, M., Bär, K. and Götz, A. E.: What classic greywacke (litharenite) can reveal about feldspar diagenesis: An example from Permian Rotliegend sandstone in Hessen, Germany, *Sediment. Geol.*, 326, 79–93, doi:10.1016/j.sedgeo.2015.07.002, 2015.

Moon, V. and Jayawardane, J.: Geomechanical and geochemical changes during early stages of weathering of Karamu Basalt, New Zealand, *Eng. Geol.*, 74(1–2), 57–72, doi:10.1016/j.enggeo.2004.02.002, 2004a.

Moon, V. and Jayawardane, J.: Geomechanical and geochemical changes during early stages of weathering of Karamu Basalt, New Zealand, *Eng. Geol.*, 74(1–2), 57–72, doi:10.1016/j.enggeo.2004.02.002, 2004b.

Neaman, A., Chorover, J. and Brantley, S. L.: Implications of the evolution of organic acid moieties for basalt weathering over geological time, *Am. J. Sci.*, 305(2), 147–185, doi:10.2475/ajs.305.2.147, 2005.

Nesbitt, H. W.: Mobility and fractionation of rare earth elements during weathering of a granodiorite, *Nature*, 279(5710), 206–210, doi:10.1038/279206a0, 1979a.

Nesbitt, H. W.: Mobility and fractionation of rare earth elements during weathering of a granodiorite, *Nature*, 279(5710), 206–210, doi:10.1038/279206a0, 1979b.

Nesbitt, H. W. and Markovics, G.: Weathering of granodioritic crust, long-term storage of elements in weathering profiles, and petrogenesis of siliciclastic sediments., 1997.

Nesbitt, H. W. and Young, G. M.: Early proterozoic climates and plate motions inferred from major element chemistry of lutites, *Nature*, 299(5885), 715–717, doi:10.1038/299715a0, 1982.

Nesbitt, H. W. and Young, G. M.: Prediction of some weathering trends of plutonic and volcanic rocks based on thermodynamic and kinetic considerations, *Geochim. Cosmochim. Acta*, 48(7), 1523–1534, doi:10.1016/0016-7037(84)90408-3, 1984.

- 
- Nesbitt, H. W. and Young, G. M.: Formation and diagenesis of weathering profiles, *J. Geol.*, 97, 129–147, doi:<https://doi.org/10.1086/629290>, 1989a.
- Nesbitt, H. W. and Young, G. M.: Formation and diagenesis of weathering profiles, *J. Geol.*, 97(2), 129–147, doi:[10.1086/629290](https://doi.org/10.1086/629290), 1989b.
- Nesbitt, H. W., Markovics, G. and Price, R. C.: Chemical processes affecting alkalis and alkaline earths during continental weathering, *Geochim. Cosmochim. Acta*, 44(11), 1659–1666, doi:[10.1016/0016-7037\(80\)90218-5](https://doi.org/10.1016/0016-7037(80)90218-5), 1980.
- Nguetnkam, J. P., Solleiro-Rebolledo, E., Díaz-Ortega, J. and Tématio, P.: Evaluating weathering of palaeosols in Cameroon (Central Africa) as a tool for paleoenvironmental reconstruction, *Catena*, 194(May), 104688, doi:[10.1016/j.catena.2020.104688](https://doi.org/10.1016/j.catena.2020.104688), 2020.
- Oelkers, E. H. and Schott, J.: Experimental study of anorthite dissolution and the relative mechanism of feldspar hydrolysis., 1995.
- Opluštil, S. and Cleal, C. J.: A comparative analysis of some late carboniferous basins of Variscan Europe, *Geol. Mag.*, 144(3), 417–448, doi:[10.1017/S0016756807003330](https://doi.org/10.1017/S0016756807003330), 2007.
- Palmer, M. R. and Edmond, J. M.: Cesium and rubidium in submarine hydrothermal fluids: evidence for recycling of alkali elements, *Earth Planet. Sci. Lett.*, 95, 8–14, 1989.
- Panahi, A., Young, G. M. and Rainbird, R. H.: Behavior of major and trace elements (including REE) during Paleoproterozoic pedogenesis and diagenetic alteration of an Archean granite near Ville Marie, Quebec, Canada, *Geochim. Cosmochim. Acta*, 64(13), 2199–2220, doi:[10.1016/S0016-7037\(99\)00420-2](https://doi.org/10.1016/S0016-7037(99)00420-2), 2000.
- Parcerisa, D., Thiry, M. and Schmitt, J. M.: Albitisation related to the triassic unconformity in igneous rocks of the morvan massif (France), *Int. J. Earth Sci.*, 99(3), 527–544, doi:[10.1007/s00531-008-0405-1](https://doi.org/10.1007/s00531-008-0405-1), 2010.
- Parker, A.: An Index of Weathering for Silicate Rocks, *Geol. Mag.*, 107(6), 501–504, doi:[10.1017/S0016756800058581](https://doi.org/10.1017/S0016756800058581), 1970.
- Parrish, J. T.: Climate of the supercontinent Pangea, *J. Geol.*, 101(2), 215–233, doi:[10.1086/648217](https://doi.org/10.1086/648217), 1993.

---

Parrish, J. T.: Geologic Evidence of Permian Climate, in *The Permian of Northern Pangea: Volume 1: Paleogeography, Paleoclimates, Stratigraphy*, edited by P. A. Scholle, T. M. Peryt, and D. S. Ulmer-Scholle, pp. 53–61, Springer Berlin Heidelberg, Berlin, Heidelberg., 1995.

Patino, L. C., Velbel, M. A., Price, J. R. and Wade, J. A.: Trace element mobility during spheroidal weathering of basalts and andesites in Hawaii and Guatemala, *Chem. Geol.*, 202(3–4), 343–364, doi:10.1016/j.chemgeo.2003.01.002, 2003.

Pearce, J. A.: A User's Guide to Basalto Discriminant Diagrams, *Geol. Assoc. Canada, Short Course Notes*, 79–113, 1996.

Perri, F.: Chemical weathering of crystalline rocks in contrasting climatic conditions using geochemical proxies: An overview, *Palaeogeogr. Palaeoclimatol. Palaeoecol.*, 556, 109873, doi:10.1016/j.palaeo.2020.109873, 2020.

Petschick, R., Kuhn, G. and Gingele, F.: Clay mineral distribution in surface sediments of the South Atlantic: Sources, transport, and relation to oceanography, *Mar. Geol.*, 130(3–4), 203–229, doi:10.1016/0025-3227(95)00148-4, 1996.

Phillips, J. D.: Weathering instability and landscape evolution, *Geomorphology*, 67(1-2 SPEC. ISS.), 255–272, doi:10.1016/j.geomorph.2004.06.012, 2005.

Pokrovsky, O. S., Schott, J., Kudryavtzev, D. I. and Dupré, B.: Basalt weathering in Central Siberia under permafrost conditions, *Geochim. Cosmochim. Acta*, 69(24), 5659–5680, doi:10.1016/j.gca.2005.07.018, 2005.

Powell, C. M. A. and Conaghan, P. J.: Plate tectonics and the Himalayas, *Earth Planet. Sci. Lett.*, 20(1), 1–12, doi:10.1016/0012-821X(73)90134-9, 1973.

Prazeres, C. M., Batista, M. J., Pinto, A. J. and Gonçalves, M. A.: Uranium distribution and mobility in the weathering zone of the Nisa deposit, Portugal, *J. Iber. Geol.*, 44(3), 497–512, doi:10.1007/s41513-018-0074-2, 2018.

Qin, J., Huh, Y., Edmond, J. M., Du, G. and Ran, J.: Chemical and physical weathering in the Min Jiang, a headwater tributary of the Yangtze River, *Chem. Geol.*, 227(1–2), 53–69, doi:10.1016/j.chemgeo.2005.09.011, 2006.

---

Rasmussen, C., Brantley, S., Richter, D. de B., Blum, A., Dixon, J. and White, A. F.: Strong climate and tectonic control on plagioclase weathering in granitic terrain, *Earth Planet. Sci. Lett.*, 301(3–4), 521–530, doi:10.1016/j.epsl.2010.11.037, 2011.

Raucsik, B. and Varga, A.: Climato-environmental controls on clay mineralogy of the Hettangian-Bajocian successions of the Mecsek Mountains, Hungary: An evidence for extreme continental weathering during the early Toarcian oceanic anoxic event, *Palaeogeogr. Palaeoclimatol. Palaeoecol.*, 265(1–2), 1–13, doi:10.1016/j.palaeo.2008.02.004, 2008.

von Raumer, J. F., Bussy, F., Schaltegger, U., Schulz, B. and Stampfli, G. M.: Pre-mesozoic alpine basements-their place in the European paleozoic framework, *Bull. Geol. Soc. Am.*, 125(1–2), 89–108, doi:10.1130/B30654.1, 2013.

Reinhardt, L. and Ricken, W.: The stratigraphic and geochemical record of Playa Cycles: monitoring a Pangaeen monsoon-like system (Triassic, Middle Keuper, S. Germany). [online] Available from: [www.elsevier.nl/locate/palaeo](http://www.elsevier.nl/locate/palaeo), 2000.

Retallack, G. J.: Postapocalyptic greenhouse paleoclimate revealed by earliest Triassic paleosols in the Sydney Basin, Australia, *Bull. Geol. Soc. Am.*, 111(1), 52–70, doi:10.1130/0016-7606(1999)111<0052:PGPRBE>2.3.CO;2, 1999.

Retallack, G. J.: *Soils of the past: An introduction to paleopedology*, second edi., Blackwell Science Ltd, London., 2006.

Richardson, J. B. and King, E. K.: Regolith weathering and sorption influences molybdenum, vanadium, and chromium export via stream water at four granitoid critical zone observatories, *Front. Earth Sci.*, 6(November), 1–15, doi:10.3389/feart.2018.00193, 2018.

Riebe, C. S., Kirchner, J. W., Granger, D. E. and Finkel, R. C.: Strong tectonic and weak climatic control of long-term chemical weathering rates, *Geology*, (6), 511–514, 2001.

Riebe, C. S., Kirchner, J. W. and Finkel, R. C.: Long-term rates of chemical weathering and physical erosion from cosmogenic nuclides and geochemical mass balance, *Geochim. Cosmochim. Acta*, 67(22), 4411–4427, doi:10.1016/S0016-7037(03)00382-X, 2003.

- 
- Robinson, D., Schmidt, S. T. and Santana De Zamora, A.: Reaction pathways and reaction progress for the smectite-to-chlorite transformation: Evidence from hydrothermally altered metabasites, *J. Metamorph. Geol.*, 20(1), 167–174, doi:10.1046/j.0263-4929.2001.00361.x, 2002.
- Roscher, M. and Schneider, J. W.: Permo-Carboniferous climate: Early Pennsylvanian to Late Permian climate development of central Europe in a regional and global context, *Geol. Soc. Spec. Publ.*, 265, 95–136, doi:10.1144/GSL.SP.2006.265.01.05, 2006.
- Ruddiman, W. F.: *EARTH'S CLIMATE Past and Future, Second.*, edited by V. Raymond, A. Baker, K. O'Shaughnessy, A. Thorne, P. Hull, and T. Szczepanski, W. H. Freeman and Company New, New York., 2008.
- Sandler, A., Teutsch, N. and Avigad, D.: Sub-Cambrian pedogenesis recorded in weathering profiles of the Arabian-Nubian Shield, *Sedimentology*, 59(4), 1305–1320, doi:10.1111/j.1365-3091.2011.01307.x, 2012.
- Santos, J. C. B. dos, Le Pera, E., Souza Júnior, V. S. de, Corrêa, M. M. and Azevedo, A. C. de: Gneiss saprolite weathering and soil genesis along an east-west regolith sequence (NE Brazil), *Catena*, 150, 279–290, doi:10.1016/j.catena.2016.11.031, 2017.
- Santos, J. C. B. dos, Le Pera, E., Souza Júnior, V. S. de, Oliveira, C. S. de, Juilleret, J., Corrêa, M. M. and Azevedo, A. C. de: Porosity and genesis of clay in gneiss saprolites: The relevance of saprolithology to whole regolith pedology, *Geoderma*, 319(December 2017), 1–13, doi:10.1016/j.geoderma.2017.12.031, 2018.
- Santos, J. C. B. dos, Le Pera, E., Oliveira, C. S. de, Souza Júnior, V. S. de, Pedron, F. de A., Corrêa, M. M. and Azevedo, A. C. de: Impact of weathering on REE distribution in soil-saprolite profiles developed on orthogneisses in Borborema Province, NE Brazil, *Geoderma*, 347(April 2018), 103–117, doi:10.1016/j.geoderma.2019.03.040, 2019.
- dos Santos, J. C. B., de Oliveira, C. S., Le Pera, E., Sartor, L. R., Corrêa, M. M., da Silva, A. H. N., Müller, C. R., Santos, R. A. and de Azevedo, A. C.: Saprolithology applied to pedology: Integrated study of soil and saprolite derived from crystalline rocks to better understand properties of whole

---

regoliths along a climate gradient (NE Brazil), *Geoderma*, 409(June 2021), doi:10.1016/j.geoderma.2021.115602, 2022a.

dos Santos, J. C. B., de Oliveira, C. S., Pera, E. Le, Sartor, L. R., Corrêa, M. M., da Silva, A. H. N., Santos, R. A., da Silva, L. F. V., Müller, C. R. and de Azevedo, A. C.: Saprolithology applied to pedology: Mineral alteration in soil-saprolite profiles along a climate gradient in Triunfo Massif (NE Brazil), *Catena*, 213(March), doi:10.1016/j.catena.2022.106214, 2022b.

Scarciglia, F., Critelli, S., Borrelli, L., Coniglio, S., Muto, F. and Perri, F.: Weathering profiles in granitoid rocks of the Sila Massif uplands, Calabria, southern Italy: New insights into their formation processes and rates, *Sediment. Geol.*, 336, 46–67, doi:10.1016/j.sedgeo.2016.01.015, 2016.

Scarpato, D. J.: *Rock Fractures in Geological Processes.*, 2013.

Schäferorgrname, O.: Tectonics and sedimentation in the continental strike-slip Saar-Nahe Basin (Carboniferous-Permian, West Germany), *Zeitschrift der Dtsch. Gesellschaft für Geowissenschaften*, 162(2), 127–155, doi:10.1127/1860-1804/2011/0162-0127, 2011a.

Schäferorgrname, O.: Tektonik und Sedimentation im kontinentalen Saar-Nahe-Becken ("Strike-slip"-Modell, Karbon-Perm, Westdeutschland), *Zeitschrift der Dtsch. Gesellschaft für Geowissenschaften*, 162(2), 127–155, doi:10.1127/1860-1804/2011/0162-0127, 2011b.

Schäffer, R., Bär, K., Fischer, S., Fritsche, J. G. and Sass, I.: Mineral, thermal and deep groundwater of Hesse, Germany, *Earth Syst. Sci. Data*, 13(10), 4847–4860, doi:10.5194/essd-13-4847-2021, 2021.

Schau, M. and Henderson, J. B.: Archean chemical weathering at three localities on the Canadian shield, *Precambrian Res.*, 7(C), 81–116, doi:10.1016/S0166-2635(08)70243-3, 1983.

Schmidt, C., Busch, B. and Hilgers, C.: Lateral variations of detrital, authigenic and petrophysical properties in an outcrop analog of the fluvial Plattensandstein, Lower Triassic, Central S-Germany, *Zeitschrift der Dtsch. Gesellschaft für Geowissenschaften*, 172(4), 541–564, doi:10.1127/zdgg/2020/0234, 2021.

---

Schmidt, S. T. and Robinson, D.: Metamorphic grade and porosity and permeability controls on mafic phyllosilicate distributions in a regional zeolite to greenschist facies transition of the North Shore Volcanic Group, Minnesota, *Bull. Geol. Soc. Am.*, 109(6), 683–697, doi:10.1130/0016-7606(1997)109<0683:MGAPAP>2.3.CO;2, 1997.

Schoenborn, W. A. and Fedo, C. M.: Provenance and paleoweathering reconstruction of the Neoproterozoic Johnnie Formation, southeastern California, *Chem. Geol.*, 285(1–4), 231–255, doi:10.1016/j.chemgeo.2011.04.014, 2011.

Scholze, F., Wang, X., Kirscher, U., Kraft, J., Schneider, J. W., Götz, A. E., Joachimski, M. M. and Bachtadse, V.: A multistratigraphic approach to pinpoint the Permian-Triassic boundary in continental depositsThe Zechstein–Lower Buntsandstein transition in Germany, *Glob. Planet. Change*, 152, 129–151, doi:10.1016/j.gloplacha.2017.03.004, 2017.

Schott, J., Berner, R. A. and Sjöberg, E. L.: Mechanism of pyroxene and amphibole weathering-I. Experimental studies of iron-free minerals, *Geochim. Cosmochim. Acta*, 45(11), 2123–2135, doi:10.1016/0016-7037(81)90065-X, 1981.

Schubert, W., Lippolt, H. J. and Schwarz, W.: Early to Middle Carboniferous hornblende  $^{40}\text{Ar}/^{39}\text{Ar}$  ages of amphibolites and gabbros from the Bergsträsser Odenwald, *Mineral. Petrol.*, 72(1–3), 113–132, doi:10.1007/s007100170029, 2001.

Schulmann, K., Catalán, J. R. M., Lardeaux, J. M., Janoušek, V. and Oggiano, G.: The Variscan orogeny: Extent, timescale and the formation of the European crust, *Geol. Soc. Spec. Publ.*, 405(1), 1–6, doi:10.1144/SP405.15, 2014.

Schulz, M. S. and White, A. F.: Chemical weathering in a tropical watershed, Luquillo Mountains, Puerto Rico III: Quartz dissolution rates, *Geochim. Cosmochim. Acta*, 63(3–4), 337–350, doi:10.1016/S0016-7037(99)00056-3, 1999.

Schumacher, M. E.: Upper Rhine Graben: Role of preexisting structures during rift evolution, *Tectonics*, 21(1), 6-1-6–17, doi:10.1029/2001TC900022, 2002.



---

Schwarz, M. and Henk, A.: Evolution and structure of the Upper Rhine Graben: Insights from three-dimensional thermomechanical modelling, *Int. J. Earth Sci.*, 94(4), 732–750, doi:10.1007/s00531-004-0451-2, 2005a.

Schwarz, M. and Henk, A.: Evolution and structure of the Upper Rhine Graben: Insights from three-dimensional thermomechanical modelling, *Int. J. Earth Sci.*, 94(4), 732–750, doi:10.1007/s00531-004-0451-2, 2005b.

von Seckendorff, V., Arz, C. and Lorenz, V.: Magmatism of the late Variscan intermontane Saar-Nahe Basin (Germany): A review, *Geol. Soc. Spec. Publ.*, 223, 361–391, doi:10.1144/GSL.SP.2004.223.01.16, 2004a.

von Seckendorff, V., Timmerman, M. J., Kramer, W. and Wrobel, P.: New <sup>40</sup>Ar/<sup>39</sup>Ar ages and geochemistry of late Carboniferous-early Permian lamprophyres and related volcanic rocks in the Saxothuringian Zone of the Variscan Orogen (Germany), *Geol. Soc. Spec. Publ.*, 223, 335–359, doi:10.1144/GSL.SP.2004.223.01.15, 2004b.

Sequeira Braga, M. A., Paquet, H. and Begonha, A.: Weathering of granites in a temperate climate (NW Portugal): Granitic saprolites and arenization, *Catena*, 49(1–2), 41–56, doi:10.1016/S0341-8162(02)00017-6, 2002.

Sheldon, N. D.: Quaternary Glacial-Interglacial Climate Cycles in Hawaii, , 114, 367–376, 2006.

Sheldon, N. D. and Tabor, N. J.: Quantitative paleoenvironmental and paleoclimatic reconstruction using paleosols, *Earth Sci. Rev.*, 95(1–2), 1–52, doi:10.1016/j.earscirev.2009.03.004, 2009.

Shoenfelt, E. M., Winckler, G., Annett, A. L., Hendry, K. R. and Bostick, B. C.: Physical Weathering Intensity Controls Bioavailable Primary Iron(II) Silicate Content in Major Global Dust Sources, *Geophys. Res. Lett.*, 46(19), 10854–10864, doi:10.1029/2019GL084180, 2019.

Singer, A.: Illite in aridic soils, desert dusts and desert loess, *Sediment. Geol.*, 59(3–4), 251–259, doi:10.1016/0037-0738(88)90079-6, 1988.

Sinisi, R., Mongelli, G., Mameli, P. and Oggiano, G.: Did the Variscan relief influence the Permian climate of Mesoeuropeα Insights from geochemical and mineralogical proxies from Sardinia

---

(Italy), *Palaeogeogr. Palaeoclimatol. Palaeoecol.*, 396, 132–154, doi:10.1016/j.palaeo.2013.12.030, 2014.

Sissingh, W.: Tertiary paleogeographic and tectonostratigraphic evolution of the Rhenish Triple Junction, *Palaeogeogr. Palaeoclimatol. Palaeoecol.*, 196(1–2), 229–263, doi:10.1016/S0031-0182(03)00320-1, 2003.

Sreedevi, S., Eldho, T. I. and Jayasankar, T.: Physically-based distributed modelling of the hydrology and soil erosion under changes in landuse and climate of a humid tropical river basin, *CATENA*, 217, 106427, doi:https://doi.org/10.1016/j.catena.2022.106427, 2022.

Stataude, S., Mordhorst, T., Nau, S., Pfaff, K., Brüggmann, G., Jacob, D. E. and Markl, G.: Hydrothermal carbonates of the schwarzwald ore district, southwestern Germany: Carbon source and conditions of formation using  $\delta^{18}\text{O}$ ,  $\delta^{13}\text{C}$ ,  $87\text{Sr}/86\text{Sr}$ , and fluid inclusions, *Can. Mineral.*, 50(5), 1401–1434, doi:10.3749/canmin.50.5.1401, 2012.

Staude, S., Göb, S., Pfaff, K., Ströbele, F., Premo, W. R. and Markl, G.: Deciphering fluid sources of hydrothermal systems: A combined Sr- and S-isotope study on barite (Schwarzwald, SW Germany), *Chem. Geol.*, 286(1–2), 1–20, doi:10.1016/j.chemgeo.2011.04.009, 2011.

Stein, E.: The geology of the Odenwald Crystalline Complex, *Mineral. Petrol.*, 72(1–3), 7–28, doi:10.1007/s007100170024, 2001.

Stimac, J., Goff, F. and Goff, C. J.: Intrusion-Related Geothermal Systems, in *The Encyclopedia of Volcanoes*, pp. 799–822, Dr Jim Stimac, Copyright © 2015., 2015.

Stinchcomb, G. E., Nordt, L. C., Driese, S. G., Lukens, W. E., Williamson, F. C. and Tubbs, J. D.: A DATA-DRIVEN SPLINE MODEL DESIGNED TO PREDICT PALEOCLIMATE USING PALEOSOL GEOCHEMISTRY, *Am. J. Sci.*, 316, 746–777, doi:10.2475/08.2016.02, 2016.

Stipp, M., Stünitz, H., Heilbronner, R. and Schmid, S. M.: Dynamic recrystallization of quartz: Correlation between natural and experimental conditions, *Geol. Soc. Spec. Publ.*, 200(May 2014), 171–190, doi:10.1144/GSL.SP.2001.200.01.11, 2002.

- 
- Stollhofen, H.: Facies architecture variations and seismogenic structures in the Carboniferous-Permian Saar-Nahe Basin (SW Germany): evidence for extension-related transfer fault activity., 1998.
- Stolz, C., Grunert, J. and Füllung, A.: Quantification and dating of floodplain sedimentation in a medium-sized catchment of the German uplands: A case study from the Aar Valley in the southern Rhenish Massif, Germany, *Erde*, 144(1), 30–50, doi:10.12854/erde-144-3, 2013.
- Taylor, R. and Howard, K.: A tectono-geomorphic model of the hydrogeology of deeply weathered crystalline rock: Evidence from Uganda, *Hydrogeol. J.*, 8(3), 279–294, doi:10.1007/s100400000069, 2000.
- Taylor, R. G. and Howard, K. W. F.: Post-Palaeozoic evolution of weathered landsurfaces in Uganda by tectonically controlled deep weathering and stripping, *Geomorphology*, 25(3–4), 173–192, doi:10.1016/S0169-555X(98)00040-3, 1998.
- Taylor, S. R. and McLennan, S. M.: *The Continental Crust: Its Composition and Evolution*, Blackwell, Oxford, United Kingdom., 1985.
- Thomson, B. J., Hurowitz, J. A., Baker, L. L., Bridges, N. T., Lennon, A. M., Paulsen, G. and Zacny, K.: The effects of weathering on the strength and chemistry of Columbia River Basalts and their implications for Mars Exploration Rover Rock Abrasion Tool (RAT) results, *Earth Planet. Sci. Lett.*, 400, 130–144, doi:10.1016/j.epsl.2014.05.012, 2014.
- Timar-Geng, Z., Fügenschuh, B., Schaltegger, U. and Wetzel, A.: The impact of the Jurassic hydrothermal activity on zircon fission track data from the southern Upper Rhine Graben area, *Schweizerische Mineral. und Petrogr. Mitteilungen*, 84(3), 257–269, 2004.
- Timar-Geng, Z., Fügenschuh, B., Wetzel, A. and Dresmann, H.: Low-temperature thermochronology of the flanks of the southern Upper Rhine Graben, *Int. J. Earth Sci.*, 95(4), 685–702, doi:10.1007/s00531-005-0059-1, 2006.
- Tripathi, J. K. and Rajamani, V.: Geochemistry of the loessic sediments on Delhi ridge, eastern Thar desert, Rajasthan: implications for exogenic processes., 1999.

- 
- Tuğrul, A. and Gurpinar, O.: A proposed weathering classification for basalts and their engineering properties (Turkey), *Bull. - Int. Assoc. Eng. Geol.*, 55, 139–149, doi:10.1007/BF02635416, 1997.
- Tuğrul, A.: The effect of Chemical weathering on the engineering properties of Eocene basalts in Northeastern Turkey, *Environ. Eng. Geosci.*, 2, 225–234, doi:https://doi.org/10.2113/gseegeosci.III.2.225, 1997.
- Tuğrul, A.: The effect of weathering on pore geometry and compressive strength of selected rock types from Turkey, *Eng. Geol.*, 75(3–4), 215–227, doi:10.1016/j.enggeo.2004.05.008, 2004.
- Ündül, Ö. and Tuğrul, A.: On the variations of geo-engineering properties of dunites and diorites related to weathering, *Environ. Earth Sci.*, 75(19), doi:10.1007/s12665-016-6152-x, 2016.
- Ündül, Ö. and Tuğrul, A.: The influence of weathering on the engineering properties of dunites, *Rock Mech. Rock Eng.*, 45(2), 225–239, doi:10.1007/s00603-011-0174-1, 2012.
- Varajao, A. F. D. C., Gilkes, R. J. and Hart, R. D.: The relationships between kaolinite crystal properties and the origin of materials for a Brazilian kaolin deposit, *Clays Clay Miner.*, 49(1), 44–59, doi:10.1346/CCMN.2001.0490104, 2001.
- Vázquez, M., Ramírez, S., Morata, D., Reich, M., Braun, J. J. and Carretier, S.: Regolith production and chemical weathering of granitic rocks in central Chile, *Chem. Geol.*, 446, 87–98, doi:10.1016/j.chemgeo.2016.09.023, 2016.
- Vogt, T.: Sulitjelmfeltets geologi og petrografi, *Norges Geol. Undersokelse*, 121, 1–560, 1927.
- Wagner, G. A., Kernphysik, M. and Heidelberg, D.-: Crystalline Basement of Middle Europe, *Tracks A J. Artist. Writings*, 17(3), 277–282, 1990.
- Walter, B., Géraud, Y., Bartier, D., Kluska, J. M., Diraison, M., Morlot, C. and Raisson, F.: Petrophysical and mineralogical evolution of weathered crystalline basement in western Uganda: Implications for fluid transfer and storage, *Am. Assoc. Pet. Geol. Bull.*, 102(6), 1035–1065, doi:10.1306/0810171610917171, 2018.
- White, A. F. and Brantley, S. L.: The effect of time on the weathering of silicate minerals: Why do weathering rates differ in the laboratory and field?, *Chem. Geol.*, 202(3–4), 479–506, doi:10.1016/j.chemgeo.2003.03.001, 2003.

- 
- White, A. F., Bullen, T. D., Schulz, M. S., Blum, A. E., Huntington, T. G. and Peters, N. E.: Differential rates of feldspar weathering in granitic regoliths, *Geochim. Cosmochim. Acta*, 65(6), 847–869, doi:10.1016/S0016-7037(00)00577-9, 2001a.
- White, A. F., Bullen, T. D., Schulz, M. S., Blum, A. E., Huntington, T. G. and Peters, N. E.: Differential rates of feldspar weathering in granitic regoliths, *Geochim. Cosmochim. Acta*, 65(6), 847–869, doi:10.1016/S0016-7037(00)00577-9, 2001b.
- White, W. M.: Chapter 9: Stable isotopes Geochemistry, in *Geochemistry*, pp. 361–480. [online] Available from: <https://www.imwa.info/geochemistry/Chapters/Chapter09.pdf>, 2009.
- Willner, A. P., Massonne, H. J. and Krohe, A.: Tectono-thermal evolution of a part of a Variscan magmatic arc: The Odenwald in the Mid-German Crystalline Rise, *Geol. Rundschau*, 80(2), 369–389, doi:10.1007/BF01829372, 1991.
- Wu, C., Long, H., Cheng, T., Liu, L., Qian, P., Wang, H., Ren, S., Zhou, L. and Zheng, X.: Quantitative estimations of iron oxide minerals in the Late Pleistocene paleosol of the Yangtze River Delta: Implications for the chemical weathering, sedimentary environment, and burial conditions, *Catena*, 207(July), 105662, doi:10.1016/j.catena.2021.105662, 2021.
- Wu, K., Paton, D. and Zha, M.: Unconformity structures controlling stratigraphic reservoirs in the north-west margin of Junggar basin, North-west China, *Front. Earth Sci.*, 7(1), 55–64, doi:10.1007/s11707-012-0344-9, 2013.
- Yang, M., Liang, X., Ma, L., Huang, J., He, H. and Zhu, J.: Adsorption of REEs on kaolinite and halloysite: A link to the REE distribution on clays in the weathering crust of granite, *Chem. Geol.*, 525(June), 210–217, doi:10.1016/j.chemgeo.2019.07.024, 2019.
- Zeh, A. and Brätz, H.: Timing of Upper Carboniferous-Permian horst-basin formation and magmatism in the NW Thuringian Forest, central Germany: A review, *Geol. Soc. Spec. Publ.*, 223, 319–334, doi:10.1144/GSL.SP.2004.223.01.14, 2004.
- Zeh, A. and Gerdes, A.: Baltica- and Gondwana-derived sediments in the Mid-German Crystalline Rise (Central Europe): Implications for the closure of the Rheic ocean, *Gondwana Res.*, 17(2–3), 254–263, doi:10.1016/j.gr.2009.08.004, 2010.

---

Zeh, A. and Will, T. M.: The mid-German crystalline zone, Pre-Mesozoic Geol. Saxo-Thuringia. From Cadomian Act. Margin to Variscan Orogen, 195–220, 2008.

Zhou, L., Friis, H., Yang, T. and Nielsen, A. T.: Geochemical interpretation of the Precambrian basement and overlying Cambrian sandstone on Bornholm, Denmark: Implications for the weathering history, *Lithos*, 286–287, 369–387, doi:10.1016/j.lithos.2017.06.019, 2017.

Ziegler, P. A.: Triassic rifts and facies patterns in Western and Central Europe, *Geol. Rundschau*, 71(3), 747–772, doi:10.1007/BF01821101, 1982.

Ziegler, P. A. and Dèzes, P.: Evolution of the lithosphere in the area of the rhine rift system, *Int. J. Earth Sci.*, 94(4), 594–614, doi:10.1007/s00531-005-0474-3, 2005.

Ziegler, P. A., Schumacher, M. E., Dèzes, P., van Wees, J. D. and Cloetingh, S.: Post-Variscan evolution of the lithosphere in the Rhine Graben area: Constraints from subsidence modelling, *Geol. Soc. Spec. Publ.*, 223, 289–317, doi:10.1144/GSL.SP.2004.223.01.13, 2004.

## Appendix

### Appendix II-I

Table A 1: The XRD results of basaltic andesite and gabbroic diorite in GA1

	depth	Plagio- clase	K-feld- spar	Pyroxene	Amphi- bole	Quartz	Il- lite/Mus- lite	Vermicu- lite	Kaolinite
Basaltic andesite	13.9	0.0	0.0	0.0	0.0	6.1	0.0	6.6	5.1
	14.5	53.8	0.0	3.0	0.0	6.7	8.9	3.5	0.0
	15.3	66.1	0.0	2.9	0.0	4.6	6.3	4.4	1.9
	16.3	58.0	0.0	2.5	0.0	13.2	4.7	3.8	1.9
	17.8	66.4	0.0	2.8	0.0	11.7	0.0	2.9	2.3
	19.3	76.8	0.0	3.8	0.0	0.9	0.0	0.0	1.5
Gabbroic diorites	20.6	7.6	0.0	0.0	0.0	16.7	48.9	0.0	2.6
	21.5	7.2	4.8	0.0	0.0	25.8	24.1	0.0	0.0
	22.5	29.0	0.0	0.0	0.0	13.1	55.5	0.0	1.6
	23.5	27.7	0.0	0.0	0.0	7.5	60.9	1.9	0.5
	24.5	32.2	0.0	0.0	4.7	12.5	49.2	0.0	0.0
	25.5	38.8	0.0	0.0	5.2	11.5	42.2	0.0	0.5
	26.5	36.5	0.0	0.0	4.9	16.4	40.4	0.0	0.0
	27.5	26.9	0.0	0.0	7.9	7.0	56.2	0.9	0.5
	28.7	40.6	0.0	0.0	3.2	7.1	46.8	1.0	0.7
	55.5	45.1	0.0	0.0	19.1	11.6	20.6	0.9	0.7
56.5	41.5	0.0	0.0	18.1	5.9	25.0	0.8	0.7	

Table A 1 continued.

	depth	Mixed layer I-S	Anatase	Hematite	Calcite	Dolomite
Basaltic andesite	13.9	75.4	2.0	2.5	2.4	0.0
	14.5	0.0	0.7	2.3	21.0	0.0
	15.3	0.0	0.8	3.0	10.2	0.0
	16.3	0.0	0.7	0.8	14.3	0.0
	17.8	0.0	0.7	2.4	6.1	4.7
	19.3	0.0	1.0	3.5	11.1	1.5
Gabbroic diorites	20.6	19.0	0.0	0.7	4.5	0.0
	21.5	28.3	0.2	1.1	0.0	8.5
	22.5	0.0	0.0	0.2	0.6	0.0
	23.5	0.0	0.0	0.2	0.2	1.0
	24.5	0.0	0.0	0.4	0.6	0.5
	25.5	0.0	0.0	0.5	1.0	0.4
	26.5	0.0	0.0	0.5	0.8	0.6
	27.5	0.0	0.0	0.3	0.2	0.3
	28.7	0.0	0.0	0.2	0.3	0.2
	55.5	0.0	0.0	1.2	0.8	0.0
56.5	6.9	0.2	0.5	0.5	0.0	



Table A 2: The major elements results of sedimentary rock, basaltic andesite and gabbroic diorite in GA1

	Depth(m)	MgO	Al <sub>2</sub> O <sub>3</sub>	CaO	K <sub>2</sub> O	Na <sub>2</sub> O	SiO <sub>2</sub>	P <sub>2</sub> O <sub>5</sub>	TiO <sub>2</sub>	MnO	Fe <sub>2</sub> O <sub>3</sub>	LOI
sedimentary rock	5.5	1.2	14.4	0.5	4.8	1.0	66.3	0.1	0.4	0.0	3.6	7.1
	6.6	1.3	15.3	0.6	4.8	1.0	64.7	0.1	0.4	0.0	1.7	9.7
	7.2	1.1	15.3	0.5	5.3	1.1	69.8	0.1	0.3	0.0	3.3	2.9
	8.4	1.5	16.5	0.6	5.5	1.0	66.9	0.1	0.4	0.0	4.2	2.9
	11.3	1.6	15.4	0.8	4.5	0.9	66.7	0.1	0.7	0.0	5.7	3.2
	12.2	1.2	12.3	7.3	4.3	1.4	65.9	0.0	0.3	0.1	3.0	3.7
	13.6	1.1	11.4	13.8	3.8	1.4	57.1	0.1	0.3	0.3	5.3	5.1
Basaltic andesite	13.9	2.6	22.8	1.6	5.9	0.1	47.3	0.3	1.7	0.0	8.7	8.5
	14.3	1.9	16.0	11.4	3.1	2.6	44.7	0.2	1.2	0.2	5.8	13.0
	15.3	2.4	17.5	6.3	2.7	3.3	45.9	0.2	1.3	0.1	11.3	8.9
	16.3	2.4	15.2	11.8	1.5	3.4	46.2	0.1	1.0	0.2	4.8	13.2
	17.8	3.2	13.9	9.9	0.3	4.4	45.1	0.1	0.9	0.2	8.5	13.6
	19.3	1.8	13.8	12.3	0.6	5.6	41.4	0.2	1.0	0.2	10.3	12.2
Gabbroic diorites	20.6	3.2	16.0	5.8	3.9	0.9	51.9	0.2	0.8	0.1	7.6	9.3
	21.5	5.0	13.7	5.8	4.0	0.8	48.3	0.1	0.7	0.2	8.9	12.0
	22.5	2.4	18.3	4.1	2.1	2.9	57.9	0.2	0.9	0.1	6.6	4.5
	23.5	3.2	15.9	6.4	1.8	2.8	54.2	0.2	0.7	0.1	8.8	5.8
	24.5	2.9	17.0	5.8	1.9	3.2	55.2	0.2	0.8	0.1	9.7	3.0
	25.5	3.0	17.3	5.9	1.9	3.2	55.9	0.2	0.8	0.1	8.5	2.9
	26.7	3.0	17.4	5.7	1.8	3.1	56.0	0.2	0.9	0.1	9.0	3.0
	27.1	3.0	17.4	5.8	1.9	3.2	56.0	0.2	0.9	0.1	8.4	2.7
	28.5	3.0	17.5	5.4	1.8	3.2	56.2	0.2	0.8	0.1	8.6	3.4
	55.5	3.2	18.1	7.0	1.5	3.4	55.0	0.2	0.9	0.2	9.3	1.1
	56.5	3.2	18.0	6.8	1.6	3.4	55.4	0.2	0.9	0.2	9.0	1.0

Table A 3: The trace elements results of sedimentary rock, basaltic andesite and gabbroic diorite in GA1

Depth(m)	Sc	Ti	V	Cr	Mn	Co	Ni	Cu	Zn	Ga	Ge	Rb	Sr	
sedimen- tary rock	5.48	10.1	3268.2	44.5	38.0	247.2	270.3	18.0	11.7	27.4	17.4	2.4	196.9	
	6.6	10.8	1144.1	21.2	44.9	623.7	73.2	15.3	17.9	19.0	12.6	1.6	262.7	
	7.23	8.9	1626.9	28.9	28.7	535.8	107.6	13.1	8.4	15.1	13.7	1.6	210.7	
	8.38	9.8	5656.4	34.5	38.3	350.7	63.7	16.3	5.8	23.3	25.7	1.7	239.9	
	11.3	12.9	653.1	53.4	245.3	153.7	75.3	36.7	6.8	38.0	11.7	1.7	104.5	
	12.24	10.2	1216.8	29.2	74.7	312.4	99.5	36.0	5.0	19.7	12.7	1.7	193.5	
	13.56	6.6	1153.6	98.9	22.4	553.6	65.2	43.3	9.0	22.7	15.4	1.8	30.5	292.4
	13.9	46.1	11277.	391.1	769.7	393.6	38.1	229.8	11.0	96.5	28.1	3.7	381.0	45.5
	14.3	32.4	7095.2	159.3	432.7	1828.3	24.5	160.5	11.9	45.1	15.9	2.4	186.8	68.7
	15.3	32.6	7614.6	233.3	543.6	1030.2	35.7	186.8	21.0	51.8	18.7	3.3	159.5	68.9
Basaltic andesite	16.3	31.7	6399.9	195.2	429.2	1979.8	48.3	213.8	8.7	66.5	15.6	2.2	84.7	86.7
	17.8	26.8	5744.4	160.4	446.5	1403.7	49.1	158.7	7.0	90.3	14.1	2.4	17.3	123.1
	19.3	28.7	6257.3	155.5	447.9	1500.8	27.1	117.6	11.9	59.7	13.7	2.9	32.4	122.6
	20.6	15.2	4812.8	160.9	21.2	988.6	28.0	54.1	6.5	58.4	19.4	2.6	208.8	61.6
	21.5	14.4	4071.5	145.4	15.6	1353.1	56.4	91.6	33.0	86.3	16.3	3.1	227.2	66.9
	22.5	22.1	5121.1	150.5	23.5	541.9	30.1	24.7	14.1	99.3	19.5	2.2	106.8	235.6
	23.5	19.2	4465.1	157.8	45.5	1013.8	28.2	10.4	21.8	92.3	18.7	2.6	83.2	326.7
	24.5	19.0	4944.1	165.7	101.7	869.9	32.8	8.8	18.5	90.5	20.0	2.8	80.9	342.2
	25.5	18.4	4848.7	159.7	64.9	897.1	31.6	4.9	17.3	88.7	19.6	2.4	65.0	348.3
	26.7	19.3	5159.6	166.6	50.3	900.5	95.7	6.4	21.0	92.1	19.7	2.6	72.0	338.2
Gabbroic diorites	27.1	17.1	5223.4	159.7	120.4	1008.5	31.1	5.6	15.9	92.8	20.0	2.5	68.8	348.1
	28.5	19.7	4787.5	155.2	77.1	1025.9	29.4	5.8	21.4	97.9	20.3	2.4	66.1	348.0
	55.5	20.7	5199.1	173	319.6	1256	39.1	11.8	19.8	86.6	21.1	2.6	43.4	413.2
	56.5	20.5	5111.7	190.2	230.2	1179.4	27.8	10.6	21.8	88.6	21.0	2.6	46.2	417.9

Table A3 continued.

	Depth(	Y	Zr	Nb	Cs	Ba	Hf	Ta	Pb	Th	U
sedimen- tary rock	5.48	48.0	135.8	8.3	178.4	669.8	4.0	1.9	23.2	5.9	1.6
	6.6	10.1	58.9	3.3	150.6	1048.8	1.7	2.3	18.0	7.9	1.1
	7.23	11.9	84.6	5.7	155.3	317.2	2.5	2.8	23.1	10.0	1.2
	8.38	10.9	197.9	17.1	193.3	312.0	5.5	2.2	19.4	6.1	1.5
	11.3	10.3	47.9	2.3	180.3	335.1	1.5	1.9	11.7	8.6	1.5
	12.24	9.1	71.3	4.3	121.3	215.9	2.0	2.7	16.1	4.9	0.8
	13.56	11.2	68.6	5.4	121.0	366.9	1.8	2.9	20.8	5.7	1.2
Basaltic andesite	13.9	37.5	175.6	8.9	128.0	74.0	4.6	0.6	14.9	5.5	3.6
	14.3	34.1	113.2	5.7	45.2	56.5	3.1	0.4	9.7	3.7	2.0
	15.3	29.0	118.6	5.9	46.6	64.7	3.4	0.4	12.7	3.8	1.9
	16.3	34.9	113.4	5.0	21.3	31.8	2.9	0.4	10.1	3.3	6.9
	17.8	26.4	98.5	4.6	8.1	34.9	2.6	0.3	17.0	3.1	1.5
	19.3	36.0	106.2	5.0	7.6	62.1	2.7	0.4	17.7	3.1	3.1
	20.6	14.7	103.0	6.0	50.3	978.4	2.9	0.5	6.7	3.7	1.6
Gabbroic diorites	21.5	23.7	117.4	5.2	49.0	254.4	3.4	0.7	19.4	5.2	2.5
	22.5	10.4	69.6	6.1	39.4	391.4	2.1	0.6	10.3	4.8	1.2
	23.5	29.6	104.5	6.1	18.3	724.5	3.0	0.7	12.4	4.3	1.5
	24.5	23.6	113.8	7.1	14.8	404.5	3.3	1.1	12.7	5.9	1.8
	25.5	25.8	119.7	6.3	10.9	414.3	3.4	0.8	12.2	7.2	1.8
	26.7	26.1	121.6	6.1	13.5	471.8	3.5	1.8	13.3	5.1	1.7
	27.1	24.1	102.3	6.2	10.2	496.9	3.0	0.7	10.7	4.1	1.7
	28.5	24.0	100.4	5.8	9.2	497.8	2.8	0.7	11.6	4.0	1.4
	55.5	28.6	111.6	6.5	2.7	402.8	3.1	0.8	11.3	4.8	2.3
	56.5	28.7	109.4	6.3	3.3	432.4	3.0	0.6	12.3	3.7	1.5

Table A 4: The REE results of sedimentary rock, basaltic andesite and gabbroic diorite in GA1

	depth(m)	La	Ce	Pr	Nd	Sm	Eu	Gd	Tb	Dy	Ho	Er	Tm	Yb	Lu
<b>sedimentary rock</b>	5.5	17.1	35.9	4.5	21.6	11.9	3.0	13.2	1.8	9.9	1.8	4.7	0.6	3.5	0.5
	6.6	20.8	42.8	4.9	18.0	3.2	0.8	2.6	0.4	2.1	0.4	1.2	0.2	1.1	0.2
	7.2	19.3	41.9	4.4	15.8	3.4	0.9	3.4	0.4	2.3	0.4	1.3	0.2	1.2	0.2
	8.4	17.3	36.5	4.3	16.6	3.2	0.9	2.8	0.4	2.3	0.4	1.2	0.2	1.2	0.2
	11.3	10.4	19.0	2.3	8.7	1.8	0.5	1.9	0.3	2.1	0.5	1.4	0.2	1.7	0.3
	12.2	29.3	52.7	5.1	15.6	2.5	0.8	2.3	0.4	2.1	0.4	1.2	0.2	1.5	0.2
	13.6	24.0	35.4	3.8	13.7	2.7	0.9	2.6	0.4	2.3	0.5	1.3	0.2	1.4	0.2
<b>Basaltic andesite</b>	13.9	17.1	43.1	5.6	24.3	6.4	1.7	6.8	1.1	6.7	1.4	3.5	0.5	2.8	0.4
	14.3	15.1	37.6	4.8	20.7	5.2	1.3	5.5	0.9	5.8	1.2	3.2	0.4	2.8	0.4
	15.3	12.5	30.7	3.9	16.7	4.2	1.1	4.5	0.8	4.8	1.0	2.8	0.4	2.7	0.4
	16.3	17.6	37.5	5.1	21.5	4.9	1.4	5.6	0.9	5.4	1.2	3.1	0.4	2.8	0.4
	17.8	14.7	31.0	4.1	17.3	3.9	1.2	4.4	0.7	4.5	1.0	2.5	0.4	2.3	0.4
	19.3	19.0	42.2	5.8	25.2	6.1	1.5	6.3	1.0	5.6	1.2	3.0	0.4	2.4	0.4
<b>Gabbroic diorites</b>	20.6	14.3	26.6	3.4	13.3	2.8	0.6	2.7	0.4	2.5	0.5	1.4	0.2	1.4	0.2
	21.5	17.8	41.3	5.6	21.5	4.9	1.2	4.6	0.8	4.8	1.0	2.7	0.4	2.7	0.4
	22.5	15.8	40.1	5.3	21.2	3.8	1.0	2.8	0.4	2.2	0.4	1.2	0.2	1.2	0.2
	23.5	22.0	46.9	6.0	23.7	5.2	1.3	5.0	0.8	4.9	1.1	3.0	0.4	2.9	0.5
	24.5	19.3	41.5	5.3	20.7	4.4	1.1	4.1	0.7	4.1	0.9	2.4	0.4	2.4	0.4
	25.5	18.8	41.1	5.4	21.2	4.7	1.2	4.5	0.7	4.5	0.9	2.6	0.4	2.6	0.4
	26.7	18.7	39.6	5.3	22.0	5.0	1.2	4.8	0.8	4.8	1.0	2.7	0.4	2.6	0.4
	27.1	17.7	38.2	5.1	20.6	4.6	1.2	4.3	0.7	4.3	0.9	2.4	0.4	2.2	0.4
	28.5	17.9	38.6	5.0	20.1	4.6	1.2	4.4	0.7	4.4	0.9	2.5	0.4	2.3	0.4
	55.5	22.4	46.9	6.2	24.8	5.4	1.4	5.0	0.8	5.0	1.0	2.8	0.4	2.6	0.4
	56.5	21.2	45.5	5.9	24.4	5.4	1.4	5.3	0.9	5.2	1.1	2.9	0.4	2.6	0.4

Table A 5: The  $\tau$  value results of sedimentary rock, basaltic andesite and gabbroic diorite in GA1

well depth(m)	Basaltic andesite				
	13.9	14.3	15.3	16.3	17.8
MgO	-0.20	-0.10	0.01	0.24	0.83
Al <sub>2</sub> O <sub>3</sub>	-0.06	-0.01	-0.02	0.06	0.05
CaO	-0.93	-0.21	-0.60	-0.07	-0.15
K <sub>2</sub> O	4.22	3.14	2.27	1.24	-0.44
K <sub>2</sub> O <sub>corr</sub>	-0.59	-0.35	-0.32	-0.21	-0.08
Na <sub>2</sub> O	-0.99	-0.61	-0.55	-0.42	-0.18
SiO <sub>2</sub>	-0.35	-0.08	-0.14	0.08	0.14
P <sub>2</sub> O <sub>5</sub>	-0.07	0.05	-0.09	-0.11	-0.05
MnO	-0.87	0.06	-0.46	0.25	0.03
Fe <sub>2</sub> O <sub>3</sub>	-0.52	-0.51	-0.15	-0.55	-0.13
Sc	-0.11	0.00	-0.07	0.08	0.02
V	-0.05	-0.10	0.23	0.23	0.12
Cr	-0.05	-0.15	0.00	-0.06	0.09
Co	-0.22	-0.20	0.08	0.74	0.98
Ni	0.08	0.20	0.31	0.78	0.47
Cu	-0.49	-0.12	0.44	-0.29	-0.36
Zn	-0.10	-0.33	-0.29	0.09	0.65
Ga	0.14	0.02	0.12	0.11	0.12
Ge	-0.29	-0.26	-0.06	-0.25	-0.10
Rb	5.53	4.09	3.05	1.56	-0.42
Sr	-0.79	-0.51	-0.54	-0.31	0.09
Y	-0.42	-0.17	-0.34	-0.05	-0.20
Zr	-0.08	-0.06	-0.08	0.04	0.01
Nb	-0.01	0.01	-0.02	-0.01	0.01
Cs	8.36	4.25	4.04	1.75	0.16
Ba	-0.34	-0.20	-0.14	-0.50	-0.39
La	-0.50	-0.30	-0.46	-0.10	-0.16
Ce	-0.43	-0.21	-0.40	-0.13	-0.20
Pr	-0.47	-0.27	-0.45	-0.15	-0.23
Nd	-0.46	-0.28	-0.46	-0.16	-0.25
Sm	-0.41	-0.24	-0.44	-0.20	-0.29
Eu	-0.37	-0.22	-0.41	-0.06	-0.14
Gd	-0.41	-0.23	-0.42	-0.13	-0.24
Tb	-0.35	-0.16	-0.37	-0.08	-0.18
Dy	-0.34	-0.09	-0.30	-0.06	-0.14
Ho	-0.35	-0.07	-0.26	0.01	-0.09
Er	-0.37	-0.08	-0.24	-0.01	-0.09
Tm	-0.35	-0.04	-0.17	0.07	-0.01
Yb	-0.35	0.01	-0.10	0.11	0.03
Lu	-0.40	-0.01	-0.09	0.13	0.05
Hf	-0.06	0.03	0.02	0.06	0.06
Ta	-0.13	0.01	-0.09	-0.04	0.03
Pb	-0.53	-0.52	-0.41	-0.44	0.05
Th	-0.03	0.04	0.00	0.03	0.06
U	-0.35	-0.44	-0.49	1.18	-0.48

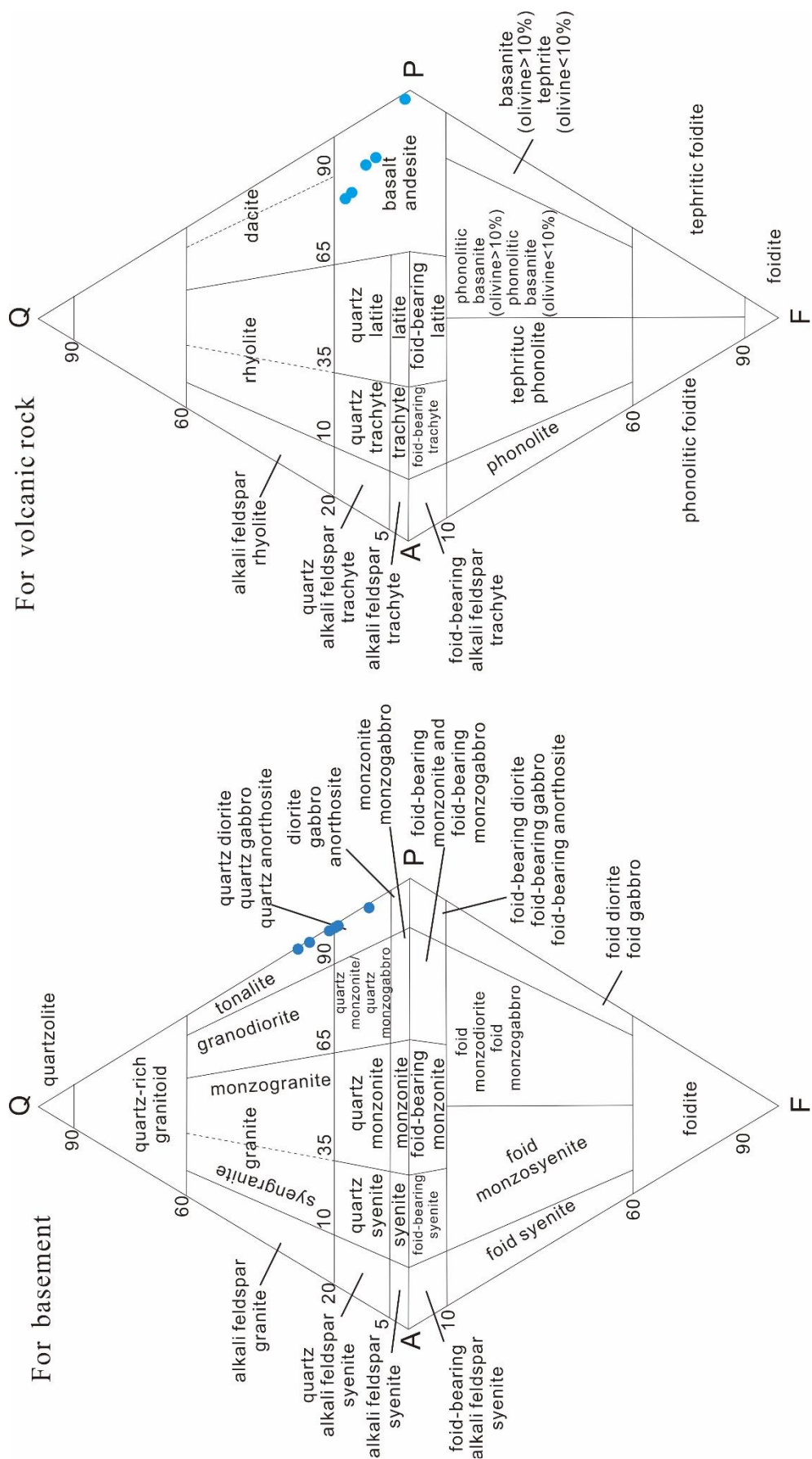
Table A5 continued.

well	Gabbroic diorites								
	20.6	21.5	22.5	23.5	24.5	25.5	26.7	27.1	28.5
MgO	0.17	1.21	-0.19	0.22	0.07	0.05	0.01	0.01	0.09
Al <sub>2</sub> O <sub>3</sub>	0.04	0.08	0.09	0.10	0.10	0.07	0.05	0.03	0.12
CaO	0.01	0.21	-0.36	0.17	-0.01	-0.03	-0.09	-0.08	-0.09
K <sub>2</sub> O	1.80	2.50	0.41	0.42	0.39	0.29	0.22	0.24	0.31
K <sub>2</sub> O <sub>corr</sub>	-0.26	-0.23	-0.01	0.04	0.07	0.03	-0.01	-0.01	0.07
Na <sub>2</sub> O	-0.69	-0.67	-0.10	0.04	0.09	0.06	-0.02	0.01	0.08
SiO <sub>2</sub>	0.10	0.24	0.11	0.22	0.16	0.12	0.10	0.07	0.17
P <sub>2</sub> O <sub>5</sub>	-0.01	-0.60	-0.02	-0.06	0.01	-0.08	-0.12	-0.04	0.02
MnO	-0.04	0.60	-0.50	0.04	-0.17	-0.14	-0.17	-0.14	0.01
Fe <sub>2</sub> O <sub>3</sub>	-0.02	0.40	-0.22	0.22	0.25	0.05	0.08	-0.01	0.10
Sc	-0.21	-0.11	0.08	0.07	-0.04	-0.05	-0.07	-0.18	0.03
V	-0.05	0.01	-0.17	0.00	-0.05	-0.06	-0.08	-0.13	-0.08
Cr	-0.92	-0.93	-0.91	-0.81	-0.61	-0.75	-0.82	-0.57	-0.70
Co	-0.10	1.13	-0.09	-0.03	0.02	0.00	1.86	-0.08	-0.05
Ni	4.18	9.37	1.22	0.07	-0.18	-0.53	-0.43	-0.50	-0.44
Cu	-0.66	1.01	-0.32	0.21	-0.07	-0.12	0.01	-0.24	0.11
Zn	-0.29	0.25	0.14	0.22	0.08	0.08	0.05	0.05	0.20
Ga	-0.02	-0.02	-0.07	0.02	-0.01	-0.01	-0.06	-0.06	0.03
Ge	0.05	0.51	-0.15	0.14	0.12	-0.03	-0.02	-0.06	0.00
Rb	4.00	5.43	1.40	1.15	0.88	0.54	0.61	0.52	0.59
Sr	-0.84	-0.80	-0.43	-0.09	-0.14	-0.11	-0.19	-0.17	-0.10
Y	-0.45	0.05	-0.63	0.19	-0.14	-0.04	-0.09	-0.17	-0.10
Zr	0.00	0.35	-0.37	0.09	0.07	0.15	0.10	-0.09	-0.02
Nb	0.00	0.02	-0.05	0.09	0.16	0.04	-0.05	-0.05	-0.03
Cs	17.02	19.78	12.27	6.08	4.16	2.88	3.52	2.37	2.33
Ba	1.51	-0.23	-0.06	1.00	0.01	0.05	0.13	0.17	0.28
La	-0.30	0.04	-0.27	0.16	-0.08	-0.08	-0.14	-0.20	-0.12
Ce	-0.38	0.13	-0.13	0.17	-0.06	-0.05	-0.14	-0.18	-0.10
Pr	-0.41	0.17	-0.12	0.15	-0.09	-0.06	-0.12	-0.17	-0.11
Nd	-0.42	0.10	-0.13	0.11	-0.12	-0.08	-0.11	-0.18	-0.12
Sm	-0.45	0.14	-0.30	0.10	-0.16	-0.08	-0.08	-0.16	-0.08
Eu	-0.50	0.08	-0.26	0.07	-0.13	-0.09	-0.09	-0.14	-0.05
Gd	-0.43	0.13	-0.45	0.13	-0.16	-0.07	-0.08	-0.18	-0.08
Tb	-0.44	0.17	-0.53	0.10	-0.16	-0.08	-0.07	-0.16	-0.08
Dy	-0.47	0.20	-0.57	0.12	-0.16	-0.06	-0.05	-0.17	-0.06
Ho	-0.46	0.17	-0.59	0.14	-0.13	-0.06	-0.07	-0.17	-0.07
Er	-0.45	0.19	-0.57	0.21	-0.12	-0.01	-0.03	-0.15	-0.05
Tm	-0.45	0.25	-0.56	0.23	-0.08	0.01	-0.01	-0.15	-0.04
Yb	-0.44	0.33	-0.54	0.30	-0.03	0.06	0.01	-0.15	-0.03
Lu	-0.42	0.31	-0.52	0.34	0.00	0.10	0.04	-0.13	0.01
Hf	0.00	0.42	-0.30	0.15	0.11	0.18	0.15	-0.05	0.00
Ta	-0.21	0.30	-0.04	0.15	0.67	0.22	1.67	0.04	0.08
Pb	-0.39	1.08	-0.13	0.21	0.12	0.10	0.12	-0.11	0.06
Th	-0.06	0.53	0.14	0.17	0.43	0.78	0.19	-0.06	0.01
U	-0.08	0.69	-0.35	-0.09	0.03	0.05	-0.09	-0.09	-0.20

Fig. A1. Drill core characteristics of GA1



Fig. A2. Lithology classification for GA1





## Appendix III-I

Table A 1: The major element results of GA1, GA2 and BK2/05

well	lithology	Depth(m)	MgO	Al <sub>2</sub> O <sub>3</sub>	CaO	K <sub>2</sub> O	Na <sub>2</sub> O	SiO <sub>2</sub>	P <sub>2</sub> O <sub>5</sub>	TiO <sub>2</sub>	MnO	Fe <sub>2</sub> O <sub>3</sub>	LOI	
GA1	Basaltic andesite	13.9	2.6	22.8	1.6	5.9	0.1	47.3	0.3	1.7	0.0	8.7	8.5	
		14.3	1.9	16.0	11.4	3.1	2.6	44.7	0.2	1.2	0.2	0.2	5.8	13.0
		15.3	2.4	17.5	6.3	2.7	3.3	45.9	0.2	1.3	0.1	0.1	11.3	8.9
		16.3	2.4	15.2	11.8	1.5	3.4	46.2	0.1	1.0	0.2	0.2	4.8	13.2
		17.8	3.2	13.9	9.9	0.3	4.4	45.1	0.1	0.9	0.2	0.2	8.5	13.6
		19.3	1.8	13.8	12.3	0.6	5.6	41.4	0.2	1.0	0.2	0.2	10.3	12.2
		20.6	3.2	16.0	5.8	3.9	0.9	51.9	0.2	0.8	0.1	0.1	7.6	9.3
		21.5	5.0	13.7	5.8	4.0	0.8	48.3	0.1	0.7	0.2	0.2	8.9	12.0
		22.5	2.4	18.3	4.1	2.1	2.9	57.9	0.2	0.9	0.1	0.1	6.6	4.5
	23.5	3.2	15.9	6.4	1.8	2.8	54.2	0.2	0.7	0.1	0.1	8.8	5.8	
	24.5	2.9	17.0	5.8	1.9	3.2	55.2	0.2	0.8	0.1	0.1	9.7	3.0	
	25.5	3.0	17.3	5.9	1.9	3.2	55.9	0.2	0.8	0.1	0.1	8.5	2.9	
	26.7	3.0	17.4	5.7	1.8	3.1	56.0	0.2	0.9	0.1	0.1	9.0	3.0	
	27.1	3.0	17.4	5.8	1.9	3.2	56.0	0.2	0.9	0.1	0.1	8.4	2.7	
28.5	3.0	17.5	5.4	1.8	3.2	56.2	0.2	0.8	0.1	0.1	8.6	3.4		
55.5	3.2	18.1	7.0	1.5	3.4	55.0	0.2	0.9	0.2	0.2	9.3	1.1		
56.5	3.2	18.0	6.8	1.6	3.4	55.4	0.2	0.9	0.2	0.2	9.0	1.0		
	Gabbroic diorites													

Table A 1 continued

well	lithology	Depth( m)	MgO	Al <sub>2</sub> O <sub>3</sub>	CaO	K <sub>2</sub> O	Na <sub>2</sub> O	SiO <sub>2</sub>	P <sub>2</sub> O <sub>5</sub>	TiO <sub>2</sub>	MnO	Fe <sub>2</sub> O <sub>3</sub>	LOI
GA2	Granodiorite	55.7	1.36	14.74	1.50	4.23	1.98	66.31	0.10	0.40	0.05	5.59	3.61
		56.8	1.27	14.46	3.02	3.77	1.85	64.84	0.09	0.40	0.07	5.26	4.74
		58.3	1.58	18.24	8.25	3.02	5.06	50.00	0.10	0.49	0.12	5.03	8.28
		59.7	1.29	15.03	1.37	3.74	3.71	68.03	0.09	0.42	0.04	3.32	2.33
		60.9	1.51	15.66	2.02	4.34	3.40	65.96	0.10	0.46	0.06	3.62	2.75
		61.5	1.05	14.24	4.87	3.78	3.51	64.71	0.08	0.35	0.10	2.84	4.52
		62.45	1.19	15.27	3.22	4.46	3.26	64.79	0.09	0.43	0.06	3.30	4.12
		63.9	1.61	14.86	2.78	3.64	3.34	65.50	0.09	0.50	0.07	4.11	3.13
		64.9	1.22	15.25	3.43	2.87	3.49	67.54	0.08	0.39	0.06	3.58	2.03
		65.5	1.47	15.07	2.69	3.94	3.45	65.54	0.10	0.47	0.07	4.44	2.30
		66.5	1.47	15.09	2.67	3.89	3.40	65.53	0.10	0.47	0.07	4.37	2.27
		72.7	1.18	14.81	2.50	3.37	3.50	68.36	0.08	0.38	0.05	3.44	1.66
		73.3	1.33	15.26	2.93	3.82	3.42	66.41	0.09	0.41	0.06	3.80	2.13

Table A 1 continued

well	lithology	Depth(m)	MgO	Al <sub>2</sub> O <sub>3</sub>	CaO	K <sub>2</sub> O	Na <sub>2</sub> O	SiO <sub>2</sub>	P <sub>2</sub> O <sub>5</sub>	TiO <sub>2</sub>	MnO	Fe <sub>2</sub> O <sub>3</sub>	LOI
BK2/05	Granite	61.9	2.32	14.11	1.48	7.55	0.242	66.95	0.224	0.455	0.047	3.42	4.41
		62.1	1.03	15.2	0.873	6.21	2.27	70.28	0.161	0.398	0.025	3.13	1.54
		62.3	0.942	14.8	1.08	6.07	2.48	70.51	0.14	0.424	0.03	3.33	1.33
		62.5	1.07	15.44	1.38	4.38	3.36	69.77	0.138	0.464	0.036	4	1.46
		62.7	1.24	15.66	0.745	7.79	1.5	68.18	0.203	0.432	0.032	3.28	2.18
		62.9	4.52	13.29	5.33	7.3	1.04	55.92	0.158	0.326	0.106	2.97	10.16
		63.2	1.33	15.36	1.62	5.57	3.08	68.25	0.193	0.37	0.04	3.46	1.96
		63.4	0.932	15.68	1.22	5.87	3.12	69.15	0.181	0.41	0.033	3.29	1.2
		63.6	1.12	16.16	1.65	4.92	3.69	67.75	0.238	0.446	0.045	4.31	1.33
		63.8	1.16	15.4	1.42	5.61	2.96	68.61	0.312	0.44	0.037	3.73	1.34
		64.1	1.03	15.94	1.76	5.16	3.47	67.53	0.255	0.407	0.043	3.72	1.68
		64.3	0.924	14.64	1.42	4.92	3.27	70.48	0.257	0.402	0.038	3.49	1.35
		64.5	1.01	15.42	1.32	4.98	3.42	68.96	0.182	0.457	0.038	3.81	1.38
		64.7	0.837	16.68	1.06	7.27	3.11	66.72	0.166	0.47	0.038	3.51	1.04
		64.9	0.955	16.63	1.45	6.14	3.44	67.12	0.215	0.455	0.043	3.67	1.12
		65.1	1.05	15.4	1.51	4.59	3.5	69.3	0.269	0.537	0.04	4.04	1.07
65.3	1.02	16.22	1.46	4.95	3.71	68.57	0.243	0.441	0.038	3.8	0.97		
65.5	0.949	15.63	1.06	5.9	2.98	69.66	0.172	0.406	0.031	3.23	1.08		
65.7	1.06	15.63	1.59	4	3.87	69.41	0.241	0.468	0.04	4.06	1.05		
65.9	1.04	16	1.44	4.81	3.7	68.51	0.17	0.556	0.044	4.57	0.78		
71.5	0.999	16.21	1.29	5.1	3.81	67.6	0.16	0.486	0.038	3.97	1.31		
72.8	0.723	17.05	0.917	6.99	3.57	67.09	0.145	0.327	0.022	2.71	1		

Table A 2. Fracture angle characteristics

Drill core	Fracture angles											
GA1 basaltic andesite	18	141	33	29	114	22	44	56	149	72	93	133
GA1 gabbroic diorite	74	148	59	127	31	152	94	108	85	19	98	138
GA2	18	30	38	68	125	103	61	156	170	90	113	126
BK2/05	95	136										

Drill core	Fracture angles											
GA1 basaltic andesite	113	27	68	102	134	70	148	61	37	82	31	132
GA1 gabbroic diorite	107	37	118	15	38	73	64	37	116	146	21	127
GA2	18	65	125	165	164	70	95	107	113	57	154	31

Drill core	Fracture angles											
GA1 basaltic andesite	98	149	102	21	103	110	96	54	70	80	58	146
GA1 gabbroic diorite	85	84	96	101	125	77	57	110	50	152	148	103
GA2	80	165	89	177	22	36	77	110	14	16	133	120

Drill core	Fracture angles											
GA1 basaltic andesite	73	101	170	24	61	71	170	67	35	28	44	65
GA1 gabbroic diorite	15	147	87	98	93	17	33	33	65	69	117	117
GA2	41	101	95	83	82	109	165	132	116	153		

Drill core	Fracture angles											
GA1 basaltic andesite	163	96	167	69	100	123	132	26	29	111	52	107
GA1 gabbroic diorite	131	57	147	48	140	47	153	56	62	22	137	111

Drill core	Fracture angles			
GA1 basaltic andesite	165	22	71	25
GA1 gabbroic diorite	151	89	68	109

Table A 3. Fracture area characteristics

well	lithology	depth (m)	Vision No.	Fv (µm2)	Fc (µm2)	Fcl (µm2)	T (µm2)
GA1	basaltic andesite	13.9	1	66579.4	0	0	949682.9
			2	11125.13	0	0	945509.9
			3	4797.816	0	0	942769.4
			4	3331.635	0	0	942749.8
			5	2116.638	0	0	948293.7
			6	12030.43	0	0	945529.5
			7	86756.89	0	0	945529.5
			8	5565.96	0	0	942749.8
			9	6862.791	0	0	942769.4
			10	8450.22	0	0	945509.9
			11	2451.638	0	0	942749.8
			12	486.496	0	0	945529.5
			13	794.666	0	0	945518.3
			14	6308.05	0	0	942749.8
			15	4050.552	0	0	942769.4
		14.3	1	224.629	0	0	945518.3
			2	1290.778	0	0	945529.5
			3	420.385	0	0	951070.3
			4	195.452	0	0	945518.3
			5	0	0	0	945518.3
			6	527.534	0	0	942769.4
			7	132.671	0	0	945518.3
			8	1386.416	0	0	945509.9
			9	239.815	0	0	945529.5
			10	334.523	0	0	945518.3
			11	618.331	0	0	945518.3
			12	0	0	0	945518.3
			13	0	0	0	945518.3
			14	0	0	0	945518.3
			15	0	0	0	945518.3
		17.9	1	0	0	0	945518.3
			2	0	0	0	945518.3
			3	0	0	0	945518.3
			4	0	0	0	945518.3
			5	0	0	0	945518.3
			6	0	0	0	945518.3
			7	0	0	0	945518.3
			8	0	0	0	945518.3
			9	0	0	0	945518.3
			10	0	0	0	945518.3
			11	0	0	0	945518.3
			12	0	0	0	945518.3
			13	0	0	0	945518.3
			14	0	0	0	945518.3
			15	0	0	0	945518.3

Table A3 continued

well	lithology	depth (m)	Vision No.	Fv ( $\mu\text{m}^2$ )	Fc ( $\mu\text{m}^2$ )	Fcl ( $\mu\text{m}^2$ )	T ( $\mu\text{m}^2$ )
GA1	Gabbroic diorite	20.6	1	3482.965	72617.69	128796.8	945509.9
			2	5192.124	92583.56	50957.69	943450.7
			3	4709.596	102580.1	66512.63	942769.4
			4	516.916	234412.8	44902.85	942769.4
			5	1380.09	12990.12	54082.82	943450.7
			6	0	125523.7	41688.68	942769.4
			7	0	178061.1	48158.34	942749.8
			8	1321.176	279307.9	31725.53	945529.5
			9	3693.601	121741	37768.45	942769.4
			10	3937.761	42722.31	50599.18	942769.4
			11	1770.942	87194.99	21157.59	940013.4
			12	0	87020.44	30098.04	945518.3
			13	0	207541	44406.27	942769.4
			14	0	161637.5	40282.2	951061.8
			15	0	39318.17	67996.93	945518.3
		21.5	1	36259.27	50220.43	47316.67	943450.7
			2	48208.9	0	62432.98	942769.4
			3	47042.26	0	27536.88	945518.3
			4	754.456	47933.76	37540.08	945509.9
			5	1420.81	769.269	49209.91	945509.9
			6	16702.05	59573.49	55282.22	942769.4
			7	55031.22	26258.14	24742.87	943449.5
			8	6567.233	18690.69	41690.11	942769.4
			9	9348.719	0	39835.58	942749.8
			10	2360.149	0	56416.78	945529.5
			11	15510.09	37922.07	30476.46	940013.4
			12	0	7685.444	33804.14	942769.4
			13	0	0	25528.95	942769.4
			14	41636.84	0	52320.54	948293.7
			15	1228.452	13806.33	38452.33	945518.3
		23.5	1	5272.174	0	6462.15	945509.9
			2	4541.19	0	13041.06	942769.4
			3	0	18487.22	13986.04	940013.4
			4	21451.94	0	16030.6	942749.8
			5	0	0	13015.14	942769.4
			6	6410.836	0	34889.85	948282.4
			7	23288.27	0	39066.01	942769.4
			8	0	0	17575.26	945509.9
			9	0	0	13969.11	948293.7
			10	4101.704	0	14819	948293.7
			11	0	0	11241.39	948282.4
			12	1312.135	0	16145.35	945529.5
			13	14893.92	0	11338.63	948282.4
			14	36203.39	0	14500.42	942749.8
			15	0	3655.348	12159.87	945518.3

Table A3 continued

well	lithology	depth (m)	Vision No.	Fv ( $\mu\text{m}^2$ )	Fc ( $\mu\text{m}^2$ )	Fcl ( $\mu\text{m}^2$ )	T ( $\mu\text{m}^2$ )
GA1	Gabbroic diorite	25.5	1	0	0	4470.545	947591
			2	0	0	9296.509	940013.4
			3	0	0	3581.749	948293.7
			4	0	0	4216.071	942769.4
			5	0	0	1399.027	942769.4
			6	0	0	6237.432	948293.7
			7	0	0	4688.782	948293.7
			8	0	0	1926.215	948293.7
			9	0	0	9675.073	945518.3
			10	0	0	8855.072	942769.4
			11	0	0	3373.317	945509.9
			12	0	0	8315.618	945518.3
			13	0	0	7298.785	945529.5
			14	0	0	10419.99	947169.2
			15	0	0	3043.758	942769.4
		27.1	1	0	0	2274.81	942769.4
			2	0	0	394.736	945518.3
			3	0	0	633.149	942769.4
			4	0	0	954.33	945518.3
			5	0	0	1626.724	951070.3
			6	0	0	2661.583	945518.3
			7	0	0	3165.553	942769.4
			8	0	0	1422.431	942769.4
			9	0	0	1676.848	945509.9
			10	0	0	2139.403	948293.7
			11	0	0	1047.259	942769.4
			12	0	0	478.854	948293.7
			13	0	0	335.136	951070.3
			14	0	0	2156.644	942749.8
			15	0	0	1441.382	948293.7
		56.5	1	0	0	0	945518.3
			2	0	0	0	945518.3
			3	0	0	0	945518.3
			4	0	0	0	945518.3
			5	0	0	0	945518.3
			6	0	0	0	945518.3
			7	0	0	0	945518.3
			8	0	0	0	945518.3
			9	0	0	0	945518.3
			10	0	0	0	945518.3
			11	0	0	0	945518.3
			12	0	0	0	945518.3
			13	0	0	0	945518.3
			14	0	0	0	945518.3
			15	0	0	0	945518.3

Table A3 continued

well	lithology	depth (m)	Vision No.	Fv ( $\mu\text{m}^2$ )	Fc ( $\mu\text{m}^2$ )	Fcl ( $\mu\text{m}^2$ )	T ( $\mu\text{m}^2$ )
GA2	granodiorite	55.7	1	31461.22	0	116032.2	945529.5
			2	20223.17	0	71092.01	948274
			3	0	0	136351.7	942749.8
			4	17302.43	0	65910.72	945490.2
			5	0	0	21465.1	943450.7
			6	0	0	18893.39	942769.4
			7	0	0	18848.74	948293.7
			8	0	0	8995.633	945518.3
			9	1184.016	0	24847.21	945518.3
			10	0	0	25538	945518.3
			11	0	0	25581.96	948293.7
			12	14915.54	0	32984.75	942769.4
			13	25650.39	0	15310.1	945529.5
			14	0	0	76719.35	948282.4
			15	0	0	0	945518.3
		58.3	1	0	12101.2	3678.624	945518.3
			2	0	38757.17	0	948293.7
			3	0	60729.15	0	948293.7
			4	0	25409.56	0	951070.3
			5	0	47703.9	0	951061.8
			6	0	0	59448.41	951070.3
			7	0	81655.29	0	947599.4
			8	0	35999.58	0	948282.4
			9	0	22115.33	0	951070.3
			10	0	0	48861.97	951061.8
			11	0	47177.41	0	948293.7
			12	0	58193.15	0	948293.7
			13	0	23546.09	0	945529.5
			14	0	0	52109.48	948293.7
			15	0	51375.11	0	951061.8
		61.5	1	0	0	3780.382	945509.9
			2	0	0	25840.04	945509.9
			3	0	0	28812.13	945529.5
			4	0	0	15813.96	942769.4
			5	0	0	44.052	945518.3
			6	0	0	8118.712	948293.7
			7	0	0	7885.751	951070.3
			8	0	0	11169.49	945509.9
			9	0	0	11460.04	945518.3
			10	0	0	6308.658	945518.3
			11	0	0	13534.16	942769.4
			12	0	0	4220.541	948293.7
			13	0	0	53571.95	945518.3
			14	0	0	5516.61	948282.4
			15	0	0	3241.999	948293.7



Table A3 continued

well	lithology	depth (m)	Vision No.	Fv ( $\mu\text{m}^2$ )	Fc ( $\mu\text{m}^2$ )	Fcl ( $\mu\text{m}^2$ )	T ( $\mu\text{m}^2$ )
GA2	Gabbroic diorite	63.9	1	0	0	1718.025	945518.3
			2	0	0	3067.33	942749.8
			3	0	0	34167.63	945529.5
			4	0	0	6231.712	945518.3
			5	0	0	43.955	943442.3
			6	0	0	8771.72	945518.3
			7	0	0	0	942769.4
			8	0	0	3897.19	948293.7
			9	0	0	2751.225	945518.3
			10	0	0	1159.972	945529.5
			11	0	0	3859.616	945509.9
			12	0	0	9364.718	942769.4
			13	0	0	4191.328	942769.4
			14	0	0	3252.613	942749.8
			15	0	0	5765.763	945509.9
		66.5	1	0	0	1664.412	948293.7
			2	0	0	1301.893	948293.7
			3	0	0	325.884	940013.4
			4	0	0	8559.539	945518.3
			5	0	0	1917.124	945518.3
			6	0	0	164.473	945518.3
			7	0	0	130.809	945518.3
			8	0	0	290.167	948293.7
			9	0	0	0	948293.7
			10	0	0	2395.421	948293.7
			11	0	0	6305.402	945529.5
			12	0	0	3420.132	951042.1
			13	0	0	2085.189	948293.7
			14	0	0	7330.205	948293.7
			15	0	0	1766.694	945518.3
		73.3	1	0	0	0	945518.3
			2	0	0	0	945518.3
			3	0	0	0	945518.3
			4	0	0	0	945518.3
			5	0	0	0	945518.3
			6	0	0	0	945518.3
			7	0	0	0	945518.3
			8	0	0	0	945518.3
			9	0	0	0	945518.3
			10	0	0	0	945518.3
			11	0	0	0	945518.3
			12	0	0	0	945518.3
			13	0	0	0	945518.3
			14	0	0	0	945518.3
			15	0	0	0	945518.3

Table A3 continued

well	lithology	depth (m)	Vision No.	Fv ( $\mu\text{m}^2$ )	Fc ( $\mu\text{m}^2$ )	Fcl ( $\mu\text{m}^2$ )	T ( $\mu\text{m}^2$ )
BK2/05	granite	61.9	1	37623.7	5407.64	14286.29	948293.7
			2		159819	38746.27	942769.4
			3	0	268014.4	0	945529.5
			4	0	0	17402.28	945529.5
			5	0	44017.12	7218.63	948282.4
			6	0	0	4418.872	948293.7
			7	0	26781.38	13987.69	945509.9
			8	0	0	10734.79	951070.3
			9	0	0	2605.821	951070.3
			10	0	0	13756.51	945518.3
			11	3471.2	0	3226.757	948293.7
			12	0	59234	0	948293.7
			13	0	55432.24	0	948293.7
			14	0	35968.18	16034.55	945529.5
			15	0	15842.18	2026.392	945529.5
		62.1	1	0	0	9339.585	945518.3
			2	0	0	0	942769.4
			3	0	0	0	942769.4
			4	0	0	0	942769.4
			5	0	0	0	942769.4
			6	0	0	12322.04	945518.3
			7	0	0	0	942769.4
			8	0	0	0	942769.4
			9	0	0	4278.236	948293.7
			10	0	0	0	942769.4
			11	0	0	0	942769.4
			12	0	0	3531.201	948293.7
			13	0	0	4038.076	951070.3
			14	0	0	5485.622	951070.3
			15	0	0	0	942769.4
		62.3	1	0	0	4054.124	945518.3
			2	0	0	8652.717	942769.4
			3	0	0	8136.857	945509.9
			4	0	0	6899.431	945529.5
			5	0	0	10226.99	945518.3
			6	0	0	0	942769.4
			7	0	0	0	942769.4
			8	0	0	0	942769.4
			9	0	0	0	942769.4
			10	0	0	0	942769.4
			11	0	0	0	942769.4
			12	0	0	7918.436	942749.8
			13	0	0	0	942769.4
			14	0	0	1683.32	948293.7
			15	0	0	15242.17	945518.3

Table A3 continued

well	lithology	depth (m)	Vision No.	Fv ( $\mu\text{m}^2$ )	Fc ( $\mu\text{m}^2$ )	Fcl ( $\mu\text{m}^2$ )	T ( $\mu\text{m}^2$ )
BK2/05	Granite	62.7	1	0	7737.527	34578.26	951070.3
			2	0	0	18572.02	945518.3
			3	0	51514.97	32018.43	951070.3
			4	0	0	0	942769.4
			5	0	26061.74	7161.688	951070.3
			6	0	0	0	942769.4
			7	0	0	5691.902	951070.3
			8	0	0	3382.272	942749.8
			9	0	26409.01	0	948282.4
			10	0	0	7996.289	945509.9
			11	0	0	0	942769.4
			12	0	0	2397.163	948293.7
			13	0	0	2501.16	948293.7
			14	0	0	15901.73	948293.7
			15	0	0	7321.853	945518.3
		72.8	1	0	0	0	945518.3
			2	0	0	0	945518.3
			3	0	0	0	945518.3
			4	0	0	0	945518.3
			5	0	0	0	945518.3
			6	0	0	0	945518.3
			7	0	0	0	945518.3
			8	0	0	0	945518.3
			9	0	0	0	945518.3
			10	0	0	0	945518.3
			11	0	0	0	945518.3
			12	0	0	0	945518.3
			13	0	0	0	945518.3
			14	0	0	0	945518.3
			15	0	0	0	945518.3

Table A4. CIA normalization

Well	Depth(m)	CIAcorr	time (year)	TWM	CWA	$\lambda_s$	n	$\lambda_{sN}(100000)$	$\lambda_{sN}(10000)$	$\lambda_{sN}(1000)$	$\lambda_{sN}(100)$	CIA <sub>sN</sub> $\lambda(100000)$	CIA <sub>sN</sub> $\lambda(10000)$	CIA <sub>sN</sub> $\lambda(1000)$	CIA <sub>sN</sub> $\lambda(100)$
GA1	13.9	96.55	100000	2.5E-08	2.5E-08	1.31	1.69	0.51	0.53	0.56	82.80	83.92	85.23		
	14.3	64.03	100000	9.4E-09	9.4E-09	0.53		0.21	0.22	0.23	66.17	66.63	67.16		
	15.3	60.42	10000	3.4E-09	3.4E-09	0.45		0.17	0.18	0.19	64.33	64.71	65.15		
	16.3	56.38				0.35		0.14	0.14	0.15	62.26	62.56	62.91		
	17.8	47.68				0.14		0.05	0.06	0.06	57.81	57.93	58.07		
	19.3	41.80				0.00		0.00	0.00	0.00	54.81	54.81	54.81		
	20.6	79.63	100000	1.6E-08	1.6E-08	0.37	0.87	0.44	0.45	0.46	78.87	79.44	80.10		
	21.5	79.31	100000	6.0E-09	6.0E-09	0.36		0.43	0.44	0.45	78.51	79.07	79.72		
	22.5	62.37	10000	2.2E-09	2.2E-09	0.07		0.08	0.09	0.09	59.45	59.57	59.69		
	23.5	59.54				0.02		0.03	0.03	0.03	56.28	56.31	56.35		
	24.5	58.44				0.00		0.00	0.00	0.00	55.04	55.05	55.05		
	25.5	58.44				0.00		0.00	0.00	0.00	55.03	55.04	55.04		
	26.7	59.82				0.03		0.03	0.03	0.03	56.59	56.63	56.68		
	27.1	58.54				0.01		0.01	0.01	0.01	55.15	55.16	55.17		
28.5	59.02				0.01		0.02	0.02	0.02	55.69	55.71	55.73			
55.5	58.30				0.00		0.00	0.00	0.00	54.88	54.88	54.89			
56.5	58.17				0.00		0.00	0.00	0.00	54.73	54.73	54.73			

Table A4. Continued

Well	Depth(m)	CIAcor <sub>r</sub>	time (year)	TWM	CWA	$\lambda_s$	n	$\lambda_{sN}(100000)$	$\lambda_{sN}(10000)$	$\lambda_{sN}(1000)$	$\lambda_{sN}(100)$	CIAsN $\lambda(1000)$	CIAsN $\lambda(1000)$	CIAsN $\lambda(1000)$
GA2	55.7	66.23	100000 0	1.5E- 08	1.5E- 08	0.30	1.17	0.29	0.29	0.29	0.29	70.45	70.50	70.55
	56.8	60.72	100000	5.8E- 09	5.8E- 09	0.19		0.18	0.18	0.18	0.18	64.81	64.84	64.88
	59.7	55.44	10000	2.2E- 09	2.2E- 09	0.09		0.08	0.08	0.08	0.08	59.40	59.42	59.43
	60.9	54.71				0.07		0.07	0.07	0.07	0.07	58.65	58.66	58.68
	61.5	47.63				0.06		0.05	0.05	0.05	0.05	57.69	57.70	57.71
	62.45	50.72				0.00		0.00	0.00	0.00	0.00	54.57	54.57	54.57
	63.9	50.93				0.00		0.00	0.00	0.00	0.00	54.79	54.79	54.79
	64.9	49.23				-0.03		-0.03	-0.03	-0.03	-0.03	53.05	53.04	53.04
	65.5	51.19				0.00		0.00	0.00	0.00	0.00	55.06	55.06	55.06
	66.5	51.43				0.01		0.01	0.01	0.01	0.01	55.30	55.30	55.31
72.7	51.27				0.01		0.01	0.01	0.01	0.01	55.14	55.14	55.14	
73.3	50.63				-0.01		-0.01	-0.01	-0.01	-0.01	54.48	54.48	54.48	

Table A4. Continued

Well	Depth( m)	CIACor r	time (year)	TWM	CWA	$\lambda_s$	n	$\lambda_{sN}(10$ 00000)	$\lambda_{sN}(10$ 0000)	$\lambda_{sN}(10$ 000)	CIAsN $\lambda(1000$	CIAsN $\lambda(1000$	CIAsN $\lambda(1000$
	61.9	77.22				0.41	1.00	0.41	0.41	0.41	77.22	77.22	77.22
	62.1	61.58	100000	1.7E-08	1.7E-08	0.12		0.12	0.12	0.12	61.58	61.58	61.58
	62.3	58.87	100000	6.4E-09	6.4E-09	0.07		0.07	0.07	0.07	58.87	58.87	58.87
	62.5	54.42	10000	2.5E-09	2.5E-09	-0.01		-0.01	-0.01	-0.01	54.42	54.42	54.42
	62.7	67.25				0.23		0.23	0.23	0.23	67.25	67.25	67.25
	62.9	64.87				0.18		0.18	0.18	0.18	64.87	64.87	64.87
	63.2	54.69				0.00		0.00	0.00	0.00	54.69	54.69	54.69
	63.4	56.60				0.03		0.03	0.03	0.03	56.60	56.60	56.60
	63.6	53.46				-0.02		-0.02	-0.02	-0.02	53.46	53.46	53.46
	63.8	56.83				0.04		0.04	0.04	0.04	56.83	56.83	56.83
	64.1	53.65				-0.02		-0.02	-0.02	-0.02	53.65	53.65	53.65
	64.3	54.32				-0.01		-0.01	-0.01	-0.01	54.32	54.32	54.32
	64.5	54.67				0.00		0.00	0.00	0.00	54.67	54.67	54.67
	64.7	58.33				0.06		0.06	0.06	0.06	58.33	58.33	58.33
	64.9	55.57				0.01		0.01	0.01	0.01	55.57	55.57	55.57
	65.1	54.01				-0.01		-0.01	-0.01	-0.01	54.01	54.01	54.01
	65.3	54.24				-0.01		-0.01	-0.01	-0.01	54.24	54.24	54.24
	65.5	57.83				0.06		0.06	0.06	0.06	57.83	57.83	57.83
	65.7	52.45				-0.04		-0.04	-0.04	-0.04	52.45	52.45	52.45
	65.9	53.72				-0.02		-0.02	-0.02	-0.02	53.72	53.72	53.72
	71.5	54.11				-0.01		-0.01	-0.01	-0.01	54.11	54.11	54.11
	72.8	57.37				0.05		0.05	0.05	0.05	57.37	57.37	57.37

Table A5. C and O isotope characteristics

Well	Depth(m)	dolomite		calcite	
		$\delta^{13}\text{C}$ (PDB ‰)	$\delta^{18}\text{O}$ (PDB ‰)	$\delta^{13}\text{C}$ (PDB ‰)	$\delta^{18}\text{O}$ (PDB ‰)
GA1	13.9			-11.59	-8.12
	14.5			-9.49	-11.03
	15.3			-10.09	-12.58
	16.3			-10.39	-12.35
	17.8	-4.42	-15.18	-10.29	-11.97
	19.3	-3.90	-17.08	-10.09	-10.33
	20.6			-10.29	-12.19
	21.5	-3.17	-18.21	-9.89	-12.39
	22.5			-8.79	-11.59
	23.5	-4.38	-16.30	-10.59	-12.79
	24.5	-2.21	-15.30	-9.19	-10.09
	25.5	-2.53	-15.84	-8.79	-10.89
	26.5	-3.14	-16.66	-9.39	-9.59
	27.5	-3.69	-14.98	-9.29	-9.89
	28.7	-3.46	-18.51	-9.19	-10.09
GA2	55.70	-2.68	-17.33	-6.21	-10.75
	56.80	-3.83	-18.01	-3.88	-12.34
	58.30			-6.08	-8.08
	59.70	-1.91	-17.39	-4.66	-10.88
	60.90	-4.36	-16.51	-5.09	-12.39
	61.50	-4.48	-17.16	-4.60	-10.89
	62.45	-3.11	-17.61	-4.10	-11.59
	63.90	-4.61	-17.46	-5.89	-10.19
	64.90	-4.79	-18.26	-5.79	-9.89
	65.50	-3.42	-17.42	-5.49	-10.29
66.50	-4.88	-17.93	-5.29	-10.19	
KB2-05	61.9	-6.39	-14.19		
	62.7	-6.29	-16.88		
	62.9	-6.59	-14.39		

## Appendix IV-I

Table A1. Fracture area characteristics

well	lithology	depth (m)	Vision No.	Fv ( $\mu\text{m}^2$ )	Fc ( $\mu\text{m}^2$ )	Fcl ( $\mu\text{m}^2$ )	T ( $\mu\text{m}^2$ )
GA1	basaltic andesite	13.9	1	66579.4	0	0	949682.9
			2	11125.13	0	0	945509.9
			3	4797.816	0	0	942769.4
			4	3331.635	0	0	942749.8
			5	2116.638	0	0	948293.7
			6	12030.43	0	0	945529.5
			7	86756.89	0	0	945529.5
			8	5565.96	0	0	942749.8
			9	6862.791	0	0	942769.4
			10	8450.22	0	0	945509.9
			11	2451.638	0	0	942749.8
			12	486.496	0	0	945529.5
			13	794.666	0	0	945518.3
			14	6308.05	0	0	942749.8
			15	4050.552	0	0	942769.4
		14.3	1	224.629	0	0	945518.3
			2	1290.778	0	0	945529.5
			3	420.385	0	0	951070.3
			4	195.452	0	0	945518.3
			5	0	0	0	945518.3
			6	527.534	0	0	942769.4
			7	132.671	0	0	945518.3
			8	1386.416	0	0	945509.9
			9	239.815	0	0	945529.5
			10	334.523	0	0	945518.3
			11	618.331	0	0	945518.3
			12	0	0	0	945518.3
			13	0	0	0	945518.3
			14	0	0	0	945518.3
			15	0	0	0	945518.3
		17.9	1	0	0	0	945518.3
			2	0	0	0	945518.3
			3	0	0	0	945518.3
			4	0	0	0	945518.3
			5	0	0	0	945518.3
			6	0	0	0	945518.3
			7	0	0	0	945518.3
			8	0	0	0	945518.3
			9	0	0	0	945518.3
			10	0	0	0	945518.3
			11	0	0	0	945518.3
			12	0	0	0	945518.3
			13	0	0	0	945518.3
			14	0	0	0	945518.3
			15	0	0	0	945518.3



Table A1 continued

well	lithology	depth (m)	Vision No.	Fv ( $\mu\text{m}^2$ )	Fc ( $\mu\text{m}^2$ )	Fcl ( $\mu\text{m}^2$ )	T ( $\mu\text{m}^2$ )
GA1	Gabbroic diorite	20.6	1	3482.965	72617.69	128796.8	945509.9
			2	5192.124	92583.56	50957.69	943450.7
			3	4709.596	102580.1	66512.63	942769.4
			4	516.916	234412.8	44902.85	942769.4
			5	1380.09	12990.12	54082.82	943450.7
			6	0	125523.7	41688.68	942769.4
			7	0	178061.1	48158.34	942749.8
			8	1321.176	279307.9	31725.53	945529.5
			9	3693.601	121741	37768.45	942769.4
			10	3937.761	42722.31	50599.18	942769.4
			11	1770.942	87194.99	21157.59	940013.4
			12	0	87020.44	30098.04	945518.3
			13	0	207541	44406.27	942769.4
			14	0	161637.5	40282.2	951061.8
			15	0	39318.17	67996.93	945518.3
		21.5	1	36259.27	50220.43	47316.67	943450.7
			2	48208.9	0	62432.98	942769.4
			3	47042.26	0	27536.88	945518.3
			4	754.456	47933.76	37540.08	945509.9
			5	1420.81	769.269	49209.91	945509.9
			6	16702.05	59573.49	55282.22	942769.4
			7	55031.22	26258.14	24742.87	943449.5
			8	6567.233	18690.69	41690.11	942769.4
			9	9348.719	0	39835.58	942749.8
			10	2360.149	0	56416.78	945529.5
			11	15510.09	37922.07	30476.46	940013.4
			12	0	7685.444	33804.14	942769.4
			13	0	0	25528.95	942769.4
			14	41636.84	0	52320.54	948293.7
			15	1228.452	13806.33	38452.33	945518.3
		23.5	1	5272.174	0	6462.15	945509.9
			2	4541.19	0	13041.06	942769.4
			3	0	18487.22	13986.04	940013.4
			4	21451.94	0	16030.6	942749.8
			5	0	0	13015.14	942769.4
			6	6410.836	0	34889.85	948282.4
			7	23288.27	0	39066.01	942769.4
			8	0	0	17575.26	945509.9
			9	0	0	13969.11	948293.7
			10	4101.704	0	14819	948293.7
			11	0	0	11241.39	948282.4
			12	1312.135	0	16145.35	945529.5
			13	14893.92	0	11338.63	948282.4
			14	36203.39	0	14500.42	942749.8
			15	0	3655.348	12159.87	945518.3

Table A1 continued

well	lithology	depth (m)	Vision No.	Fv ( $\mu\text{m}^2$ )	Fc ( $\mu\text{m}^2$ )	Fcl ( $\mu\text{m}^2$ )	T ( $\mu\text{m}^2$ )
GA1	Gabbroic diorite	25.5	1	0	0	4470.545	947591
			2	0	0	9296.509	940013.4
			3	0	0	3581.749	948293.7
			4	0	0	4216.071	942769.4
			5	0	0	1399.027	942769.4
			6	0	0	6237.432	948293.7
			7	0	0	4688.782	948293.7
			8	0	0	1926.215	948293.7
			9	0	0	9675.073	945518.3
			10	0	0	8855.072	942769.4
			11	0	0	3373.317	945509.9
			12	0	0	8315.618	945518.3
			13	0	0	7298.785	945529.5
			14	0	0	10419.99	947169.2
			15	0	0	3043.758	942769.4
		27.1	1	0	0	2274.81	942769.4
			2	0	0	394.736	945518.3
			3	0	0	633.149	942769.4
			4	0	0	954.33	945518.3
			5	0	0	1626.724	951070.3
			6	0	0	2661.583	945518.3
			7	0	0	3165.553	942769.4
			8	0	0	1422.431	942769.4
			9	0	0	1676.848	945509.9
			10	0	0	2139.403	948293.7
			11	0	0	1047.259	942769.4
			12	0	0	478.854	948293.7
			13	0	0	335.136	951070.3
			14	0	0	2156.644	942749.8
			15	0	0	1441.382	948293.7
		56.5	1	0	0	0	945518.3
			2	0	0	0	945518.3
			3	0	0	0	945518.3
			4	0	0	0	945518.3
			5	0	0	0	945518.3
			6	0	0	0	945518.3
			7	0	0	0	945518.3
			8	0	0	0	945518.3
			9	0	0	0	945518.3
			10	0	0	0	945518.3
			11	0	0	0	945518.3
			12	0	0	0	945518.3
			13	0	0	0	945518.3
			14	0	0	0	945518.3
			15	0	0	0	945518.3

Table A1 continued

well	lithology	depth (m)	Vision No.	Fv ( $\mu\text{m}^2$ )	Fc ( $\mu\text{m}^2$ )	Fel ( $\mu\text{m}^2$ )	T ( $\mu\text{m}^2$ )		
GA2	granodiorite	55.7	1	31461.22	0	116032.2	945529.5		
			2	20223.17	0	71092.01	948274		
			3	0	0	136351.7	942749.8		
			4	17302.43	0	65910.72	945490.2		
			5	0	0	21465.1	943450.7		
			6	0	0	18893.39	942769.4		
			7	0	0	18848.74	948293.7		
			8	0	0	8995.633	945518.3		
			9	1184.016	0	24847.21	945518.3		
			10	0	0	25538	945518.3		
			11	0	0	25581.96	948293.7		
			12	14915.54	0	32984.75	942769.4		
			13	25650.39	0	15310.1	945529.5		
			14	0	0	76719.35	948282.4		
			15	0	0	0	945518.3		
				58.3	1	0	12101.2	3678.624	945518.3
					2	0	38757.17	0	948293.7
					3	0	60729.15	0	948293.7
					4	0	25409.56	0	951070.3
					5	0	47703.9	0	951061.8
					6	0	0	59448.41	951070.3
					7	0	81655.29	0	947599.4
					8	0	35999.58	0	948282.4
					9	0	22115.33	0	951070.3
					10	0	0	48861.97	951061.8
					11	0	47177.41	0	948293.7
					12	0	58193.15	0	948293.7
					13	0	23546.09	0	945529.5
					14	0	0	52109.48	948293.7
					15	0	51375.11	0	951061.8
				61.5	1	0	0	3780.382	945509.9
					2	0	0	25840.04	945509.9
					3	0	0	28812.13	945529.5
					4	0	0	15813.96	942769.4
					5	0	0	44.052	945518.3
					6	0	0	8118.712	948293.7
					7	0	0	7885.751	951070.3
					8	0	0	11169.49	945509.9
					9	0	0	11460.04	945518.3
					10	0	0	6308.658	945518.3
					11	0	0	13534.16	942769.4
					12	0	0	4220.541	948293.7
					13	0	0	53571.95	945518.3
					14	0	0	5516.61	948282.4
					15	0	0	3241.999	948293.7

Table A1 continued

well	lithology	depth (m)	Vision No.	Fv ( $\mu\text{m}^2$ )	Fc ( $\mu\text{m}^2$ )	Fcl ( $\mu\text{m}^2$ )	T ( $\mu\text{m}^2$ )
GA2	Gabbroic diorite	63.9	1	0	0	1718.025	945518.3
			2	0	0	3067.33	942749.8
			3	0	0	34167.63	945529.5
			4	0	0	6231.712	945518.3
			5	0	0	43.955	943442.3
			6	0	0	8771.72	945518.3
			7	0	0	0	942769.4
			8	0	0	3897.19	948293.7
			9	0	0	2751.225	945518.3
			10	0	0	1159.972	945529.5
			11	0	0	3859.616	945509.9
			12	0	0	9364.718	942769.4
			13	0	0	4191.328	942769.4
			14	0	0	3252.613	942749.8
			15	0	0	5765.763	945509.9
		66.5	1	0	0	1664.412	948293.7
			2	0	0	1301.893	948293.7
			3	0	0	325.884	940013.4
			4	0	0	8559.539	945518.3
			5	0	0	1917.124	945518.3
			6	0	0	164.473	945518.3
			7	0	0	130.809	945518.3
			8	0	0	290.167	948293.7
			9	0	0	0	948293.7
			10	0	0	2395.421	948293.7
			11	0	0	6305.402	945529.5
			12	0	0	3420.132	951042.1
			13	0	0	2085.189	948293.7
			14	0	0	7330.205	948293.7
			15	0	0	1766.694	945518.3
		73.3	1	0	0	0	945518.3
			2	0	0	0	945518.3
			3	0	0	0	945518.3
			4	0	0	0	945518.3
			5	0	0	0	945518.3
			6	0	0	0	945518.3
			7	0	0	0	945518.3
			8	0	0	0	945518.3
			9	0	0	0	945518.3
			10	0	0	0	945518.3
			11	0	0	0	945518.3
			12	0	0	0	945518.3
			13	0	0	0	945518.3
			14	0	0	0	945518.3
			15	0	0	0	945518.3

Table A1 continued

well	lithology	depth (m)	Vision No.	Fv ( $\mu\text{m}^2$ )	Fc ( $\mu\text{m}^2$ )	Fcl ( $\mu\text{m}^2$ )	T ( $\mu\text{m}^2$ )		
BK2/05	granite	61.9	1	37623.7	5407.64	14286.29	948293.7		
			2		159819	38746.27	942769.4		
			3	0	268014.4	0	945529.5		
			4	0	0	17402.28	945529.5		
			5	0	44017.12	7218.63	948282.4		
			6	0	0	4418.872	948293.7		
			7	0	26781.38	13987.69	945509.9		
			8	0	0	10734.79	951070.3		
			9	0	0	2605.821	951070.3		
			10	0	0	13756.51	945518.3		
			11	3471.2	0	3226.757	948293.7		
			12	0	59234	0	948293.7		
			13	0	55432.24	0	948293.7		
			14	0	35968.18	16034.55	945529.5		
			15	0	15842.18	2026.392	945529.5		
				62.1	1	0	0	9339.585	945518.3
					2	0	0	0	942769.4
					3	0	0	0	942769.4
					4	0	0	0	942769.4
					5	0	0	0	942769.4
					6	0	0	12322.04	945518.3
					7	0	0	0	942769.4
					8	0	0	0	942769.4
					9	0	0	4278.236	948293.7
					10	0	0	0	942769.4
					11	0	0	0	942769.4
					12	0	0	3531.201	948293.7
					13	0	0	4038.076	951070.3
					14	0	0	5485.622	951070.3
					15	0	0	0	942769.4
				62.3	1	0	0	4054.124	945518.3
					2	0	0	8652.717	942769.4
					3	0	0	8136.857	945509.9
					4	0	0	6899.431	945529.5
					5	0	0	10226.99	945518.3
					6	0	0	0	942769.4
					7	0	0	0	942769.4
					8	0	0	0	942769.4
					9	0	0	0	942769.4
					10	0	0	0	942769.4
					11	0	0	0	942769.4
					12	0	0	7918.436	942749.8
					13	0	0	0	942769.4
					14	0	0	1683.32	948293.7
					15	0	0	15242.17	945518.3

Table A1 continued

well	lithology	depth (m)	Vision No.	Fv ( $\mu\text{m}^2$ )	Fc ( $\mu\text{m}^2$ )	Fcl ( $\mu\text{m}^2$ )	T ( $\mu\text{m}^2$ )
BK2/05	Granite	62.7	1	0	7737.527	34578.26	951070.3
			2	0	0	18572.02	945518.3
			3	0	51514.97	32018.43	951070.3
			4	0	0	0	942769.4
			5	0	26061.74	7161.688	951070.3
			6	0	0	0	942769.4
			7	0	0	5691.902	951070.3
			8	0	0	3382.272	942749.8
			9	0	26409.01	0	948282.4
			10	0	0	7996.289	945509.9
			11	0	0	0	942769.4
			12	0	0	2397.163	948293.7
			13	0	0	2501.16	948293.7
			14	0	0	15901.73	948293.7
			15	0	0	7321.853	945518.3
		72.8	1	0	0	0	945518.3
			2	0	0	0	945518.3
			3	0	0	0	945518.3
			4	0	0	0	945518.3
			5	0	0	0	945518.3
			6	0	0	0	945518.3
			7	0	0	0	945518.3
			8	0	0	0	945518.3
			9	0	0	0	945518.3
			10	0	0	0	945518.3
			11	0	0	0	945518.3
			12	0	0	0	945518.3
			13	0	0	0	945518.3
			14	0	0	0	945518.3
			15	0	0	0	945518.3

Table A1 continued

well	lithology	depth (m)	Vision No.	Fv ( $\mu\text{m}^2$ )	Fc ( $\mu\text{m}^2$ )	Fcl ( $\mu\text{m}^2$ )	T ( $\mu\text{m}^2$ )
TB8	tonalite	0	1	52199.4		8519.3	942749.8
			2	49348.6	5327.7	16203.7	947624.9
			3	118079.0		0.0	937388.9
			4	31804.6		15230.5	947618.1
			5	36343.7		9002.5	947595.5
			6	20744.4		13925.7	940768.4
			7	21544.3		8261.5	944178.8
			8	27480.6		10629.3	947624.9
			9	81948.6		11314.3	947618.1
			10	26569.9		12894.9	939082.4
			11	35244.7		8849.4	944194.7
			12	23605.6		14218.7	946770.7
			13	51579.1		12274.0	947624.9
			14	35884.5		14288.4	940784.2
			15	80674.1		12249.5	947624.9
		2.5	1	33066.6		9678.8	942749.8
			2	64581.6		3858.6	945529.5
			3		22122.4	11054.2	948282.4
			4	22362.2	9164.8	6490.6	951070.3
			5	33213.3		4826.4	948274.0
			6	16516.2		15790.5	941385.3
			7	8512.2	19965.3	0.0	945518.3
			8	27117.3		1034.5	945518.3
			9	81512.4		9261.5	945518.3
			10	59779.5		0.0	945529.5
			11	21536.3		1365.0	942749.8
			12		57913.4	88779.5	948282.4
			13		47587.0	0.0	953862.2
			14	44022.3	33622.9	4153.9	951061.8
			15	21754.9		0.0	953862.2
		4.5	1	0.0	0.0	0.0	942769.4
			2		6544.2	6692.7	942769.4
			3			13537.9	948293.7
			4	14750.7	4976.3	0.0	945518.3
			5	18003.2		0.0	942769.4
			6			27030.7	948293.7
			7	37268.5		0.0	945518.3
			8	0.0	0.0	0.0	945518.3
			9			4325.1	945518.3
			10			57581.8	945518.3
			11	26656.7		9974.3	942769.4
			12		55993.9	56172.2	948293.7
			13	0.0	0.0	0.0	948293.7
			14			122155.5	948293.7
			15	48605.9	40086.3	0.0	939965.8

Table A1 continued

well	lithology	depth (m)	Vision No.	Fv ( $\mu\text{m}^2$ )	Fc ( $\mu\text{m}^2$ )	Fcl ( $\mu\text{m}^2$ )	T ( $\mu\text{m}^2$ )
TB8	tonalite	<b>6.4</b>	1	27822.1		0.0	951061.8
			2			14623.0	948282.4
			3			50428.4	945509.9
			4		43279.6	6184.4	948293.7
			5		107388.1	39178.9	951061.8
			6			11790.0	948293.7
			7			26450.0	948282.4
			8	0.0	0.0	0.0	948282.4
			9	0.0	0.0	0.0	948282.4
			10		16646.9	3412.5	948274.0
			11	0.0	0.0	0.0	948274.0
			12			18095.2	945509.9
			13	18554.2			951070.3
			14	2183.7	39604.0		945518.3
			15			18167.6	945509.9
		<b>10.5</b>	1	0.0	0.0	28159.6	943874.3
			2	0.0	0.0	0.0	945043.1
			3	0.0	12274.6	15794.6	945428.5
			4	0.0	0.0	33657.3	944790.2
			5	0.0	18472.1	0.0	945061.7
			6	0.0	0.0	0.0	944965.3
			7	0.0	4949.0	17675.1	943884.3
			8	0.0	0.0	0.0	945596.9
			9	0.0	0.0	0.0	944417.9
			10	0.0	0.0	17080.4	945261.4
			11	0.0	0.0	9095.4	945622.9
			12	0.0	0.0	0.0	944771.4
			13	0.0	38632.2	23979.6	945525.5
			14	0.0	0.0	0.0	945330.5
			15	0.0	0.0	0.0	943711.2
		<b>14.5</b>	1	0.0	0.0	0.0	945632.4
			2	0.0	0.0	39135.2	944398.0
			3	0.0	0.0	0.0	944178.3
			4	0.0	0.0	0.0	944426.2
			5	0.0	0.0	0.0	943766.8
			6	0.0	0.0	3415.4	945053.0
			7	0.0	0.0	0.0	945189.1
			8	0.0	0.0	24464.7	944913.0
			9	0.0	0.0	0.0	945514.6
			10	0.0	0.0	15529.1	944822.4
			11	0.0	0.0	0.0	944343.9
			12	0.0	0.0	0.0	944185.4
			13	0.0	0.0	0.0	943950.3
			14	0.0	0.0	0.0	944574.2
			15	0.0	0.0	6515.0	944890.5



Table A2. XRD results for mineral composition.

Well	Dept h(m)	Pla- gio- clase	Quart z	K- feld- spar	Py- rox- ene	Am- phi- bole	Bio- tite	Il- lite/ Mus- ulite	Ver- mic- ulite	Kao- linite	Chlo- rite	Mixe d layer	Ana- tase	Mag- ne- site	Hem- atite	Cal- cite	Do- lo- mite
	0.0	0.0	6.1	0.0	0.0	0.0	0.0	0.0	6.6	5.1	0.0	75.4	2.0	0.0	2.5	2.4	0.0
	0.4	53.8	6.7	0.0	3.0	0.0	0.0	8.9	3.5	0.0	0.0	0.0	0.7	0.0	2.3	21.0	0.0
	1.4	66.1	4.6	0.0	2.9	0.0	0.0	6.3	4.4	1.9	0.0	0.0	0.8	0.0	3.0	10.2	0.0
	2.4	58.0	13.2	0.0	2.5	0.0	0.0	4.7	3.8	1.9	0.0	0.0	0.7	0.0	0.8	14.3	0.0
	3.9	66.4	11.7	0.0	2.8	0.0	0.0	0.0	2.9	2.3	0.0	0.0	0.7	0.0	2.4	6.1	4.7
	5.4	76.8	0.9	0.0	3.8	0.0	0.0	0.0	0.0	1.5	0.0	0.0	1.0	0.0	3.5	11.1	1.5
	0.0	7.6	16.7	0.0	0	0.0	0.0	48.9	0.0	2.6	0.0	19.0	0.0	0.0	0.7	4.5	0.0
	0.9	7.2	25.8	4.8	0	0.0	0.0	24.1	0.0	0.0	0.0	28.3	0.2	0.0	1.1	0.0	8.5
GAI	1.9	29.0	13.1	0.0	0	0.0	0.0	55.5	0.0	1.6	0.0	0.0	0.0	0.0	0.2	0.6	0.0
	2.9	27.7	7.5	0.0	0	0.0	0.0	60.9	1.9	0.5	0.0	0.0	0.0	0.0	0.2	0.2	1.0
	3.9	32.2	12.5	0.0	0	4.7	0.0	49.2	0.0	0.0	0.0	0.0	0.0	0.0	0.4	0.6	0.5
	4.9	38.8	11.5	0.0	0	5.2	0.0	42.2	0.0	0.5	0.0	0.0	0.0	0.0	0.5	1.0	0.4
	6.1	36.5	16.4	0.0	0	4.9	0.0	40.4	0.0	0.0	0.0	0.0	0.0	0.0	0.5	0.8	0.6
	6.5	26.9	7.0	0.0	0	7.9	0.0	56.2	0.9	0.5	0.0	0.0	0.0	0.0	0.3	0.2	0.3
	7.9	40.6	7.1	0.0	0	3.2	0.0	46.8	1.0	0.7	0.0	0.0	0.0	0.0	0.2	0.3	0.2
	34.9	45.1	11.6	0.0	0	19.1	0.0	20.6	0.9	0.7	0.0	0.0	0.0	0.0	1.2	0.8	0.0
	35.9	41.5	5.9	0.0	0	18.1	0.0	25.0	0.8	0.7	0.0	6.9	0.2	0.0	0.5	0.5	0.0

Table A2 continued

Well	Dept h(m)	Pla- gio- clase	Quart z	K- feld- spar	Py- rox- ene	Am- phi- bole	Bio- tite	Il- lite/ Mus-	Ver- mic- ulite	Kao- linite	Chlo- rite	Mixe d layer	Ana- tase	Mag- ne- site	Hem- atite	Cal- cite	Do- lo- mite
	0.00	23.20	40.68	11.33	0	0	4.91	0.00	0.00	0.64	0.0	16.28	0.34	0.0	0.86	1.35	0.41
	0.80	23.12	42.60	10.48	0	0	4.91	0.00	0.00	0.69	0.0	13.69	0.41	0.0	0.91	2.78	0.40
	2.60	70.71	3.28	3.53	0	0	3.19	0.00	0.00	0.00	0.0	12.91	0.89	0.0	0.54	4.95	0.00
	4.00	35.67	32.96	14.47	0	0	2.92	0.00	0.00	0.38	0.0	11.48	0.57	0.0	0.23	0.84	0.49
	5.20	26.87	26.81	19.52	0	0	6.93	0.00	0.00	0.48	0.0	16.62	0.83	0.0	0.19	1.14	0.61
	5.80	37.73	30.03	16.26	0	0	2.70	0.00	0.00	0.49	0.0	8.13	0.65	0.0	0.24	3.13	0.63
GA2	6.75	40.29	24.22	17.31	0	0	3.23	0.00	0.00	0.40	0.0	11.20	0.56	0.0	0.28	1.87	0.63
	8.20	30.49	29.81	13.13	0	0	9.97	0.00	0.00	0.47	0.0	13.85	0.67	0.0	0.13	1.04	0.43
	9.20	36.74	33.92	10.62	0	0	6.65	0.00	0.00	0.63	0.0	9.50	0.66	0.0	0.14	0.76	0.39
	9.80	36.57	27.73	12.92	0	0	9.02	0.00	0.00	0.00	0.0	11.94	0.59	0.0	0.12	0.70	0.40
	10.80	28.12	31.81	15.03	0	0	9.62	0.00	0.00	0.49	0.0	12.60	0.71	0.0	0.24	0.89	0.49
	17.00	30.01	34.19	14.04	0	0	7.24	0.00	0.76	0.66	0.0	10.94	0.74	0.0	0.20	0.70	0.52
	17.60	32.17	31.58	14.96	0	0	6.65	0.00	0.82	0.59	0.0	10.84	0.83	0.0	0.15	0.88	0.51

Table A2 continued

Well	Dept h(m)	Pla- gio- clase	Quart z	K- feld- spar	Py- rox- ene	Am- phi- bole	Bio- tite	Il- lite/ Mus- ulite	Ver- mic- ulite	Kao- linite	Chlo- rite	Mixe d layer	Ana- tase	Mag- ne- site	Hem- atite	Cal- cite	Do- lo- mite
	0	26.7	13.1	0.0	0	0.0	0.0	0.0	0.00	2.0	0.0	30.6	0.00	0.0	0.5	25.4	1.7
	0.5	38.3	17.2	0.0	0	0.0	0.0	0.0	0.00	3.8	0.0	17.3	0.00	0.0	0.5	22.0	0.9
	1	32.2	30.8	0.0	0	0.0	0.0	0.0	0.00	10.3	4.2	14.3	0.00	0.0	0.3	6.1	1.8
	1.5	22.1	15.3	0.0	0	0.0	0.0	0.0	0.00	6.8	0.0	35.1	0.00	0.0	1.3	12.1	7.4
	2.5	26.3	12.0	0.0	0	0.0	0.0	0.0	0.00	4.7	0.0	38.9	0.00	0.0	0.9	3.3	14.0
	3.5	40.0	14.5	0.0	0	0.0	0.0	9.9	0.00	12.7	0.0	0.0	0.00	4.3	0.3	15.7	2.7
	4.5	35.6	20.5	0.0	0	0.0	0.0	0.0	0.00	4.1	14.3	16.2	0.00	1.8	0.4	6.3	0.8
	5.3	0.0	58.6	0.0	0	0.0	0.0	0.0	0.00	7.2	2.7	18.3	0.00	4.5	1.2	6.4	1.1
TB8	6.4	0.0	37.6	0.0	0	0.0	0.0	0.0	0.00	18.9	20.4	0.0	0.00	7.6	2.5	9.5	3.4
	7.5	29.4	39.3	0.0	0	0.0	0.0	0.0	0.00	5.4	2.5	10.8	0.00	5.6	0.7	5.5	0.8
	8.5	48.4	15.1	11.3	0	0.0	11.3	0.0	0.00	6.6	17.8	0.0	0.00	0.0	0.7	0.0	0.0
	9.5	27.9	24.1	11.9	0	0.0	11.9	0.0	0.00	0.0	35.1	0.0	0.00	0.0	1.0	0.0	0.0
	10.6	29.4	35.1	23.9	0	0.0	23.9	0.0	0.00	0.0	7.0	0.0	0.00	0.0	1.5	0.0	3.0
	11.5	36.4	18.4	6.7	0	25.0	6.7	0.0	0.00	0.0	9.5	0.0	0.00	0.0	2.3	0.0	1.7
	12.5	41.7	21.1	6.0	0	25.2	6.0	0.0	0.00	0.0	3.9	0.0	0.00	0.0	2.1	0.0	0.0
	13.5	42.1	40.9	11.7	0	0.0	11.7	0.0	0.00	0.0	3.7	0.0	0.00	0.0	0.7	0.0	1.0
	14.5	41.3	41.8	14.8	0	0.0	14.8	0.0	0.00	0.0	1.2	0.0	0.00	0.0	1.0	0.0	0.0

Table A2 continued

Well	Dept h(m)	Pla- gio- clase	Quar- tz	K- feld- spar	Py- rox- ene	Am- phi- bole	Bio- tite	Il- lite/ Mus	Ver- mic- ulite	Kao- linite	Chlo- rite	Mix- ed layer	Ana- tase	Mag- nesite	Hem- atite	Cal- cite	Do- lo- mite
	0	0	49.7	25.5	0.4	0.0	7.2	14.7	0.00	1.2	0.0	0.0	0.00	0.0	0.0	0.0	1.3
	0.2	20.7	35.3	31.6	0.3	0.0	8.7	3.4	0.00	0	0.0	0.0	0.00	0.0	0.0	0.0	0
	0.4	23.4	34.8	31.1	0	0.0	8.1	2.6	0.00	0	0.0	0.0	0.00	0.0	0.0	0.0	0
	0.6	35.3	36	17	2.3	0.0	9.4	0	0.00	0	0.0	0.0	0.00	0.0	0.0	0.0	0
	0.8	3.3	37.5	38.8	0	0.0	7.6	10.5	0.00	0	0.0	0.0	0.00	0.0	0.0	0.0	2.3
	1	9.6	30.7	21	0	0.0	9.2	9.6	0.00	0	0.0	0.0	0.00	0.0	0.0	0.0	19.9
	1.3	23.4	40.8	25.9	0	0.0	7.3	2.6	0.00	0	0.0	0.0	0.00	0.0	0.0	0.0	0
	1.5	23.5	33.5	33.6	1.2	0.0	8.2	0	0.00	0	0.0	0.0	0.00	0.0	0.0	0.0	0
<b>KB2-05</b>	1.7	35.5	38.2	15.4	2.1	0.0	8.8	0	0.00	0	0.0	0.0	0.00	0.0	0.0	0.0	0
	1.9	27	45.2	16.1	2.6	0.0	9.1	0	0.00	0	0.0	0.0	0.00	0.0	0.0	0.0	0
	2.2	34.2	40.4	12.6	2.5	0.0	10.3	0	0.00	0	0.0	0.0	0.00	0.0	0.0	0.0	0
	2.4	25.4	48.9	15.8	2.3	0.0	7.6	0	0.00	0	0.0	0.0	0.00	0.0	0.0	0.0	0
	2.6	30.4	38.3	19.2	1.6	0.0	10.5	0	0.00	0	0.0	0.0	0.00	0.0	0.0	0.0	0
	2.8	27.5	28.1	36.1	1.2	0.0	7.1	0	0.00	0	0.0	0.0	0.00	0.0	0.0	0.0	0
	3	32.1	35.2	22	2.3	0.0	8.4	0	0.00	0	0.0	0.0	0.00	0.0	0.0	0.0	0
	3.2	37.7	35.2	18.5	1.2	0.0	7.4	0	0.00	0	0.0	0.0	0.00	0.0	0.0	0.0	0
	3.4	29.4	46.1	17.5	0.2	0.0	6.8	0	0.00	0	0.0	0.0	0.00	0.0	0.0	0.0	0

Table A3. Major and element characteristics

Well	GA1											
	Depth(m)	0.0	0.4	1.4	2.4	3.9	5.4	0.0	0.9	1.9	2.9	3.9
MgO	2.6	1.9	2.4	2.4	3.2	1.8	3.2	5.0	2.4	3.2	2.9	
Al <sub>2</sub> O <sub>3</sub>	22.8	16.0	17.5	15.2	13.9	13.8	16.0	13.7	18.3	15.9	17.0	
CaO	1.6	11.4	6.3	11.8	9.9	12.3	5.8	5.8	4.1	6.4	5.8	
K <sub>2</sub> O	5.9	3.1	2.7	1.5	0.3	0.6	3.9	4.0	2.1	1.8	1.9	
Na <sub>2</sub> O	0.1	2.6	3.3	3.4	4.4	5.6	0.9	0.8	2.9	2.8	3.2	
SiO <sub>2</sub>	47.3	44.7	45.9	46.2	45.1	41.4	51.9	48.3	57.9	54.2	55.2	
P <sub>2</sub> O <sub>5</sub>	0.3	0.2	0.2	0.1	0.1	0.2	0.2	0.1	0.2	0.2	0.2	
TiO <sub>2</sub>	1.7	1.2	1.3	1.0	0.9	1.0	0.8	0.7	0.9	0.7	0.8	
MnO	0.0	0.2	0.1	0.2	0.2	0.2	0.1	0.2	0.1	0.1	0.1	
Fe <sub>2</sub> O <sub>3</sub> T	8.7	5.8	11.3	4.8	8.5	10.3	7.6	8.9	6.6	8.8	9.7	
LOI	8.5	13.0	8.9	13.2	13.6	12.2	9.3	12.0	4.5	5.8	3.0	
Sc	46.1	32.4	32.6	31.7	26.8	28.7	15.2	14.4	22.1	19.2	19.0	
Cu	11.0	11.9	21.0	8.7	7.0	11.9	6.5	33.0	14.1	21.8	18.5	
Zn	96.5	45.1	51.8	66.5	90.3	59.7	58.4	86.3	99.3	92.3	90.5	
Rb	381.0	186.8	159.5	84.7	17.3	32.4	208.8	227.2	106.8	83.2	80.9	
Sr	45.5	68.7	68.9	86.7	123.1	122.6	61.6	66.9	235.6	326.7	342.2	
Y	37.5	34.1	29.0	34.9	26.4	36.0	14.7	23.7	10.4	29.6	23.6	
Zr	175.6	113.2	118.6	113.4	98.5	106.2	103.0	137.4	69.6	104.5	113.8	
Nb	8.9	5.7	5.9	5.0	4.6	5.0	6.0	5.2	6.1	6.1	7.1	
Cs	128.0	45.2	46.6	21.3	8.1	7.6	50.3	49.0	39.4	18.3	14.8	
Ba	74.0	56.5	64.7	31.8	34.9	62.1	978.4	254.4	391.4	724.5	404.5	
Pb	14.9	9.7	12.7	10.1	17.0	17.7	6.7	19.4	10.3	12.4	12.7	
Th	5.5	3.7	3.8	3.3	3.1	3.1	3.7	5.2	4.8	4.3	5.9	
U	3.6	2.0	1.9	6.9	1.5	3.1	1.6	2.5	1.2	1.5	1.8	
La	17.1	15.1	12.5	17.6	14.7	19.0	14.3	17.8	15.8	22.0	19.3	
Ce	43.1	37.6	30.7	37.5	31.0	42.2	26.6	41.3	40.1	46.9	41.5	
Pr	5.6	4.8	3.9	5.1	4.1	5.8	3.4	5.6	5.3	6.0	5.3	
Nd	24.3	20.7	16.7	21.5	17.3	25.2	13.3	21.5	21.2	23.7	20.7	
Sm	6.4	5.2	4.2	4.9	3.9	6.1	2.8	4.9	3.8	5.2	4.4	
Eu	1.7	1.3	1.1	1.4	1.2	1.5	0.6	1.2	1.0	1.3	1.1	
Gd	6.8	5.5	4.5	5.6	4.4	6.3	2.7	4.6	2.8	5.0	4.1	
Tb	1.1	0.9	0.8	0.9	0.7	1.0	0.4	0.8	0.4	0.8	0.7	
Dy	6.7	5.8	4.8	5.4	4.5	5.6	2.5	4.8	2.2	4.9	4.1	
Ho	1.4	1.2	1.0	1.2	1.0	1.2	0.5	1.0	0.4	1.1	0.9	
Er	3.5	3.2	2.8	3.1	2.5	3.0	1.4	2.7	1.2	3.0	2.4	
Tm	0.5	0.4	0.4	0.4	0.4	0.4	0.2	0.4	0.2	0.4	0.4	
Yb	2.8	2.8	2.7	2.8	2.3	2.4	1.4	2.7	1.2	2.9	2.4	
Lu	0.4	0.4	0.4	0.4	0.4	0.4	0.2	0.4	0.2	0.5	0.4	

Table A3 continued

Well	GA1						GA2				
	4.9	6.1	6.5	7.9	34.9	35.9	0.0	0.8	2.6	4.0	5.2
MgO	3.0	3.0	3.0	3.0	3.2	3.2	1.4	1.3	1.6	1.3	1.5
Al <sub>2</sub> O <sub>3</sub>	17.3	17.4	17.4	17.5	18.1	18.0	14.7	14.5	18.2	15.0	15.7
CaO	5.9	5.7	5.8	5.4	7.0	6.8	1.5	3.0	8.2	1.4	2.0
K <sub>2</sub> O	1.9	1.8	1.9	1.8	1.5	1.6	4.2	3.8	3.0	3.7	4.3
Na <sub>2</sub> O	3.2	3.1	3.2	3.2	3.4	3.4	2.0	1.9	5.1	3.7	3.4
SiO <sub>2</sub>	55.9	56.0	56.0	56.2	55.0	55.4	66.3	64.8	50.0	68.0	66.0
P <sub>2</sub> O <sub>5</sub>	0.2	0.2	0.2	0.2	0.2	0.2	0.1	0.1	0.1	0.1	0.1
TiO <sub>2</sub>	0.8	0.9	0.9	0.8	0.9	0.9	0.4	0.4	0.5	0.4	0.5
MnO	0.1	0.1	0.1	0.1	0.2	0.2	0.0	0.1	0.1	0.0	0.1
Fe <sub>2</sub> O <sub>3</sub> T	8.5	9.0	8.4	8.6	9.3	9.0	5.6	5.3	5.0	3.3	3.6
LOI	2.9	3.0	2.7	3.4	1.1	1.0	3.6	4.7	8.3	2.3	2.8
Sc	18.4	19.3	17.1	19.7	20.7	20.5	6.5	6.5	8.9	7.1	8.2
Cu	17.3	21.0	15.9	21.4	19.8	21.8	4.9	3.6	4.6	39.2	6.3
Zn	88.7	92.1	92.8	97.9	86.6	88.6	46.5	42.6	69.8	41.9	49.0
Rb	65.0	72.0	68.8	66.1	43.4	46.2	186.8	185.7	125.7	110.5	146.1
Sr	348.3	338.2	348.1	348.0	413.2	417.9	30.3	42.0	132.7	77.0	90.6
Y	25.8	26.1	24.1	24.0	28.6	28.7	17.4	12.9	29.7	8.6	14.6
Zr	152.8	156.7	34.1	100.4	83.4	83.5	85.3	111.9	141.4	73.6	120.0
Nb	6.3	6.1	6.2	5.8	6.5	6.3	7.5	7.5	8.6	6.6	7.3
Cs	10.9	13.5	10.2	9.2	2.7	3.3	87.3	113.9	38.4	22.1	14.1
Ba	414.3	471.8	496.9	497.8	402.8	432.4	229.0	196.1	248.4	465.4	828.0
Pb	12.2	13.3	10.7	11.6	11.3	12.3	7.0	7.2	9.9	9.0	13.8
Th	7.2	5.1	4.1	4.0	4.8	3.7	18.3	17.9	18.1	19.7	18.5
U	1.8	1.7	1.7	1.4	2.3	1.5	1.3	1.5	3.1	5.9	2.6
La	18.8	18.7	17.7	17.9	22.4	21.2	13.1	30.0	35.9	16.2	17.8
Ce	41.1	39.6	38.2	38.6	46.9	45.5	32.3	51.7	69.6	34.7	39.3
Pr	5.4	5.3	5.1	5.0	6.2	5.9	3.7	4.7	7.8	3.9	4.7
Nd	21.2	22.0	20.6	20.1	24.8	24.4	14.5	14.2	27.4	13.6	17.0
Sm	4.7	5.0	4.6	4.6	5.4	5.4	3.3	2.6	5.2	2.4	3.4
Eu	1.2	1.2	1.2	1.2	1.4	1.4	0.8	0.6	1.2	0.5	0.8
Gd	4.5	4.8	4.3	4.4	5.0	5.3	3.3	2.8	5.0	2.1	3.0
Tb	0.7	0.8	0.7	0.7	0.8	0.9	0.5	0.4	0.8	0.3	0.5
Dy	4.5	4.8	4.3	4.4	5.0	5.2	3.1	2.2	4.5	1.6	2.6
Ho	0.9	1.0	0.9	0.9	1.0	1.1	0.6	0.4	0.9	0.3	0.5
Er	2.6	2.7	2.4	2.5	2.8	2.9	1.6	1.2	2.5	0.9	1.4
Tm	0.4	0.4	0.4	0.4	0.4	0.4	0.2	0.2	0.4	0.1	0.2
Yb	2.6	2.6	2.2	2.3	2.6	2.6	1.3	1.2	2.4	0.9	1.4
Lu	0.4	0.4	0.4	0.4	0.4	0.4	0.2	0.2	0.4	0.1	0.2

Table A3 continued

Well	GA2									TB8	
	5.8	6.8	8.2	9.2	9.8	10.8	17.0	17.6	0.0	0.5	1.0
MgO	1.1	1.2	1.6	1.2	1.5	1.5	1.2	1.3	2.3	2.0	1.7
Al <sub>2</sub> O <sub>3</sub>	14.2	15.3	14.9	15.2	15.1	15.1	14.8	15.3	15.2	13.8	13.7
CaO	4.9	3.2	2.8	3.4	2.7	2.7	2.5	2.9	15.6	15.3	8.5
K <sub>2</sub> O	3.8	4.5	3.6	2.9	3.9	3.9	3.4	3.8	3.1	2.2	1.5
Na <sub>2</sub> O	3.5	3.3	3.3	3.5	3.4	3.4	3.5	3.4	1.4	2.5	3.4
SiO <sub>2</sub>	64.7	64.8	65.5	67.5	65.5	65.5	68.4	66.4	41.4	44.9	56.9
P <sub>2</sub> O <sub>5</sub>	0.1	0.1	0.1	0.1	0.1	0.1	0.1	0.1	n.d.	n.d.	0.2
TiO <sub>2</sub>	0.4	0.4	0.5	0.4	0.5	0.5	0.4	0.4	1.0	0.5	0.7
MnO	0.1	0.1	0.1	0.1	0.1	0.1	0.1	0.1	0.9	1.1	0.5
Fe <sub>2</sub> O <sub>3</sub> T	2.8	3.3	4.1	3.6	4.4	4.4	3.4	3.8	3.8	3.4	3.4
LOI	4.5	4.1	3.1	2.0	2.3	2.3	1.7	2.1	16.1	15.1	8.6
Sc	6.6	7.4	7.8	6.9	7.4	7.9	6.3	6.6	151.6	122.3	75.5
Cu	10.7	4.0	5.9	4.5	6.1	4.8	4.9	5.7	19.3	20.2	23.9
Zn	31.4	48.5	61.0	45.5	47.4	54.1	45.5	49.5	82.9	80.3	109.4
Rb	120.0	155.2	136.2	115.7	126.6	140.0	120.1	129.0	676.0	467.4	258.5
Sr	71.6	103.4	142.6	199.1	124.0	155.3	175.8	186.8	265.0	307.5	396.7
Y	22.4	13.3	14.5	14.6	11.5	12.8	9.7	12.9	110.0	125.7	56.2
Zr	102.1	95.4	123.0	100.5	79.4	79.5	86.5	106.4	156.1	289.4	744.1
Nb	5.8	6.7	8.0	7.2	7.6	7.6	6.6	6.6	3.3	6.2	9.9
Cs	15.8	38.5	12.5	10.7	13.0	15.8	9.5	8.8	234.9	153.7	74.3
Ba	972.1	798.9	555.1	454.4	494.8	837.5	619.2	803.4	228.1	436.1	478.4
Pb	11.0	14.3	15.4	15.4	13.4	15.6	15.6	17.7	23.2	19.8	20.3
Th	12.9	14.5	15.6	18.5	18.0	20.9	17.9	15.6	5.9	13.9	21.0
U	3.9	2.4	3.7	3.1	6.3	5.5	5.9	5.9	11.6	9.0	7.7
La	25.9	18.5	28.3	28.4	23.4	30.2	24.6	26.0	31.3	41.2	19.8
Ce	55.8	33.6	51.6	53.8	44.6	57.1	48.9	49.7	82.3	107.9	53.2
Pr	6.4	3.9	5.9	5.9	4.9	6.2	5.4	5.4	12.7	16.0	7.4
Nd	23.4	13.7	20.8	20.9	17.1	21.7	18.9	19.2	62.8	73.1	34.2
Sm	4.7	2.6	3.8	3.7	3.0	3.8	3.3	3.5	20.5	21.6	9.7
Eu	1.2	0.6	0.8	0.9	0.7	0.8	0.8	0.8	6.2	6.2	2.8
Gd	4.3	2.5	3.3	3.3	2.7	3.2	2.8	3.1	24.2	25.2	11.5
Tb	0.7	0.4	0.5	0.5	0.4	0.4	0.4	0.4	3.5	3.8	1.8
Dy	3.7	2.2	2.7	2.6	2.0	2.3	2.0	2.3	21.2	23.4	11.1
Ho	0.7	0.4	0.5	0.5	0.4	0.5	0.4	0.5	4.1	4.7	2.3
Er	2.0	1.2	1.4	1.3	1.1	1.3	1.0	1.3	11.6	13.8	6.9
Tm	0.3	0.2	0.2	0.2	0.2	0.2	0.1	0.2	1.5	1.9	1.0
Yb	2.0	1.2	1.5	1.4	1.1	1.3	1.0	1.2	9.8	12.7	7.2
Lu	0.3	0.2	0.2	0.2	0.2	0.2	0.2	0.2	1.4	1.8	1.2

Table A3 continued

Well	TB8										
Depth(m)	1.5	2.5	3.5	4.5	5.3	6.4	7.5	8.5	9.5	10.6	11.5
MgO	4.1	5.9	3.6	3.7	3.9	8.0	4.8	8.3	9.4	4.6	5.6
Al <sub>2</sub> O <sub>3</sub>	14.8	13.8	14.4	13.9	7.5	10.0	10.6	19.1	15.8	14.3	15.7
CaO	11.3	10.7	15.8	9.5	8.1	9.5	6.9	3.6	2.1	5.1	5.1
K <sub>2</sub> O	2.5	3.0	0.9	1.5	0.6	0.5	0.6	1.1	1.7	1.4	1.5
Na <sub>2</sub> O	1.3	2.1	2.0	3.3	0.2	n.d.	2.3	1.9	1.4	1.9	2.8
SiO <sub>2</sub>	39.9	39.6	36.3	47.6	55.8	37.3	49.4	47.4	51.1	54.6	55.0
P <sub>2</sub> O <sub>5</sub>	n.d.	0.1	n.d.	0.1	n.d.	n.d.	0.1	0.1	0.1	0.1	0.1
TiO <sub>2</sub>	0.6	0.7	1.1	1.2	0.6	0.7	1.7	1.3	0.9	1.6	1.1
MnO	1.6	0.9	0.9	0.6	0.7	1.2	0.8	0.4	0.4	0.4	0.4
Fe <sub>2</sub> O <sub>3</sub> T	9.0	6.2	7.0	7.8	9.7	16.3	10.2	10.6	11.6	12.9	9.9
LOI	15.7	16.1	17.7	10.4	11.8	16.8	12.5	6.5	6.0	3.3	3.1
Sc	138.1	128.5	168.4	126.1	77.4	126.5	156.7	156.7	127.3	164.6	125.5
Cu	56.9	48.9	96.1	98.4	55.4	75.5	84.8	122.2	78.5	126.8	87.3
Zn	407.5	361.1	278.9	344.5	259.2	630.5	374.3	644.1	657.3	423.8	474.0
Rb	594.6	620.1	196.9	317.8	153.9	132.7	215.1	228.9	401.3	364.6	349.2
Sr	336.4	572.7	468.3	404.3	175.4	279.0	234.6	474.8	403.9	703.1	676.7
Y	72.8	93.4	108.7	85.7	77.2	85.3	80.5	93.8	78.3	72.0	76.9
Zr	88.6	90.9	130.8	286.2	155.4	78.2	681.2	127.1	226.3	253.7	232.8
Nb	12.1	5.8	4.7	8.5	3.2	0.0	10.4	<0,002	3.6	4.3	4.5
Cs	260.1	227.8	98.5	212.1	86.9	72.8	159.4	93.3	176.8	162.0	123.8
Ba	192.4	204.1	2328	2094	389.4	134.0	149.8	543.0	839.8	732.8	845.6
Pb	32.9	17.1	23.1	27.4	12.0	16.5	24.5	33.8	15.4	46.0	25.6
Th	4.8	3.0	4.6	11.5	4.4	2.9	22.3	4.1	10.2	11.6	9.2
U	10.5	4.8	3.5	5.8	4.1	7.1	8.1	7.2	4.5	4.9	4.3
La	20.0	33.3	70.2	36.4	26.5	30.0	26.8	52.8	36.4	46.1	29.3
Ce	47.8	70.6	166.6	86.2	65.6	72.4	66.9	106.5	75.7	104.6	67.6
Pr	6.7	9.8	22.1	11.8	9.5	10.0	9.7	13.4	10.5	13.5	9.4
Nd	31.7	46.9	95.8	51.4	45.3	45.1	44.3	58.7	49.8	57.9	43.6
Sm	8.6	13.0	21.4	13.7	12.7	12.6	12.8	15.1	13.6	13.9	11.8
Eu	3.0	4.0	6.2	4.4	3.4	4.0	3.4	5.3	3.9	4.6	4.8
Gd	11.7	16.4	21.4	15.5	14.4	14.9	14.3	18.3	16.3	14.6	14.0
Tb	1.8	2.5	3.2	2.7	2.4	2.6	2.5	3.0	2.7	2.4	2.3
Dy	11.7	15.1	19.3	17.6	15.7	17.3	16.6	18.9	15.7	15.4	15.2
Ho	2.5	3.2	4.0	3.8	3.2	3.5	3.5	4.0	3.2	3.2	3.1
Er	7.2	8.8	10.9	11.6	9.5	10.5	10.8	10.8	9.1	9.6	9.2
Tm	1.0	1.2	1.6	1.7	1.5	1.5	1.7	1.5	1.3	1.4	1.3
Yb	6.7	7.4	9.5	11.6	10.1	10.6	11.7	9.4	8.3	9.7	8.8
Lu	1.0	1.1	1.5	1.7	1.5	1.5	1.8	1.3	1.2	1.5	1.3



Table A3 continued

Well	TB8						KB2/05					
	Depth(m)	12.5	13.5	14.5	0.0	0.2	0.4	0.6	0.8	1.0	1.3	1.5
MgO	5.0	3.3	5.3	2.3	1.0	0.9	1.1	1.2	4.5	1.3	0.9	
Al <sub>2</sub> O <sub>3</sub>	15.5	13.8	15.0	14.1	15.2	14.8	15.4	15.7	13.3	15.4	15.7	
CaO	5.5	3.3	2.7	1.5	0.9	1.1	1.4	0.7	5.3	1.6	1.2	
K <sub>2</sub> O	1.3	1.5	1.7	7.6	6.2	6.1	4.4	7.8	7.3	5.6	5.9	
Na <sub>2</sub> O	3.2	3.2	4.2	0.2	2.3	2.5	3.4	1.5	1.0	3.1	3.1	
SiO <sub>2</sub>	56.7	63.0	58.8	67.0	70.3	70.5	69.8	68.2	55.9	68.3	69.2	
P <sub>2</sub> O <sub>5</sub>	0.2	0.1	n.d.	0.2	0.2	0.1	0.1	0.2	0.2	0.2	0.2	
TiO <sub>2</sub>	1.1	1.2	0.7	0.5	0.4	0.4	0.5	0.4	0.3	0.4	0.4	
MnO	0.4	0.3	0.2	0.0	0.0	0.0	0.0	0.0	0.1	0.0	0.0	
Fe <sub>2</sub> O <sub>3</sub> T	9.2	8.4	7.7	3.4	3.1	3.3	4.0	3.3	3.0	3.5	3.3	
LOI	2.3	2.2	3.4	4.4	1.5	1.3	1.5	2.2	10.2	2.0	1.2	
Sc	113.6	92.2	103.3	6.4	4.7	4.1	4.7	4.9	4.3	4.4	4.2	
Cu	110.4	136.7	86.8	22.7	3.6	3.3	3.4	2.9	3.0	3.4	3.2	
Zn	424.0	353.2	492.2	76.5	59.9	54.8	66.6	57.0	44.7	54.2	50.0	
Rb	306.1	314.8	331.7	187.0	165.0	170.0	144.0	188.0	167.0	154.0	176.0	
Sr	757.4	528.8	496.7	114.0	460.0	494.0	479.0	389.0	303.0	504.0	578.0	
Y	97.9	140.8	68.1	10.5	6.9	6.5	6.3	7.8	8.7	7.5	7.9	
Zr	322.5	611.3	144.3	183.0	176.0	167.0	166.0	155.0	125.0	148.0	144.0	
Nb	7.0	14.4	2.7	11.0	9.4	9.3	10.5	9.1	6.9	8.3	7.8	
Cs	90.6	65.4	152.4	33.0	18.6	14.3	14.3	17.4	13.8	14.8	11.2	
Ba	1083	1194	714.0	620.0	1314	1430	604.0	1452	1360	1156	1528	
Pb	26.0	29.6	24.9	13.1	28.3	29.1	23.1	28.6	24.4	27.1	36.1	
Th	12.0	22.4	29.4	19.1	14.7	16.6	17.8	15.7	12.2	13.8	18.9	
U	3.9	5.9	6.6	10.5	1.7	1.7	1.6	1.6	1.4	1.7	1.9	
La	38.9	46.5	27.6	45.0	48.6	55.5	57.6	49.7	47.3	53.4	63.6	
Ce	88.0	114.3	48.5	71.3	76.8	88.3	98.3	84.3	78.4	85.8	108.0	
Pr	12.1	16.6	6.1	9.4	9.3	11.0	11.8	10.1	9.8	10.5	12.3	
Nd	55.5	78.8	27.9	35.3	34.6	38.1	41.6	36.1	36.2	38.4	45.1	
Sm	14.7	22.2	8.1	5.1	4.5	5.0	6.1	5.2	5.6	5.2	6.3	
Eu	5.4	4.5	2.6	0.7	0.8	1.0	1.1	1.0	1.3	1.2	1.3	
Gd	17.7	25.8	11.4	4.1	3.7	4.1	4.4	4.1	4.1	3.8	4.8	
Tb	2.9	4.3	1.9	0.6	0.4	0.5	0.5	0.5	0.6	0.5	0.6	
Dy	19.2	28.1	12.4	2.9	2.2	2.1	2.3	2.4	2.4	2.3	2.6	
Ho	4.0	5.9	2.7	0.4	0.3	0.3	0.3	0.3	0.3	0.3	0.3	
Er	12.0	17.9	7.7	1.5	0.9	0.9	1.0	1.1	1.1	1.0	1.1	
Tm	1.7	2.7	1.2	0.1	0.1	0.1	0.1	0.1	0.1	0.1	0.1	
Yb	11.7	18.4	7.7	1.1	0.6	0.6	0.7	0.8	0.7	0.7	0.7	
Lu	1.8	2.9	1.1	0.1	0.1	0.1	0.1	0.1	0.1	0.1	0.1	

Table A3 continued

Well	KB2-05										
Depth(m)	1.7	1.9	2.2	2.4	2.6	2.8	3.0	3.2	3.4	3.6	3.8
MgO	1.1	1.2	1.0	0.9	1.0	0.8	1.0	1.1	1.0	0.9	1.1
Al <sub>2</sub> O <sub>3</sub>	16.2	15.4	15.9	14.6	15.4	16.7	16.6	15.4	16.2	15.6	15.6
CaO	1.7	1.4	1.8	1.4	1.3	1.1	1.5	1.5	1.5	1.1	1.6
K <sub>2</sub> O	4.9	5.6	5.2	4.9	5.0	7.3	6.1	4.6	5.0	5.9	4.0
Na <sub>2</sub> O	3.7	3.0	3.5	3.3	3.4	3.1	3.4	3.5	3.7	3.0	3.9
SiO <sub>2</sub>	67.8	68.6	67.5	70.5	69.0	66.7	67.1	69.3	68.6	69.7	69.4
P <sub>2</sub> O <sub>5</sub>	0.2	0.3	0.3	0.3	0.2	0.2	0.2	0.3	0.2	0.2	0.2
TiO <sub>2</sub>	0.4	0.4	0.4	0.4	0.5	0.5	0.5	0.5	0.4	0.4	0.5
MnO	0.0	0.0	0.0	0.0	0.0	0.0	0.0	0.0	0.0	0.0	0.0
Fe <sub>2</sub> O <sub>3</sub> T	4.3	3.7	3.7	3.5	3.8	3.5	3.7	4.0	3.8	3.2	4.1
LOI	1.3	1.3	1.7	1.4	1.4	1.0	1.1	1.1	1.0	1.1	1.1
Sc	4.8	4.7	4.8	4.3	5.5	5.0	5.7	5.1	4.9	4.3	5.1
Cu	3.3	3.5	2.9	3.3	4.5	3.5	3.6	5.9	3.0	3.2	3.7
Zn	61.9	61.4	57.4	52.6	54.4	48.3	55.9	61.9	58.1	49.7	55.8
Rb	158.0	170.0	163.0	155.0	172.0	201.0	184.0	163.0	163.0	166.0	145.0
Sr	612.0	535.0	537.0	527.0	598.0	713.0	660.0	561.0	597.0	547.0	557.0
Y	8.9	12.0	9.6	10.0	7.0	7.5	9.4	11.4	9.3	7.1	9.6
Zr	144.0	160.0	162.0	156.0	157.0	153.0	163.0	200.0	160.0	147.0	170.0
Nb	11.0	9.9	8.7	9.4	9.9	9.4	11.5	13.5	9.6	9.2	10.9
Cs	11.6	14.2	12.7	10.3	11.2	9.4	10.6	11.5	10.3	12.2	10.9
Ba	1041	1247	1024	1235	1139	2221	1731	1040	1220	1499	737.0
Pb	31.2	28.6	27.8	28.7	28.2	45.8	39.4	29.9	29.2	30.8	25.6
Th	17.2	20.9	16.8	16.8	19.2	19.8	17.7	23.0	19.2	16.9	19.3
U	1.9	2.0	1.8	1.9	1.8	2.0	2.0	2.3	1.8	2.0	1.9
La	67.3	73.0	60.0	60.7	69.7	66.3	66.9	77.6	67.9	53.9	69.4
Ce	109.0	122.0	98.5	99.6	111.0	104.0	111.0	125.0	105.0	84.7	116.0
Pr	13.0	15.0	12.2	12.4	13.6	13.4	12.7	16.0	13.5	10.1	13.7
Nd	44.9	55.3	44.2	43.3	49.5	46.9	47.1	56.5	46.7	37.3	48.5
Sm	6.5	8.0	6.5	6.1	6.1	6.1	6.8	7.8	6.4	5.4	6.8
Eu	1.2	1.3	1.3	1.2	1.2	1.2	1.6	1.5	1.1	1.0	1.2
Gd	4.6	5.9	5.0	5.0	5.7	4.7	5.1	6.4	5.4	4.1	5.6
Tb	0.7	0.8	0.7	0.6	0.5	0.6	0.7	0.8	0.7	0.5	0.6
Dy	3.0	3.4	2.7	2.8	2.8	2.7	2.9	3.5	2.7	2.3	2.9
Ho	0.3	0.5	0.4	0.4	0.3	0.3	0.4	0.4	0.4	0.3	0.4
Er	1.2	1.6	1.3	1.3	1.3	1.1	1.3	1.6	1.3	0.9	1.3
Tm	0.1	0.2	0.2	0.1	0.1	0.1	0.1	0.2	0.1	0.1	0.2
Yb	0.8	1.1	0.9	0.9	0.6	0.7	0.9	1.0	0.9	0.6	0.9
Lu	0.1	0.1	0.1	0.1	0.1	0.1	0.1	0.1	0.1	0.1	0.1

Table A4.  $\tau$  value of GA1, GA2, TB8 and BK2/05

well	GA1	GA1	GA1	GA1	GA1	GA1	GA1	GA1	GA1	GA1	GA1
Depth(m)	0	0.4	1.4	2.4	3.9	5.4	0	0.9	1.9	2.9	3.9
MgO	-0.20	-0.10	0.01	0.24	0.83	0.00	0.17	1.21	-0.19	0.22	0.07
Al <sub>2</sub> O <sub>3</sub>	-0.06	-0.01	-0.02	0.06	0.05	0.00	0.04	0.08	0.09	0.10	0.10
CaO	-0.93	-0.21	-0.60	-0.07	-0.15	0.00	0.01	0.21	-0.36	0.17	-0.01
K <sub>2</sub> O	4.22	3.14	2.27	1.24	-0.44	0.00	1.80	2.50	0.41	0.42	0.39
Na <sub>2</sub> O	-0.99	-0.61	-0.55	-0.42	-0.18	0.00	-0.69	-0.67	-0.10	0.04	0.09
SiO <sub>2</sub>	-0.35	-0.08	-0.14	0.08	0.14	0.00	0.10	0.24	0.11	0.22	0.16
P <sub>2</sub> O <sub>5</sub>	-0.07	0.05	-0.09	-0.11	-0.05	0.00	-0.01	-0.60	-0.02	-0.06	0.01
Fe <sub>2</sub> O <sub>3</sub>	-0.52	-0.51	-0.15	-0.55	-0.13	0.00	-0.02	0.40	-0.22	0.22	0.25
Sc	-0.11	0.00	-0.07	0.08	0.02	0.00	-0.21	-0.11	0.08	0.07	-0.04
Mn	-0.85	0.07	-0.44	0.29	0.02	0.00	-0.13	0.41	-0.55	-0.04	-0.26
Cu	-0.49	-0.12	0.44	-0.29	-0.36	0.00	-0.66	1.01	-0.32	0.21	-0.07
Zn	-0.10	-0.33	-0.29	0.09	0.65	0.00	-0.29	0.25	0.14	0.22	0.08
Rb	5.53	4.09	3.05	1.56	-0.42	0.00	4.00	5.43	1.40	1.15	0.88
Sr	-0.79	-0.51	-0.54	-0.31	0.09	0.00	-0.84	-0.80	-0.43	-0.09	-0.14
Y	-0.42	-0.17	-0.34	-0.05	-0.20	0.00	-0.45	0.05	-0.63	0.19	-0.14
Zr	-0.08	-0.06	-0.08	0.04	0.01	0.00	0.32	1.09	-0.16	0.45	0.42
Nb	-0.01	0.01	-0.02	-0.01	0.01	0.00	0.00	0.02	-0.05	0.09	0.16
Cs	8.36	4.25	4.04	1.75	0.16	0.00	17.02	19.78	12.27	6.08	4.16
Ba	-0.34	-0.20	-0.14	-0.50	-0.39	0.00	1.51	-0.23	-0.06	1.00	0.01
La	-0.50	-0.30	-0.46	-0.10	-0.16	0.00	-0.30	0.04	-0.27	0.16	-0.08
Ce	-0.43	-0.21	-0.40	-0.13	-0.20	0.00	-0.38	0.13	-0.13	0.17	-0.06
Pr	-0.47	-0.27	-0.45	-0.15	-0.23	0.00	-0.41	0.17	-0.12	0.15	-0.09
Nd	-0.46	-0.28	-0.46	-0.16	-0.25	0.00	-0.42	0.10	-0.13	0.11	-0.12
Sm	-0.41	-0.24	-0.44	-0.20	-0.29	0.00	-0.45	0.14	-0.30	0.10	-0.16
Eu	-0.37	-0.22	-0.41	-0.06	-0.14	0.00	-0.50	0.08	-0.26	0.07	-0.13
Gd	-0.41	-0.23	-0.42	-0.13	-0.24	0.00	-0.43	0.13	-0.45	0.13	-0.16
Tb	-0.35	-0.16	-0.37	-0.08	-0.18	0.00	-0.44	0.17	-0.53	0.10	-0.16
Dy	-0.34	-0.09	-0.30	-0.06	-0.14	0.00	-0.47	0.20	-0.57	0.12	-0.16
Ho	-0.35	-0.07	-0.26	0.01	-0.09	0.00	-0.46	0.17	-0.59	0.14	-0.13
Er	-0.37	-0.08	-0.24	-0.01	-0.09	0.00	-0.45	0.19	-0.57	0.21	-0.12
Tm	-0.35	-0.04	-0.17	0.07	-0.01	0.00	-0.45	0.25	-0.56	0.23	-0.08
Yb	-0.35	0.01	-0.10	0.11	0.03	0.00	-0.44	0.33	-0.54	0.30	-0.03
Lu	-0.40	-0.01	-0.09	0.13	0.05	0.00	-0.42	0.31	-0.52	0.34	0.00
Pb	-0.53	-0.52	-0.41	-0.44	0.05	0.00	-0.39	1.08	-0.13	0.21	0.12
Th	-0.03	0.04	0.00	0.03	0.06	0.00	-0.06	0.53	0.14	0.17	0.43
U	-0.35	-0.44	-0.49	1.18	-0.48	0.00	-0.08	0.69	-0.35	-0.09	0.03

Table A4 continued

well	GA1	GA1	GA1	GA1	GA1	GA1	GA2	GA2	GA2	GA2	GA2
Depth(m)	4.9	6.1	6.5	7.9	34.9	35.9	0	0.8	2.6	4	5.2
MgO	0.05	0.01	0.01	0.09	0.06	0.00	0.06	-0.01	0.01	-0.03	0.04
Al <sub>2</sub> O <sub>3</sub>	0.07	0.05	0.03	0.12	0.05	0.00	-0.04	-0.06	-0.03	-0.05	-0.10
CaO	-0.03	-0.09	-0.08	-0.09	0.07	0.00	-0.46	0.09	1.44	-0.52	-0.36
K <sub>2</sub> O	0.29	0.22	0.24	0.31	-0.02	0.00	0.16	0.03	-0.32	-0.01	0.05
Na <sub>2</sub> O	0.06	-0.02	0.01	0.08	0.05	0.00	-0.44	-0.47	0.17	0.02	-0.15
SiO <sub>2</sub>	0.12	0.10	0.07	0.17	0.03	0.00	-0.03	-0.06	-0.40	-0.04	-0.15
P <sub>2</sub> O <sub>5</sub>	-0.08	-0.12	-0.04	0.02	0.07	0.00	0.13	0.09	-0.02	0.03	0.02
Fe <sub>2</sub> O <sub>3</sub>	0.05	0.08	-0.01	0.10	0.07	0.00	0.52	0.43	0.12	-0.13	-0.13
Sc	-0.05	-0.07	-0.18	0.03	0.00	0.00	-0.08	-0.06	0.02	0.04	0.06
Mn	-0.22	-0.26	-0.18	-0.09	0.02	-0.02	-0.17	0.13	0.71	-0.26	-0.04
Cu	-0.12	0.01	-0.24	0.11	-0.06	0.06	-0.15	-0.37	-0.35	6.04	-0.01
Zn	0.08	0.05	0.05	0.20	-0.02	0.02	-0.10	-0.16	0.10	-0.16	-0.14
Rb	0.54	0.61	0.52	0.59	-0.04	0.04	0.39	0.39	-0.25	-0.15	-0.02
Sr	-0.11	-0.19	-0.17	-0.10	-0.01	0.01	-0.85	-0.78	-0.45	-0.60	-0.58
Y	-0.04	-0.09	-0.17	-0.10	-0.01	0.01	0.43	0.07	0.97	-0.27	0.08
Zr	0.95	0.88	-0.60	0.30	-0.01	0.01	-0.18	0.08	0.10	-0.27	0.04
Nb	0.04	-0.05	-0.05	-0.03	0.01	-0.01	0.05	0.07	-0.02	-0.05	-0.07
Cs	2.88	3.52	2.37	2.33	-0.10	0.10	7.78	10.58	2.12	1.29	0.28
Ba	0.05	0.13	0.17	0.28	-0.04	0.04	-0.70	-0.74	-0.74	-0.38	-0.03
La	-0.08	-0.14	-0.20	-0.12	0.02	-0.02	-0.52	0.11	0.06	-0.39	-0.41
Ce	-0.05	-0.14	-0.18	-0.10	0.01	-0.01	-0.39	-0.02	0.06	-0.33	-0.34
Pr	-0.06	-0.12	-0.17	-0.11	0.01	-0.01	-0.38	-0.20	0.08	-0.32	-0.29
Nd	-0.08	-0.11	-0.18	-0.12	0.00	0.00	-0.30	-0.30	0.08	-0.32	-0.26
Sm	-0.08	-0.08	-0.16	-0.08	-0.01	0.02	-0.12	-0.27	0.15	-0.32	-0.17
Eu	-0.09	-0.09	-0.14	-0.05	-0.01	0.01	-0.12	-0.34	0.12	-0.41	-0.18
Gd	-0.07	-0.08	-0.18	-0.08	-0.04	0.04	0.03	-0.13	0.27	-0.33	-0.15
Tb	-0.08	-0.07	-0.16	-0.08	-0.02	0.02	0.18	-0.08	0.44	-0.34	-0.05
Dy	-0.06	-0.05	-0.17	-0.06	-0.02	0.02	0.32	-0.04	0.55	-0.31	0.01
Ho	-0.06	-0.07	-0.17	-0.07	-0.02	0.02	0.37	0.01	0.64	-0.28	0.06
Er	-0.01	-0.03	-0.15	-0.05	-0.02	0.02	0.32	0.02	0.66	-0.28	0.05
Tm	0.01	-0.01	-0.15	-0.04	-0.01	0.01	0.24	0.01	0.66	-0.25	0.06
Yb	0.06	0.01	-0.15	-0.03	-0.01	0.01	0.09	-0.03	0.57	-0.26	0.02
Lu	0.10	0.04	-0.13	0.01	0.01	-0.01	0.08	-0.05	0.56	-0.25	0.01
Pb	0.10	0.12	-0.11	0.06	-0.05	0.05	-0.61	-0.60	-0.56	-0.48	-0.31
Th	0.78	0.19	-0.06	0.01	0.12	-0.12	0.01	0.00	-0.19	0.12	-0.08
U	0.05	-0.09	-0.09	-0.20	0.21	-0.21	-0.79	-0.77	-0.61	-0.05	-0.64

Table A4 continued

well	GA2	GA2	GA2	GA2	GA2	GA2	GA2	GA2	TB8	TB8	TB8
Depth(m)	5.8	6.75	8.2	9.2	9.8	10.8	17	17.6	0	0.5	1
MgO	-0.07	-0.12	0.02	-0.01	-0.03	-0.01	-0.02	0.02	-0.53	-0.58	-0.67
Al <sub>2</sub> O <sub>3</sub>	0.06	-0.06	-0.21	0.04	-0.17	-0.15	0.02	-0.02	0.08	0.05	-0.07
CaO	1.00	0.10	-0.19	0.29	-0.18	-0.17	-0.04	0.04	5.19	5.44	2.20
K <sub>2</sub> O	0.17	0.15	-0.19	-0.18	-0.09	-0.09	-0.03	0.03	0.99	0.48	-0.07
Na <sub>2</sub> O	0.13	-0.13	-0.23	0.03	-0.17	-0.17	0.05	-0.05	-0.64	-0.33	-0.19
SiO <sub>2</sub>	0.07	-0.11	-0.23	0.02	-0.19	-0.18	0.05	-0.05	-0.26	-0.14	-0.02
P <sub>2</sub> O <sub>5</sub>	0.12	-0.01	-0.10	0.01	-0.04	-0.04	0.00	0.00	n	n	n
Fe <sub>2</sub> O <sub>3</sub>	-0.12	-0.15	-0.09	0.01	0.02	0.02	-0.01	0.01	-0.47	-0.50	-0.55
Sc	0.09	0.04	-0.05	0.11	0.04	0.01	0.01	-0.01	-0.05	0.62	-0.26
Mn	1.01	0.01	0.00	0.10	0.00	0.04	-0.07	0.06	3.53	4.49	1.46
Cu	1.14	-0.32	-0.12	-0.13	0.05	-0.24	-0.04	0.04	-0.86	-0.68	-0.72
Zn	-0.30	-0.07	0.02	-0.01	-0.09	-0.05	-0.01	0.01	-0.89	-0.78	-0.77
Rb	0.03	0.13	-0.14	-0.04	-0.08	-0.07	0.00	0.00	0.32	0.92	-0.21
Sr	-0.58	-0.48	-0.38	0.13	-0.38	-0.29	0.01	-0.01	-0.65	-0.16	-0.19
Y	1.12	0.07	0.02	0.34	-0.07	-0.06	-0.11	0.10	0.05	1.52	-0.16
Zr	0.13	-0.10	0.01	0.08	-0.25	-0.32	-0.07	0.07	-0.30	1.74	4.23
Nb	-0.06	-0.08	-0.04	0.13	0.05	-0.05	0.04	-0.03	-0.21	2.16	4.64
Cs	0.83	2.80	0.07	0.20	0.29	0.43	0.08	-0.07	0.00	0.38	-0.51
Ba	0.45	0.02	-0.38	-0.34	-0.37	-0.02	-0.10	0.09	-0.79	-0.17	-0.32
La	0.09	-0.34	-0.12	0.16	-0.16	-0.01	0.01	-0.01	-0.27	1.03	-0.27
Ce	0.21	-0.38	-0.17	0.13	-0.18	-0.04	0.03	-0.03	0.10	2.04	0.11
Pr	0.25	-0.35	-0.15	0.13	-0.18	-0.06	0.04	-0.03	0.35	2.57	0.23
Nd	0.31	-0.35	-0.13	0.13	-0.18	-0.05	0.03	-0.03	0.46	2.57	0.25
Sm	0.47	-0.30	-0.13	0.12	-0.18	-0.07	0.02	-0.02	0.64	2.63	0.22
Eu	0.56	-0.36	-0.19	0.12	-0.22	-0.17	0.03	-0.02	0.59	2.32	0.12
Gd	0.55	-0.24	-0.11	0.15	-0.17	-0.10	-0.02	0.02	0.38	2.03	0.03
Tb	0.71	-0.14	-0.08	0.17	-0.16	-0.12	-0.03	0.03	0.21	1.75	-0.03
Dy	0.83	-0.06	-0.02	0.25	-0.14	-0.10	-0.05	0.05	0.11	1.58	-0.09
Ho	0.90	-0.02	0.00	0.25	-0.08	-0.09	-0.08	0.08	0.01	1.39	-0.12
Er	0.89	-0.03	0.01	0.22	-0.08	-0.07	-0.07	0.07	-0.02	1.46	-0.08
Tm	0.94	0.01	0.07	0.29	-0.06	-0.04	-0.08	0.07	-0.13	1.27	-0.10
Yb	0.95	0.00	0.05	0.25	-0.08	-0.06	-0.08	0.07	-0.18	1.25	-0.06
Lu	0.96	-0.02	0.05	0.25	-0.10	-0.07	-0.06	0.06	-0.18	1.21	0.04
Pb	-0.29	-0.22	-0.27	-0.04	-0.27	-0.22	-0.03	0.03	-0.40	0.08	-0.18
Th	-0.18	-0.22	-0.26	0.14	-0.02	0.03	0.11	-0.10	-0.87	-0.36	-0.28
U	-0.29	-0.63	-0.51	-0.46	-0.04	-0.22	0.03	-0.03	0.15	0.87	0.18

Table A4 continued

well	TB8	TB8	TB8	TB8	TB8	TB8	TB8	TB8	TB8	TB8	TB8
Depth(m)	1.5	2.5	3.5	4.5	5.3	6.4	7.5	8.5	9.5	10.6	11.5
MgO	-0.17	0.20	-0.51	-0.23	-0.12	0.38	0.22	-0.09	0.54	-0.06	0.12
Al <sub>2</sub> O <sub>3</sub>	0.05	-0.01	-0.31	0.02	-0.40	-0.39	-0.05	-0.26	-0.08	0.04	0.10
CaO	3.51	3.28	3.22	2.89	2.59	2.24	2.46	-0.23	-0.31	1.07	1.02
K <sub>2</sub> O	0.58	0.90	-0.62	-0.02	-0.57	-0.73	-0.48	-0.63	-0.10	-0.06	-0.04
Na <sub>2</sub> O	-0.67	-0.45	-0.66	-0.13	-0.94	-1.00	-0.25	-0.74	-0.71	-0.50	-0.30
SiO <sub>2</sub>	-0.28	-0.28	-0.56	-0.11	0.13	-0.42	0.13	-0.53	-0.24	0.01	-0.02
P <sub>2</sub> O <sub>5</sub>	n	n	n	n	n	n	n	n	n	n	n
Fe <sub>2</sub> O <sub>3</sub>	0.25	-0.13	-0.35	0.12	0.51	0.95	0.79	-0.19	0.32	0.83	0.36
Sc	0.43	0.15	-0.04	-0.33	-0.11	0.12	-0.41	-0.25	-0.05	-0.35	-0.29
Mn	6.92	3.37	2.07	2.22	2.73	3.86	4.18	-0.02	0.68	1.00	0.96
Cu	-0.30	-0.48	-0.35	-0.37	-0.24	-0.20	-0.62	-0.30	-0.30	-0.40	-0.41
Zn	-0.12	-0.32	-0.67	-0.61	-0.37	0.17	-0.70	-0.35	0.03	-0.65	-0.43
Rb	0.91	0.73	-0.65	-0.47	-0.45	-0.63	-0.75	-0.66	-0.07	-0.55	-0.38
Sr	-0.28	0.07	-0.44	-0.55	-0.58	-0.49	-0.82	-0.53	-0.37	-0.42	-0.20
Y	0.14	0.27	-0.06	-0.31	0.35	0.14	-0.54	-0.32	-0.11	-0.57	-0.34
Zr	-0.35	-0.42	-0.46	0.09	0.28	-0.51	0.84	-0.57	0.21	-0.28	-0.05
Nb	-0.32	-0.39	-0.19	0.34	0.43	-0.49	0.51	-0.24	0.03	-0.34	-0.02
Cs	0.82	0.38	-0.62	-0.23	-0.32	-0.56	-0.59	-0.70	-0.11	-0.56	-0.52
Ba	-0.71	-0.74	0.93	0.62	-0.35	-0.83	-0.92	-0.62	-0.09	-0.58	-0.30
La	-0.23	0.11	0.50	-0.27	0.14	-0.01	-0.62	-0.06	0.02	-0.32	-0.38
Ce	0.05	0.35	1.03	-0.02	0.61	0.36	-0.46	0.08	0.20	-0.11	-0.18
Pr	0.17	0.48	1.14	0.07	0.86	0.50	-0.38	0.09	0.32	-0.09	-0.09
Nd	0.21	0.56	1.03	0.02	0.94	0.48	-0.38	0.04	0.38	-0.15	-0.08
Sm	0.13	0.48	0.56	-0.06	0.87	0.42	-0.38	-0.08	0.30	-0.29	-0.15
Eu	0.24	0.47	0.43	-0.06	0.61	0.45	-0.47	0.03	0.18	-0.27	0.11
Gd	0.10	0.34	0.11	-0.25	0.51	0.20	-0.51	-0.21	0.11	-0.47	-0.28
Tb	-0.01	0.20	0.00	-0.22	0.54	0.25	-0.48	-0.22	0.08	-0.49	-0.28
Dy	0.00	0.12	-0.08	-0.22	0.51	0.27	-0.48	-0.25	-0.02	-0.49	-0.28
Ho	-0.01	0.10	-0.12	-0.20	0.44	0.22	-0.48	-0.26	-0.07	-0.50	-0.31
Er	0.00	0.06	-0.16	-0.16	0.48	0.25	-0.45	-0.30	-0.09	-0.48	-0.30
Tm	-0.05	-0.02	-0.17	-0.18	0.50	0.21	-0.44	-0.35	-0.11	-0.49	-0.32
Yb	-0.07	-0.11	-0.28	-0.17	0.56	0.25	-0.41	-0.40	-0.18	-0.49	-0.33
Lu	-0.05	-0.10	-0.25	-0.17	0.60	0.21	-0.40	-0.43	-0.18	-0.46	-0.32
Pb	0.41	-0.37	-0.45	-0.39	-0.43	-0.40	-0.62	-0.33	-0.52	-0.24	-0.40
Th	-0.83	-0.90	-0.91	-0.78	-0.82	-0.91	-0.70	-0.93	-0.73	-0.84	-0.82
U	0.71	-0.32	-0.69	-0.52	-0.26	-0.01	-0.52	-0.46	-0.47	-0.69	-0.62

Table A4 continued

well	TB8	TB8	TB8	BK2/05	BK2/05	BK2/05	BK2/05	BK2/05	BK2/05
Depth(m)	12.5	13.5	14.5	0	0.2	0.4	0.6	0.8	1
MgO	0.01	-0.25	0	1.48	0.26	0.08	0.12	0.40	5.75
Al <sub>2</sub> O <sub>3</sub>	0.11	0.11	0	-0.07	0.15	0.05	0.00	0.09	0.22
CaO	1.19	0.50	0	0.23	-0.17	-0.04	0.12	-0.35	5.16
K <sub>2</sub> O	-0.15	0.06	0	0.58	0.49	0.36	-0.10	0.72	1.13
Na <sub>2</sub> O	-0.17	-0.08	0	-0.93	-0.27	-0.25	-0.08	-0.56	-0.59
SiO <sub>2</sub>	0.03	0.29	0	0.06	0.27	0.20	0.08	0.13	0.23
P <sub>2</sub> O <sub>5</sub>	n	n	n	0.50	0.23	0.00	-0.10	0.43	0.47
Fe <sub>2</sub> O <sub>3</sub>	0.28	0.32	0	-0.15	-0.05	-0.08	0.13	-0.13	0.26
Sc	-0.32	-0.49	0	0.24	-0.05	-0.13	0.00	0.11	0.21
Mn	0.96	0.67	0	0.32	-0.20	-0.10	-0.01	-0.05	3.16
Cu	-0.21	-0.09	0	3.57	-0.24	-0.27	-0.25	-0.30	-0.13
Zn	-0.47	-0.59	0	0.25	0.02	-0.01	0.20	0.10	0.07
Rb	-0.43	-0.45	0	0.03	-0.06	0.02	-0.13	0.22	0.34
Sr	-0.05	-0.39	0	-0.83	-0.28	-0.18	-0.20	-0.31	-0.33
Y	-0.11	0.19	0	0.35	-0.07	-0.09	-0.11	0.18	0.65
Zr	0.39	1.44	0	0.04	0.15	0.02	-0.07	-0.07	0.00
Nb	0.61	2.08	0	-0.01	-0.12	-0.09	0.04	-0.03	-0.09
Cs	-0.63	-0.75	0	1.93	0.72	0.39	0.40	0.83	0.80
Ba	-0.06	-0.04	0	-0.63	-0.17	-0.05	-0.60	0.04	0.20
La	-0.13	-0.03	0	-0.46	-0.39	-0.26	-0.23	-0.29	-0.16
Ce	0.12	0.36	0	-0.44	-0.38	-0.24	-0.15	-0.22	-0.10
Pr	0.24	0.57	0	-0.38	-0.37	-0.21	-0.14	-0.22	-0.06
Nd	0.23	0.63	0	-0.33	-0.32	-0.21	-0.13	-0.19	0.00
Sm	0.12	0.58	0	-0.24	-0.31	-0.19	-0.01	-0.09	0.23
Eu	0.31	0.01	0	-0.49	-0.37	-0.22	-0.14	-0.12	0.35
Gd	-0.03	0.30	0	-0.32	-0.36	-0.24	-0.20	-0.20	0.01
Tb	-0.06	0.32	0	-0.11	-0.29	-0.12	-0.11	-0.02	0.29
Dy	-0.04	0.31	0	0.03	-0.22	-0.18	-0.11	0.00	0.24
Ho	-0.06	0.28	0	0.45	0.02	-0.03	-0.04	0.21	0.57
Er	-0.03	0.34	0	0.21	-0.23	-0.19	-0.09	0.05	0.34
Tm	-0.07	0.33	0	0.32	0.06	-0.05	0.02	0.24	0.61
Yb	-0.06	0.37	0	0.46	-0.14	-0.07	0.03	0.24	0.38
Lu	-0.05	0.44	0	0.42	-0.08	-0.11	-0.12	0.21	0.53
Pb	-0.35	-0.32	0	-0.65	-0.21	-0.14	-0.31	-0.09	-0.04
Th	-0.75	-0.56	0	-0.20	-0.36	-0.24	-0.18	-0.22	-0.25
U	-0.63	-0.48	0	2.94	-0.35	-0.29	-0.34	-0.29	-0.21

Table A4 continued

well	BK2/05	BK2/05	BK2/05	BK2/05	BK2/05	BK2/05	BK2/05	BK2/05
Depth(m)	1.3	1.5	1.7	1.9	2.2	2.4	2.6	2.8
MgO	0.75	0.11	0.22	0.28	0.23	0.12	0.08	-0.13
Al <sub>2</sub> O <sub>3</sub>	0.24	0.15	0.09	0.05	0.17	0.09	0.01	0.06
CaO	0.65	0.12	0.39	0.22	0.63	0.33	0.09	-0.15
K <sub>2</sub> O	0.43	0.36	0.05	0.22	0.21	0.17	0.04	0.47
Na <sub>2</sub> O	0.06	-0.03	0.06	-0.14	0.09	0.04	-0.05	-0.16
SiO <sub>2</sub>	0.33	0.21	0.09	0.12	0.19	0.26	0.08	0.02
P <sub>2</sub> O <sub>5</sub>	0.58	0.34	0.62	1.15	0.90	0.94	0.21	0.07
Fe <sub>2</sub> O <sub>3</sub>	0.30	-0.04	0.42	0.09	0.26	0.13	0.04	-0.16
Sc	0.05	0.04	0.17	0.04	0.04	-0.04	0.24	0.14
Mn	0.38	0.03	0.29	0.08	0.35	0.21	0.06	0.03
Cu	-0.15	-0.19	-0.15	-0.19	-0.33	-0.22	0.04	-0.17
Zn	0.10	0.04	0.29	0.15	0.06	0.01	0.04	-0.05
Rb	0.05	0.23	0.10	0.07	0.01	0.00	0.10	0.32
Sr	-0.06	0.11	0.18	-0.07	-0.08	-0.07	0.05	0.29
Y	0.19	0.30	0.46	0.77	0.39	0.51	0.05	0.16
Zr	0.04	-0.09	-0.16	-0.06	0.03	0.01	-0.11	-0.16
Nb	-0.08	-0.11	0.26	0.02	-0.11	-0.01	0.04	0.01
Cs	0.63	0.27	0.31	0.44	0.28	0.07	0.16	0.00
Ba	-0.14	0.17	-0.20	-0.14	-0.30	-0.12	-0.20	0.61
La	-0.20	-0.02	0.04	0.01	-0.18	-0.14	-0.02	-0.04
Ce	-0.17	0.07	0.08	0.09	-0.13	-0.09	0.01	-0.03
Pr	-0.15	0.03	0.09	0.13	-0.09	-0.04	0.04	0.05
Nd	-0.10	0.08	0.08	0.20	-0.06	-0.04	0.09	0.06
Sm	-0.05	0.19	0.23	0.37	0.10	0.06	0.06	0.09
Eu	0.02	0.19	0.11	0.10	0.02	0.04	-0.02	0.07
Gd	-0.22	0.03	-0.02	0.14	-0.05	-0.02	0.12	-0.06
Tb	-0.02	0.14	0.40	0.46	0.14	0.09	-0.06	0.11
Dy	0.00	0.17	0.32	0.37	0.07	0.17	0.13	0.12
Ho	0.20	0.33	0.36	0.83	0.56	0.46	0.10	0.05
Er	0.07	0.16	0.29	0.52	0.23	0.24	0.21	0.07
Tm	0.20	0.13	0.50	0.72	0.61	0.44	0.17	0.17
Yb	0.19	0.21	0.49	0.75	0.38	0.48	0.04	0.14
Lu	0.18	0.15	0.38	0.44	0.26	0.37	0.05	0.23
Pb	-0.10	0.24	0.07	-0.12	-0.15	-0.09	-0.11	0.48
Th	-0.28	0.01	-0.08	0.00	-0.20	-0.17	-0.06	-0.01
U	-0.20	-0.09	-0.12	-0.16	-0.22	-0.16	-0.22	-0.13



Table A4 continued

well	BK2/05	BK2/05	BK2/05	BK2/05	BK2/05	BK2/05	BK2/05	BK2/05
Depth(m)	3	3.2	3.4	3.6	3.8	4	9.6	10.9
MgO	0.02	-0.05	0.13	0.14	0.10	-0.09	0.00	0.08
Al <sub>2</sub> O <sub>3</sub>	0.10	-0.14	0.10	0.15	0.00	-0.14	0.00	0.56
CaO	0.20	0.06	0.25	-0.02	0.28	-0.02	0.00	0.06
K <sub>2</sub> O	0.29	-0.19	0.07	0.38	-0.19	-0.18	0.00	1.04
Na <sub>2</sub> O	-0.04	-0.17	0.07	-0.06	0.05	-0.15	0.00	0.39
SiO <sub>2</sub>	0.06	-0.07	0.12	0.23	0.07	-0.11	0.00	0.48
P <sub>2</sub> O <sub>5</sub>	0.44	0.52	0.67	0.29	0.56	-0.07	0.00	0.35
Fe <sub>2</sub> O <sub>3</sub>	-0.03	-0.18	0.12	-0.05	0.14	0.02	0.00	0.05
Sc	0.23	-0.09	0.08	0.02	0.06	-0.06	0.00	-0.04
Mn	0.21	-0.05	0.10	-0.02	0.09	0.01	0.00	-0.14
Cu	-0.18	0.09	-0.31	-0.20	-0.21	-0.15	0.00	-0.04
Zn	0.03	-0.07	0.09	0.01	-0.01	-0.06	0.00	-0.17
Rb	0.14	-0.18	0.02	0.14	-0.14	-0.15	0.00	0.53
Sr	0.12	-0.22	0.03	0.03	-0.09	-0.11	0.00	0.63
Y	0.36	0.34	0.37	0.14	0.34	-0.02	0.00	0.02
Zr	-0.07	-0.03	-0.06	-0.06	-0.06	-0.10	-0.11	0.00
Nb	0.16	0.11	-0.01	0.02	0.05	0.06	0.00	-0.09
Cs	0.06	-0.06	0.05	0.35	0.04	-0.09	0.00	-0.04
Ba	0.17	-0.42	-0.16	0.13	-0.52	-0.33	0.00	1.23
La	-0.09	-0.14	-0.06	-0.19	-0.10	-0.12	0.00	-0.20
Ce	-0.03	-0.11	-0.06	-0.18	-0.02	-0.07	0.00	-0.15
Pr	-0.06	-0.04	0.01	-0.17	-0.03	-0.07	0.00	-0.19
Nd	0.00	-0.02	0.01	-0.12	-0.01	-0.04	0.00	-0.20
Sm	0.14	0.07	0.09	0.01	0.08	0.03	0.00	-0.14
Eu	0.28	-0.01	-0.06	-0.11	-0.09	-0.17	0.00	-0.05
Gd	-0.04	-0.03	0.03	-0.16	0.01	-0.09	0.00	-0.26
Tb	0.14	0.10	0.18	-0.11	0.06	-0.04	0.00	-0.16
Dy	0.15	0.13	0.06	-0.01	0.09	-0.11	0.00	-0.08
Ho	0.37	0.35	0.44	0.16	0.31	-0.02	0.00	0.04
Er	0.19	0.21	0.26	-0.02	0.16	-0.08	0.00	0.02
Tm	0.25	0.44	0.48	0.26	0.54	0.09	0.00	-0.06
Yb	0.39	0.30	0.36	0.12	0.40	0.01	0.00	0.03
Lu	0.23	0.12	0.36	0.32	0.32	0.04	0.00	0.08
Pb	0.19	-0.26	-0.10	0.04	-0.26	-0.25	0.00	0.89
Th	-0.17	-0.12	-0.08	-0.12	-0.13	-0.12	0.00	-0.20
U	-0.15	-0.21	-0.23	-0.09	-0.22	-0.15	0.00	-0.21

---

## Appendix IV-II

### Integrated concept for the quantification of palaeo-weathering

#### 1 Physical weathering degree quantification

Physical weathering is an ubiquitous process in the upper crust and is crucial for providing materials for sedimentary rock and landscape modification (Camuffo 1995; Matsuoka et al. 1996). However, an index for physical weathering is still not available. Physical weathering degree is reflected by fracture density and width as well as fragmentation of the rock matrix (Camuffo 1995). The higher the physical weathering degree, the denser the spacing and width of the fractures. Therefore, physical weathering degree can be mirrored in principal by the ratio between the fracture and the total area within a specific zone. This study concentrates on the micro-scale and use petrographic analysis of thin sections. The quantification of physical weathering degree and intensity is performed by five steps in Fig.1, and detailed described in following sections.

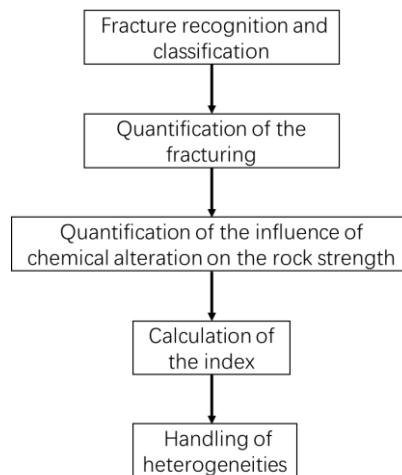


Fig. 1 Workflow for physical weathering degree quantification.

##### 1.1 Fracture recognition and classification

Fractures may be formed due to weathering and /or other factors, such as tectonic stress in natural environment. Regardless of whether the fractures are formed due to physical weathering or tectonic stress, they may be filled by secondary minerals, which may be the chemical weathering products and /or the minerals formed due to the burial diagenesis. The minerals formed during different stages should have different mineralogic and geochemical characteristics (Bauluz et al. 2008; Dill 2010). Based on which, the fractures formed during different period can be distinguished. However, the fillings of fractures can not be applied to access whether the fractures are formed due to physical weathering or tectonic stress. To fix this problem, the method for tectonic fracture recognition with fracture angle or orientation proposed by Gol'braykh et al. (1966) is applied. Therefore, the fractures are divided into four stages in this case based on the mineral and geochemical characteristics of the fillings in the fractures

---

and the angles of the fractures: i) Fractures formed due to tectonic stress; ii) Fractures formed before and/or during chemical weathering; iii) Fractures at the end of chemical weathering; iv) Fractures overprinted by burial diagenesis (Fig. 2).

#### 1.1.1 Fractures formed due to tectonic stress

The tectonic fractures may be formed before, during and /or after the chemical weathering process together with the fractures formed to physical weathering. The fractures trend to have preferential orientation and angle with the influence of tectonic stress, while the fractures were formed due to weathering, the orientation and /or the angle trend to show a random pattern (Scarpato 2013; Caspari et al. 2020). Therefore, to access the factors of the fractures, the rose diagram can be applied to illustrate the angle of the fracture along the drill cores. While the rose diagram shows a preferential angle, which indicates the weathering profile contains both tectonic- and weathering-fractures. The fracture area of the tectonic fractures along the weathering profile within the thin sections are represented by the fractures within the **p**arent rock (Fp).

#### 1.1.2 Fractures formed before and/or during chemical weathering

The weathering products may be composed of stable minerals including clay and oxide (e.g.  $\text{Fe}_2\text{O}_3$ ,  $\text{TiO}_2$ ), and unstable minerals such as calcite (Goldich 1938). The fractures formed before and /or during the chemical weathering, include both the tectonic and physical weathering-fractures will be filled by these products. For the fractures filled by clay minerals and oxide and calcite are defined as Fcl, Fx and Fc, respectively. Whereas stable minerals persist, unstable minerals will gradually be depleted (Harriss and Adams 1966). Meanwhile, the unstable minerals formed during such as hydrolysis, may transfer and precipitate accompanied with the stable minerals filled in the fracture in the lower part of the weathering profile (Nesbitt et al. 1980). These fractures filled by minerals in the weathering zone is defined as Fw in this case.

#### 1.1.3 Fractures formed at the end of chemical weathering

While the chemical weathering process come to the latest stage with a significant lower rate, the physical weathering process and /or tectonic process may continue and new **v**oid fractures may form (Fv).

#### 1.1.4 Fractures overprinted by burial diagenesis (Fb)

For a weathering profile which is overprinted by burial diagenesis, the void fractures may be filled by secondary minerals. If secondary mineral types are the same as the unstable weathering products, such as calcite, which may be formed during both weathering and burial stages, the method proposed by Michel and Tabor (2016), which used stable C and O isotopes of carbonate are applied to distinguish the formation stages.

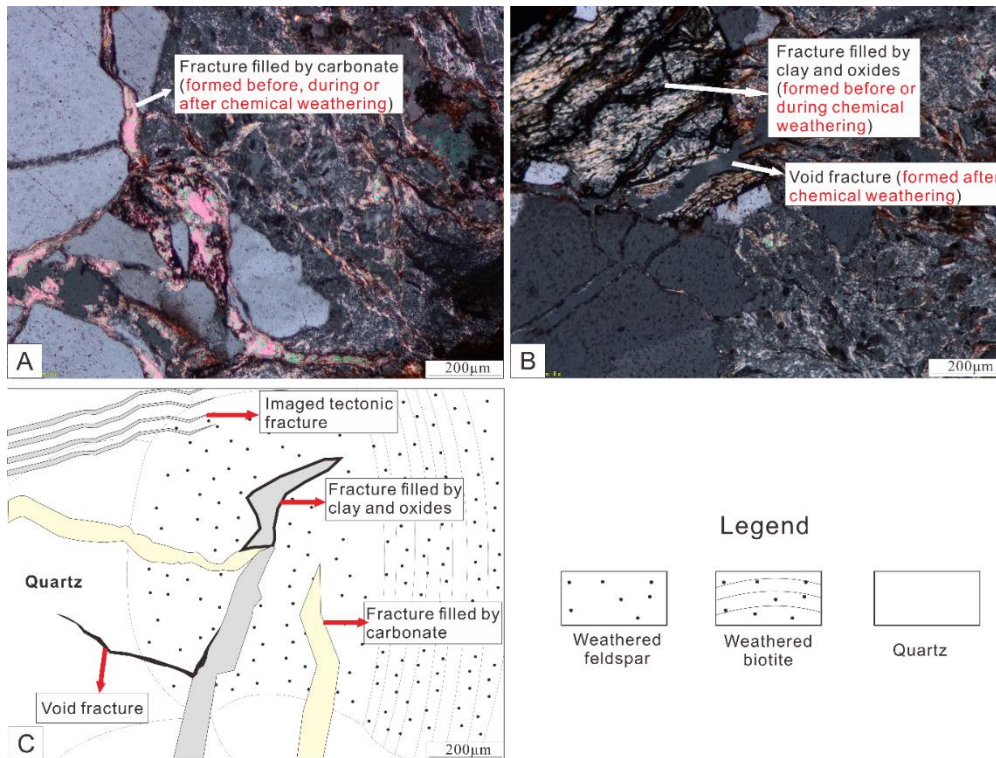


Fig 2. Different types of fractures recognized under the microscope.

## 1.2 Quantification of the fracturing

The fracture area is analysed under microscale by the polarizing microscope. In our case, best results have been gained under 10 times eye piece with 10 times objective lens. The pictures were taken by the single lens reflex camera connected with the microscope and controlled by the software named Olympus Stream Basic with plotting scale, the resolution of the photograph is 2560\*1920. To measure the fracture and the inspected area, the thin-section photo taken under the polarizing microscope with plotting scale is opened by the software ImageJ. To acquire the ratio between the fractures and the whole picture, three steps are shown in Fig. 3 and illustrated in the following paragraphs.

Step one: after we open the picture with ImageJ, we can see in the up-left corner the unit is pixel. With the “straight” button of the menu bar, we need to firstly draw a straight-line coincidence with the plotting scale line. To ensure the line that we draw has the same length as the plotting scale line, we can firstly select the magnifying glass in the menu bar and click the plotting scale part to amplify to an appropriate scale, then draw the line.

Step two, after we drawing the line, we need to define the length of the line according to the plotting scale. We can select the “Analyze” button, and click the “set scale” in the sub-menu, fill the “Known distance” with the number of the plotting scale, in the example is 100, and “Unit of length” in this case is “μm”. By clicking “OK” in the plane, the length of the line can be defined. Now we can see in the top-left corner, the pixel unit changes to

length unit ( $\mu\text{m}$ ), with the length and width of the photograph, we can calculate the area of the total inspected area ( $A_{(Ft)}$ ).

Step three, we can select the “Polygon selections” and outline the fractures manually on the digital photograph. Similar to drawing the line, we can also magnify the fracture to ensure the accuracy of the outlining if it is necessary. After which, we select the “Analyze” button, and click “Measure” in the sub-menu, the area of the outlined area will appear in the right of the photograph. For the void fracture, the area is defined as  $A_{(Fv)}$ , the fractures filled by calcite is defined as  $A_{(Fc)}$ , the fractures filled by clay minerals is defined as  $A_{(Fcl)}$ , and the sum of the area of filled fracture in the weathering zone is defined as  $A_{(Fw)}$ , the area of the fractures within the parent rock is defined as  $A_{(Fp)}$ . The statistical error is less than  $250 \mu\text{m}^2$  with a mean value around  $55 \mu\text{m}^2$ . To outline other fractures, we can just repeat Step three. With the area of both fractures and the photograph, the IPW (area ratio) can be acquired.

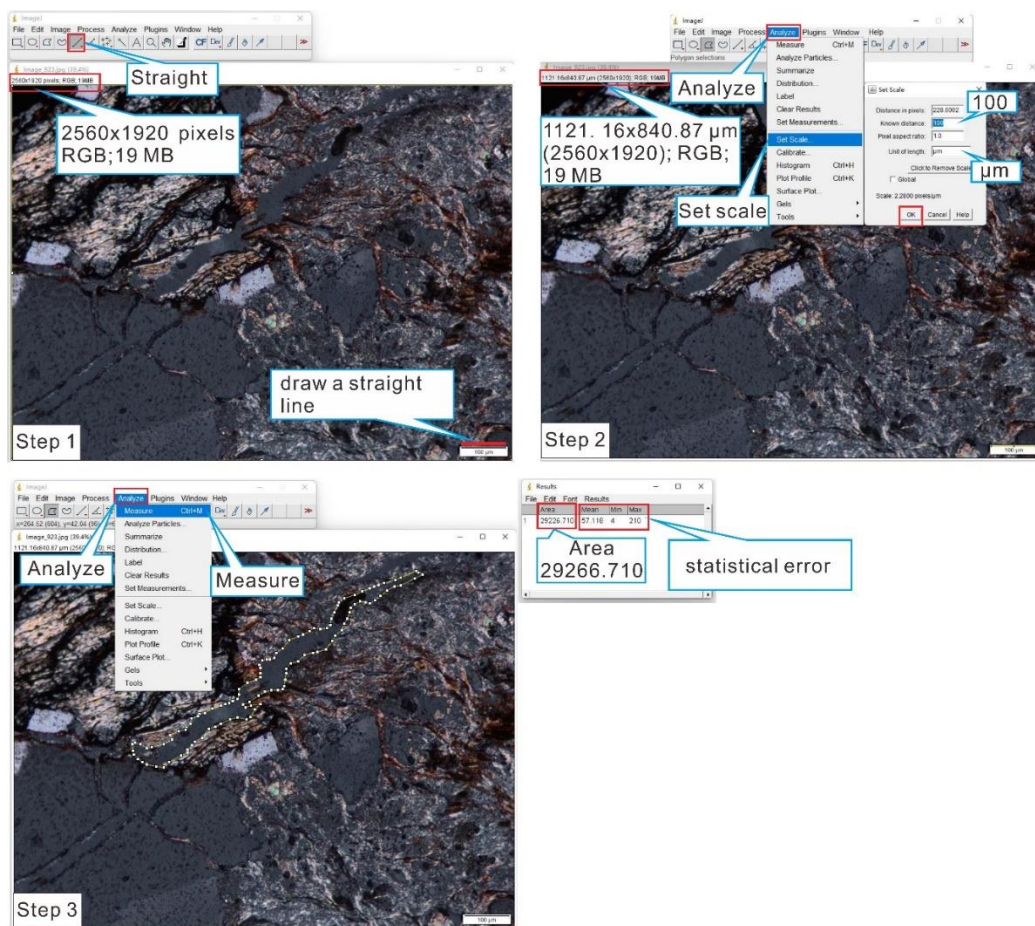


Fig. 3. Quantification of the fracturing with software ImageJ.

### 1.3 Quantification of the influence of chemical alteration on the rock strength

The susceptibilities to physical weathering among different lithologies are intrinsically different. Previous studies indicate the higher the strength of a rock, the more resistant it is to physical weathering (Jayawardena and Izawa 1994; Thomson et al. 2014). Therefore, the susceptibility of different lithologies to physical weathering can be

---

represented and normalized by rock strength to enable the comparison of physical weathering intensity among different lithologies.

The rock strength is an engineering geological term which is concerned with such as mineral composition, structure, texture and jointing (Golodkovskaia et al. 1975). It can be specified in terms of uniaxial tensile strength (UTS), uniaxial compressive strength (UCS), shear strength, and impact strength. Among which, the formation of the fractures during weathering more related to the UTS than UCS (Aadnøy and Looyeh 2019). While the UTS of rock refers to the required pulling force to rupture a rock sample, divided by the area of the cross section of the sample, the UCS is the capacity of a rock to withstand loads tending to reduce size (Aggistalis et al. 1996; Aadnøy and Looyeh 2019). These two parameters are always in linear relationship with the UTS is around 0.1 times of the UCS (Gupta and Rao 2001; Cuccuru et al. 2012; Aadnøy and Looyeh 2019). This enables both UCS and UTS can be applied for the normalization of IPW. Within the previous studies, the UCS data is much sufficient than UTS, in order to acquire more data so as to acquire a more accurate result, the UCS is applied for the normalization in this study.

In natural environment, the physical and chemical weathering process are always not isolated. The cracks formed due to physical weathering may provide pathways for fluids to promote the chemical weathering process (Bland and Rolls 1998). Meanwhile, the meteoric water and pore fluids can also penetrate the basement rock through the rock fabric and further increase the chemical weathering degree (Di Figlia et al. 2007). With ongoing chemical weathering process the rock strength will gradually decrease (Khanlari et al. 2012; Chiu and Ng 2014). The decreased rock strength will clearly enhance the formation of the physical cracks which is rock-type specific. Therefore, the chemical weathering degree needs to be considered in the normalization of physical weathering degree. Since the 2000s quantitative correlations between rock strength and chemical weathering degree were developed (Tuğrul 1997; Ündül and Tuğrul 2012; Korkanç et al. 2015). Different researchers correlated physical parameters, such as UCS, P-wave velocity with chemical parameters, such as loss on ignition (LOI), weathering potential index (WPI) and other indices with each other (Gupta and Rao 2001; Mert 2014; Ündül and Tuğrul 2016). Moreover, previous studies developed empirical formulae of the relationship between the physical strength and the chemical weathering degree for basaltic and granitic rocks, among these chemical weathering indices, the Chemical Index of Alteration (CIA) have a high relationship with the rock strength (e.g. Arel and Tuğrul 2001; Tuğrul 2004). Therefore, based on these formulae and data for basaltic and granitic rock (Ceryan et al., 2008a, 2008b; Erişiş et al., 2019; Khanlari et al., 2012; Thomson et al., 2014; Tuğrul, 1997), this study compiled data and created a regression out of two rock-specific empirical relationships between UCS and the chemical index of alteration (CIA) (Fig. 4):

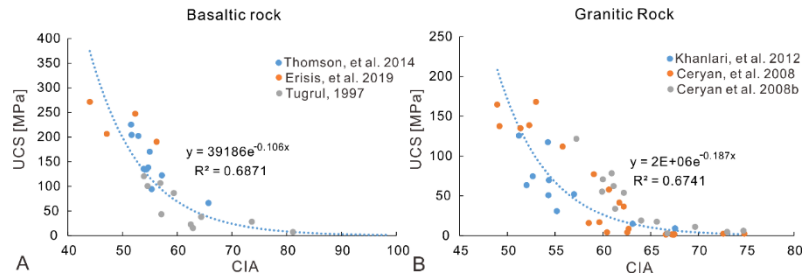


**Fig. 4** Empirical relationship between UCS and CIA (data from Ceryan et al, 2008a, 2008b; Erişiş et al., 2019; Khanlari et al., 2012; Thomson et al., 2014; Tuğrul, 1997)

$$UCS_{\text{basalticrock}} = 39186e^{-0.106CIA} \quad (r = 0.83) \quad (1)$$

$$UCS_{\text{graniticrock}} = 2E + 6 * e^{-0.187CIA} \quad (r = 0.82) \quad (2)$$

With these two empirical formulas, the UCS of basaltic and granitic rock under different chemical weathering degree can be assessed.

#### 1.4 Calculation of the index

The index for the quantification of physical weathering degree is defined as the index of physical weathering (IPW). As the fractures along the weathering profile may contain both the tectonic fractures and weathering-fractures, the tectonic fractures increase the area of the fractures within the weathering zone, which need to be eliminated. As the area of the tectonic fractures can be represented which in the parent rock, the fractures created by physical weathering in the weathering zone can be corrected as  $A_{(Fw)} + A_{(Fv)} - A_{(Fp)}$ , and the IPW can be expressed as:

$$IPW = \frac{A_{(Fw)} + A_{(Fv)} - A_{(Fp)}}{A_T} \quad (3)$$

The IPW in equation (3) can reflect the physical weathering degree and compare the physical weathering intensity for a specific rock-type. However, as the variation of the rock strength among different lithologies, the results of IPW for different types of rock may lead a contradictory conclusion while compare with each other. To solve this problem, one method is to normalize the IPW with the corresponding susceptibility to physical weathering for each type of rock. The susceptibility is represented by UCS which is explained in section 2.1.3.

As it is discussed above, physical weathering-fractures formed during different stages should represent different UCS, therefore, different fractures should be normalized by corresponding UCS. For basaltic and granitic rock, the UCS can be acquired with equation (1) and (2), respectively. For the void fractures, the rock strength at the sampling position is applied, which is expressed as  $UCS_w$ . However, as it is difficult to figure out the specific CIA value while the fracture were formed, the rock strength which the fractures stand for is represented by the average rock strength between the parent rock ( $UCS_p$ ) and the sampling position ( $UCS_w$ ), which is defined as  $UCS_A$  and express as :

$$UCS_A = \frac{UCS_p + UCS_w}{2} \quad (4)$$

While the weathering profile was influenced by tectonic fractures, the normalization process can be divided into following two situations:

i) tectonic fracture is per-existing or formed during the chemical weathering

For the per-existing tectonic fractures, their mineral filling is often related to successive processes, i.e. fluid flow and water-rock interaction during burial and uplift. This may include different generations of secondary minerals which are unstable and usually get dissolved during uplift. As consequence, the tectonic fractures experience the same process as the per-existing physical weathering-fractures. While the tectonic fractures formed during chemical weathering process, the fractures characteristics should also the same as the fractures formed by physical weathering during the same period. Therefore, to normalize the IPW, firstly, the  $A_{(Fw)}$  should minus the  $A_{(Fp)}$ , and normalized by  $UCS_A$ . and the final  $IPW_N$  can be expressed as:

$$PWI_N = \frac{A_{(Fw)} - A_{(Fp)}}{A_T} * UCS_A + \frac{A_{(Fb)} + A_{(Fv)}}{A_T} * UCS_w \quad (5)$$

ii) tectonic fracture formed in the end of the chemical weathering and/or during burial diagenesis

While the tectonic fractures formed when the chemical weathering process was about ceased or during burial diagenesis, it should be the fracture formed during these stages corrected by the fractures in the protolith zone, and normalized by the  $UCS_w$ . As the fractures filled by minerals formed during burial diagenesis should be treated as void fractures, the  $IPW_N$  can be expressed as:

$$PWI_N = \frac{A_{(Fw)}}{A_T} * UCS_A + \frac{A_{(Fb)} + A_{(Fv)} - A_{(Fp)}}{A_T} * UCS_w \quad (6)$$

### 1.5 Accounting for spatial heterogeneity

Due to the heterogeneity of fracture distribution in the thin section, one view may not able to represent the physical weathering value over the whole thin section. To figure out the most appropriate strategy for acquiring the representative  $IPW_N$  value, grids of 3\*3, 3\*5, 4\*5 over all area of the thin section were applied. The results indicate that, the variation of the average value of the IPW approaches stable values after 15 visions regardless the rock type. Therefore, a grid of 3\*5 is applied (Fig. 5).



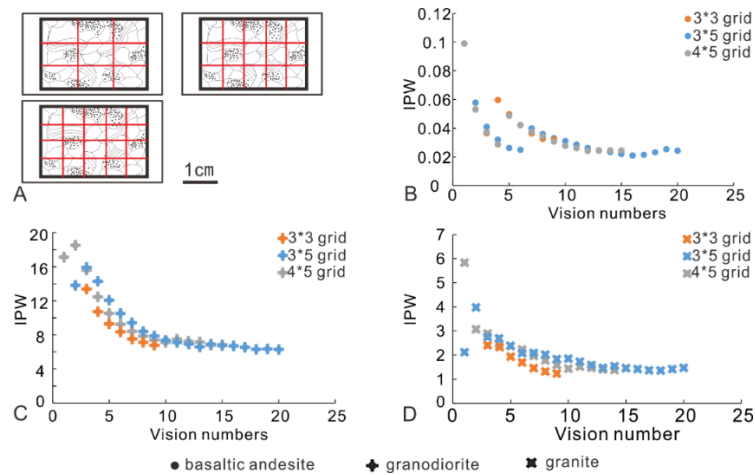


**Fig. 5** The variation of the IPW with the increase of view number and the view distribution on thin section from three different rock types in this case. A: view distribution strategy B: basaltic andesite; C: granodiorite; D: granite.

## 2 Chemical weathering indices normalization

### 2.1 Chemical weathering ability (CWA)

Quantification of chemical weathering has been well developed and widely applied (e.g. Nesbitt and Young 1982; McLennan 1993; Fedo et al. 1995; Schoenborn and Fedo 2011; Babechuk et al. 2014). The common indices can be regarded as an absolute chemical weathering degree of a certain lithology. Furthermore, weathering rates for different minerals, such as plagioclase, K-feldspar, biotite and hornblende have been quantified (e.g. Schott et al. 1981; Riebe et al. 2003). Previous studies have put a lot of efforts to determine weathering rates of fresh minerals in the laboratory (e.g. White et al. 2001b; Martinez et al. 2014). Mineral weathering in the natural environment, however, is a continuous process from fresh to weathered and field rates usually clearly underrate laboratory rates. White and Brantley (2003) concluded that the weathering rate of a mineral decreases with time. Based on an experiment with both fresh rock and weathered rock which lasted 6.2 years, they proposed an equation to depict the alteration rate ( $R/ \text{mol m}^{-2} \text{s}^{-1}$ ) in the natural environment for different minerals:

$$R = 10^{A \cdot t^b} \quad (7)$$

**Table 1** Parameters values of different minerals for equation (6) (White and Brantley 2003).

Minerals	A	b	r (coefficient)
K-feldspar	-12.49±0.32	-0.647 ± 0.076	0.83
Hornblende	-12.67±0.22	-0.623 ± 0.067	0.92
Biotite	-12.32±0.25	-0.603 ± 0.073	0.83

---

---

Plagioclase

-12.46±0.16

-0.564 ± 0.046

0.89

---

With the alteration rate among different minerals, this study develops an equation to depict the total weathering mass (TWM) between the time of  $t_1$  and  $t_2$ , which corresponds to the integral function of the weathering rate:

$$TWM = \int_{t_2}^{t_1} R \quad (8)$$

Based on the TWM of mineral types and the mineralogical composition of a rock, its ability to weather chemically, in this case, which is defined as chemical weathering ability (CWA) can be expressed as the sum of the TWM for each type of minerals with the coefficient of proportions:

$$CWA = p_1 * TWM_1 + p_2 * TWM_2 + p_3 * TWM_3, \dots \quad (9)$$

In which,  $p$  is the proportion of each type of mineral within the rock, which can be acquired by XRD. The formula provides a measure that rocks with higher CWA are easier to be weathered under the same natural environment. Therefore, the CWA can be applied to evaluate the susceptibility of different rock to chemical weathering. Due to “un-weatherable minerals” with an extremely chemical weathering rate under natural environment, such as quartz (weathering rate from  $10^{-14.5}$  to  $10^{-15.1}$  mol  $m^{-2}s^{-1}$  in natural environment) which is several orders of magnitude slower than for other primary silicate minerals (Schulz and White 1999). The CWA of a certain rock type is mainly concern with “weatherable minerals”, such as plagioclase, biotite. Therefore, the CWA for different types of rock in this case is represented by “weatherable minerals”, the quartz part is ignored. The formula provides a measure that rocks with higher CWA are easier to be weathered under the same natural environment, which can be applied to access the susceptibility for different types of rock to chemical weathering.

## 2.2 Normalization of chemical weathering indices using CWA

The CWA for different igneous parent rock provides a chance to figure out the relationship for the chemical weathering degree under the same weathering intensity. As the chemical weathering degree can be well quantified by the chemical weathering indices, such as CIA, PIA, CIW, to compare the chemical weathering intensity among different rock types, the final purpose is to normalize a chemical weathering index and make the values among different lithologies comparable. In order to do that, an appropriate solution is to firstly set a reference rock, and evaluate the chemical weathering degree of the reference rock under the same weathering condition of the rock to be normalized based on the CWA relationship (Fig. 6).

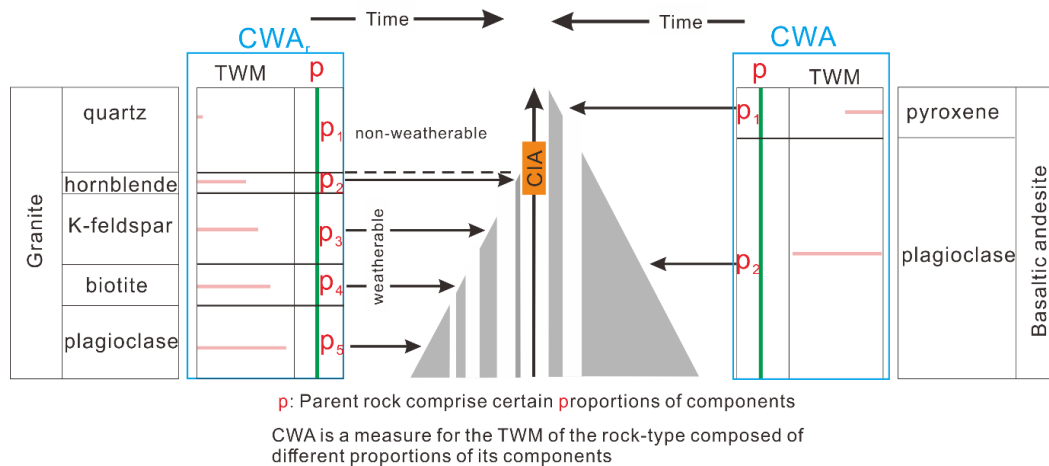


Fig. 6. Relationship and definition of total weathering mass (TWM) chemical weathering ability (CWA) and chemical weathering degree (CIA), (example based on granite and basaltic andesite in this case).

The methods for the quantification of chemical weathering degree in previous studies are mainly based on the ratio between the sum of residual “mobile elements” (such as Na, Ca and K) and “immobile elements”(such as Al)(Nesbitt and Young 1982; Harnois 1988; Fedo et al. 1995). As Na, Ca, K and Al exist in most common weatherable rock-forming minerals (Deer et al. 2013), the classic chemical weathering index CIA (Nesbitt and Young 1982), which contains all these elements is taken as an example for the explanation of chemical weathering degree normalization. The normalized values mirror the chemical weathering intensity among different lithologies. Therefore, the results can provide a clue to evaluate the climate variation with the lithologies intrinsically have different susceptibility to chemical weathering.

For the normalization of CIA values of the sampled rock with the reference rock, the detailed process is divided into three steps and expressed as following:

i) Calculate the deviation degree of the CIA values compare to fresh parent rock zone

Firstly, a parameter  $\lambda$  is defined to represent the deviation degree of CIA compared to the un-weathered fresh parent rock ( $CIA_f$ ):

$$\lambda = \frac{CIA}{CIA_f} - 1 \quad (10)$$

For the reference rock, the deviation of CIA is defined as  $\lambda_r$ , and for the sampled rock to be normalized is defined as  $\lambda_s$ .

ii) Normalize the deviation range of CIA for sampled rock type

By definition, the maximum CIA value is 100 if the mobile elements Na, Ca, and K are completely leached from silicates. However, for different minerals, the proportions of Na, Ca, K and Al within the silicate are different. As a result, the CIA values vary with rock types and mineral types, e.g. the CIA value for feldspars is 50; for biotite

between 50 and 55, for hornblende 10 to 30 and for pyroxene between 0 and 20 (Nesbitt and Young 1984; McLennan 1993). This means that chemically fresh mafic rocks dominantly composed of pyroxene or hornblende, show CIA values lower than felsic rocks mainly consisting of feldspars and biotite.

In conclusion, the maximum  $\lambda$  value, which represents the deviation range strongly varies for different rock types. Thus, a correction coefficient  $n$  is introduced to correct the variation range of CIA between the reference rock and the sampled rock, which to be normalized to the same range:

$$n = \frac{CIA_{fr} * (100 - CIA_{fs})}{CIA_{fs} * (100 - CIA_{fr})} \quad (11)$$

In which,  $CIA_{fs}$  refers to un-weathered fresh part of the sampled rock and  $CIA_{fr}$  means the un-weathered fresh part of the reference rock.

### iii) Normalization of CIA for sampled rock type with CWA

With the correction of  $n$ , the variation range of CIA between the sampled rock and reference rock is within the same range. However, due to the difference of the susceptibility to chemical weathering, the deviation degree should be further considered the discrepancy of the CWA between these two lithologies. Therefore, the  $\lambda_s$  should be normalized based on the CWA between the sampled rock ( $CWA_s$ ) and reference rock ( $CWA_r$ ) and the correction coefficient  $n$ , the result is defined as  $\lambda_N$ :

$$\lambda_N = \frac{\lambda_s * CWA_r}{n * CWA_s} \quad (12)$$

It is noticeable that the maximum of CIA value for different type of rock is 100, to maintain the accuracy, it is better to also keep the CIA value of the sample with higher CWA lower than 100 after the normalization. Thus, the CIA values of the sampled rock which to be normalized ( $CIA_N$ ) can be expressed by the CIA value of fresh part of the reference rock ( $CIA_{fr}$ ) as:

$$CIA_N = CIA_{fr} * (1 + \lambda_N) \quad (13)$$

The  $CIA_N$  represents the chemical weathering degree for the reference rock under the same weathering condition of the sampled rock. Thus, for the different types of rock are all normalized by the same reference rock, the chemical weathering intensity can be compared. However, what needs to be aware is that for the fresh rock to reach a certain chemical weathering degree (CIA value) with different time scale suggests different chemical weathering intensity. This means that with the specific CIA value, the shorter the weathering period, the more intense of the chemical weathering will be. Therefore, when apply the method to the specific cases, it is important to evaluate the weathering time scale, with the weathering time scale closer to the actual weathering condition, the more accurate of the  $CIA_N$  will be.

### 3 Integrative evaluation of weathering condition

Previous studies about weathering degree in palaeoenvironments emphasize the absolute chemical weathering degree mostly via such as CIA, CIA-K and  $\Sigma$  Bases/Al values (Maynard 1992; Fedo et al. 1995; Retallack 1999; Zhou et al. 2017). The characteristics formed by physical weathering are less considered. Here we pursue a twofold strategy to improve this deficit in palaeoweathering studies: (i) petrographic analysis of physical weathering via fracture analysis, and (ii) normalization of the CIA to rock types. The detailed workflow is depicted in Fig. 7. For the chemical weathering part, the values of weathering indices are firstly calculated, the time scale of the supergene alteration and reference rock is then evaluated and chosen. The TWM and CWA can be calculated based on the time scale and the composition of the parent while the  $\lambda$  is acquired based on the reference rock. With these three parameters, the weathering indices can be normalized following equation 10-13 to reflect the chemical weathering intensity among different lithologies. For the physical weathering aspect, the fracture under microscope is firstly analyzed, after the correction of area ratio between fractures and total area, the IPW is acquired. To normalize the IPW, the formation stages of the fractures are evaluated and normalized with corresponding rock strength. As it mentioned above, the corresponding rock strength (UCS) is calculated based on the relationship between CIA values and UCS. Finally, the  $IPW_N$  can be acquired as the sum of the product between the ratio of different stage fracture with the total area and the corresponding UCS. With both the physical and chemical weathering characteristics, the integrative weathering condition of the rock sample is depicted.

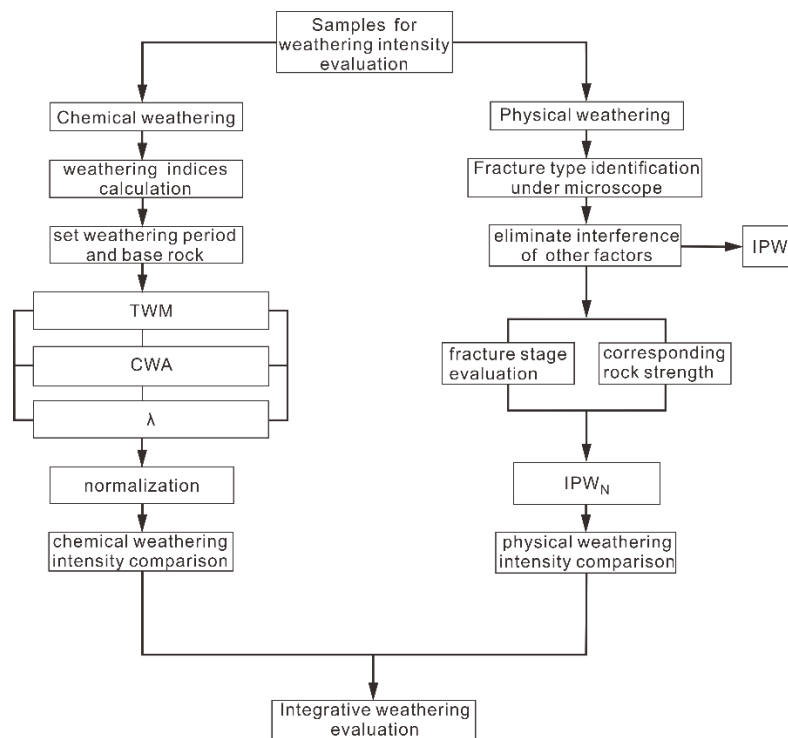


**Fig. 7** Workflow for integrative weathering evaluation



---

**Statement of personal contribution in publications**

**Rock alteration at the post-Variscan nonconformity: implications for Carboniferous-Permian surface weathering versus burial diagenesis and paleoclimate evaluation.**

---

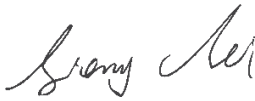
## Statement of personal contribution

### **Rock alteration at the post-Variscan nonconformity: implications for Carboniferous-Permian surface weathering versus burial diagenesis and paleoclimate evaluation.**

Fei Liang, Jun Niu, Adrian Linsel, Matthias Hinderer, Dirk Scheuven and Rainer Petschick

*Solid Earth*, 2021,12(5), 1165–1184.

- (i) Fei Liang as the first author collected and prepared all the samples, conceptualized and prepared the paper.
- (ii) Jun Niu provided the foundation and helped measure the trace and major elements.
- (iii) Dirk Scheuven and Rainer Petschick helped conducted the SEM and XRD measurements.
- (iv) Matthias Hinderer and Adrian Linsel helped revise the manuscript and supervised this research.

Signature: 

Date: Darmstadt, 2.3.2023



---


## Statement of personal contribution

### **Rock alteration at the post-Variscan nonconformity: implications for Carboniferous-Permian surface weathering versus burial diagenesis and paleoclimate evaluation.**

Fei Liang, Jun Niu, Adrian Linsel, Matthias Hinderer, Dirk Scheuven and Rainer Petschick

*Solid Earth*, 2021,12(5), 1165–1184.

- (i) Fei Liang as the first author collected and prepared all the samples, conceptualized and prepared the paper.
- (ii) Jun Niu provided the foundation and helped measure the trace and major elements.
- (iii) Dirk Scheuven and Rainer Petschick helped conducted the SEM and XRD measurements.
- (iv) Matthias Hinderer and Adrian Linsel helped revise the manuscript and supervised this research.

Signature: 

Date: Darmstadt, 2.3.2023

---

## Statement of personal contribution

### **Rock alteration at the post-Variscan nonconformity: implications for Carboniferous-Permian surface weathering versus burial diagenesis and paleoclimate evaluation.**

Fei Liang, Jun Niu, Adrian Linsel, Matthias Hinderer, Dirk Scheuven and Rainer Petschick

*Solid Earth*, 2021,12(5), 1165–1184.

- (i) Fei Liang as the first author collected and prepared all the samples, conceptualized and prepared the paper.
- (ii) Jun Niu provided the foundation and helped measure the trace and major elements.
- (iii) Dirk Scheuven and Rainer Petschick helped conducted the SEM and XRD measurements.
- (iv) Matthias Hinderer and Adrian Linsel helped revise the manuscript and supervised this research.

Signature:



Date: Darmstadt, 2.3.2023

## Statement of personal contribution

**Rock alteration at the post-Variscan nonconformity: implications for Carboniferous-Permian surface weathering versus burial diagenesis and paleoclimate evaluation.**

Fei Liang, Jun Niu, Adrian Linsel, Matthias Hinderer, Dirk Scheuven and Rainer Petschick  
*Solid Earth*, 2021,12(5), 1165–1184.

- (i) Fei Liang as the first author collected and prepared all the samples, conceptualized and prepared the paper.
- (ii) Jun Niu provided the foundation and helped measure the trace and major elements.
- (iii) Dirk Scheuven and Rainer Petschick helped conducted the SEM and XRD measurements.
- (iv) Matthias Hinderer and Adrian Linsel helped revise the manuscript and supervised this research.

Signature:



Date:

5.3.2023

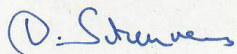
*Note: Adrian Linsel changed his name to Adrian Vogel due to marriage.*

## Statement of personal contribution

### **Rock alteration at the post-Variscan nonconformity: implications for Carboniferous-Permian surface weathering versus burial diagenesis and paleoclimate evaluation.**

Fei Liang, Jun Niu, Adrian Linsel, Matthias Hinderer, Dirk Scheuven and Rainer Petschick  
*Solid Earth*, 2021,12(5), 1165–1184.

- (i) Fei Liang as the first author collected and prepared all the samples, conceptualized and prepared the paper.
- (ii) Jun Niu provided the foundation and helped measure the trace and major elements.
- (iii) Dirk Scheuven and Rainer Petschick helped conducted the SEM and XRD measurements.
- (iv) Matthias Hinderer and Adrian Linsel helped revise the manuscript and supervised this research.

Signature: 

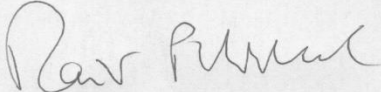
Date: 02-03-2023

## Statement of personal contribution

### **Rock alteration at the post-Variscan nonconformity: implications for Carboniferous-Permian surface weathering versus burial diagenesis and paleoclimate evaluation.**

Fei Liang, Jun Niu, Adrian Linsel, Matthias Hinderer, Dirk Scheuvens and Rainer Petschick  
*Solid Earth*, 2021, 12(5), 1165–1184.

- (i) Fei Liang as the first author collected and prepared all the samples, conceptualized and prepared the paper.
- (ii) Jun Niu provided the foundation and helped measure the trace and major elements.
- (iii) Dirk Scheuvens and Rainer Petschick helped conducted the SEM and XRD measurements.
- (iv) Matthias Hinderer and Adrian Linsel helped revise the manuscript and supervised this research.

Signature: 

Date: 3.3.2023

---

**Quantification of Physical and Chemical Paleoweathering at the Microscale - A  
New Concept**

---

## Statement of personal contribution

### **Quantification of Physical and Chemical Paleoweathering at the Microscale - A New Concept.**

Liang Fei, Matthias Hinderer, Jens Hornung

*International Journal of Earth Sciences*, 2022 (online: <https://doi.org/10.1007/s00531-022-02281-3> ).

- (i) Fei Liang as the first author developed the methodological concept, prepared all the figures, and tables, verified the method with a case study, and wrote the paper.
- (ii) Matthias Hinderer and Jens Hornung supervised this research and helped revise the structure of the manuscript, build the conceptual pictures, and polish the language problems.

Signature: 

Date: 3.3.2023

---

## Statement of personal contribution

### Quantification of Physical and Chemical Paleoweathering at the Microscale - A New Concept.

Liang Fei, Matthias Hinderer, Jens Hornung

*International Journal of Earth Sciences*, 2022 (online: <https://doi.org/10.1007/s00531-022-02281-3>).

- (i) Fei Liang as the first author developed the methodological concept, prepared all the figures, and tables, verified the method with a case study, and wrote the paper.
- (ii) Matthias Hinderer and Jens Hornung supervised this research and helped revise the structure of the manuscript, build the conceptual pictures, and polish the language problems.

Signature:



Digital unterschrieben von Dr. Jens Hornung  
DN: cn=Dr. Jens Hornung, o=Technische  
Universität Darmstadt, ou  
email=j.hornung@geo.tu-darmstadt.de, c=DE  
Datum: 2023.03.03 00:14:00 +0100

Date: Darmstadt, 2.3.2023



---

**Palaeo-weathering of different basement rocks along a first order nonconformity -  
case study at the post-Variscan nonconformity (Germany)**

---

## Statement of personal contribution

### **Palaeo-weathering of different basement rocks along a first-order nonconformity – case study at the post-Variscan nonconformity (Germany)**

Liang Fei, Matthias Hinderer, Jens Hornung

*Catena, 2023 (accepted by Catena).*

- (i) Fei Liang as the first author collected and prepared all the samples, conceptualized the outline, and prepared the paper.
- (ii) Matthias Hinderer helped conceptualized and supervised this research.
- (iii) Jens Hornung helped revise and polish the manuscript.

Signature: 

Date: 3.3.2023

---

## Statement of personal contribution

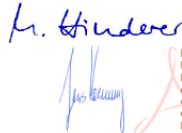
### **Palaeo-weathering of different basement rocks along a first-order nonconformity – case study at the post-Variscan nonconformity (Germany)**

Liang Fei, Matthias Hinderer, Jens Hornung

*Catena*, 2023 (accepted by *Catena*).

- (i) Fei Liang as the first author collected and prepared all the samples, conceptualized the outline, and prepared the paper.
- (ii) Matthias Hinderer helped conceptualized and supervised this research.
- (iii) Jens Hornung helped revise and polish the manuscript.

Signature:



Digital unterschrieben von Dr. Jens  
Hornung  
DN: cn=Dr. Jens Hornung,  
o=Technische Universität Darmstadt,  
ou=email-hornung@geo.tu-  
darmstadt.de, c=DE  
Datum: 2023.03.03 00:16:54 +0100

Date: Darmstadt, 2.3.2023

